Synthesis and characterisation of single-source CVD precursors for M-N-Si composites

Cosham, Samuel

Award date:
2010

Awarding institution:
University of Bath

Synthesis and Characterisation of Single-Source CVD Precursors for M-N-Si Composites

Samuel David Cosham

A thesis submitted for the degree of Doctor of Philosophy

University of Bath

Department of Chemistry

May 2010

Copyright

University of Bath, May 2010

Abstract

As advances within microelectronic technology have made through the miniaturisation of integrated circuits, inherent problems have become more apparent and consequently more of an issue. The use of copper interconnects to overcome several of these problems requires the inclusion of a diffusion barrier between the interconnect and substrate. Subsequently, ternary metal nitrides, including TiNSi and TaNSi, have been found to be effective diffusion barrier materials. The principle objective of the work presented was the synthesis and characterisation of early transition metal complexes containing metal, nitrogen and silicon components which may potentially be used as single-source CVD precursors for the deposition of diffusion barrier materials.

Chapter 1 provides the reader with a brief background into the history and internal structure of the integrated circuit. The function of the diffusion barrier within this structure is discussed in further detail, including the materials commonly employed. Current methods used in the fabrication of diffusion barrier materials are reviewed. The limitations of such methods and the requirement for an effective single-source CVD precursor are highlighted.

Chapter 2 describes the synthesis, characterisation and structures of a series of Group 4 metal complexes which have been prepared using primary aminosilanes of general formula $[RR'_2SiNH_2]$.The metal complexes presented typically contain a planar four-membered $\{M_2N_2\}$ ring. The π-bonding within the $\{M_2N_2\}$ ring is discussed in further detail.

Chapter 3 describes the synthesis, characterisation and structures of several titanium complexes prepared using bidentate aminosilanes of general formula $[R_2Si(NHR')_2]$. In addition, the reaction between the titanium complex $[Ti(N^tBu)Cl_2(py)_2]$ and lithium hexamethyldisilazane is described. The formation within the resulting titanium complex of a four-membered {TiNSiC} ring via γ-hydrogen elimination is discussed.

Chapter 4 describes the reactions between the primary aminosilanes presented in Chapter 2 and the tantalum organometallic reagent $Ta(NMe_2)_5$. As part of a wider study, the reactivity of these aminosilanes with zinc and manganese organometallic reagents is explored.

Chapter 5 describes the thermal profiling of Group 4 and tantalum metal complexes presented in Chapter 2 to 4. Suitable compounds are subsequently selected from these complexes to perform a series of depositions by AACVD. The compositions of the thin films obtained are discussed.

Chapter 6 contains experimental details and characterisation data for Chapter 2 to 5.

Appendices list the data for X-ray structural determinations presented in this thesis.

Contents

We shall never get people whose time is money to take much interest in atoms.

- Samuel Butler, *The Notebooks*, c.1880

‘If you spend your whole time thinking about the universe, you tend to forget the less important bits of it. Like your pants. And ninety-nine out of a hundred ideas (philosophers) come up with are totally useless.’

‘Why doesn’t anyone lock them away safely, then? They don’t sound much use to *me*,’ said Brutha.

‘Because the hundredth idea,’ said Om, ‘is generally a humdinger.’

- Terry Pratchett, *Small Gods*, 1992

Acknowledgements

I have been a student at the University of Bath since 2001 – a long time on paper, although it doesn't seem it. Looking back, I realise that two people in particular are to thank/blame for that. As a college student visiting the department on an open day, I remembered being taken on a tour of the facilities by Kieran Molloy, which helped convince me to apply to the university. As a final year undergraduate at the university, I was convinced by Andy Johnson to apply to do a PhD. I'd like to thank both Andy and Kieran for the opportunity to work with them, their enthusiasm, guidance, support and most of all their patience.

Many thanks also to members of the Johnson, Molloy and Raithby groups, both past and present, for their friendship, support and countless favours! Such people include Steve Richards, Alex Willcocks, Hazel Davies, Nathan Hollingsworth, Teresa Savarese, Olivia Koentjoro, Simon Brayshaw and Mark Warren.

I would also like to thank the folks at SAFC HiTech on both sides of the Pond. At Bromborough, I'd like to thank Andy Kingsley and Raj Odedra for their expertise and help with the TGA and VP studies, and for looking after me during my visit to the Wirral. At Haverhill I'd like to thank Jeff Anthis in particular for the lifts to and from work through the snow and his help with thermal depositions, and in general also Adam, Brian, Jason, Nam, Heather, Ravi, Brian, Rick, Kathy, Cathy, Mike, Brian and everyone else who made me feel welcome during my five week stay Stateside. Apologies to anyone who I've missed out – probably Brian!

I am also indebted to the University of Bath, SAFC HiTech and EPSRC for providing the facilities and funding to perform the work presented.

I should like to thank John Lowe for his help with the NMR and David Morgan for providing XPS analysis.

On a more personal note I'd like to thank Iwan and Jeremy for the countless numbers of healthy debates/whinges over a cup of tea! They definitely helped to keep me (relatively) sane over the past few years!

To Ruth, I am indebted for her love, for her encouragement and support, and for keeping me calm when my computer died for the umpteenth time. Finally I'd like to thank my parents and sister, whose constant love, support and encouragement keep me going. Just knowing you are there helped me along, through good times and bad. Thankyou.

Declaration

The work described in this thesis was conducted by the author at the University of Bath between October 2005 and September 2009. It represents the author's original and independent work, except where specific reference is made to the contrary. Neither the whole nor any part of this thesis has been submitted previously in support of a degree at this or any other university. It does not exceed the prescribed limit, including tables, references and appendices.

Abbreviations

AACVD	Aerosol-Assisted Chemical Vapour Deposition
α	Alpha
Å	Angstrom
ap	Apparent
APCVD	Atmospheric Pressure Chemical Vapour Deposition
ALCVD	Atomic Layer Chemical Vapour Deposition
ALD	Atomic Layer Deposition
ALE	Atomic Layer Epitaxy
at. %	Atomic percentage
β	Beta
br	Broad
^{n}Bu	butyl
^{i}Bu	*iso*-butyl
^{t}Bu	*tert*-butyl
CMP	Chemical Mechanical Polishing
CVD	Chemical Vapour Deposition
J	Coupling Constant
Cp	Cyclopentadienyl, $C_5H_5^-$
^{o}	Degree
δ	Delta, Chemical shift
Δ	Delta
DFT	Density Functional Theory
k	Dielectric constant
DLI	Direct Liquid Injection
d	Doublet
eV	Electron Volt
EDX	Energy-Dispersive X-ray spectroscopy

η	Eta
Et	Ethyl
FET	Field-Effect Transistor
FBR	Fluidised-Bed Reactor
X	Halide
HMDS	Hexamethyldisilazane, $HN\{Si(CH_3)_3\}_2$
HOMO	Highest Occupied Molecular Orbital
hr	Hour
IR	Infra-red
IC	Integrated Circuit
L	Ligand
L/min	Litres Per Minute
LPCVD	Low Pressure Chemical Vapour Deposition
LUMO	Lowest Unoccupied Molecular Orbital
M	Mass
M	Metal
MN	Metal Nitride
MOCVD	Metalorganic Chemical Vapour Deposition
MOSFET	Metal-Oxide Field-Effect Transistor
Me	Methyl
µm	Micrometre
µΩ-cm	MicroOhm Per Centimetre
mg	Milligram
mL	Millilitre
MO	Molecular Orbital
µ	Mu
m	Multiplet
nm	Nanometres

n-type	Negative-type
Nph	Neophyl
n	non-bonding
NMR	Nuclear Magnetic Resonance
P	Partial pressure
ppm	Parts Per Million
Pa	Pascal
PDMAT	Pentakis(dimethylamido)titanium, $Ta\{N(CH_3)_2\}_5$
%	Percentage
Ph	Phenyl
PVD	Physical Vapour Deposition
π	Pi
PACVD	Plasma-Assisted Chemical Vapour Deposition
PECVD	Plasma Enhanced Chemical Vapour Deposition
p-type	Positive-type
^{i}Pr	*iso*-propyl
py	Pyridine, C_5H_5N
q	Quartet
SEM	Scanning Electron Microscopy
sept	Septet
σ	Sigma
σ*	Sigma Anti-bonding
s	Singlet
Σ	Sum of
τ	Tau
thf	Tetrahydrofuran, C_4H_8O
TDEAT	Tetrakis(diethylamido)titanium, $Ti\{N(CH_2CH_3)_2\}_4$
TDMAT	Tetrakis(dimethylamido)titanium, $Ti\{N(CH_3)_2\}_4$

TEMAT	Tetrakis(ethylmethylamido)titanium, $Ti\{N(CH_2CH_3)(CH_3)\}_4$
TGA	Thermogravimetric Analysis
t	Triplet
TEM	Tunneling Electron Microscopy
VP	Vapour Pressure
VT-NMR	Variable Temperature Nuclear Magnetic Resonance
W	Watt
XRD	X-ray Diffraction
XPS	X-ray Photoelectron Spectroscopy

Key to Compound Numbering

1. $[Ph_3SiNH_2]$
2. $[Ph_2HSiNH_2]$
3. $[Et_3SiNH_2]$
4. $[^tBuMe_2SiNH_2]$
5. $[(Me_2N)_3SiNH_2]$
6. $[\{(Me_2N)_2Ti(\mu_2\text{-}NSiPh_3)\}_2]$
7. $[\{(Me_2N)_2Zr(\mu_2\text{-}NSiPh_3)\}_2]$
8. $[\{(Me_2N)_2Hf(\mu_2\text{-}NSiPh_3)\}_2(HNMe_2)]$
9. $[\{(Me_2N)_2Ti(\mu_2\text{-}N^tBu)\}_2]$
10. $[\{(Me_2N)_2Ti(\mu_2\text{-}NSiEt_3)\}_2]$
11. $[\{(Me_2N)_2Zr(\mu_2\text{-}NSiEt_3)\}_2]$
12. $[\{(Me_2N)_2Hf(\mu_2\text{-}NSiEt_3)\}_2]$
13. $[\{(Me_2N)_2Ti(\mu_2\text{-}NSi^tBuMe_2)\}_2]$
14. $[\{(Me_2N)_2Zr(\mu_2\text{-}NSi^tBuMe_2)\}_2]$
15. $[\{(Me_2N)_2Hf(\mu_2\text{-}NSi^tBuMe_2)\}_2]$
16. $[\{(Me_2N)_2Ti(\mu_2\text{-}NSi[NMe_2]_3)\}_2]$
17. $[\{(Me_2N)_2Zr(\mu_2\text{-}NSi[NMe_2]_3)\}_2]$
18. $[\{(Me_2N)_2Hf(\mu_2\text{-}NSi[NMe_2]_3)\}_2]$

19. $[Me_2Si(NH^tBu)_2]$
20. $[Me_2Si(NH^iPr)_2]$
21. $[Me_2Si(NHCH_2CH_2NMe_2)_2]$
22. $[Ph_2Si(NH^tBu)_2]$
23. $[Me_2Si(N[Li]^tBu)_2]$
24. $[Ph_2Si(N[Li]^tBu)_2]$
25. $[\{Me_2Si(N^tBu)_2\}_2Ti]$
26. $[\{Ph_2Si(N^tBu)_2\}_2Ti]$
27. $[Ti(N^tBu)Cl_2(py)_2]$
28. $[\{[Me_2Si(N^tBu)_2]Ti(\mu_2\text{-}N^tBu)\}_2]$
29. $[\{[Ph_2Si(N^tBu)_2]Ti(\mu_2\text{-}N^tBu)\}_2]$
30. $[\{(Me_3SiNSiMe_2CH_2)Ti(N^tBu)\}_2]$

31. $[(Me_2N)_3TaNSiPh_3]$
32. $[(Me_2N)_3TaNSi(NMe_2)_3]$
33. $[\{MeZnNHSiPh_3\}_2]$
34. $[\{MeZnNHSi(NMe_2)_3\}_2]$
35. $[\{(MeCp)MnNHSiPh_3\}_2]$

Chapter 1

Introduction

1.1 Evolution of computers

In the modern world in which we live today, many aspects of human activity are controlled or affected by computers and digital software, from personal computers and mobile phones to cookers and car manufacture and operation. As greater demands are put on the functions of these computers, so advancements in the materials and methods used in their fabrication are required to meet them.

1.1.1 Brief history of computer

A computer is defined in the Oxford English Dictionary as "A device or machine for performing or facilitating calculation".[1] Various mechanical calculating devices have been designed and used by mankind for centuries, from the abacus and slide rule to Charles Babbage's 'Analytical Engine', designed in 1837, which first allowed some programmability. However, it was not until the 1940s that electronic devices recognisable to modern computers were first developed. These first-generation computers included: [2, 3]

- The Z3, designed by Konrad Zuse in Germany, in 1941, was the first program-controlled, fully automatic digital computer, and was based on 2000 electromechanical relay switches.
- Colossus, designed by Tommy Flowers and built at Bletchley Park, Great Britain, in 1944, was the first electronic digital computer, and was based on an array of electronic thermionic valves (1500 in the Mk1, then 2400 in the Mk2 which was 5 times faster).
- And ENIAC (Electronic Numerical Integrator And Computer), designed by John Mauchly and J. Presper Eckert at the University of Pennsylvania, USA, in 1945, was the first general-purpose electronic programmable computer, and was based on an array of over 17000 thermionic valves.

Like Colossus and ENIAC, many other first-generation computers employed the use of thermionic valves, as did many other early-generation electronics such as televisions and radios. Invented by Sir John A. Fleming in 1904, the thermionic valve consists of an insulating, temperature-resistant bulb (usually made of glass) from which all air has been removed. Within this vacuum are two electrodes – a thin wire filament that forms the cathode and a metal plate, which has a positive charge relative to the filament, forming the anode. When the filament is heated by passing a current through it, electrons are emitted in a process of thermionic emission. These electrons are drawn to the positive anode, creating an electrical flow in one direction only, from cathode to anode, much like a modern diode. The later introduction of a third electrode by Lee de Forest, a fine wire mesh situated in the space between the anode and cathode, enabled the valve to act like a switch by adjusting the voltage on this mesh to affect the electron flow between the two original electrodes (figure 1.1).[3, 4]

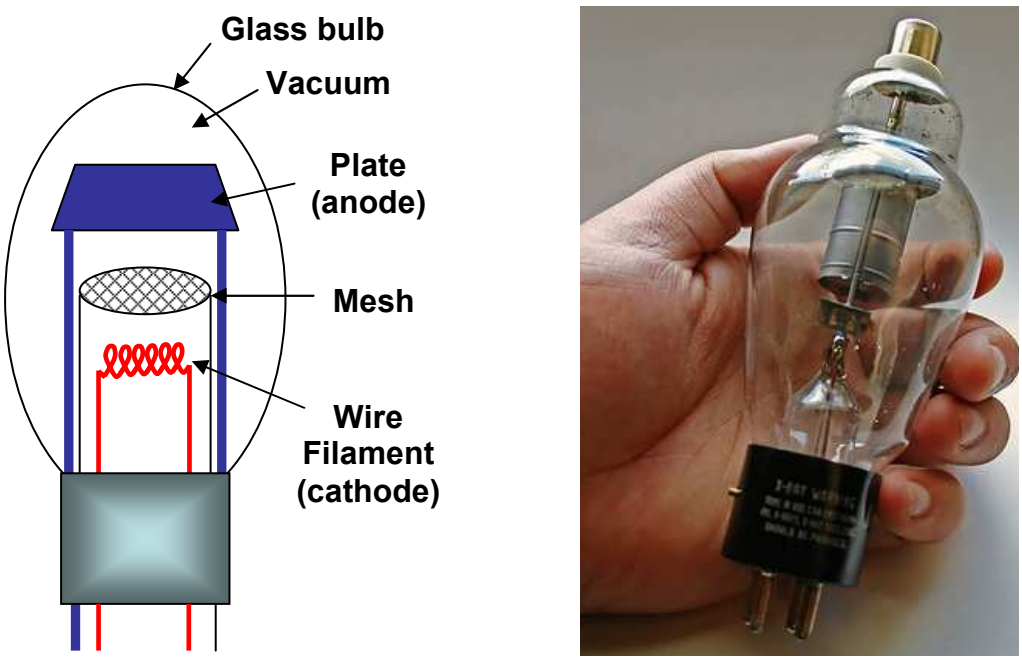

Figure 1.1: Schematic of a thermionic valve (left), and picture (right).

However, the use of thermionic valves has several disadvantages. Compared to later technologies, thermionic valves are relatively unreliable, often suffering device failure due to small amounts of air within the bulb oxidising the cathode and impeding its emission

capabilities. Any gas molecules present within the tube may also themselves be ionised, which can interfere with the flow of electrons between the cathode and anode. They also require vast amounts of electrical power to heat the cathode, which in turn can lead to problems with heat dissipation – a large temperature difference between the cathode and anode is essential to prevent thermionic emission from the anode countering the flow from the cathode. Another important factor is size – the vast numbers of valves required to perform calculations meant computers like Colossus and ENIAC filled entire rooms (Figure 1.2).

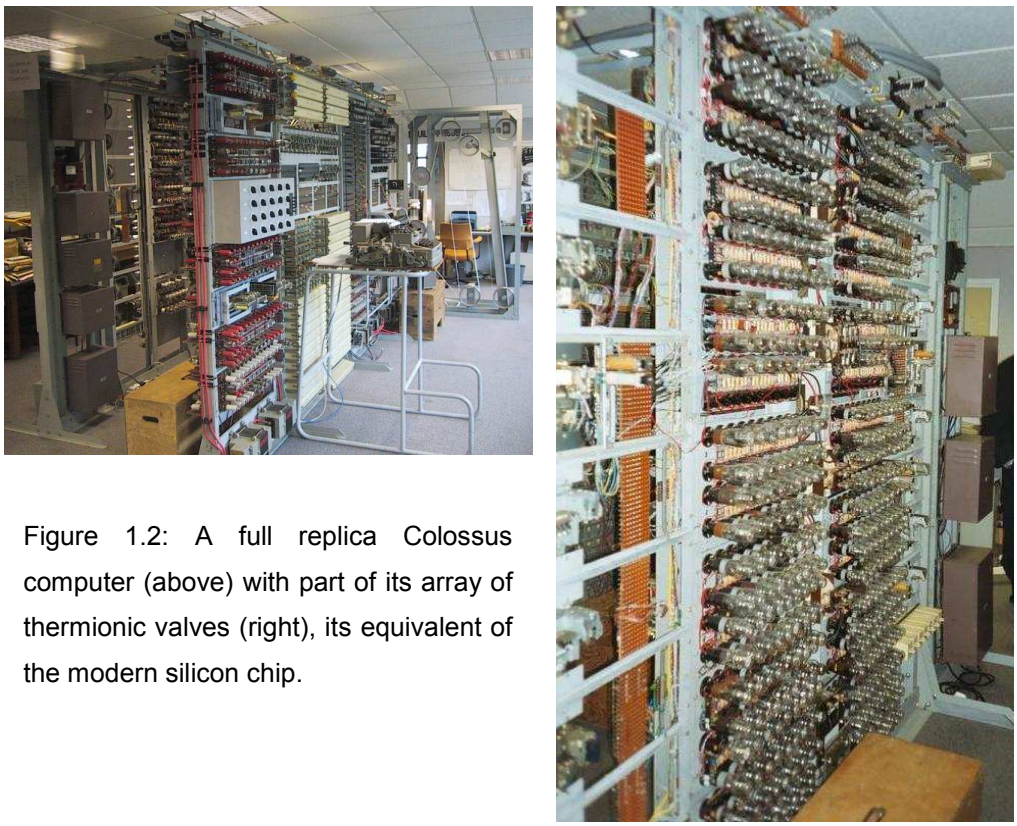

Figure 1.2: A full replica Colossus computer (above) with part of its array of thermionic valves (right), its equivalent of the modern silicon chip.

A key step in the evolution of electronics came with the development of semiconductors and the resulting invention of the transistor. Whilst the principle behind a transistor was first patented in 1925 by Austrian-Hungarian physicist Julius Edgar Lilienfield,[5] it was not until 1947 that an operational transistor was developed by William Shockley, John Bardeen and Walter Houser Brattain.[2 - 4] For this work they were jointly awarded the Nobel Prize in physics in 1956.

Created from a single piece of semiconducting material the transistor, like the thermionic valve, has three electrodes that can act like a switch, with the current flowing between the two terminals being controlled by the voltage on the third ‘gate’ or ‘base’ terminal (figure 1.3). However, they were proven to be more advantageous than the valve, being smaller, cheaper, more reliable and requiring less electrical power to work, in part due to the fact that they contain no cathode requiring heating. Consequently transistors were used in the second-generation of computers and were capable of more sophisticated calculations than earlier first generation computers such as Colossus.[4]

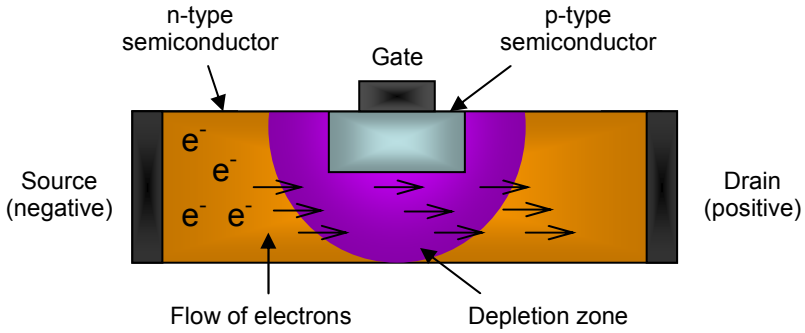

Figure 1.3: Schematic of a field effect transistor (FET). Altering of the potential at the gate terminal can create a depletion zone in the n-type semiconductor, preventing the flow of electrons from the source electrode to the drain electrode.[4]

Original work on transistors primarily used germanium as the basic semiconducting material. This was soon superseded by silicon, as silicon is more thermally stable. By the late 1950s several groups had combined several transistors, along with other electrical components such as capacitors and resistors, formed together on a single substrate to create a discrete working circuit (figure 1.4). These ‘integrated’ circuits (ICs) were smaller and cheaper than circuits constructed using separate components, and also used less power – ideal qualities for their use in one of the driving forces behind the development of the IC at this time, the ‘space race’ between the USA and the USSR. These benefits resulted in third- and future-generation computers operating using silicon chip ICs.[4, 6]

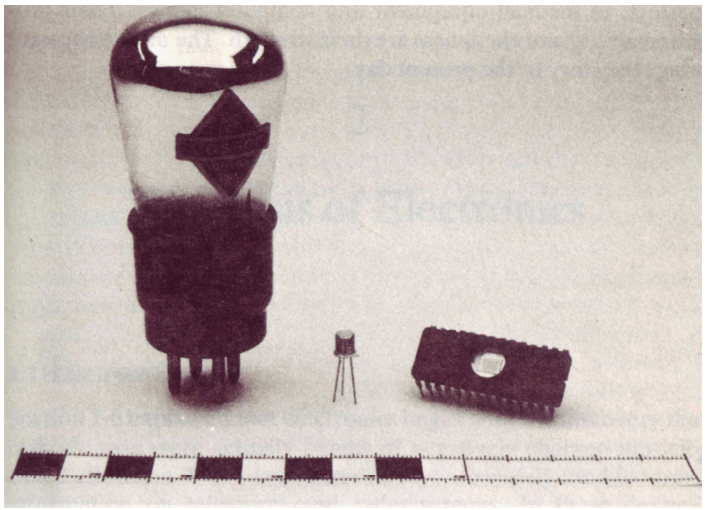

Figure 1.4: Comparison in size of a thermionic valve (left), discrete transistor (centre), and integrated circuit (right).[4]

1.1.2 Evolution of the silicon chip

The starting point for the formation of the silicon chip is a very thin wafer of extremely pure crystalline silicon, cut from a single crystal fabricated from a silicon melt using the Czochralski method.[4, 7] This wafer is treated at high temperatures with a dopant gas to enhance the intrinsic semiconducting properties of the silicon substrate. Doping with a Group 13 element, such as gallium or boron, will lead to atoms within the wafer that are nominally 'electron-deficient' with respect to the bulk material. These electron deficiencies can be considered as positively charged holes. Silicon doped in this way is referred to as a p-type (positive) semiconductor. Alternatively, doping with a Group 15 element, such as phosphorus or arsenic, will result in 'electron-rich' sites within the bulk silicon. These extra electrons give an overall negative charge to the silicon, which is referred to as an n-type (negative) semiconductor (figure 1.5).[4]

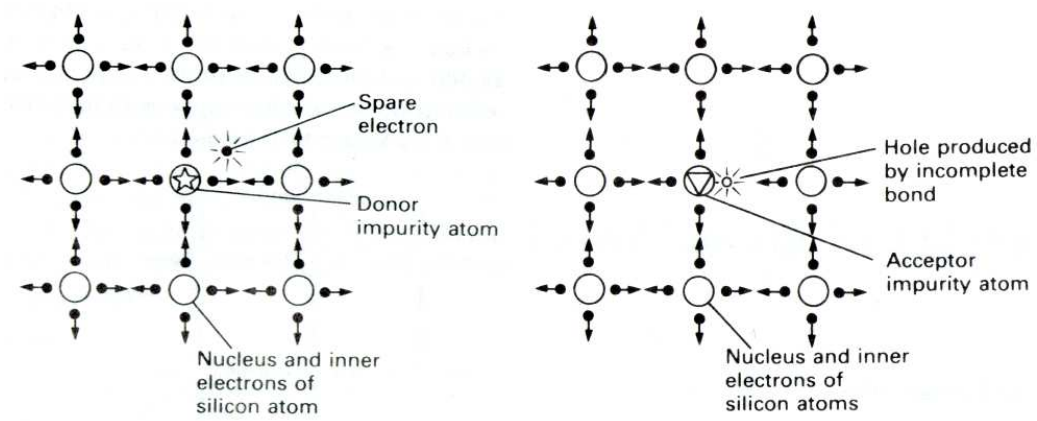

Figure1.5: Schematic of an electron rich site within an n-type semiconductor (left), and of a 'hole' within a p-type semiconductor (right).[4]

Doping of the silicon wafer is followed by heating at approximately 1000 ^{o}C in an oxygen atmosphere to form a layer of SiO_2 on the surface to act as an insulting layer – the dielectric.[4] Using a process called lithography a required pattern is mapped out on the surface and any exposed dielectric is then etched away to create holes and vias down to the silicon substrate, into which either dopant gas or metal for the interconnects, historically aluminium, can be deposited (figure 1.6). Any excess material can be removed and the substrate planarized using techniques such as chemical mechanical polishing (CMP). This reduces the topography of the substrate in order to allow greater resolution of smaller features.[8] Over several hundred steps of repeated doping, patterning, etching and deposition of metal, pure silicon and dielectric a chip that contains an integrated circuit of many levels can be created that consists purely of Si, SiO_2, and metal.

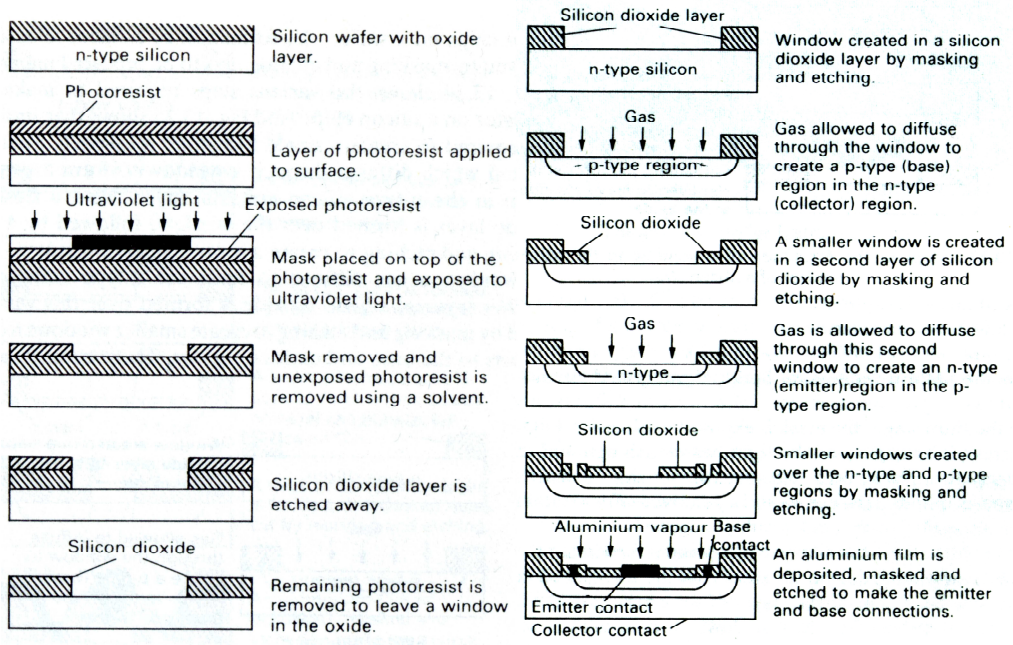

Figure 1.6: The basic steps of lithography to create a via in the dielectric (left), and the further steps involved in the formation of a single npn transistor on a silicon chip (right).[4]

As advancements in microelectronics have progressed, the IC has inadvertently evolved in concordance with predictions made by Gordon Moore, the cofounder of Intel, in 1965, that stated the number of components per chip, i.e. transistor density, would double every year whilst also keeping costs to a minimum.[6] This was later revised in 1975 to doubling every two years.[9] Consequently the number of components on a single silicon chip has increased from the tens of transistors in the original Small-Scale Integration (SSI) devices, to over 1 billion for a modern Ultra-Large Scale Integration (ULSI) devices such as the Dual-Core Intel 2 Processor (Figure 1.7).[10]

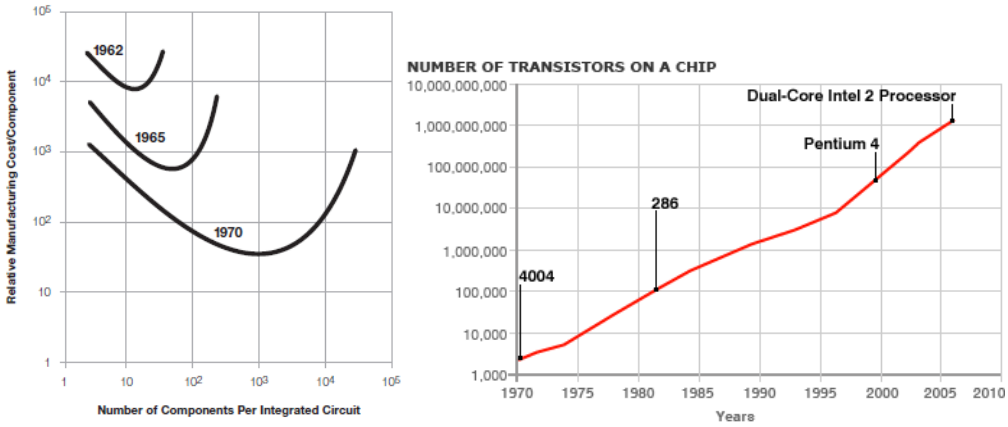

Figure 1.7: No. of components per integrated circuits vs the relative manufacturing costs (left),[6] and the increase in the number of transistors per chip since 1970 (right).[10]

Whilst increasing transistor density through miniaturisation within ICs brings benefits in terms of faster processing speeds, a reduction in switching power consumption and lower production costs per unit, inherent problems within the IC become more apparent and consequently more of an issue. These problems include:

- Electromigration; a mass transport process involving the gradual movement of ions encountered within the metal interconnects of the IC. The high momentum of electrons flowing through the interconnect is transferred to the corresponding metal ions, forcing them in the direction of current. This may result in the formation of hillocks at the anode creating a short circuit, or voids at the cathode consequently increasing the resistance or ultimately breaking the circuit. This process becomes increasingly prominent as current density increases, as encountered in the miniaturization of ICs reducing the cross-sectional area of metal interconnects, as well as at higher temperatures.[11, 12]

- Increased resistance and capacitance times resulting in small but significant time delays to the electrical signal, reducing the speed at which ICs can perform calculations.[8, 13, 14]

- An increase in heat generated as the transistors work due to an increase in transistor density. This may have serious implications including increases in electrical resistance. Consequently a thermal limit to miniaturization will exist, where the amount of heat generated offsets any efficiency gained by having more transistors present in the IC.

These problems have led to aluminium being replaced by copper as the metal of choice for interconnects within ICs due to copper's lower electrical resistivity compared to aluminium (bulk values 1.7 vs 2.7 μΩ-cm, respectively)[13] and superior resistance to electromigration (copper diffusity being approximately 1/15 that of polygranular aluminium).[11, 15]

However, the use of copper invokes a new set of problems to overcome. At high temperatures, such as those encountered during the manufacturing process of ICs, copper atoms can readily diffuse into the silicon and SiO_2 substrates, a phenomenon that is the subject of several studies.[13, 16, 17] This diffusion of copper atoms into the substrate can cause device failure in a two-fold manner. Firstly, copper atoms form good sites for the recombination of electrons and 'holes',[18] destroying the n-type and p-type silicon. Secondly, copper and silicon are capable of reacting to form more uniformly stoichiometric materials such as copper silicide, Cu_3Si (Figure 1.8), which can significantly increase the resistance of the substrate.[19 - 21] To prevent this diffusion of copper atoms a barrier is needed between the Cu and SiO_2/Si substrate. Alternative metals to copper for the interconnect have been investigated, including silver, as it has a lower bulk resistivity than copper,[22] and also gold.[23] Unfortunately, like copper they too diffuse rapidly into silicon, and therefore also require a diffusion barrier, whilst susceptibility of the metal to electromigration may be increased, especially for silver.[12, 22, 23] Additionally, with the cost of silver and gold being disproportionately more with respect to copper, the use of silver and gold presents an expensive option and is therefore commercially unfavourable.

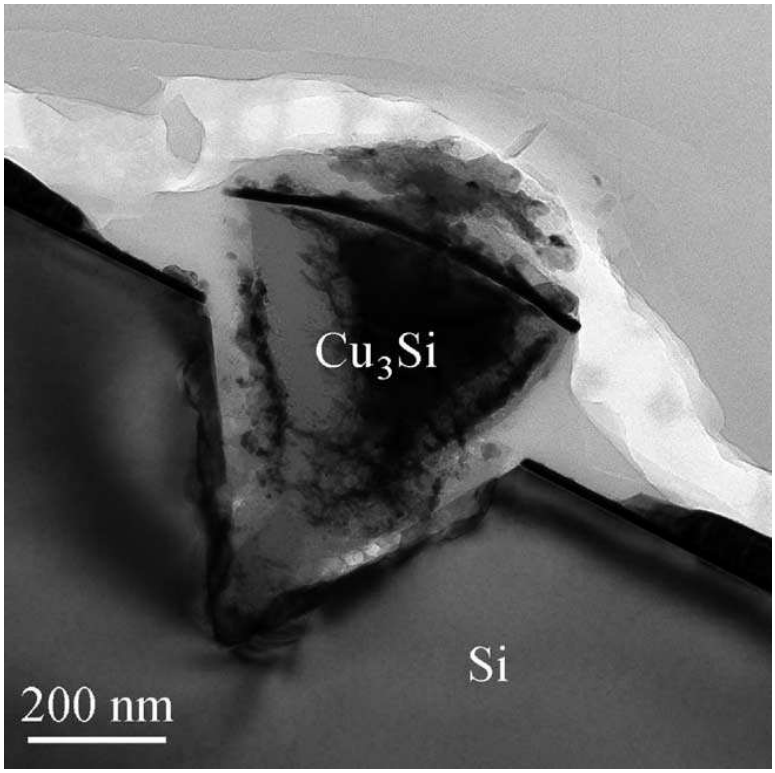

Figure 1.8: Cross-sectional TEM image of $Cu/Ta_{56}Si_{19}N_{25}/Si$ sample after annealing at 630^{o}C for 1 h. Wedge-shaped Cu_3Si crystallites are often observed growing into the Si substrate upon barrier failure.[20]

Concurrent to this change from aluminium to alternative metals such as copper is an increasing shift in the dielectric layer material from SiO_2 to materials with a lower dielectric constant (k) in an effort to reduce capacitance and the cross-talk between copper interconnects.[8, 16, 24] Materials that have been used include fluorosilicate glasses, organosilicate glasses,[25] aerogels [14] and organic polymers such as polyimide.[26, 27] Many of these materials are to varying degrees porous, as a function of decreasing the weight density of the material, i.e. by increasing the porosity, is to decrease k. A consequence of this porosity is, again, a low resistance to copper atoms diffusing into the dielectric layer. These pores may be sealed with a thin layer of material, such as the organic polymer Parylene, to help prevent penetration of the dielectric during fabrication processes of the IC,[28] however a barrier layer is still required to increase reliability of the IC during operation and to help promote adhesion of the copper layer.[28, 29]

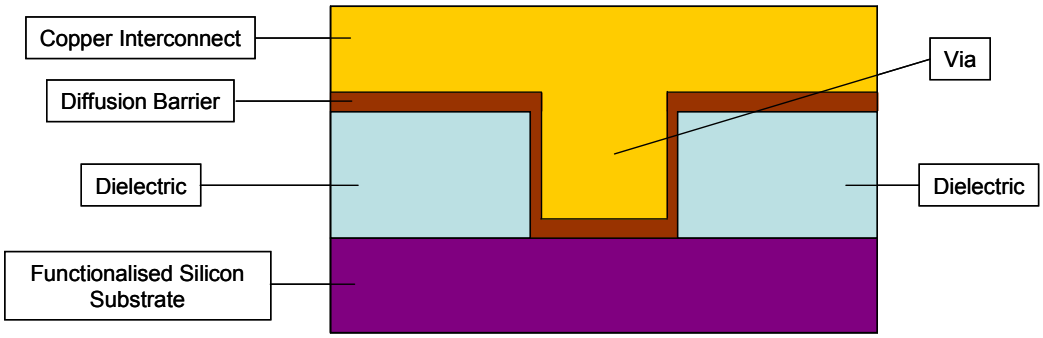

Figure 1.9: Simplified schematic representation of the cross-section of an integrated circuit.

1.2 Diffusion Barriers

As has been discussed, to prevent device failure caused by the diffusion of copper atoms from the interconnects into surrounding layers within the IC a thin barrier layer between the two is required. For a material to be an effective candidate for use as a diffusion barrier it has to meet several requirements: [13, 18, 30]

- Resistance to the diffusion of copper; closely linked to this is the requirement for promoting the adhesion of copper to the substrate during the manufacturing process. In general Cu doesn't adhere that well to dielectric materials.[11, 28] Strong adhesion to the copper is crucial to help reduce the effect of electromigration.[31] Whilst copper is more resistant to this than aluminium, movement of copper atoms and the resulting thinning of the interconnect at the cathode may still occur over time. The dominant diffusion pathways by which electromigration occurs are usually grain boundaries, or, as is predominantly the case for copper interconnects, at interfaces between the interconnect and surrounding materials.[12, 15, 32, 33]

- Effective at a very low thickness; as miniaturisation increases, space within the chip is at a premium and can therefore not afford to be wasted. Additionally, if less space is taken up by the diffusion barrier then less of a strain is put upon the amount of

space that can be occupied by the interconnect, increasing the potential for a greater cross-sectional area and therefore reducing its electrical resistance. In sub-0.25 μm features it has been suggested that the barrier should be effective at thicknesses less than or equal to 10 nm.[34, 35]

- High stability at elevated temperatures to reactivity with dielectric and interconnect layers, as well as any stress within the film that may result in defects occurring.

- Low electrical resistance; ideally this should be less than 1000 μΩ-cm. Although it acts as a barrier between the copper and the silicon, any electrical signal must still be able to pass efficiently between the two in order to minimize any increase in resistance and capacitance time delays.[34] Additionally, in the event of the electromigration of metal atoms starting to create voids within the interconnect, the barrier material may be required to act as alternative path through which the current can flow to bypass the voids.[12]

- Excellent film-forming properties; good growth on and adhesion to the dielectric and Si substrate. With many small holes and vias present (high aspect-ratio features), the ability to provide excellent conformal coverage is paramount. Ideally it should be able to deposit at relatively low temperatures, in part due to the thermal instability of some dielectric materials and also the increased likelihood of copper starting to diffuse into the barrier material at higher temperatures. Semiconductor chip manufacturing has an upper limit of 400 ^{o}C.[34]

- Films free from impurities. These often result in a degradation of its required properties, most commonly by increasing the electrical resistivity of the film.[36]

- Compatible with other processes used within the production process, such as chemical mechanical polishing (CMP).

- A density close to that of the bulk material, with a minimum amount of pinholes, voids, grain boundaries and other defects that may otherwise promote the diffusion of copper atoms.

- Chemical inertness; ideally it should prevent the diffusion of oxygen to the surface of the copper which would otherwise cause oxidation and degradation of the copper interconnect.[30]

Ultimately the diffusion barrier has the function of maintaining the electrical integrity of the integrated circuit.[26] How well the diffusion barrier meets the criteria outlined above will depend on two main factors – the material that is actually used and the method by which a thin film of the chosen material is fabricated.[31]

1.3 Materials of interest

At the forefront of materials that have been investigated and developed for use as diffusion barriers are early transition metal nitrides, including titanium nitride, tantalum nitride and tungsten nitride.[13, 18, 30] Niobium nitride has also been investigated, and should have similar properties to tantalum nitride.[34] Some of these materials have been suggested as being viable candidates in the electrodes of the transistors themselves.[37, 38]

Titanium nitride, with the stochiometry TiN, has been used for many applications. Its high hardness properties have been exploited for use as wear-resistant coatings of tools, whilst its golden colouring makes it an attractive and cheap replacement for elemental gold in decorative coatings.[39] As a diffusion barrier material it has been the most extensively studied.[19, 26, 29, 34, 36, 39 - 45] It is deposited as TiN, where titanium is formally in the +3 oxidation state, which adopts a rock-salt

'halite' crystal lattice.[46] Within the halite lattice each titanium atom occupies an octahedral site, coordinated to 6 nitrogen atoms (figure 1.10). As a result of this environment the Ti^{3+} ion experiences an octahedral crystal field splitting pattern. In this the t_{2g} set of orbitals on each titanium atom point towards other titanium atoms (figure 1.11). As a consequence there is some overlap of these orbitals, which when considered over the whole film can be considered as a continuous and conjugated orbital or "band", in a similar fashion to the oxide "TiO". This band is partially filled by the single d-electrons of Ti^{3+}, meaning that, as with TiO, TiN can conduct like a metallic structure as opposed to a purely ionic lattice, which would normally act as an insulator. This can explain how the film can still conduct electricity.

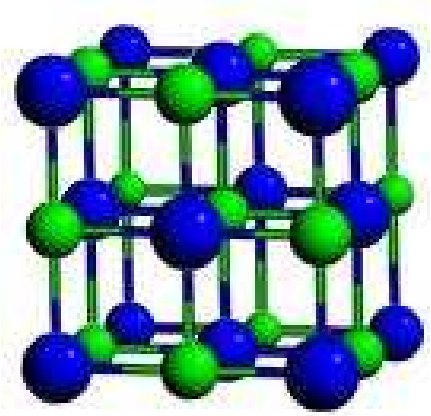

Figure 1.10: Rock-salt 'halite' crystal lattice.

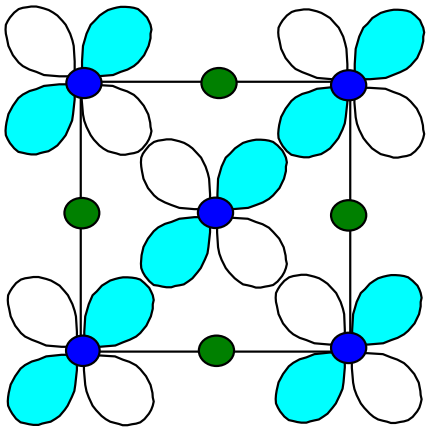

Figure 1.11: Schematic of the overlap of the titanium t_{2g} orbitals within the crystal lattice.

Consequently, transition metal binary nitrides can be considered as metallic in nature in a similar manner to carbides (another class of materials that have been investigated for use in diffusion barriers).[47] The unique physical properties that this imbues in the corresponding materials has led to binary transition metal nitrides having many applications, including as high temperature ceramics, magnetic materials, catalysts, superconductors to name but a few.[48]

Whilst TiN has a relatively low resistivity (resistivity of bulk TiN = 22 μΩ-cm)[39] and can be effective as a diffusion barrier at a high thickness, it has one major intrinsic flaw. During the deposition process, TiN grows in a manner resulting in a columnar structure, in which grain boundaries that are approximately perpendicular to the surface of the substrate run through the deposited film. These boundaries may act as rapid diffusion pathways,[21, 49] causing device failure as copper atoms migrate down them to the silicon substrate, a problem that becomes more prominent as the thickness of the barrier material decreases and consequently TiN barriers are unsuitable for next generation integrated circuits.[34] They also oxidise readily at relatively low temperatures of 450 ^{o}C.[50]

Consequently, the microstructure of the diffusion barrier material plays a critical role in its effectiveness in preventing atom migration. The microstructure of a thin film may be classified as being single-crystal, polycrystalline, nano-crystalline (where the grain size is below 5 nm) and amorphous, as shown in Figure 1.12. Whilst single crystal films would be ideal diffusion barrier materials due to their lack of grain boundaries to act as rapid diffusion pathways, their formation is highly impractical due to limitations including the high temperatures required for their fabrication and lattice mismatch with the underlying substrate. For these reasons nano-crystalline or amorphous films are instead more advantageous.[13, 51]

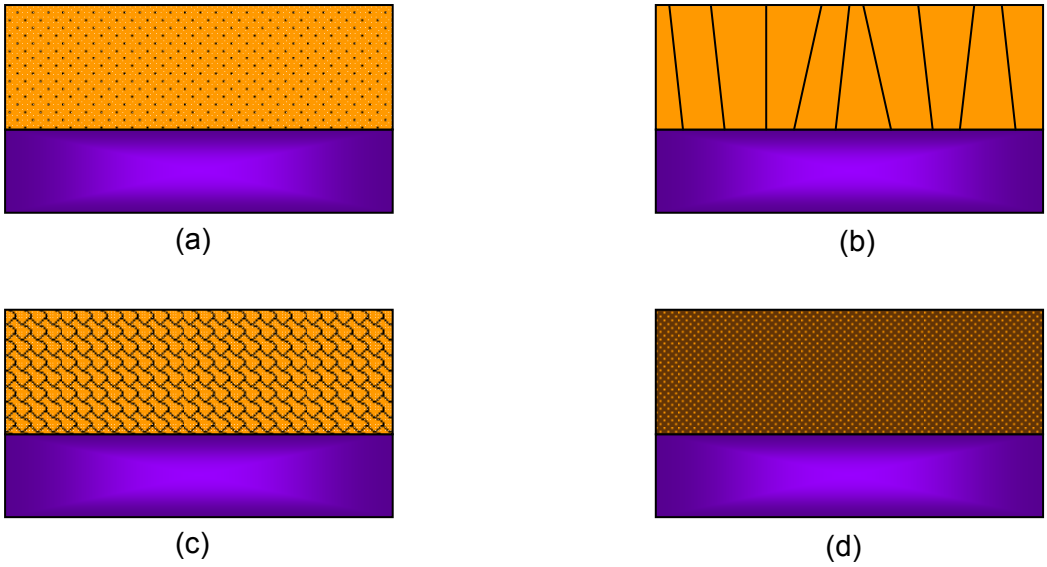

Figure 1.12: Schematic of the microstructures displayed by thin films – (a) Single crystal, (b) polycrystalline (columnar), (c) nanocrystalline, (d) amorphous.[13]

Tantalum(III) nitride (TaN) provides an attractive alternative binary metal nitride to TiN, with films deposited by Physical Vapour Deposition (PVD) techniques being reported to have restivities of <600 μΩ-cm and being stable to copper diffusion after annealing at 700 ^{o}C for 30 min. These superior properties have been attributed to the microcrystalline nature of TaN films, with a greater disorder in the grain boundary structure compared to the columnar TiN.[34, 52 - 54]

Tantalum nitride generally occurs in three phases – TaN, Ta_3N_5 and the slightly rarer Ta_2N, commonly used in resistors. Of these tetragonal Ta_3N_5 is an insulator, whilst TaN is the more favourable material for use in diffusion barriers. Again, like TiN, TaN adopts a cubic rocksalt crystal lattice, but as crystallites are smaller and not columnar the film appears amorphous by X-ray diffraction analysis.[34] In this form the tantalum is formally Ta^{3+}. Unfortunately, due to the more suitable deposition methods used for device fabrication requiring volatile precursors, as discussed later in this chapter, Ta_3N_5 is often observed in deposited films. This is due to tantalum only being volatile in the Ta(V) oxidation state, with the corresponding reduction to Ta(III) being

thermodynamically unfavourable and difficult to promote at temperatures compatible with the device fabrication process.[34]

Niobium(III) nitride, NbN, is isostructural to TaN and consequently should exhibit similar physical and chemical properties. Like tantalum, niobium is volatile in the Nb(V) oxidation state. However niobium may be reduced with greater ease than tantalum, with Nb_3N_4, NbN or Nb_4N_3 being potentially deposited, dependent on the deposition conditions.[34]

Tungsten nitride, WN, has been reported to possess even more advantageous properties than even TaN, with even lower electrical resistance and greater adhesion to copper.[30, 35] However the properties can depend on the technique and conditions used to deposit the tungsten nitride film. The form of tungsten nitride that shows the least electrical resistance is β-W_2N as this has a face-centred cubic structure, similar to that of the rocksalt structures of TiN and TaN. Other forms of tungsten nitride do exist, with WN being reported to form during deposition via ALD,[30] although by their very nature materials such as TiN, TaN and WN are difficult to form and often contain metal centres in a range of oxidation states. As a result the exact structure of these non-stoichiometric materials are debatable and hence they exhibit a range of electrical resistances.

1.3.1 Ternary Metal Nitrides

The introduction of a third element, such as boron or more commonly silicon, in the composition of the diffusion barrier material has been reported to enhance the barrier properties of the corresponding film. The presence of small amounts of atoms of the third element results in a greater disruption to the crystal lattice of pure MN, consequently making the film more amorphous in nature and therefore removing the low energy diffusion pathways along grain boundaries (figure 1.13).[13, 21, 55, 56] These boundaries may also act as diffusion pathways for oxygen, therefore the removal of these helps increase the anti-oxidation properties of the film.[50]

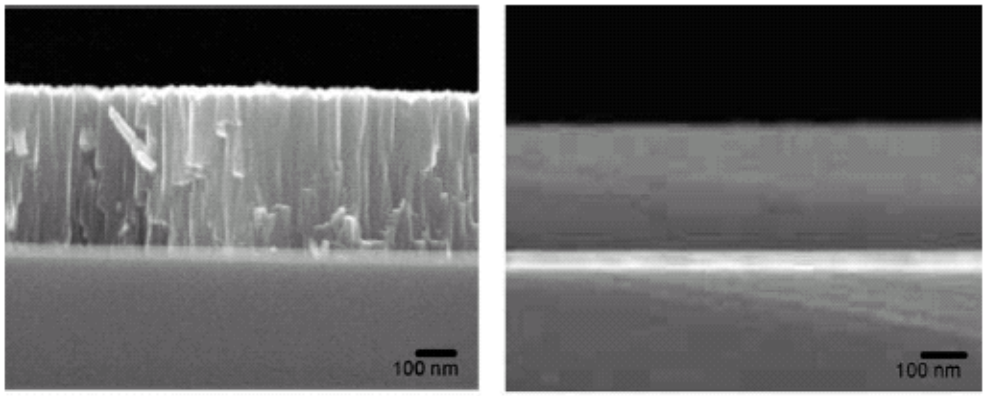

Figure 1.13: Cross-sectional SEM images of TiN and TiSiN films formed on SiO_2 substrates: (a) TiN film with columnar structure for P_{TiCl4} = 0.024 Torr and P_{NH3} = 0.08 Torr, (b) TiSiN film without columnar structure for P_{TiCl4} = 0.024 Torr, P_{NH3} = 0.08 Torr, and P_{SiH4} = 0.8 Torr.[50]

Amorphous ternary nitrides that have been demonstrated to possess good diffusion barrier properties include TiSiN, TaSiN, WSiN and MoSiN. Diffusion barriers fabricated from these ternary systems fail only at high temperatures (900 ^{o}C for TaSiN, 850 ^{o}C for TiSiN) when crystallization, and the associated formation of grain boundaries, occurs, highlighting the prime interest in this class of materials.[34] (Incidentally, the introduction of silicon into TiN films is additionally beneficial in terms of use as wear-resistant coatings for tools, increasing the hardness and resistance to oxidation of the film, therefore extending the lifetime of a tool approximately seven-fold in some cases).[57 - 59]

The actual composition of these films can have a significant bearing on their properties. Investigations by Hübner *et*. *al*. have shown that increasing the percentage of nitrogen in the film raises the temperature at which the film starts to form a polycrystalline microstructure as opposed to an amorphous one and consequently increases its resistance to Cu diffusion, as well as making the film less reactive with the Si substrate.[20] Whilst the introduction of small amounts of a third element such as silicon can help enhance the barrier properties of the material, as has been shown by an increased Si content in TiSiN films resulting in an improvement in its anti-oxidation performance, excessive amounts

can be detrimental to the electronic properties. The effectiveness of the film decreases as larger crystallites of non-conducting Si_3N_4, a material used within microelectronics as a non-conducting encapsulation material to prevent oxidation,[60] can begin to form within the film. This results in a loss of crystallinity in the metal nitride lattice, consequently leading to a breaking up of the metallic nature of the film and a corresponding increase in resistivity.[18, 50, 61] Film resistivity may increase exponentially with increasing silicon content,[34] however the exact properties will vary from film to film as the composition may alter depending on the film thickness.[38]

1.4 Methods of deposition

The method by which deposition of a thin film occurs will also often affect the properties of the film that is formed. Within the microelectronics industry several methods are frequently used, with the most common being PVD, CVD and ALD techniques. These techniques are all relatively well established, with many reviews existing within the literature.[7, 8, 61 - 68] An extensive review of these techniques is beyond the scope of this thesis; therefore only brief descriptions of the techniques will be included, with the interested reader being directed to the relevant texts.

1.4.1 Physical Vapour Deposition

Physical Vapour Deposition (PVD) techniques have been used for many years for depositing thin films. PVD covers a wide range of deposition techniques in which physical processes are used to create a vapour of the target compound and condense said vapour onto the substrate surface. These techniques include: [7, 8, 61 - 63]

- Evaporation
- Sputtering and sputter deposition
- Cathodic arc ion deposition
- Pulsed Laser deposition

Sputtering is the more commonly used PVD technique for depositing thin films within ICs. Charged particles generated within a plasma are accelerated towards a target of material to be incorporated in the thin film, which is held at a negative potential. Upon impact the kinetic energy of the particles is transferred to atoms within the target, breaking bonds and ejecting atoms from the surface out into the reactor. These ejected, or sputtered, atoms can condense on a nearby substrate, resulting in the deposition of a thin film (figure 1.14).[8, 61]

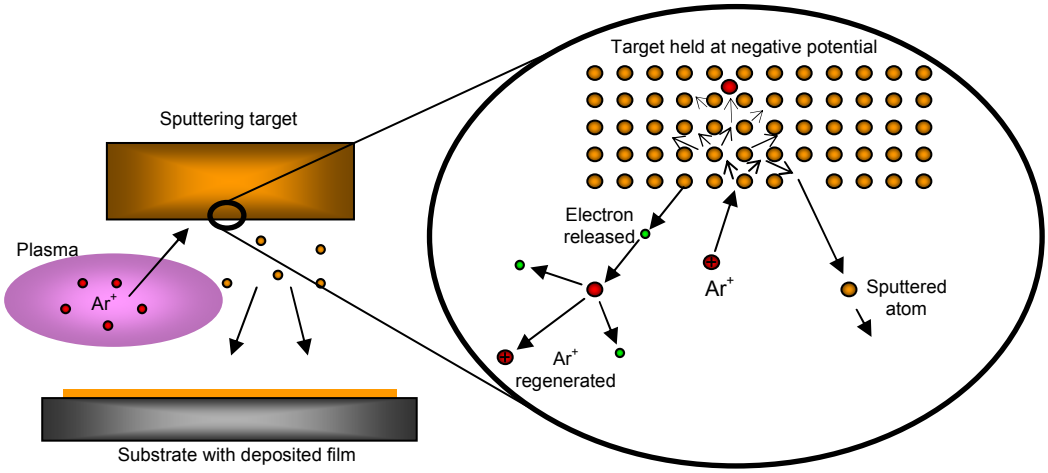

Figure 1.14: Schematic of the sputtering process. Ions from the plasma impact the target, with the resulting dispersion of energy displacing atoms of the target and ejecting them out into the reactor towards the substrate.[8]

PVD has the advantage of being able to deposit a much wider range of materials compared to other deposition techniques, including materials with high melting points that are otherwise difficult to deposit. Films formed bond strongly to the substrate and generally possess a high purity, with the composition of the deposited film being the same as that of the target. Introduction of a reactive gas can result in chemical reactions between the gas and the sputtered atoms, a process generically known as reactive sputtering. In this way, by using O_2 or N_2, oxides and nitrides respectively can easily be deposited. PVD techniques also have the ability to deposit films with an amorphous structure.[7, 46, 62]

1.4.2 Chemical Vapour Deposition

An alternative to PVD that is more advantageous for the microelectronics industry is Chemical Vapour Deposition, CVD. CVD proceeds via the chemisorption of small precursor molecules to the surface of a substrate, where decompostion occurs through a series of chemical reactions. These reactions are usually initiated thermally through heating the substrate, and result in the formation of a stable solid film and the release of gaseous by-products or ligands that may desorb and be readily removed under reduced pressure.[64, 67, 68]

Many different variants of CVD exist, such as thermally activated CVD, plasma enhanced CVD (PECVD), photo assisted and metalorganic CVD (MOCVD) to name but a few. The flexibility of CVD enables the process to be tailored to handle the precursor that is used and how its decomposition is activated, as well as allowing some tailoring of the molecular structure of the film formed, although the use of the more sophisticated variants can increase the cost.

The actual construction of a CVD apparatus varies depending on its exact use, but in general it consists of three stages; a precursor supply system to generate the required vapour and transport it to the reactor (often using a carrier gas such as Ar or H_2), the reactor itself which contains the heated substrate onto which the precursor is deposited, and an exhaust system, like a liquid nitrogen trap, that can neutralize and remove the exhaust gases which contain any unreacted precursor and by-products from the decomposition (figure 1.15).

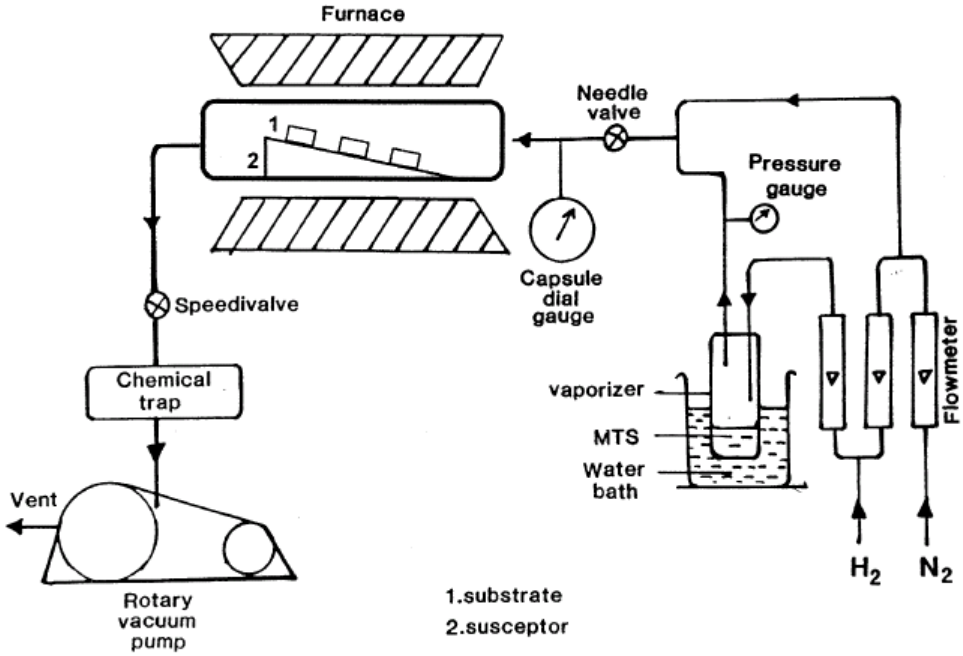

Figure 1.15: Schematic diagram of a typical set-up of a CVD apparatus.[64]

The temperature within the reactor and the temperature at which the decomposition of the precursor occurs partly determines what kind of films will be formed and their quality. If the temperature of the atmosphere within the reactor is higher than the decomposition

temperature of the precursor then the gas phase reactions will occur homogeneously in the vapour phase above the substrate, resulting in a powdery product being formed that adheres poorly to the substrate. Furthermore incomplete reaction of the precursor may happen, all issues that can lead to contamination and overall poor quality within the film deposited.

A more favourable situation for the formation of diffusion barriers is when the atmospheric temperature within the reactor is lower than the decomposition temperature of the precursor. In this case the decomposition occurs heterogeneously, with the precursor adsorbing to the surface of the substrate before undergoing chemical reactions, with the resulting deposit diffusing over the surface to crystallisation centres, promoting the growth of a film (figure 1.16). Therefore it is useful to know the thermal profile of the precursor in order for the operating conditions to be tailored accordingly. Additionally, reducing the pressure within the reaction chamber also lessens the chance of homogeneous reactions occurring as the number of collisions between molecules within the gas phase which may result in reaction are reduced.

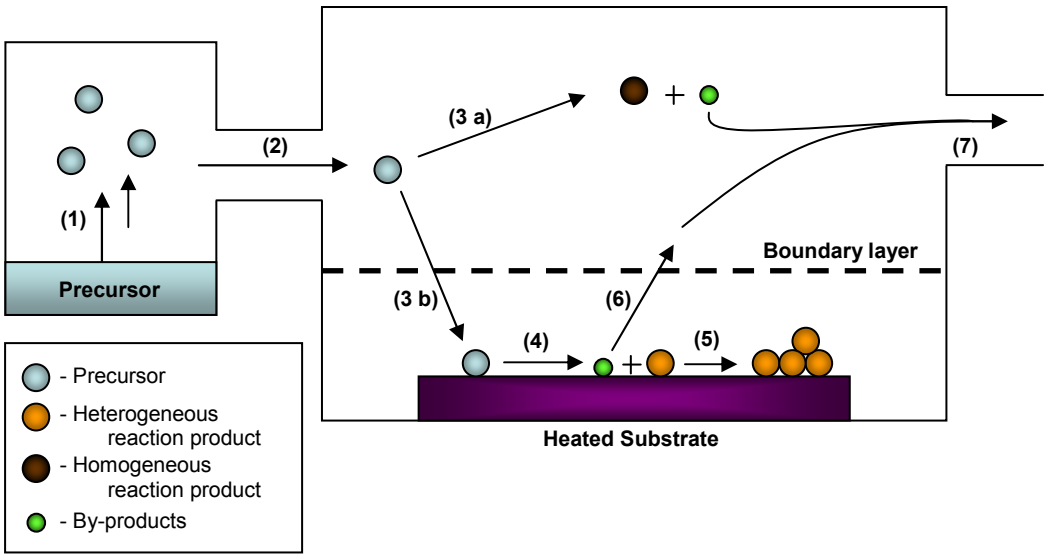

Figure 1.16: Schematic of the CVD process & key steps: - 1) Volatilization of the precursor, 2) Transport to reaction chamber, 3a) Homogeneous gas-phase reactions resulting in powdery product, 3b) Diffusion across thermal boundary layer & adsorption to substrate, 4) Heterogeneous reactions and decomposition, 5) Diffusion of product across surface for crystallization and growth of film, 6) Desorption of gaseous by-products and diffusion across thermal boundary, & 7) Removal of gaseous by-products from reaction chamber.[64]

In addition to the nature of the substrate, what properties the deposited film has depends very much on several parameters within the reactor – the temperature, the pressure, the concentration of precursor in the gas phase and the total flow of the gas. All these factors, as well as the chemical reactions by which the atoms are deposited, affect the nucleation and growth of the film on the surface of the substrate. This determines what the microstructure of the film will be, which in turn affects its properties. For a comprehensive overview of CVD the reader is directed to the extensive review by Choy,[64] whilst specific applications are highlighted in the books by Kodas [65] and Rees.[66]

1.4.3 Atomic Layer Deposition

One deposition method that has attracted increased interest in recent years is atomic layer deposition (ALD), often refered to alternatively as atomic layer epitaxy (ALE) or atomic layer chemical vapour deposition (ALCVD). A variant of CVD, ALD involves the introduction of gaseous

reactants to the substrate individually in alternate pulses, with a purge pulse (usually of an inert gas such as Ar) between preventing mixing of the precursors.[67]

Upon introduction to the reaction chamber, molecules of the first precursor adsorb to available sites on the substrate surface by chemisorption, with any excess precursor molecules being removed from the chamber during the subsequent purge pulse. When the second precursor is introduced it can react with the first reactant adsorbed on the substrate surface in a self-limiting manner to form a thin film and gaseous by-products, which can be removed along with any unreacted reagent in a second purge pulse to complete 1 cycle (figure 1.17). By repeating this cycle the thickness of the thin film can be increased in a controllable manner, with theoretically 1 complete monolayer being deposited with each cycle, although the actual coverage is likely to be less due to sterics of the precursors preventing complete saturation of the substrate surface.[68]

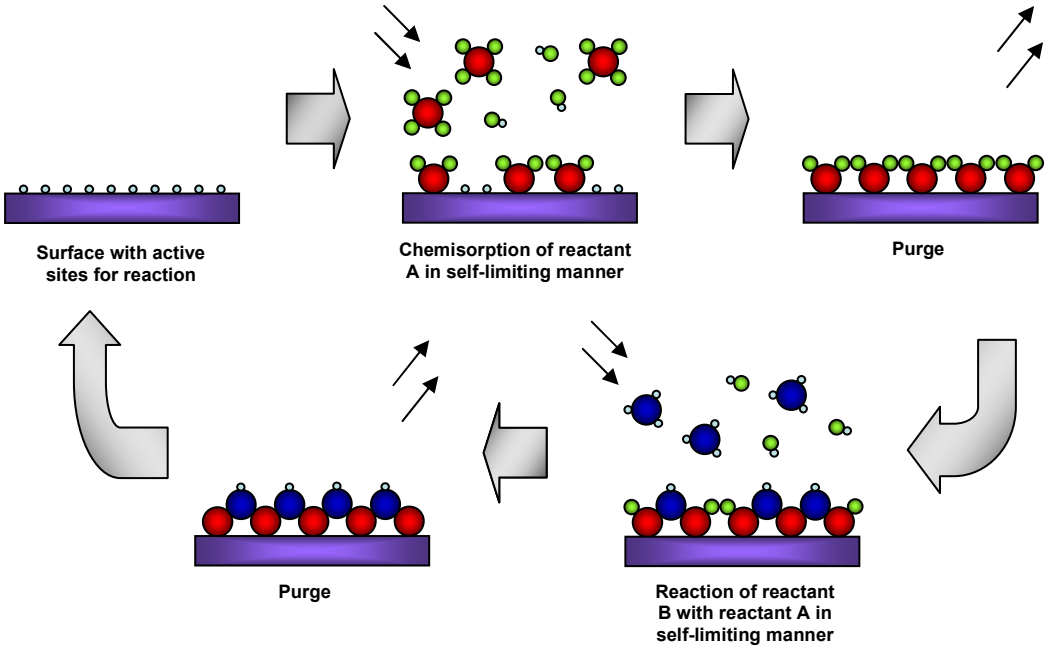

Figure 1.17: Schematic of an ALD 4-step system, with separate introductions of the two precursors with purging of the chamber between.

As ALD relies on surface reactions of adsorbed precursor molecules to deposit thin films rather than thermal decomposition of the precursor as

in the case of CVD, lower operating temperatures may be used. However careful consideration of temperatures used is still required for ALD to occur. If the temperature of the substrate is too low this may lead to insufficient reactivity at the surface or condensation of the precursors, too high and precursor molecules may undergo desorption from the substrate or decompose in the manner of CVD. The region between at which temperatures pure ALD can occur has been coined the 'ALD window'.[67]

The introduction of a vacuum 'pump-down' step between each precursor introduction and subsequent purge can potentially help improve the quality of the subsequent film by lowering the partial pressure of gases above the substrate, consequently promoting the desorption of reaction by-product molecules which may otherwise hinder film growth by occupying active sites on the substrate surface or decompose on the substrate leading to a higher concentration of impurities within the thin film.[69]

ALD as a process brings many advantages over more traditional CVD methods. The manner in which deposition occurs results in not only ease of control of the final thickness of the thin film by monitoring the number of deposition cycles, but also dense, pinhole-free films with a high conformality, homogeneity and uniformity over a large area, suitable for the ever increasingly complex aspect ratios required within silicon chip fabrication. Additionally, since only one precursor is present within the reaction chamber at a given time, this eliminates any unfavourable gas-phase reactions which may occur during CVD. These can lead to a higher concentration of impurites and small particulates, resulting in a poor film with low adhesion. However, the time required to perform every step in a full cycle can mean lower deposition rates compared to CVD, whilst the lower deposition temperatures at which ALD can operate may lead to a lower degree of crystallinity in the deposited film, being potentially detrimental to the film's desired properties.[40, 61, 67, 70]

1.4.4 Focus of this thesis

PVD techniques have been extensively investigated for the deposition of binary and ternary metal nitrides, with the deposition of several diffusion barrier materials summarized in Table 1.1. However, deposition of thin films through CVD techniques are of increasingly greater interest in the field of microelectronics. This is due to the increasing trend towards high-aspect ratio features within ICs.[14, 34, 71] CVD (and ALD) utilises small molecules that may adsorb to and desorb from the substrate several times, migrating across the surface, before depositing as a result of reaction and decomposition.[34] In comparison, during PVD deposited atoms bind strongly to the substrate consequently preventing them from being mobile enough to migrate across the surface to other areas.[61] Coupled with the directional nature of the particles ejected from the target towards the substrate (with PVD often being referred to as a line-of-sight process due to this phenomenon), this may result in the bottom of holes and vias not being sufficiently covered.[36, 72] As a result thin films deposited by CVD have a greater degree of conformality than those deposited by PVD.

Whilst PVD and CVD are both well understood and have been extensively researched for use in the deposition of diffusion barrier materials, there are relatively few reports within the literature where ALD is used, as summarised in Table 1.2. Deposition of binary metal nitrides in this instance is primarily by the use of alternate pulses of the metal halide and ammonia, with the mechanism by which ALD of TiN occurs on silica having been studied by XPS and IR.[70, 73] However, to the best of our knowledge, no reports of ALD precursors for ternary metal nitride systems exist within the literature. Due to the thermal requirements and ligands present affecting a molecule's ability to adsorb and react with surface sites, only a limited number of compounds may be viable precursors for ALD.

Consequently the focus of this thesis will be CVD precursors for the deposition of metal nitrides for use as diffusion barriers. Therefore within

the remainder of Chapter 1 the required properties of CVD precursors and those that have previously been investigated for the deposition of diffusion barrier materials are discussed.

Table 1.1: Summary of the deposition of diffusion barrier materials using PVD techniques

PVD Method	**Target/precursors**	**Film Composition**	**Substrate**	**Film Thickness (nm)**	**Resistivity (μΩ-cm)**	**Ref.**
		Binary Systems				
Sputtering	Ti, N_2/Ar gas	Ti/Ti_2N, TiN	Si	200 – 300	55 - 260	[44]
Vacuum Cathode Arc Deposition	Ti, N_2/Ar gas	"TiN"	Polyimide	180		[26]
Sputtering	Ta, N_2/Ar gas (flow ratio 0.075-0.3:1)	$TaN_{0.3-1.4}$	SiO_2	25		[54]
ICP-assisted Sputtering	Ta, N_2/Ar gas	TaN_x / δ-Ta_2N	Si	100		[53]
Sputtering	Ta, N_2/Ar gas	"TaN"	Si	50		[21]
Sputtering	Ta, N_2/Ar gas (1:3)	"TaN"	Si	60		[74]
Sputtering	Ta, N_2/Ar gas	"TaN"	Si	5, 8, 25		[51]
Sputtering	Ta, CH_4/Ar gas	"TaC"	Si	5, 8, 25		[51]
Sputtering	Ta_5Si_3, Ar gas	$Ta_{73}Si_{27}$	Si	10	215	[20]
Co-sputtering	$TaSi_2$, C (100:0W power ratio), Ar gas	$Ta_{34}Si_{63}$	Si	5		[75]

Sputtering	Mo, N_2/Ar gas (1:3)	"MoN"	Si	60		[74]
Sputtering	W, N_2/Ar gas (1:3)	"WN"	Si	60		[74]
Sputtering	W, N_2/Ar gas	"W_2N"	Si	5, 8, 25		[51]
Sputtering	Wi_5Si_3	$W_5Si_{0.8}$	C, Si, SiO_2			[76]
Sputtering	$WiSi_2$	$WSi_{1.33}$	C, Si, SiO_2			[76]
Ternary Systems						
Cathodic Arc Ion Plating	$Ti_{80}Si_{20}$ alloy, N_2/Ar gas	$Ti_{1-x}Si_xN$	WC	1500		[57]
Cathodic Arc Plasma Evaporation	TiSi 80:20 wt. % alloy, N_2 (0.13 - 4.0 Pa), Ar (0.1 Pa)	$Ti_{47.6}Si_{2.8}N_{49.6}$ – $Ti_{39.8}Si_{9.8}N_{50.4}$	WC	2000 – 6100		[56]
Sputtering	Ti_5Si_3, N_2/Ar gas (0.036:1 flow ratio)	$Ti_{27\pm2}Si_{20\pm1}N_{53\pm4}$	SiO_2	100	110 – 1800	[23]
Ion Beam Assisted Deposition	Ti, B, N-ion beam bombardment	$Ti_{33}B_{55}N_{12}$	Si/TiN	"1500"		[77]

Sputtering	Ti/5% at. Zr alloy, N_2/Ar gas	$(Ti,Zr)N_{0-1.01}$	Si	6	59 – 312	[19]
Co-sputtering	Hf, Si, N_2	“HfSiN”	HfO_2, $HfSiO_x$			[37]
Co-sputtering	Nb, Si (110:6-100W power ratio), N_2 (0.08 of 0.4 Pa)	“NbSiN”	Si	1100 – 1900	200 – 2800	[78]
Co-sputtering	Ta, Si, N_2	“TaSiN”	HfO_2, $HfSiO_x$			[37]
Sputtering	$TaSi_2$, N_2/Ar gas	“TaSiN”	Si	60		[49]
Sputtering	Ta_5Si_3, N_2/Ar gas	“TaSiN”	Si	60	400 – 4500	[49]
Sputtering	Ta_5Si_3, N_2/Ar gas (0.4:1 flow ratio)	$Ta_{56}Si_{19}N_{25}$	Si	10	220	[20]
Sputtering	Ta_5Si_3, N_2/Ar gas (0.8:1 flow ratio)	$Ta_{30}Si_{18}N_{52}$	Si	10	1700	[20]
Co-sputtering	Ta, Ge (200:100W power ratio), N_2/Ar gas	“TaGeN”	Si	50		[21]

Co-sputtering	$TaSi_2$, C (100:100W power ratio), Ar gas	$Ta_{39}Si_{36}C_{24}$	Si	5		[75]
Co-sputtering	$TaSi_2$, C (100:200W power ratio), Ar gas	$Ta_{33}Si_{32}C_{34}$	Si	5		[75]
Co-sputtering	Mo, Si, N_2	"MoSiN"	HfO_2, $HfSiO_x$			[37]
Sputtering	Mo_5Si_3, N_2/Ar gas	"MoSiN"	Si	60	250 – 1700	[49]
Sputtering	MoV alloy, N_2/Ar gas (50:50)	$Mo_{58}V_{5.7}N_{36.3}$	Si	8	550	[79]
Sputtering	WSi_2, N_2/Ar gas	"WSiN"	Si	60		[49]
Sputtering	W_5Si_3, N_2/Ar gas	"WSiN"	Si	60	100 – 1000	[49]
Sputtering	$WiSi_2$, N_2/Ar gas	$W_{24}Si_{42}N_{34}$ – $W_{16}Si_{31}N_{53}$	C, Si, SiO_2			[76]
Sputtering	Wi_5Si_3, N_2/Ar gas	$W_{58}Si_{21}N_{21}$ – $W_{30}Si_{16}N_{54}$	C, Si, SiO_2			[76]

Table 1.2: Summary of the deposition of diffusion barrier materials using ALD

Precursors	Temp. (°C)	Film Composition	Substrate	Growth Rate (Å/cycle)	Resistivity (μΩ-cm)	Ref.
$TiCl_4$, NH_3	400	'TiN'	Si powder			[73]
$TiCl_4$, NH_3, N_2 purge	390	'TiN'	SiO_2			[40]
$TiCl_4$, NH_3, Ar purge	300 – 500	TiN	Si / SiO_2	0.3	≈ 500	[69]
$TiCl_4$, NH_3, Ar purge	450	TiN	Si		120	[36]
$TiCl_4$, NH_3	400	$TiN_{1.2 - 1.4}$	Ni foil	0.4		[70]
$Zr(NEtMe)_4$, NH_3	200	'ZrN'	Ni foil			[70]
$TaCl_5$, NH_3	250	'TaN'	Ni foil			[70]
$(Me_2N)_3Ta{=}NC(Et)(Me_2)$, NH_3, Ar purge		$TaN_{1.31}$		1.2	Not measurable	[80]
$(Me_2N)_3Ta{=}NC(Et)(Me_2)$, H_2 plasma		$TaN_{0.71}$		0.9	366	[80]
$(Et_2N)_3Ta{=}N^tBu$, NH_3, Ar purge	270	'TaN'	Si / SiO_2	0.1 – 1		[81]
$W(N^tBu)_2(NMe_2)_2$, NH_3	250 – 350	$WN_{1.1 \pm 0.1}$	Si	1	1500	[30]

1.5 CVD precursors for the deposition of diffusion barrier materials

As described earlier in this chapter, CVD utilises the decomposition of a vapour of precursor molecules to deposit a thin film, with the subsequent elimination of gaseous by-products.[64 - 66] For the deposition of thin films containing several different elements multiple source precursors have traditionally been used to introduce each desired element individually. Alternatively, a single-source precursor may be used in which the precursor compound already contains the required individual elements bonded in a single molecule, often in the correct ratio.[82]

For a compound to be potentially used as a precursor for CVD there are several properties it ideally has to possess: [64 - 66]

- It must be stable at room temperature and easy to handle, having a low toxicity and not being explosive or readily inflammable.

- It must have an extremely high purity, as even the smallest amount of impurity can have a detrimental effect on the film. The pathway by which the precursor decomposes will also have some bearing on the amount of contamination in the film product.

- It must be volatile, having a low vapourisation temperature.

- The vapour itself must be stable at relatively low temperatures before decomposing at a higher temperature. This is so the precursor does not readily decompose in the vapour phase before it reaches the reactor, therefore depleting the amount of precursor that will actually reach the substrate.

- The temperature at which the precursor decomposes is low enough that the substrate will not be detrimentally affected.

Also lower temperatures are beneficial due to the fact more defects can occur at higher temperatures, creating more diffusion paths for the copper.

- It decomposes at a suitable rate. The slower the precursor decomposes as it passes over the substrate, the thinner the resulting films will be. However, changing other parameters, such as the gas flow, can also alter this.

- From an industrial view it should also be cheap and cost-effective.

When designing precursors for CVD the ligands that surround the metal centre need to be carefully considered, as it is these that will predominantly affect the volatility of the precursor and the mechanism by which decomposition will occur.

With a high volatility desired for transporting the precursor to the substrate relatively easily and consequently promoting the growth rate of the film, ligands that break up the symmetry of the precursor molecule and minimize the crystallinity of the precursor material are often employed. These include the use of large alkyl or fluorinated ligands as well as heteroleptic sets of ligands, whilst polydentate or sterically bulky ligands can coordinatively saturate the metal centre thereby preventing oligomerisation.[83] Alternatively, methods such as aerosol-assisted CVD (AACVD) exist that lessen the volatility requirement of the precursor and enable the use of alternative ligand groups.[64]

A number of compounds have been studied as precursors for the CVD of metal nitride thin films, with several summarized in Table 1.3.

Table 1.3: Summary of the deposition by CVD of diffusion barrier materials

CVD Method	Precursors	Substrate Temp. (^oC)	Film Composition	Substrate	Film Thickness (nm)	Resistivity (μΩ-cm)	Ref.
CVD using multiple precursors							
APCVD	$TiCl_4$, NH_3, H_2 carrier	600 - 900	TiN	Si		800 – 23.7	[39]
APCVD	$NbCl_5$, $HN(SiMe_3)_2$, N_2 carrier	(300) - 400 – 550	NbN	SiO_2 glass		500	[84]
APCVD	$TaCl_5$, $HN(SiMe_3)_2$, N_2 carrier	(300) - 400 – 550	TaN	SiO_2 glass		500	[84]
CVD	Organometallic Ti, SiH_4, NH_3		"TiSiN"	HfO_2, $HfSiO_x$			[37]
MOCVD	$Ti(NMe_2)_4$, H_2/N_2 plasma, SiH_4	350	"TiSiN"	SiO_2			[85]
MOCVD	$Ti(NEt_2)_4$, SiH_4, NH_3	300 - 400	"TiSiN"	SiO_2	5 – 20		[38]
AP/FBR-CVD	$TiCl_4$, $SiCl_4$, NH_3, Al_2O_3 bed, Ar/H_2 carrier	850	"TiSiN"	Steel	2000		[59]
LPCVD	$TiCl_4$, SiH_4, N_2, H_2	550	TiN – $Ti_{36}Si_{14}N_{50}$	Si, steel			[86]

PECVD	$TiCl_4$, SiH_4, CH_4, N_2, H_2, Ar	600	$Ti_{50}C_{30}N_{20}$ – $Ti_{28}Si_{23}C_{30}N_{20}$	Si, steel		2200	[87]
MOCVD	$Ti(NMe_2)_4$, SiH_4, (H_2/N_2 plasma post-deposition),	400	$Ti_{0.9}Si_{0.14}N_{1.1}$	SiO_2	5	240 (160 annealed)	[88]
APCVD	$TiCl_4$, SiH_4, NH_3, Ar carrier	600	Approx. $Ti_{52}Si_2N_{40}$ – $Ti_{10}Si_{34}N_{42}$	Si / SiO_2	50 – 150	500 – 8000	[50]
LPCVD	$TiCl_x$, SiH_4, NH_3, Ar/H_2 carrier		$Ti_{0.47}Si_{0.07}N_{0.46}$	Si / SiO_2	30		[89]
CVD	$Ti(NEt_2)_4$, SiH_4, NH_3		$Ti_{27}Si_{14}N_{59}$ – $Ti_{18}Si_{18}N_{64}$	SiO_2	5 – 20		[38]
TPCVD	$(Me_6Si_3N_3H_3)Ti(NMe_2)_3$, Ar/$N_2$/$H_2$ plasma		“TiSiCN”	Steel			[82]
TPCVD	$(Me_6Si_3N_3H_3)Ti(NEt_2)_3$, Ar/$N_2$/$H_2$ plasma		“TiSiCN”	Steel			[82]
LPCVD	$TaCl_x$, SiH_4, NH_3, Ar/H_2 carrier		$Ta_{0.35}Si_{0.11}N_{0.54}$	Si	30		[89]
PECVD	$Ta(NEt_2)_5$, Ar/H_2 plasma, Ar carrier	230 - 350	$TaN_{1.05}C_{0.27}$ – $TaN_{0.28}C_{0.76}$	Si	30?	2670 – 219	[18]
PECVD	$Ta(NEt_2)_5$, SiH_4, Ar/H_2 plasma, Ar carrier	230 - 350	$TaSi_0N_{1.32}C_{0.39}$ – $TaSi_{0.95}N_{1.32}C_{0.82}$	Si	30?	1000 - 5360	[18]

LPCVD	WCl_x, SiH_4, NH_3, Ar/H_2 carrier		$W_{0.54}Si_{0.12}N_{0.34}$	Si / SiO_2	30		[89]
LPCVD	$ReCl_x$, SiH_4, NH_3, Ar/H_2 carrier		"ReSiN"	Si / SiO_2	30		[89]
<u>CVD using single-source precursor approach</u>							
MOCVD	$Ti(NMe_2)_4$, H_2/N_2 plasma	350	"TiN"	SiO_2 Aerogel	20 – 50		[14]
MOCVD	$Ti(NEtMe)_4$, Ar/H_2 gas	250 - 375	"TiN"	Si / SiO_2			[42]
MOCVD	$Ti(NEtMe)_4$, He carrier	250 - 350	"TiN" (18% at. C, 10% at. O)	SiO_2	130	15000 - 2500	[71]
LPCVD	$Ti(BH_4)_3(CH_3OCH_2CH_2OCH_3)$, Ar carrier	170 - 900	$TiB_{2.4}$ – $TiB_{1.5}$	Si	5 – 60	275	[90]
LPCVD	$(NEt_2)_3Ta{=}N^tBu$, Ar carrier	450 - 600	TaN	Si	60		[74]
LPCVD	$(NEt_2)_2Mo{=}(N^tBu)_2$, Ar carrier	450 - 600	MoN	Si	60	3300 – 600	[74]
LPCVD	$(^tBuNH)_2W{=}(N^tBu)_2$, Ar carrier	450 - 600	WN	Si	60	7500 – 620	[74]
AACVD	$(CH_3CN)W(N^iPr)Cl_4$, PhCN, H_2 carrier	450 -750		Si			[35]
	$Ti(NMe_2)_4$, N_2/He carrier	350 - 400	$TiN_{1.3}C_{1.5}$ – $TiNC_{1.4}$	Si, C, B	100 - 500	"1500 – 3000"	[41]
	$Ti(NEt_2)_4$, He carrier	350 - 400		Si, C, B	100 - 500	"1500 – 3000"	[41]

	$Ti(NMe_2)_3(^tBu)$, N_2 carrier	300 – 400	$TiN_{1.2}C_{1.5}$ – $TiN_{1.1}C_{1.5}$	Si, C, B	100 - 500	“1500 – 3000”	[41]
AACVD	$[Ti(\mu\text{-}N^tBu)(NMe_2)_2]_2$, hexane, He carrier	350 - 400	$TiNC_{1.4}$ – $TiN_{1.1}C_{1.2}$	Si, C, B	100 - 500	“1500 – 3000”	[41]
	$Ti(NC_4H_8)_4$, N_2/He carrier	350 - 400		Si, C, B	100 - 500	“1500 – 3000”	[41]
	$Ti(NC_5H_{10})_4$, N_2/He carrier	350 - 400		Si, C, B	100 - 500	“1500 – 3000”	[41]
LPCVD	$^tBuCH{=}Ta(CH_2{}^tBu)_3$, Ar/H_2 carrier	350 – 550	$TaC_{0.5\text{-}1.6}O_{2.9\text{-}1}$	Si		3000	[91]
LPCVD	$^tBuN{=}Ta(CH_2{}^tBu)_3$, Ar/H_2 carrier	450 - 650	$TaC_{1.3\text{-}1.4}N_{1\text{-}0.7}O_{0.8\text{-}0.4}$	Si		1700	[91]

Traditionally a multi-source approach has been used for the deposition of MN thin films, with metal halides and ammonia being used to source the metal and nitrogen atoms respectively.[39, 64, 89, 92] These are usually introduced to the reaction chamber through separate lines to minimize premature decomposition reactions or the formation of unfavourable adducts, such as $TiCl_4$-NH_3.[50] Several molecular orbital studies have been performed investigating the mechanisms by which deposition occurs using these precursors,[93, 94] and consequently these processes are fairly well understood.

However, using a metal halide can be problematic. Not only can halide contamination of the film occur, which leads to degradation of the film's required properties by creating diffusion paths when the halide atoms desorb during annealing,[50] but also corrosive vapours such as HCl are formed during deposition.[84, 95]

In addition, using purely inorganic precursors such as metal halides or hydrides, which often possess a low volatility due to electrostatic association, can also mean that deposition reactions occur at relatively high temperatures.[34, 71, 95] Whilst PACVD using $TaBr_5$ instead of $TaCl_5$ has been used to lower the deposition temperature of tantalum nitride from over 900 ^oC to 450 ^oC, in both cases the resulting phase may be influenced by the deposition parameters and the nitrogen source – using a N_2/H_2 mixture affords TaN, whilst the use of ammonia results in the formation of Ta_3N_5.[34]

MOCVD and the use of organometallic/ metalorganic precursors, which generally have a higher volatility, provides another option to deposition that can occur at lower temperatures. Consequently metal amides provide a good alternative to the metal halides. The inclusion of a pre-established strong M-N bond within the precursor, such as an imido double bond (M=NR) or nitride triple bond (M≡N), can help promote the inclusion of nitrogen in desired stochiometries into the deposited film.[91, 96] Subsequently complexes containing both the metal and nitrogen elements, such as metal amides and metal imido complexes, may be used on their own as single-source precursors for the deposition of MN thin films.[91, 96] Alternatively, a nitrogen-

containing reducing reagent such as ammonia may also be used with the same organometallic complex in a multi-source approach.[97]

1.5.1 Titanium precursors for the deposition of TiN films and mechanistic studies

Commonly used MOCVD precursors for the deposition of TiN are metal amides of the form $Ti(NRR')_4$, in particular tetrakis(dimethyl amido)titanium ($Ti(NMe_2)_4$, TDMAT). The mechanisms by which decomposition of these precursors occur have been the subject of several investigations, using IR, temperature-programmed desorption and DFT studies,[42, 98 - 100] since this is often the main factor by which contamination of the deposited film may occur. However it should be cautioned that these mechanisms of decomposition reactions are often harder to predict than the volatility, since results from commonly performed mechanistic studies carried out in solution at relatively low temperatures may not translate to CVD conditions.[83]

Studies by Rodriguez-Reyes *et*. *al*. suggest initial adsorption of a molecule of TDMAT to a silicon-based substrate is through an amido ligand, specifically the nitrogen lone pair, as steric hindrance by the ligand prevents direct interaction with a Ti-N bond. Dissociative adsorption may then occur, either through cleavage of the Ti-N bond or a N-C bond as shown in Figure 1.18. The latter route is the more thermodynamically favourable, with the formation of an Si-C bond imparting a stabilization of the surface. Although a high kinetic barrier exists for this route with respect to cleavage of the Ti-N bond, this stabilization energy can mean (potentially unfavourable) carbon contamination of the deposited film may be unavoidable.[98, 99]

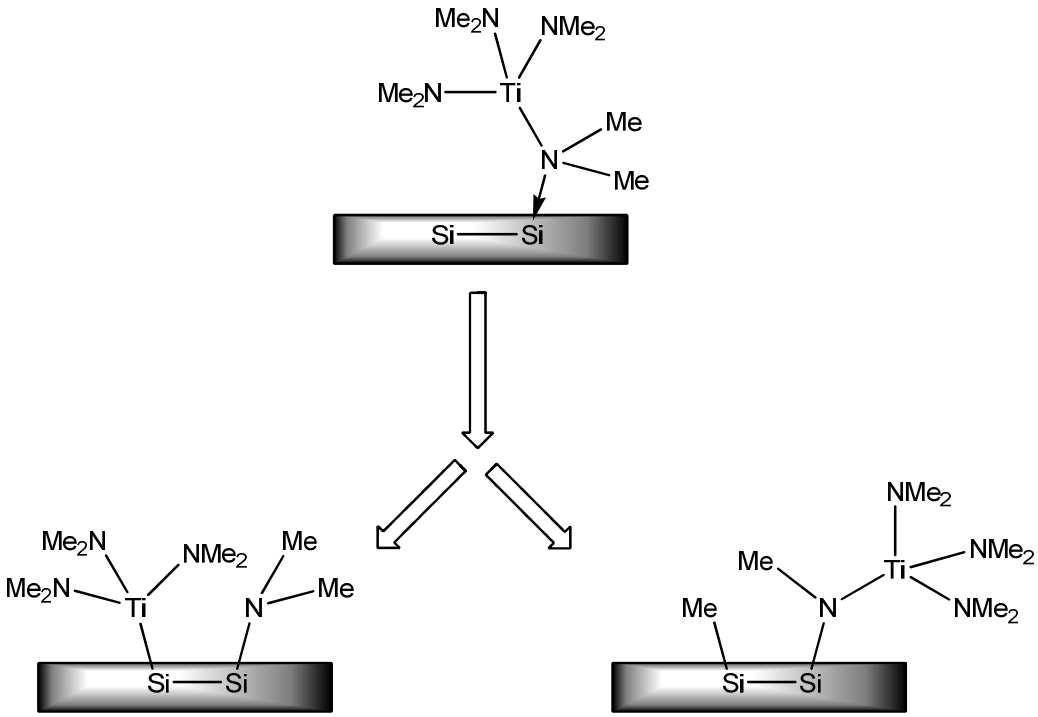

Figure 1.18: Coordination of TDMAT to a silicon surface through a nitrogen lone pair, followed by dissociative adsorption through cleavage of a Ti-N bond (left) or N-C bond (right).[98, 99]

An alternative possibility to carbon contamination of the deposited film is the occurrence of β-hydrogen activation leading to a greater degree of Ti-bound carbon within the deposited film, as shown in Figure 1.19.[41]

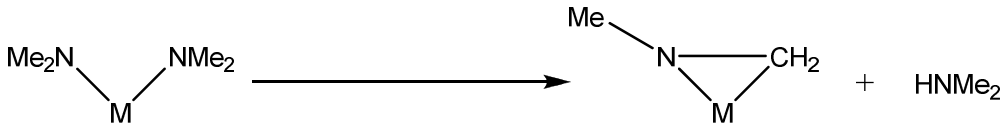

Figure 1.19: β-hydrogen activation

To reduce carbon contamination the use of ammonia as a co-precursor is a viable option. Transamination reactions between TDMAT and ammonia results in the elimination of carbon from the Ti-precursor as volatile dimethylamine, as shown in Figure 1.20. Alternative methods to reduce the carbon content of the deposited film also include thermal or plasma treatment of the film post-deposition.[34, 98, 99]

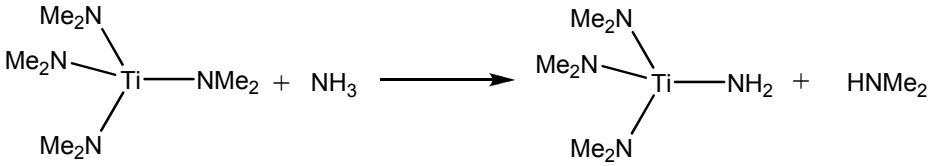

Figure 1.20: Transamination reaction between TDMAT and ammonia

An alternative to the use of methyl substituents, either within an amide ligand or bound to the metal centre directly, is instead the use of ethyl or *t*-butyl substituents or similar groups possessing a β-hydrogen. Substituents fulfilling this criterion have the potential to cleanly decompose via a β-hydrogen elimination mechanism (Figure 1.21), with minimal carbon contamination of the deposited film. Consequently films deposited using tetrakis(ethylmethylamido)titanium ($Ti(NEtMe)_4$, TEMAT) and tetrakis(diethylamido)titanium ($Ti(NEt_2)_4$, TDEAT) have been shown to possess improved physical properties due to a lower level of carbon contamination compared to those deposited using TDMAT as the precursor.[42, 71]

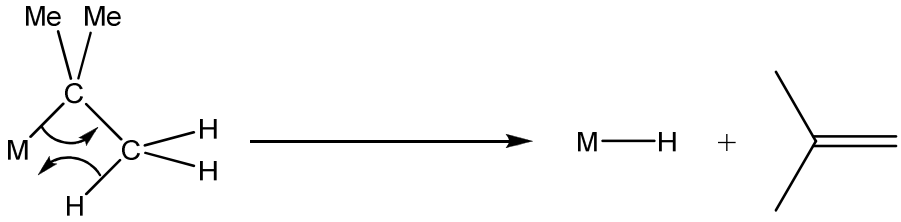

M = metal or nitrogen

Figure 1.21: Mechanism for β-hydrogen elimination

1.5.2 Tantalum precursors for the deposition of TaN films

Similar organometallic amides to the titanium amides mentioned are often used as precursors for the deposition of TaN, with pentakis(dimethylamido)tantalum ($Ta(NMe_2)_5$, PDMAT) commonly being used. However, as mentioned previously in this chapter, TaN is difficult to deposit at low temperatures without the deposition of large amounts of insulating Ta_3N_5. The nature of the amido substituent may also play a significant role, with the selectivity between TaN and Ta_3N_5 in the deposited film often being variable depending on the deposition parameters when diethylamido substituents are present, in a manner comparable to when using

tantalum halide precursors.[34] Mixed tantalum amides and imido containing complexes such as [(EtNCHCH$_3$)Ta(NEt$_2$)$_3$] and [(Et$_2$N)$_3$Ta=NEt] have also been tested as single-source precursors for TaN, with the strong Ta=N imido bond being used to promote the growth of the cubic phase TaN.[83] However the formation of Ta_3N_5 may still often be prevalent, with in addition the resulting films often containing high amounts of carbon contamination, up to 20%.[84]

An alternative potential solution to the problem of TaN/Ta_3N_5 selectivity in the deposition of TaN films is the use of hydrazine-derived ligands, with dialkylhydrazido ligands (-NNR$_2$) having been reported to promote the reduction of the metal atom during the deposition process. Whilst the ability for the ligand to promote reduction may be useful in the deposition of many MN films, it is especially significant in promoting the deposition of TaN tantalum (III) nitride films.[34, 83]

The number of organometallic precursors that have been investigated for use in the deposition of WN films is relatively few compared to those used for depositing TiN and TaN. Of the organometallic complexes used for WN, the bis-amido bis-imido complex (^{t}BuN)$_2$W(NH^{t}Bu)$_2$ is most commonly used, with many other precursors also possessing a strong W=N imido bond.[35]

1.5.3 Deposition of ternary systems

The formation of metal silicon nitride films is usually performed in two ways, either deposited via the simultaneous introduction of the metal, silicon and nitrogen precursors into the reaction chamber,[50, 89] or alternatively through the post-deposition treatment of a binary metal nitride film with a gaseous silicon precursor.[85, 88] In both instances the silicon precursor commonly used is silane, SiH_4, a highly reactive gas that has the added potential of enhancing the film growth rate due to the formation of highly reactive intermediates such as SiH_2, H_3SiSiH and Si_2H_2.[50, 101]

Unfortunately both approaches possess inherent problems. Silicon will only penetrate a pre-deposited film to a nominal depth, therefore several cycles of

deposition and treatment may be required to achieve a desired thickness. The resulting formation of 'sublayers' from this process as shown in figure 1.22 may result in concentration gradients throughout the film occurring, with an associated increase in resistivity due to the greater number of interfaces present.[88]

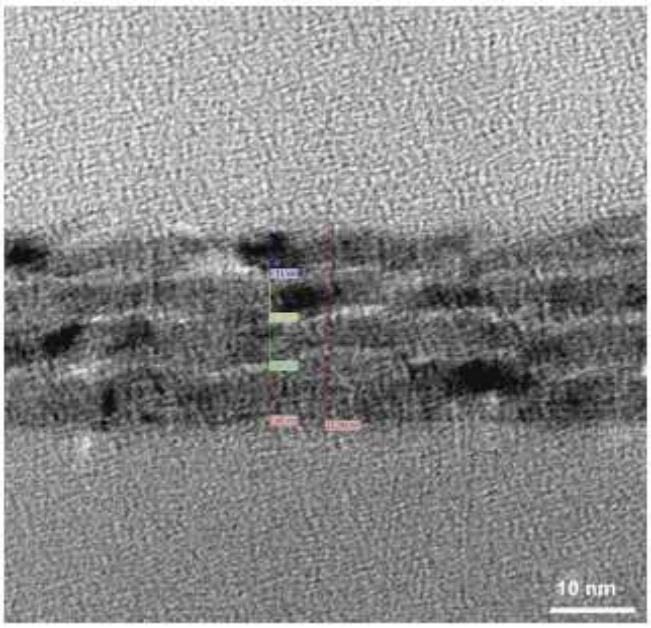

Figure 1.22: TEM cross section of a 4 x 5 nm nominal thickness TiSiN film deposited by post-deposition treatment of a TiN film with gaseous SiH_4. Pale horizontal bands in film are due to C & Si rich 'interfaces' as a result of the deposition technique used.[88]

Conversely, due to the intrinsic differences in volatility of the individual precursors, controlling the partial pressures of multiple reactants, added to the fact that those precursors decompose at different temperatures and rates to each other, means that the overall composition of the deposited film can be unpredictable and difficult to control. This is a significant problem since, as already stated, the properties of the films can vary depending on their exact composition and stoichiometry.

To overcome these problems the use of a single-source precursor is often highly advantageous. These precursors enable greater control of the deposition process, with potentially the stoichiometry of the desired elements in the precursor being the same in the final film.[82] Single-source precursors can also be more stable than the individual precursors, which may react

before reaching the reactor chamber. Unfortunately, as highlighted in Table 1.3, no effective single-source precursors for the deposition of ternary metal nitrides currently exist.

1.6 Summary for Chapter 1

Due to rapid advancements in the field of microelectronics, new materials and methods used in the fabrication of integrated circuits are required as greater demands are put on their functions. Chief amongst these requirements is the need for a diffusion barrier layer between the copper interconnects and silicon based substrate of the IC to prevent the migration of copper atoms into the substrate under operating conditions, thereby maintaining the integrity of the IC. Several transition metal nitrides, predominantly TiN, TaN and WN, have been shown to be effective diffusion barrier materials, whilst the introduction of small amounts of a third element, usually silicon, improves the efficiency further.

Traditionally fabrication of these ternary metal nitride thin films has been performed using PVD techniques. Unfortunately the conformality of thin films deposited by PVD is unsuitable for coverage of the high aspect ratio features encountered as ICs are miniaturised. Consequently CVD has become the favoured method of fabrication.

Deposition of a ternary metal nitride thin film is usually performed using multiple, individual precursors. However this approach is fraught with problems, such as the intrinsic differences in volatilities of multiple precursors allowing very little control over the deposition process and stochiometry of the subsequent film. The use of a single-source precursor, a compound already containing all the required elements for the deposited film, is often advantageous and provides a solution to many of the problems encountered using individual precursors. Unfortunately no single source CVD precursors for diffusion barrier materials currently exist.

Therefore the focus of the work detailed in this thesis is the synthesis and characterisation of a range of compounds that could potentially act as single source precursors for the deposition of TiNSi, TaNSi and WNSi thin films

1.7 References for Chapter 1

1. The Oxford English Dictionary; www.oed.com
2. R. W. Keyes, *Contemp. Phys.*, 2009, **50:6**, 647.
3. The Computer History Museum; www.computerhistory.org.
4. M. Plant *"Electronics (Teach yourself)"* **1992**, Hodder & Stoughton, London, UK.
5. J. E. Lilienfeld, *United States Patent office*, 1930, 1745175.
6. G. Moore, *Electronics*, 1965, **38**, 4.
7. A.R. West, *"Basic Solid State Chemistry Second Edition",* **2000**, John Wiley & Sons, Ltd., Chichester, UK.
8. K. Seshan, "*Handbook of Thin-Film Deposition Processes & Techniques; Principles, Methods, Equipment & Applications (2nd edition)"*, **2002**, Noyes Publications, Norwich, NY, USA.
9. G. Moore, *Electronic Devices Meeting, 1975 International*, 1975, **21**, 11.
10. http://news.bbc.co.uk/1/hi/technology/7080646.stm
11. C. F. Tsang, C. Y. Li, A Krishnamoorthy, Y. J. Su, H. Y. Li, L. Y. Wong, W. H. Li, L. J. Tang and K. Y. Ee, *Microelectr. J.*, 2004, **35**, 693.
12. C. M. Tan and A. Roy, *Mat. Sci. Eng. R*, 2007, **58**, 1.
13. A. E. Kaloyeros and E. Eisenbraun, *Annu. Rev. Mater. Sci.*, 2000, **30**, 363.
14. J. Bonitz, S. E. Schulz and T. Gessner, *Microelectron. Eng.*, 2003, **70**, 330.
15. S. M. Alam, C. L. Gan, F. L. Wei, C. V. Thompson and D. E. Troxel, *IEEE T. Device Mat. Re.*, 2005, **5**, 522.
16. W. N. Gill and J. L. Plawsky, *Thin Solid Films*, 2007, **515**, 4794.
17. J. D. McBrayer, R. M. Swanson and T. W. Sigmon, *J. Electrochem. Soc.*, 1986, **133**, 1242.
18. H-L. Park, K-M. Byun and W-J. Lee, *Jpn. J. Appl. Phys.*, 2002, **41**, 6153.
19. Y-L. Kuo, C. Lee, J-C. Lin, Y-W. Yen and W-H. Lee, *Thin Solid Films*, 2005, **484**, 265.

20. R. Hübner, M. Hecker, N. Mattern, V. Hoffmann, K. Wetzig, H. Heuer, Ch. Wenzel, H-J. Engelmann, D. Gehre and E. Zschech, *Thin Solid Films*, 2006, **500**, 259.
21. S. Rawal, D. P. Norton, H. Ajmera, T. J. Anderson, L. McElwee-White, *Appl. Phys. Lett.*, 2007, **90**, 051913.
22. L. Gao, P. Härter, Ch. Linsmeier, J. Gstöttner, R. Emling and D. Schmitt-Landsiedel, *Mat. Sci. Semicon. Proc.*, 2004, **7**, 331.
23. I. Shalish and Y. Shapira, *J. Vac. Sci. Technol. B*, 1999, **17**, 166.
24. V. Rouessac, L. Favennec, B. Rémiat, V. Jousseaume, G. Passemard and J. Durand, *Microelectron. Eng.*, 2005, **82**, 333.
25. Y. Lin, Y. Xiang, T. Y. Tsui and J. J. Vlassak, Acta Mater., 2008, **56**, 4932.
26. T. X. Liang, Y. Q. Liu, Z. Q. Fu, T. Y. Luo and K. Y. Zhang, *Thin Solid Films*, 2005, **473**, 247.
27. T. Fukuda, N. Aoi and Y. Funaki, *Jpn. J. Appl. Phys.*, 2007, **46**, 903.
28. J. S. Juneja, P-I. Wang, T. Karabacak and T-M. Lu, *Thin Solid Films*, 2006, **504**, 239.
29. C. Guedj, J-F. Guillaumond, L. Arnaud, V. Arnal, M. Aimadeddine, G. Reimbold and J. Torres, *Microelectron. Eng.*, 2005, **82**, 374.
30. J. S. Becker, S. Suh, S. Wang and R. G. Gordon, *Chem. Mater.*, 2003, **15**, 2969.
31. N. Iwamoto, N. Truong and E. Lee, *Thin Solid Films*, 2004, **469-470**, 431.
32. C. Yu, J. Liu, H. Lu and J. Chen, *Appl. Surf. Sci.*, 2007, **253**, 8652.
33. F. L. Wei, C. L. Gan, T. L. Tan, C. S. Hau-Riege, A. P. Marathe, J. J. Vlassak and C. V. Thompson, *J. Appl. Phys.*, 2008, **104**, 023529.
34. C. H. Winter, *Aldrichim. Acta*, 2000, **33**, 3.
35. O. J. Bchir, S. W. Johnston, A. C. Cuadra, T. J. Anderson, C. G. Ortiz, B. C. Brooks, D. H. Powell and L. McElwee-White, *J. Cryst. Growth*, 2003, **249**, 262.
36. J. Uhm and H. Jeon, *Jpn. J. Appl. Phys.*, 2001, **40**, 4657.
37. H. C. Wen, H. N. Alshareef, H. Luan, K. Choi, P. Lysaght, H. R. Harris, C. Huffman, G. A. Brown, G. Bersuker, P. Zeitzoff, H. Huff, P. Majhi and B. H. Lee, *2005 Symposium on VLSI Technology, Digest of Technical Papers*, 2005, 46.

38. H. Luan, H. N. Alshareef, H. R. Harris, H. C. Wen, K. Choi, Y. Senzaki, P. Majhi and B-H. Lee, *Appl. Phys. Lett.*, 2006, **88**, 142113.
39. W-Y. Uen, Z-Y. Li, S-M. Lan, T-N. Yang and S-M. Liao, *Thin Solid Films*, 2007, **516**, 99.
40. S. Li, C. Q. Sun and H. S. Park, *Thin Solid Films*, 2006, **504**, 108.
41. R. M. Fix, R. G. Gordon and D. M. Hoffman, *Chem. Mater.*, 1990, **2**, 235.
42. S. J. Kim, B-H. Kim, H-G. Woo, S-K. Kim and D-H. Kim, *Bull. Korean Chem. Soc.*, 2006, **27**, 219.
43. L. Yi, W. Zhang, J. Wu and D. Mao, *Semicond. Sci. Technol*., 2006, **21**, 250.
44. M. Wittmer, B. Studer and H. Melchior, *J. Appl. Phys.*, 1981, **52**, 5722.
45. M. Wittmer, *Appl. Phys. Lett.*, 1980, **36**, 456.
46. S.T. Oyama, *"The Chemistry of Transition Metal Carbides and Nitrides"*, **1996**, Chapman & Hall, London, UK.
47. S. V. Didziulis, K. D. Butcher and S. S. Perry, *Inorg. Chem.*, 2003, **42**, 7766.
48. R. Marchand, F. Tessier and F. J. DiSalvo, *J. Mater. Chem.*, 1999, **9**, 297.
49. S.C. Sun, H. K. Yap, C. A. Chen and P. Lin, *Solid-State and Integrated-Circuit Technology, Vols 1 and 2, Proceedings*, 2001, 397.
50. K. Jun and Y. Shimogaki, *Sci. Technol. Adv. Mat.*, 2004, **5**, 549.
51. T. Oku, H. Mori and M. Murakami, *5th International Conference on Solid-State and Integrated Circuit Technology Proceedings*, 1998, 238.
52. C. Stampfl and A. J. Freeman, *Phys. Rev. B*, 2003, **67**, 064108.
53. S-M. Kim, G-R. Lee and J-J. Lee, *Jpn. J. Appl. Phys.*, 2008, **47**, 6953.
54. J. K. Chen, C-H. Chan and F-C. Chang, *J. Electrochem. Soc.*, 2008, **155**, H852.
55. A. Winkelmann, J. M. Cairney, M. J. Hoffman, P. J. Martin and A. Bendavid, *Surf. Coat. Tech.*, 2006, **200**, 4213.
56. C-L. Chang, C-T. Lin, P-C. Tsai, W-Y. Ho, W-J. Liu and D-Y. Wang, *Surf. Coat. Tech.*, 2008, **202**, 5516.
57. C. T. Guo, D. Lee and P. C. Chen, *Appl. Surf. Sci.*, 2008, **254**, 3130.
58. S. Hao, B. Delley and C. Stampfl, *Phys. Rev. B*, 2006, **74**, 035402.
59. J. Perez-Mariano, K-H. Lau, A. Sanjurjo, J. Caro, D. Casellas and C. Colominas, *Surf. Coat. Tech.*, 2006, **201**, 2217.

60. R. G. Gordon, D. M. Hoffman and U. Riaz, *Chem. Mater.*, 1990, **2**, 480.
61. U. Schubert and N. Hüsing, *"Synthesis Of Inorganic Materials"*, **2000**, Wiley-VCH, Weinheim, NY, USA.
62. K.D. Leaver and B.N. Chapman, *"Thin Films",* **1971**, Wykeham Publications Ltd., London, UK.
63. J. Yarwood, *"Vacuum and Thin Film Technology"*, **1978**, Pergamon Press Ltd., Oxford, UK.
64. K. L. Choy, *Prog. Mater. Sci.*, 2003, **48**, 57.
65. T. Kodas and M. Hampden-Smith, *"The Chemistry of Metal CVD"*, 1994, VCH, Weinheim, NY, USA.
66. W. S. Rees Jr., *"CVD of Nonmetals"*, 1996, VCH, New York, USA.
67. M. Putkonen and L. Niinistö, *Top. Organomet. Chem.*, 2005, **9**, 125
68. R. L. Puurunen, *J. Appl. Phys.*, 2005, **97**, 121301.
69. H-E. Cheng and W-J. Lee, *Mater. Chem. Phys.*, 2006, **97**, 315.
70. H. Tiznado, M. Bouman, B-C. Kang, I. Lee and F. Zaera, *J. Mol. Catal. A-Chem.*, 2008, **281**, 35.
71. H-K. Shin, H-J. Shin, J-G. Lee, S-W. Kang and B-T. Ahn, *Chem. Mater.*, 1997, **9**, 76.
72. J. A. T. Norman, M. Perez, S. E. Schulz and T. Waechtler, *Microelectron. Eng.*, 2008, **85**, 2159.
73. M. Q. Snyder, B. A. McCool, J. DiCarlo, C. P. Tripp and W. J. DeSisto, *Thin Solid Films*, 2006, **514**, 97.
74. S.C. Sun, *5th International Conferenceon Solid-State and Integrated Circuit Technology Proceedings*, 1998, 243.
75. T-Y. Lin, H-Y. Cheng, T-S. Chin, C-F. Chiu and J-S. Fang, *Appl. Phys. Lett.*, 2007, **91**, 152908.
76. A. Vomiero, E. Boscolo Marchi, A. Quaranta, G. Della Mea, R. S. Brusa, G. Mariotto, L. Felisari, S. Frabboni, R. Tonini, G. Ottaviani, G. Mattei, A. Scandurra and O. Puglisi, *J. Appl. Phys.*, 2007, **102**, 033505.
77. S. M. Aouadi, F. Namavar, T. Z. Gorishnyy and S. L. Rohde, *Surf. Coat. Tech.*, 2002, **160**, 145.
78. C. S. Sandu, M. Benkahoul, R. Sanjinés and F. Lévy, *Surf. Coat. Tech.*, 2006, **201**, 2897.
79. P. Majumder and C. Takoudis, *J. Electrochem. Soc.*, 2008, **155**, H703.

80. J. W. Hong, K. I. Choi, Y. K. Lee, S. G. Park, S. W. Lee, J. M. Lee, S. B. Kang, G. H. Choi, S. T. Kim, U-I. Chung and J. T. Moon, *Proceedings of the IEEE International Interconnect Technology Conference*, 2004, 9.
81. S. Strehle, H. Schumacher, D. Schmidt, M. Knaut, M. Albert and J. W. Bartha, *Microelectron. Eng.*, 2008, **85**, 2064.
82. J. Wilden, A. Wank and A. Bykava, *Surf. Coat. Tech.*, 2005, **200**, 612.
83. L. McElwee-White, *Dalton Trans.*, 2006, 5327.
84. A. C. Newport, J. E. Bleau, C. J. Carmalt, I. P. Parkin and S. A. O'Neill, *J. Mater. Chem.*, 2004, **14**, 3333.
85. C. Prindle, B. Brennan, D. Denning, I. Shahvandi, S. Guggilla, L. Chen, C. Marcadal, D. Deyo and U. Bhandary, *Proceedings of the IEEE International Interconnect Technology Conference*, 2002, 182.
86. S. Vepřek and S. Reiprich, *Thin Solid Films*, 1995, **268**, 64.
87. S. Abraham, E. Y. Choi, N. Kang and K. H. Kim, *Surf. Coat. Tech.*, 2007, **202**, 915.
88. E. Varesi, G. Pavia, A. Zenkevich, Yu. Lebedinskii, P. Besana, A. Giussani and A. Modelli, *J. Phys. Chem. Solids*, 2007, **68**, 1046.
89. E. Blanquet, A.M. Dutron, V. Ghetta, C. Bernard and R. Madar, *Microelectron. Eng.*, 1997, **37/38**, 189.
90. N. Kumar, Y. Yang, W. Noh, G. S. Girolami and J. R. Abelson, *Chem. Mater.*, 2007, **19**, 3802.
91. Y-H. Chang, J-B. Wu, P-J. Chang and H-T. Chiu, *J. Mater. Chem.*, 2003, **13**, 365.
92. A. Baunemann, M. Lemberger, A. J. Bauer, H. Parala and R. A. Fischer, *Chem. Vapor Depos.,* 2007, **13**, 77.
93. J. B. Cross and H. B. Schlegel, *Chem. Mater.*, 2000, **12**, 2466.
94. A. G. Baboul and H. B. Schlegel, *J. Phys. Chem. B*, 1998, **102**, 5152.
95. J. E. Bleau, C. J. Carmalt, S. A. O'Neill, I. P. Paarkin, A. J. P. White and D. J. Williams, *Polyhedron*, 2005, **24**, 463.
96. H-T. Chiu, S-H. Chuang, C-E. Tsai, G-H. Lee and S-M. Peng, *Polyhedron*, 1998, **17**, 2187.
97. A. C. Jones and M. L. Hitchman, *"Chemical Vapour Deposition; Precursors, Processes and Applications"*, **2009**, RSC Publishing, Cambridge, UK..

98. J. C. F. Rodríguez-Reyes and A. V. Teplyakov, *J. Phys. Chem. C*, 2007, **111**, 4800.
99. J. C. F. Rodríguez-Reyes and A. V. Teplyakov, *J. Phys. Chem. C*, 2008, **112**, 9695.
100. T. R. Cundari and M. S. Gordon, *J. Am. Chem. Soc.*, 1993, **115**, 4210.
101. X. Liu, Z. Wu, H. Cai, Y. Yang, T. Chen, C. E. Vallet, R. A. Zuhr, D. B. Beach, Z-H. Peng, Y-D. Wu, T. E. Concolino, A. L. Rheingold and Z. Xue, *J. Am. Chem. Soc.*, 2001, **123**, 8011.

Chapter 2

Synthesis and characterisation of Group 4 metal complexes prepared using R_3SiNH_2 ligands

2.1 Introduction to Chapter 2

As described previously in Chapter 1, a prominent class of compounds used for the deposition of metal nitride films are metal amido (M-NR_2) and metal imido (M=NR) containing complexes. In addition, silicon amides have been used in the formation silicon nitride films.[1, 2] Therefore, the combination of metal amides/imides with silicon amides may provide a route to a range of complexes that could potentially be used as single-source precursors for the deposition of metal silicon nitride films.

Within this chapter the reaction of Group 4 metal amides with primary silicon amide reagents has been explored. In order to understand the bonding displayed within the subsequent structures of compounds presented within this chapter, a brief general introduction to transition metal and silicon amides and transition metal imides is included for this purpose.

2.1.1 Metal amido ligands, $[NR_2]^-$

The first metal amide complex, $Zn(NEt_2)_2$, was synthesised by Frankland in 1856.[3] Since then the number of metal amido-containing complexes that have been synthesised and characterised has escalated, with stable amide complexes known for almost all the elements. Metal amides are also known to exist as primary (M-NH_2), secondary (M-NHR) or more commonly tertiary amides (M-NR_2). Interest in these complexes comes from many fields of organometallic chemistry and organic synthesis, including being employed as reagents in the synthesis of complex molecules, as catalysts in olefin polymerisation or hydroamination and as precursors for the deposition of ceramic materials. Consequently the chemistry of metal amides is generally well known and has been extensively reviewed.[3, 4]

A terminal metal amido ligand, although formally a -1 charged ligand, may act as either a one electron or three electron donor to a metal centre, as illustrated in figure 2.1.

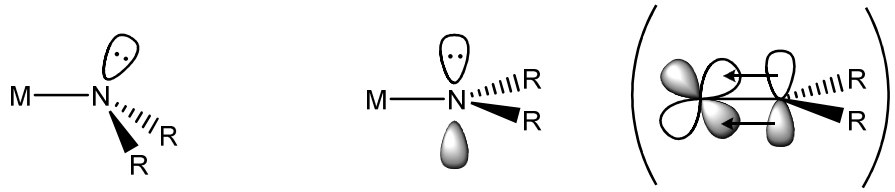

(**I**) (**IIa**) (**IIb**)

Figure 2.1: The principle bonding modes of a terminal metal amido ligand, where the nitrogen is sp^3 hybridised and donates one electron (**I**), or alternatively the nitrogen is sp^2 hybridised and may act as a one electron donor (**IIa**) or three electron donor (**IIb**).

In the first, structure (**I**), the amide ligand acts as a one electron donor and bonds to the metal centre via a single σ bond between the metal centre and an sp^3 hybrid orbital on the nitrogen. As a consequence of this hybridisation the nitrogen displays a pyramidal geometry, with the nitrogen lone pair of electrons localised on the nitrogen. Alternatively, the nitrogen of the amide ligand may display an sp^2 hybridised planar geometry as shown in structure (**II**). In this instance the amide ligand may again act as a one electron donor as before (**IIa**). Alternatively, overlap of the nitrogen p-orbital and a metal d-orbital facilitated by the planar geometry at the nitrogen enables the amide ligand to act as a three electron donor through (d←p) π-bonding, with the lone pair in the nitrogen p-orbital being donated into a vacant d-orbital of the correct symmetry and energy on the metal (**IIb**). Consequently the π-bonding often results in the M-N bond being shorter than that predicted from estimates made using the covalent radii. The π-bonding usually occurs for early transition metals that are in a high oxidation state, with relatively fewer amide complexes known for later transition metals due to suitable vacant d-orbitals being unavailable for accepting π-donation.[3, 4]

Whilst the formation of the metal-nitrogen (d←p) π bond has a significant effect on the geometry of the molecule, experiments to determine the enthalpy of formation of metal amides have shown that the π bond has a relatively small effect in terms of the strength of the M-N bond.[3, 4]

Amide ligands may also bond in a bridging fashion between two metal centres as displayed in structure (**III**), with a single covalent σ bond to one metal

centre whilst using the lone pair in a dative bond to bridge to the other metal centre as shown in figure 2.2. However steric crowding around the nitrogen from the substituents often makes the bridging system unfavourable, consequently preventing oligomerisation.[3]

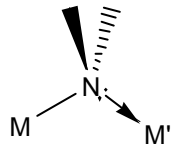

(**III**)

Figure 2.2: The bonding within a bridging metal amido ligand. The amide acts as a three electron donor – one electron to M and two electrons to M'.

Metal amide complexes have been prepared by a number of different synthetic procedures (figure 2.3).[3] Synthesis is most commonly via a transmetallation reaction between a metal halide and Group 1 metal amide such as lithium amide, eliminating a lithium halide salt, with yields from these reactions generally quite high. Other synthetic procedures such as alkane, or hydrogen elimination and transamination provide an attractive alternative, with a greater ease of purification due to generally high volatility of the by-product compared to the desired metal amide. Ammonium halide and disproportionation reactions are also popularly used, whilst several synthetic approaches including oxidative addition are becoming increasingly important.[3 - 5]

Alkane elimination:	$MR_2 + 2HNR_2 \rightarrow M(NR_2)_2 + 2RH$
Ammonium halide elimination:	$L_nMX + 2HNR_2 \rightarrow L_nMNR_2 + [R_2NH_2]X$
Hydrogen elimination:	$L_nMH + HNR_2 \rightarrow L_nMNR_2 + H_2$
Transamination:	$L_nMNR_2 + HNR'_2 \rightarrow L_nMNR'_2 + HNR_2$
Transmetallation:	$L_nMX + M'NR_2 \rightarrow L_nMNR_2 + M'X$ (M' usually Li or Na)

Figure 2.3: Main reaction routes for the synthesis of metal amide complexes.[3]

2.1.2 Metal imido ligands, $[NR]^{2-}$

Despite metal imide systems being first reported in 1956 with the synthesis of $Os(N^tBu)O_3$,[6] the interest in metal imido containing complexes has only increased significantly over the last two decades. This is in part due to the nature of frontier orbitals of an imido ligand being *pseudo*-isolobal with those of a cyclopentadienyl (Cp) ligand, to which the imido ligand provides an attractive alternative in catalysis. Although very different to the amides, with the imides having unique properties and reactions compared to the amides, both amides and imides have uses in many similar fields of organometallic chemistry and organic synthesis, such as catalysis of polymerisation reactions.[6, 7] Consequently metal imide complexes have often been developed in parallel with metal amides, a result of which is that the chemistry of metal imides has been extensively investigated, with many reviews and papers having been published.[6 - 10]

As with the amides, imido ligands, $[NR]^{2-}$, are known to bond to metal atoms in a terminal or a bridging fashion.

The bonding interactions between a transition metal and a terminal imido ligand may be considered as consisting of a single σ bond and either one or two π interactions. Consequently, although formally a -2 charged ligand, the imido ligand may act as either a two electron or four electron donor to the metal centre. Again, as observed in metal amide bonding, the hybridisation of the imido nitrogen centre and the bond order will influence the structure of the imido ligand as shown in figure 2.4.

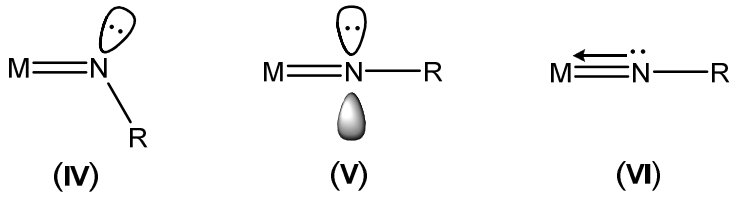

(**IV**) (**V**) (**VI**)

Figure 2.4: The main bonding modes of a terminal imido ligand – (**IV**) bent, two electron donor; (**V**) linear, two electron donor; and (**VI**) linear, four electron donor.

Structure (**IV**) displays the nitrogen as sp^2 hybridised with an M=N double bond (1σ, 1π) and a lone pair of electrons localised in an sp^2 hybrid orbital on the nitrogen. A consequence of the hybridisation of the nitrogen is a bent M-N-R linkage, and the imido ligand behaves as a two electron donor. However relatively few strongly bent imido ligands are known. More commonly imido ligands are observed as being near-linear, with an *sp* hybridised nitrogen atom as displayed in structures (**V**) and (**VI**). In (**V**), as in (**IV**), the imido ligand is bound to the metal centre through an M=N double bond (1σ, 1π) with a lone pair of electrons localised on the nitrogen atom, albeit this time in a p-orbital. Again, as with (**IV**), the imido ligand acts as a two electron donor to the metal centre. However, unless symmetry restrictions or a severe energetic mismatch between the nitrogen p-orbital and metal d-orbitals prevents it, in most systems the nitrogen lone pair will perform (d←p) π donation in a manner similar to that observed in metal amide bonding, as displayed in structure (**VI**). Accordingly the imido ligand acts as a four electron donor, with a M≡N formal bond order of 3. Consequently (**VI**) is the most common geometry, with (**IV**) generally only being favoured when adopting (**VI**) would cause the electron count of the complex to exceed 18 electrons.[6, 8 - 10]

One particular qualitative indicator of the electronic structure of the imido ligand is through the chemical shifts displayed in the ^{13}C NMR spectra, in particular the chemical shifts for α and β carbon atoms of a *tert*-butylimido ligand. These have been studied for a range of transition metal imido containing complexes, with similar observations being made for other substituents such as *iso*-propyl complexes.[8, 9] The difference in the chemical shifts (Δδ) of the quaternary carbon and methyl groups of the *tert*-butylimido group is directly related to the electron donation from the imido group to the metal centre. As a greater contribution from the lone pair of the nitrogen donating to the metal occurs, as observed in structure (**VI**), the quaternary atom consequently becomes more electropositive**.** The ensuing downfield shift of the ^{13}C signal for the quaternary carbon results in a greater Δδ. However the magnitude of Δδ will also be influenced to a certain degree by the electronegativity of the metal atoms and the ancillary ligands present.[8, 9]

The bridging mode of imido ligands most commonly encountered is μ_2-bridging between two metal atoms, either homo- or heterometallic. This μ_2-bridging is displayed below in structures (**VII**) and (**VIII**) within figure 2.5. In both instances the nitrogen atom of the imido ligand is sp^2 hybridised, with two σ bonds existing, one to each metal centre. However, although in both structures the imido ligand is behaving as a four electron donor, in structure (**VII**) the nitrogen lone pair is delocalised between the nitrogen p-orbital and d-orbitals on both metal centres, whilst in structure (**VIII**) the lone pair is localised in a formal M=N π-bond. The nature of the bridging is strongly influenced by the geometry and ancilliary ligands of the metal atoms, and consequently the orbitals involved in the bridging.[8, 11]

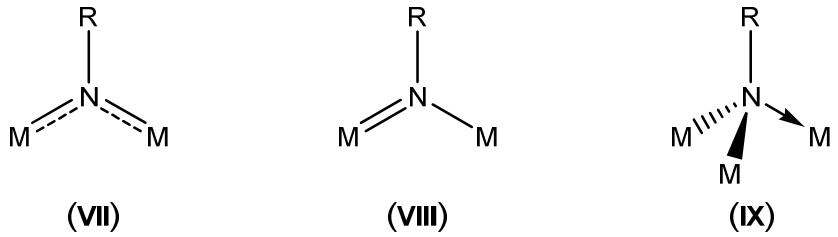

Figure 2.5: The main bridging modes of an imido ligand – (**VII**) symmetrical μ_2-bridging, donating two electrons to each metal centre; (**VIII**) unsymmetrical μ_2-bridging, donating three electrons to one metal centre and one electron to the other; and (**IX**) μ_3-bridging, donating one electron each to two metal centres and two electrons to the third metal centre.

The μ_3-bridging mode has also been reported for imido ligands, as displayed in structure (**IX**), although it is relatively rare compared to μ_2-bridging, commonly being found in cluster complexes of the iron triad.[8] As in the μ_2-bridging, the imido ligand acts as a four electron donor, although in this instance the nitrogen atom is sp^3 hybridised.

Whilst the synthesis of metal imido complexes shares some similarities with the synthesis of metal amides, several of the synthetic approaches are significantly different. However, a few of the key methods are highlighted below and in figure 2.6.

The most frequently utilised methods of synthesis involve the cleavage of a single bond between a nitrogen atom and an α-substituent. A typical example

of this approach is the deprotonation of a primary amine, RNH_2, by a metal chloride, oxide, amide or alkyl complex and the subsequent loss of a corresponding leaving group, i.e. HCl, H_2O, HNR_2 and RH respectively. Alternatively a salt metathesis reaction using a lithium (or other alkali or alkali earth metal) amide salt, LiNHR, may be used instead of the amine. In both cases a non-coordinating base may also be added to deprotonate the amine or amide and to neutralise any acid such as HCl liberated by the reaction.[6, 8, 9, 12, 13]

i. $L_nMCl_2 + RNH_2 \rightarrow L_nM(NR) + 2HCl$

ii. $L_nMO + RNH_2 \rightarrow L_nM(NR) + H_2O$

iii. $L_nM(NR'_2)_2 + RNH_2 \rightarrow L_nM(NR) + 2HNR'_2$

iv. $L_nMR'_2 + RNH_2 \rightarrow L_nM(NR) + 2R'H$

Figure 2.6: Synthetic reactions for the preparation of metal imide complexes by the deprotonation of a primary amine.[6, 8, 9]

It is worth noting that the use of a primary amine as a reagent is one of the few areas where the synthesis of metal amido & imido containing complexes overlap. However, in many instances, often when the amide is not sterically stabilised, there is a tendency for the metal amide complex formed using the primary amines to undergo a self-condensation reaction, resulting in the formation of a bridged imido complex (figure 2.7).

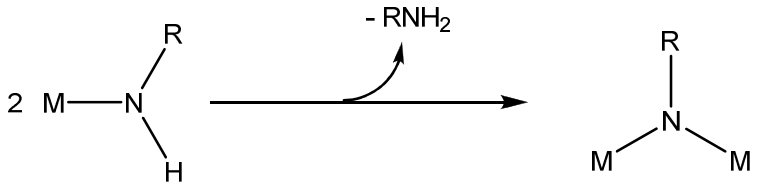

Figure 2.7: Schematic of the self-condensation of metal amido complex containing a primary amide, {NHR}, and the subsequent formation of a bridged imido species.[3, 4, 6, 8]

An equally popular method of preparing metal imido complexes, which may have particular ramifications in the context of the work presented in this thesis, involves the cleavage of N-Si bonds in silicon amide reagents. When silicon amides or $LiN(R)SiR_3$ salts are added to a metal reagent containing oxide or halide, the strong bonds that form between silicon and oxygen or

silicon and halides (in particular fluoride and chloride) results in a transfer of the SiR_3 moiety from the nitrogen to these atoms, with a corresponding cleavage of the N-Si bond (figure 2.8). Depending on the silicon amide reagent, this synthesis may often be accompanied by cleavage of an N-H bond to obtain the metal imido complex.[6, 8, 9, 14 - 18]

i. $L_nMO + RN(SiMe_3)_2 \rightarrow L_nM(NR) + (Me_3Si)_2O$

ii. $L_nMX_2 + RN(SiMe_3)_2 \rightarrow L_nM(NR) + 2Me_3SiX$

(X = F, Cl)

iii. $L_nMCl_2 + LiN(R)(SiMe_3) \rightarrow L_nM(NR) + Me_3SiCl + LiCl$

Figure 2.8: Typical reaction schemes involving cleavage of an Si-N bond and subsequent formation of a metal imido complex.[6, 8, 9, 14 - 18]

An alternative to cleaving a single bond between a nitrogen atom and an α-substituent involves [2+2] imido metathesis reactions between a M=L double bond, especially M=O bonds, and a reagent containing an element=NR double bond such as carbodiimides (RN=C=NR), phophinimines (R_3P=NR), isocyantes (O=C=NR), sulfinylamines (O=S=NR) and other such related compounds (figure 2.9). Alternatively, imido exchange between metal imido containing complexes is a possibility.[7 - 9, 19]

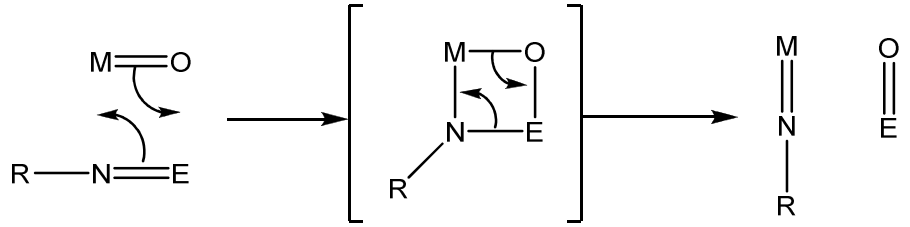

i. $L_nMO + R'_3PNR \rightarrow L_nM(NR) + R'_3PO$

ii. $L_nMO + RNCO \rightarrow L_nM(NR) + CO_2$

iii. $L_nMO + RNSO \rightarrow L_nM(NR) + SO_2$

Figure 2.9: Schematic of a [2+2] metathesis reaction mechanism. Several reaction schemes for the synthesis of metal imido complexes which proceed via this mechanism are shown.[7 - 9]

Whilst [2+2] metathesis reactions play an important role in the synthesis of metal imido containing complexes, these reactions are equally important in

the context of the M=N reactivity and its function in the catalysis of reactions such as hydroamination (figure 2.10).[7, 9]

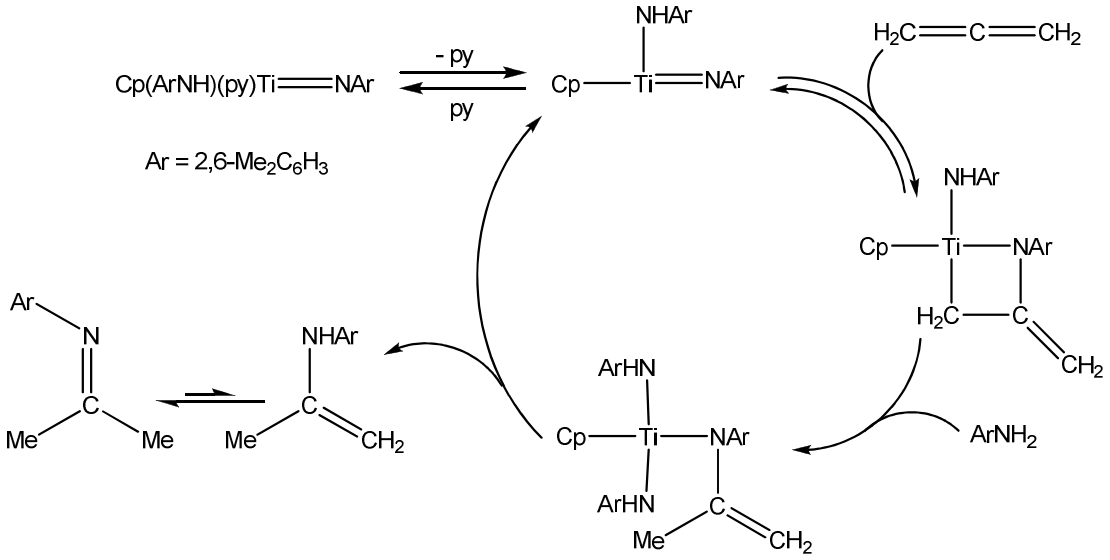

Figure 2.10: Schematic of a catalytic hydroamination reaction cycle. The reaction proceeds via a [2+2] metathesis reaction.[7]

2.1.3 Silicon Amides

Since the first preparation in 1887,[3] silicon amides have come to be amongst the most investigated of all amide complexes, commonly being used as reagents in a variety of organic and inorganic synthetic reactions. Silicon amides have also been investigated as CVD precursors for the deposition of silicon nitride, Si_3N_4.[1, 2]

Silicon amides predominantly exist with the silicon in a four-coordinate environment, with the nitrogen atom being bonded to either one [aminosilanes, $R_3SiNR'_2$, structure (**X**) within figure 2.11], two [disilazanes, $\{R_3Si\}_2NR'$, (**XI**)] or three [trisilazanes, $\{R_3Si\}_3N$, (**XII**)] silicon centres.[3] In these compounds the silicon atoms are formally assigned the +4 oxidation state, however silylenes, the analogous compounds to carbenes, are known in which the silicon is formally assigned a +2 oxidation state [structure (**XIII**), figure 2.11].[3, 4, 20]

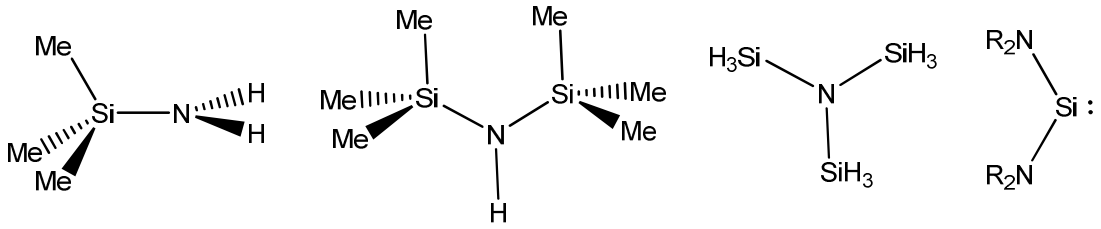

Figure 2.11: Typical structures of silicon amides, in which the silicon atom predominantly exists in a four-coordinate environment. The nitrogen atom is bonded to one (**X**), two (**XI**) or three (**XII**) silicon atoms. Silylenes containing Si-N bonds, in which the silicon is formally assigned a +2 oxidation state, are also known (**XIII**).

The bonding that occurs between the silicon and nitrogen atoms is a source for considerable debate, as detailed below, and is reflective of the arguments over the role d-orbitals play in the bonding between other main group elements.[3, 21 - 23]

Structural studies of aminosilanes by X-ray and electron diffraction often indicate the nitrogen to be in a planar environment, with the Si-N bond length being shorter than that estimated from covalent radii for a single Si-N σ-bond (1.82 – 1.87 Å).[3] These phenomena are comparable to those observed within the bonding of metal amides. Furthermore, the silicon amide $N(SiH_3)_3$ has been shown to be an extremely weak Lewis base. These observations have lead to the hypothesis that, as in metal amide bonding, delocalisation of the nitrogen lone pair from a p-orbital into a vacant d-orbital on the silicon ([d←p] π bonding) is occurring, leading to a degree of multiple bond character within the Si-N bond. Further support for this hypothesis is the observation that the Si-N bond contraction is further enhanced by the presence of electron-withdrawing substituents on the silicon, resulting in lowering in energy of the d-orbital and consequently a greater π-orbital overlap. Additionally, calculated dipole moments of Si-N bonds are shown to be relatively low, with the d←p π bonding counteracting the expected $Si^{\delta+}$-$N^{\delta-}$ σ polarity.[3]

However, the theory of d←p π bonding between silicon and nitrogen atoms fails to explain the invoked hypervalency of the silicon atom, whilst also

relying on the 3d orbital being low in energy. An alternative theory for the suggested multiple bond character observed within silicon amides is that of negative hyperconjugation. Whilst d←p π bonding may play a secondary role in this instance, delocalisation of the nitrogen lone pair is primarily from the non-bonding p-orbital of the nitrogen to an anti-bonding orbital of a Si-R σ-bond of correct symmetry ($n_N \rightarrow \sigma^*_{SiR}$). Consequently this negative hyperconjugation results in a shortening and increase in bond order of the Si-N bond, with a concomitant decrease of the bond order of the Si-R σ-bond and deformation of the SiR_3 substituent.[21] Both potential bonding modes are shown schematically below in figure 2.12.

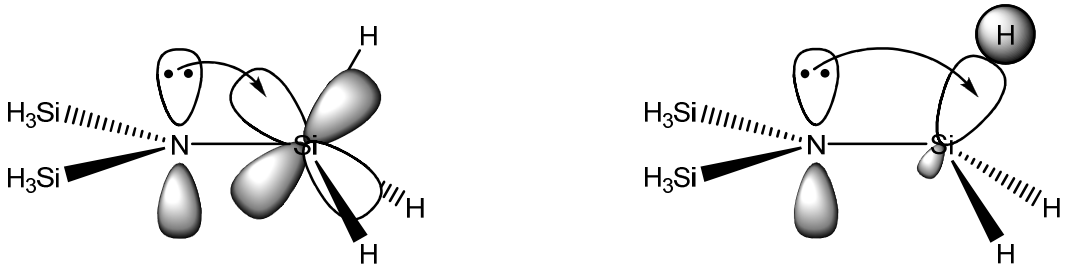

Figure 2.12: Simplified representation of the potential bonding modes within a Si-N multiple bond depicting a localised bonding description. Left; d←p π bonding, and Right; negative hyperconjugation.

The planarity at the nitrogen centre has also been explained not in terms of delocalisation but instead repulsions, both steric and, more significantly, electronic. Due to the greater difference in electronegativity between silicon and nitrogen compared to that between carbon and nitrogen, Si-N bonds possess a greater polarity. Therefore long-range coulombic repulsions between the Si-N σ-bond and other substituents on the nitrogen atom result in the adoption of a near planar configuration which is more energetically favourable, especially for $N(SiH_3)_3$.[21]

Typically silicon amides are found to be volatile, colourless liquids or solids. The synthesis of these compounds shows many similarities with the synthesis of transition metal amides mentioned earlier and subsequently follows many of the procedures already mentioned, e.g. synthesis through ammonium halide elimination, transamination or transmetallation reactions. However,

several synthetic procedures exist that are specific to silicon amides compared to metal amides. These include:

i. anionic rearrangements involving the transfer of a silyl substituent from a carbon atom to an adjacent nitrogen atom,
ii. reactions of silanols or silthianes with an amine, and
iii. the reaction of a lithium silane salt with an amine.

The majority of these specific silicon amide procedures are limited in scope and consequently very rarely used.[3]

2.2 Synthesis of R_3SiNH_2 silicon amide ligands

As mentioned previously in the introduction to this chapter and in Chapter 1, metal amides such as TDMAT and PDMAT and silicon amides have been employed as single-source precursors for the deposition of metal nitride and silicon nitride thin films respectively. However, there is potential for silicon amides to be reacted with metal amide reagents, through a series of transamination reactions, giving access to a range of compounds that may potentially act as single-source precursors for the deposition of M-N-Si materials. To this end a range of silicon amides were synthesised and investigated.

The most basic form of silicon amides that may be synthesised are primary aminosilanes, R_3SiNH_2. Compounds of this type have been investigated by Cheng *et*. *al*. as precursors for the deposition of mesoporous silicon nitride ceramics.[24] A review of the literature reveals that several metal complexes have been obtained from reaction with these silicon amides or their monolithiated derivatives. These include magnesium,[25] titanium,[26 – 29] zirconium,[29 – 32] vanadium,[33] tantalum,[34] tungsten,[35, 36] zinc,[37] boron,[38] aluminium [39 - 43] and gallium [44] complexes, which have been investigated primarily as catalytic species but in a few relevant cases as precursors to metal silicon nitride composites.[26, 39, 45]

Cheng *et*. *al*. have synthesised and investigated the aluminium complex $Al[NHSi(NMe_2)_3]_3$ and the equivalent thf-adduct as single-source precursors for the preparation of aluminoimidosilicate gels which possess large surface areas.[39, 45] Additionally, Cheng *et*. *al*. have developed the titanium-based single-source precursor $[Ti\{NHSi(NMe_2)_3\}_2\{\mu_2\text{-}NSi(NMe_2)_3\}]_2$ using the silicon amide $(Me_2N)_3SiNH_2$ for use in the formation of a mesoporous TiSiN composite (figure 2.13).[26] However, to our knowledge, this precursor and complexes of a similar nature have yet to be investigated as single-source precursors for the deposition of denser films suitable for use as diffusion barrier materials.

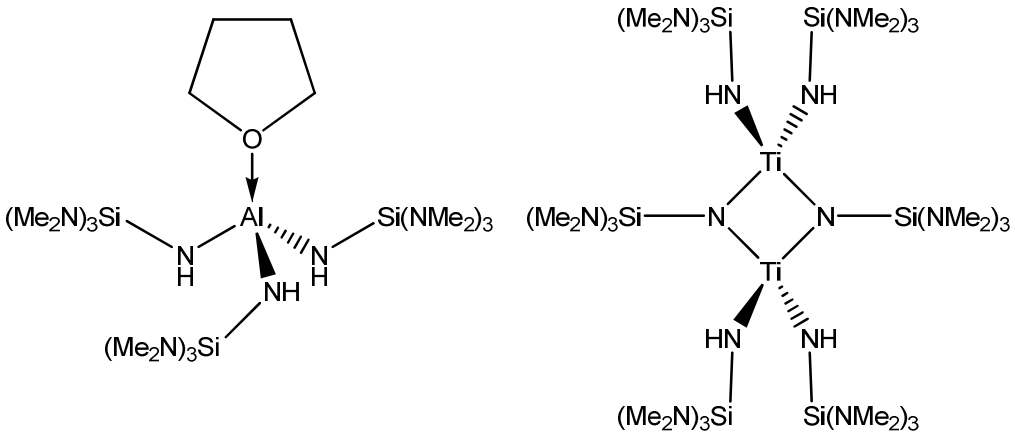

Figure 2.13: Metal complexes reported by Cheng *et*. *al*. as potential single-source precursors for the formation of mesoporous MNSi materials. Both complexes were synthesised using the monolithiated salt of the primary aminosilane $(Me_2N)_3SiNH_2$.[26, 39]

Initial investigations found the compound Ph_3SiNH_2 to be the only commercially available aminosilane of the form R_3SiNH_2. This compound is commonly encountered in the synthesis of metal complexes with respect to other R_3SiNH_2 aminosilanes, with several metal complexes reported in the literature as displayed in figure 2.14,[28, 29, 41] and therefore provided the initial focus for the work presented here.

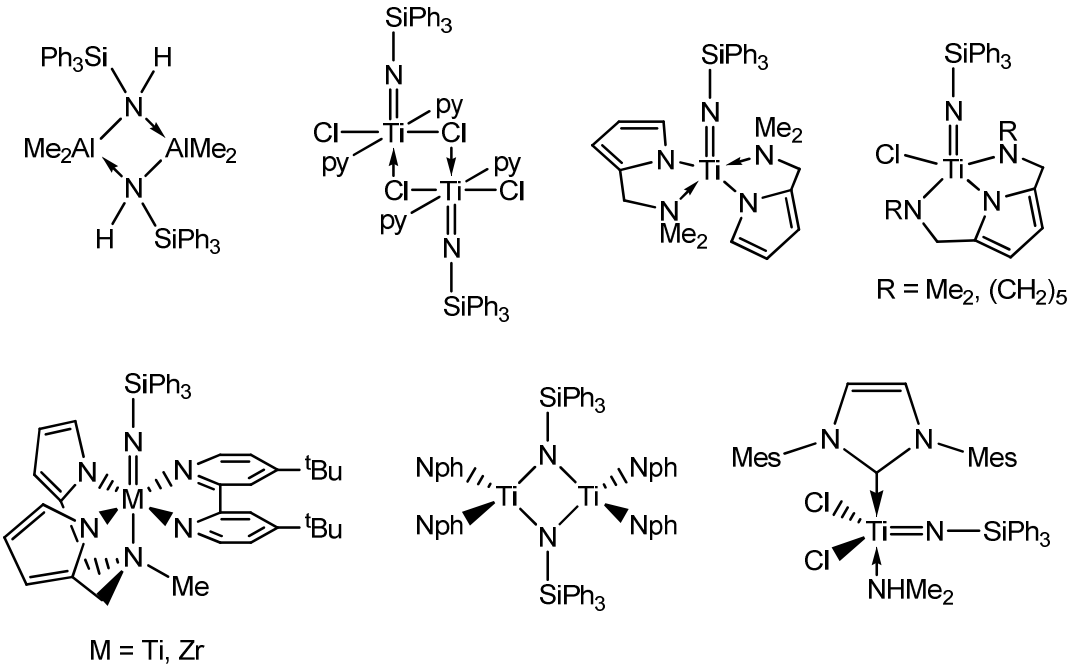

Figure 2.14: Metal complexes reported in the literature which are synthesised using the commercially available primary aminosilane Ph_3SiNH_2. [28, 29, 41]

Consequently, all the silicon amide derivatives used throughout the body of work presented here were synthesised in-house, simply and inexpensively, through the treatment of a solution of the chlorosilane derivatives, R_3SiCl, with an excess of ammonia. Upon addition of ammonia to the solution of the chlorosilane a white precipitate of ammonium chloride is immediately formed. Removal of the precipitate by filtration yields a colourless solution from which the silicon amide may be isolated.

During this synthesis there is the possibility of self-condensation reactions of the silicon amide occurring in a manner observed within metal amides as mentioned previously, however this may be prevented by the use of bulky R-substiuents. For example, the reaction of chlorotriethylsilane, Et_3SiCl, with ammonia affords the primary aminosilane Et_3SiNH_2, whilst the analogous reaction using chlorotrimethylsilane, Me_3SiCl, affords only hexamethyldisilazane (HMDS), $(Me_3Si)_2NH$, as shown below in figure 2.15.[38, 46]

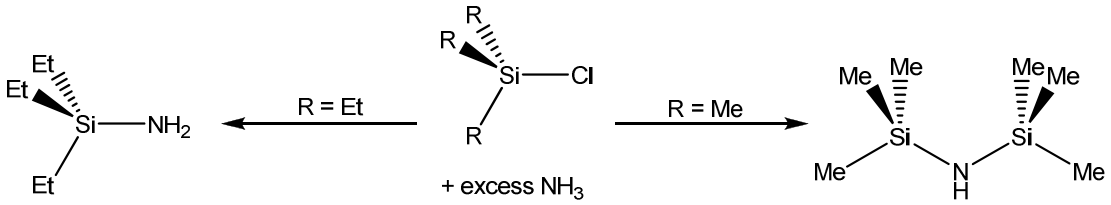

Figure 2.15: Reaction scheme for the treatment of a chlorosilane, R_3SiCl, with excess ammonia. Unless sterically stabilized, self-condensation of the resulting aminosilane is observed.

Using the reaction synthesis shown below in figure 2.16 a range of primary silicon amides have been synthesised from the corresponding chlorosilanes, as shown in table 2.1. A wide range of R groups can potentially be incorporated into the ligand using this procedure. This ability to readily introduce variation of the R groups on the silane enables the properties of the metal complex precursor formed using the silicon amide ligand to be tuned.

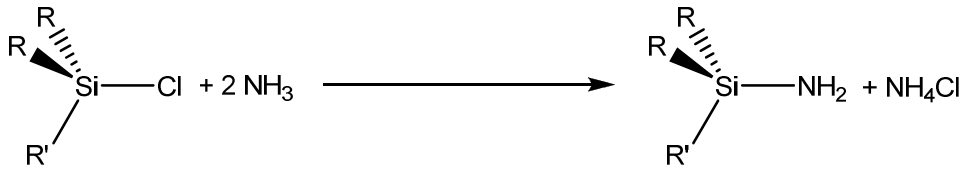

Figure 2.16: General synthetic procedure for the synthesis of aminosilane ligands of the form R_3SiNH_2

Table 2.1: Silicon amides of the form $R_2R'SiNH_2$ synthesised

Ligand	R	R'
1	Ph	Ph
2	Ph	H
3	Et	Et
4	Me	^{t}Bu
5	NMe_2	NMe_2

As mentioned above, the only silicon amide readily commercially available is triphenylsilylamine, Ph_3SiNH_2. However due to the cost being relatively inhibitive for large scale synthesis, the silicon amide was also prepared using the general synthesis displayed above in figure 2.16. Consequently, treatment of Ph_3SiCl with an excess of ammonia yields a colourless solution after

filtering, from which Ph_3SiNH_2 (**1**) was isolated in high yield (91%) as a white crystalline solid by drying *in vacuo*. The ^1H NMR spectrum for **1** displays a singlet peak due to the resonance of the {NH} protons, however the signal is relatively broad due to hydrogen bonding effects. In addition two broad multiplets are observed in the aryl region, with one signal corresponding to the para- and ortho- situated protons of the phenyl rings whilst the signal corresponding to the meta-protons displays a downfield shift.

As **1** was obtained in high percentage yield after being subjected to reduced pressures, this implied that the volatility of the compound may be relatively low, a property that is unfavourable for CVD precursors. Therefore the synthesis of Ph_2HSiNH_2 was considered, where removal of a single bulky phenyl substituent and the resultant reduction in molecular mass might help to improve the volatility of the ligand. Whilst Ph_2HSiNH_2 has been scarcely studied, with our investigations finding no reports of this compound being reacted with metal complexes, the synthesis of a similar silicon amide, $^tBu_2HSiNH_2$, and its reaction with Al^iBu_3 has been reported.[41] Consequently, using Ph_2HSiCl in the synthetic procedure displayed in figure 2.16, with the subsequent removal of solvent under reduced pressure once the reaction had reached completion, yielded the product as a pale yellow oil. Purification of this oil by distillation resulted in the isolation of Ph_2HSiNH_2 (**2**) as a colourless liquid. However, due to removal of a bulky phenyl ligand, whilst the volatility may be improved, a small degree of self-condensation may potentially have occurred due to the lower degree of steric hindrance, with a comparatively low yield (27 %) of **2** being attained.

Compounds **3** and **4**, with aliphatic substituents on the silicon centre, both display a higher degree of volatility and are consequently both isolated from their respective reaction mixtures by distillation after the solvent has itself been removed by distillation. However, whilst **3** is isolated as a colourless liquid **4** is isolated as a highly soluble colourless crystalline solid. In both cases the ^1H NMR spectra are as expected.

Silicon amides **1** – **4** were all prepared using the corresponding chlorosilane as the starting reagent. However, the chlorosilane required for the synthesis of $(Me_2N)_3SiNH_2$ (**5**), although commercially available, is prohibitively expensive for large-scale synthesis and therefore the synthetic procedure is subsequently taken back a stage to tetrachlorosilane, $SiCl_4$. Treatment of $SiCl_4$ with an excess of dimethylamine, $HNMe_2$, in an ammonium halide elimination reaction affords the tris-amido species $(Me_2N)_3SiCl$ only (figure 2.17), regardless of how large an excess of amine is present and prolonged reaction times. Further substitution by $HNMe_2$ to the tetra-amido species $Si(NMe_2)_4$ has been reported to be prevented by steric hindrance at the silicon centre, although aminolysis of the Si-Cl bond is still possible by other less sterically hindered amines.[47]

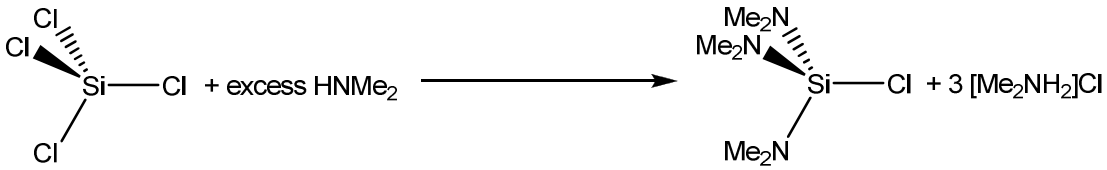

Figure 2.17: Reaction schematic for the synthesis of the tris-amido species $(Me_2N)_3SiCl$.

Once filtered to remove the resultant white precipitate of $[Me_2NH_2]Cl$, $(Me_2N)_3SiCl$ may be treated *in situ* with ammonia as before, with **5** being isolated as a colourless liquid after filtration and distillation.

However, after the reaction between $(Me_2N)_3SiCl$ and ammonia has been performed, if the clear, filtered solution is left standing for excessive periods of time before isolating the product by distillation a white precipitate is observed to slowly deposit from solution. The rationale for this observation was initially thought be the aminolysis of traces of unreacted chlorosilane by residual ammonia trapped in solution. Unfortunately, data from the ^1H NMR spectrum of the colourless liquid product isolated from the solution by distillation was inconsistent with that obtained for **5**. Whilst the ^1H NMR spectrum of **5** displays a resonance at 2.51 ppm and a smaller broad resonance at 0.25 ppm equivalent to the NMe_2 and NH_2 substituents

respectively,[39] the spectrum obtained for the isolated product in this instance showed a single resonance at 2.41 ppm only.

An alternative theory that was considered was the presence of multiple, electronegative NMe_2 groups bonded to the silicon centre increasing its susceptibility to hydrolysis, with the resultant insoluble, polymeric amino-siloxanes formed precipitating out of solution. Yet this theory, as before, cannot account for the large volume of colourless liquid isolated from the reaction solution that cannot be identified as **5**.

Interpretation of ^{29}Si NMR spectra provides information for an alternative hypothesis. The colourless liquid displays a single resonance in the ^{29}Si NMR spectrum at approximately –28 ppm, (compared to approximately –34 ppm for **5**) [39] which is equivalent to the chemical shift observed for $Si(NMe_2)_4$ (δ = -28.13 ppm).[48] Formation of $Si(NMe_2)_4$ in this instance may potentially be occurring in one of two ways as shown in figure 2.18 – firstly through the redistribution of two equivalents of $(Me_2N)_3SiCl$ to afford $Si(NMe_2)_4$ and $(Me_2N)_2SiCl_2$. The latter may then react with ammonia and undergo self-condensation to result in the formation of indeterminate polymeric silicon amides. Alternatively, although Passarelli *et*. *al*. have suggested that the formation of $Si(NMe_2)_4$ from $SiCl_4$ is kinetically unfavourable due to steric hindrance,[47] formation of $Si(NMe_2)_4$ may be thermodynamically favourable with aminolysis of the fourth Si-Cl bond by excess $HNMe_2$ still present in solution occuring over time. The observation that white precipitate is only formed when the solution is left standing for excessive periods of time before isolating the product lends some argument to this hypothesis. Consequently it is recommended that $(Me_2N)_3SiCl$ is isolated from the first step before reacting with ammonia, or alternatively is prepared through the reaction of $SiCl_4$ with three equivalents of $LiNMe_2$.

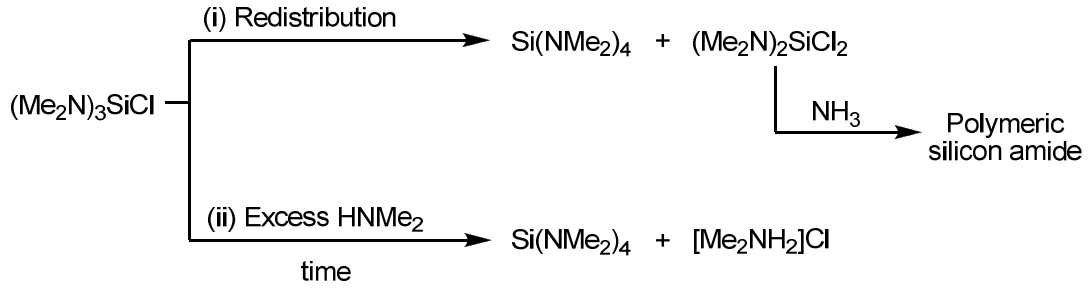

Figure 2.18: Potential reactions occurring within the reaction solution for the synthesis of **5**, resulting in the formation of $Si(NMe_2)_4$.

2.3 Synthesis of Group 4 metal complexes using R_3SiNH_2 ligands

2.3.1 Synthesis of Group 4 metal complexes using Ph_3SiNH_2 (1)

As noted earlier, the potential exists for silicon amides to be reacted directly with transition metal amide systems, such as TDMAT, with the resultant formation of potentially useful complexes containing metal, silicon and nitrogen. A potential reaction for the synthesis of transition metal imido systems is displayed below in figure 2.19, although there is very little evidence within the literature for this reaction occurring using R_3SiNH_2 compounds.

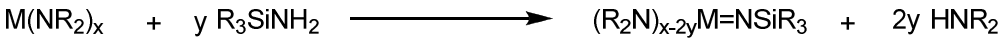

Figure 2.19: General schematic of a potential reaction between transistion metal amide systems and primary aminosilanes.

The majority of metal complexes containing the R_3SiN- moiety reported in the literature have been synthesised using the monolithiated silicon amide and a metal chloride reagent. Additionally, of the known compounds that have been prepared using the commercially available silicon amide Ph_3SiNH_2 (**1**), which have previously been shown in figure 2.14 (page 68), the majority have been synthesised from the reagent $[Ti(NSiPh_3)Cl_2(py)_2]_2$ which already contains the $Ti{=}N\text{-}SiR_3$ moiety. However, the reagent $[Ti(NSiPh_3)Cl_2(py)_2]_2$ is prepared via a transimination reaction between **1** and the imido complex $Ti(N^tBu)Cl_2(py)_3$,[29] whilst the carbene containing complex shown previously in figure 2.14 is prepared through the addition of **1** to a solution of

$TiCl_2(NMe_2)_2(IMes)$ with the subsequent elimination of $HNMe_2$.[28] Furthermore dimeric, bridged amide systems have been prepared from the reaction of R_3SiNH_2 compounds with zinc,[37] aluminium [41] and gallium [44] metal alkyl reagents.

Therefore a series of reactions were performed with **1** being refluxed with a Group 4 metal amide, $M(NMe_2)_4$ (M = Ti, Zr, Hf), in a 1:1 ratio at 70 ^oC in toluene, with the elimination of volatile $HNMe_2$ (figure 2.20).

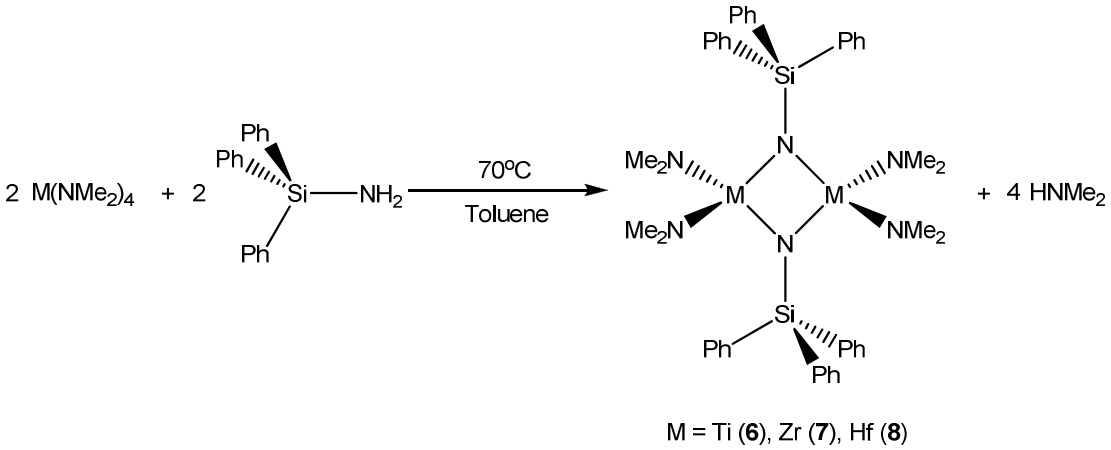

Figure 2.20: Reaction scheme for the reaction of a Group 4 metal amide of the form $M(NMe_2)_4$ and **1** in a 1:1 ratio.

The reaction of **1** with $Ti(NMe_2)_4$ produced a colour change in the solution from light orange to a deeper shade as the reaction progressed, whilst the analogous reactions with colourless solutions of the zirconium and hafnium derivatives displayed no significant difference in appearance over the course of the reaction. Upon completion the metal complexes were isolated by crystallisation at –28 ^oC from the reaction solution, with the titanium complex (**6**) being isolated as orange crystals, whilst the zirconium (**7**) and hafnium (**8**) complexes were both isolated as colourless crystals. These metal complexes have been shown to be sensitive to air and moisture. This sensitivity is highly evident for **6,** where the orange crystals will rapidly turn white upon exposure to air as titanium oxides are formed by decomposition of the complex.

Analysis of the ^{1}H NMR spectra for **6** and **7** show them to be comparable. Both spectra display two sets of multiplets in the aryl region in a manner similar to that of the free ligand, **1**, attributed to the protons of the $SiPh_3$ moiety. Additionally both spectra show a single peak (2.92 ppm for **6**, 2.72 ppm for **7**) that may be assigned to the methyl protons in the NMe_2 substituents. Integration of the resonances attributed to the $SiPh_3$ and NMe_2 moieties show them to be present in a 1:2 ratio in both **6** and **7**. This observation is consistent with the elimination of two equivalents of $HNMe_2$ and the formation of an imido species with the empirical formula $[(Me_2N)_2M{=}NSiPh_3]$. The stability of this species is likely to be improved by increasing the coordinative saturation of the metal centre through the formation of the dimeric species $[(Me_2N)_2M(\mu_2\text{-}NSiPh_3)]_2$. As only a singlet peak is observed for the NMe_2 resonances in the ^{1}H NMR spectra for complexes **6** and **7**, a high degree of fluxionality may be assumed to occur for these molecules at room temperature in solution.

The ^{1}H NMR spectrum obtained for the hafnium complex, **8**, is also comparable to the spectra obtained for **6** and **7**, with the exception of an additional singlet resonance at 1.60 ppm. Integration of the signal reveals the presence of six equivalent proton environments, the equivalent of one additional $\{NMe_2\}$ species present for every four NMe_2 amide groups. One potential explanation could be the presence of a bridging NMe_2 ligand, although this outcome is unlikely as this would require the improbable oxidation of one hafnium atom from a (+4) to a (+5) oxidation state. An alternative theory that may be more likely is the presence of a molecule of $HNMe_2$ that is liberated during synthesis. Since crystals of **8** are dried under reduced pressure this should result in the removal of any molecules of free amine. Therefore any $HNMe_2$ present within **8** must be bonded to a metal centre through a dative bond involving the nitrogen lone pair (figure 2.21). Similar complexes possessing a $\{Hf\text{-}N(H)Me_2\}$ moiety have previously been reported by Gao [49] and Hughes.[50]

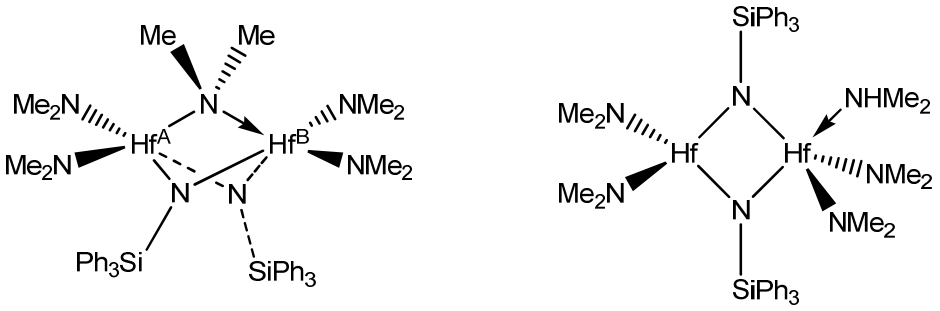

Figure 2.21: Potential reaction products for the reaction of **1** and $Hf(NMe_2)_4$, incorporating an additional $\{NMe_2\}$ fragment compared to the dimeric species observed for **6** and **7**.

Consequently, **8** is likely contain two $[(Me_2N)_2Hf{=}NSiPh_3]$ moieties but with a $HNMe_2$ amine ligand coordinated to only one of the two hafnium centres. However, as this arrangement would invoke an inequivalence between the amide ligands bound to the separate hafnium atoms, we would expect to see an increasingly complicated ^1H NMR spectrum due to splitting of the amide signal. Since no splitting is observed it must be concluded that rapid exchange of the amine between the hafnium centres is occurring in solution (figure 2.22).

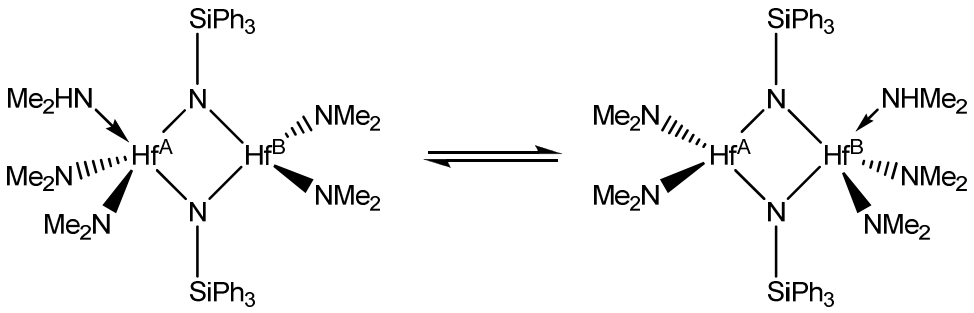

Figure 2.22: Schematic of the rapid exchange of the $HNMe_2$ ligand between the two hafnium atoms within **8**.

For all three metal complexes crystals suitable for single crystal X-ray diffraction were isolated, with the structures obtained from these studies consistent with those predicted from observations made through analysis of the ^1H NMR spectra.

The titanium complex $[\{(Me_2N)_2Ti(\mu_2\text{-}NSiPh_3)\}_2]$, **6**, is found to crystallise in the triclinic space group (*P-1*), with two halves of two dimer molecules occupying

the asymmetric unit as shown in figure 2.23. Each dimer is situated on a crystallographic inversion centre. Consequently the second half of the molecule containing Ti(1) is generated by the symmetry operator (-x, 1-y, 2-z), whilst the equivalent atoms within the molecule containing Ti(2) are generated by the symmetry operator (-x-1, -y, 1-z). The following discussion of the structure of **6** will focus on the unit containing Ti(1) as an example case, with bond lengths and angles in both the Ti(1) and Ti(2) units not too dissimilar. The molecular structure for **6** is shown in greater detail in figure 2.24, with selected bond lengths and angles for this complex given in table 2.2.

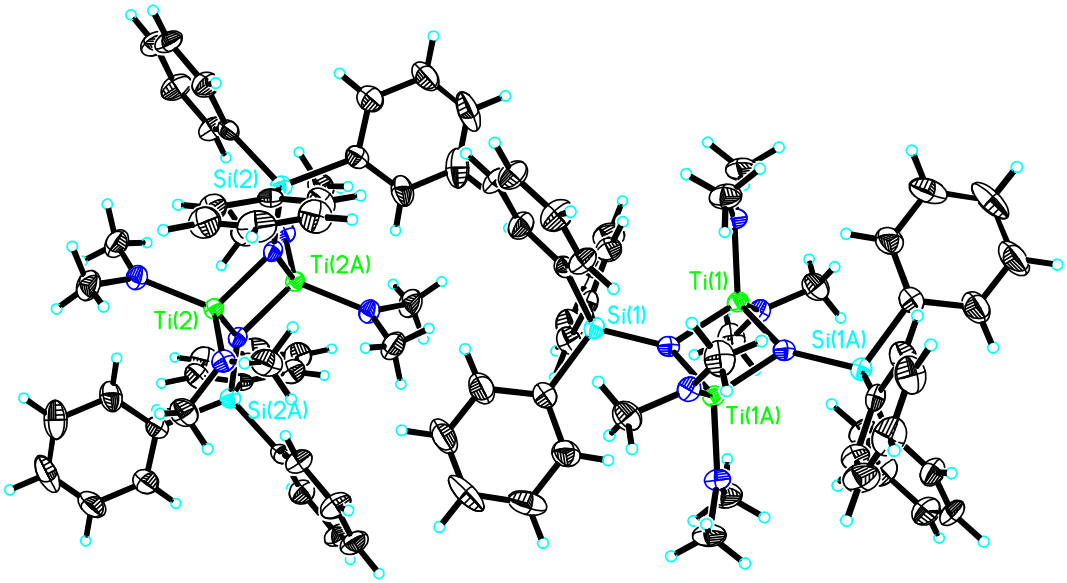

Figure 2.23: Asymmetric unit for the complex [{$(Me_2N)_2Ti(\mu_2\text{-}NSiPh_3)$}$_2$], **6**, containing two half dimers [Ti(1), Ti(2)], and the equivalent positions in each molecule [Ti(1A), Ti(2A)] generated by symmetry operations.

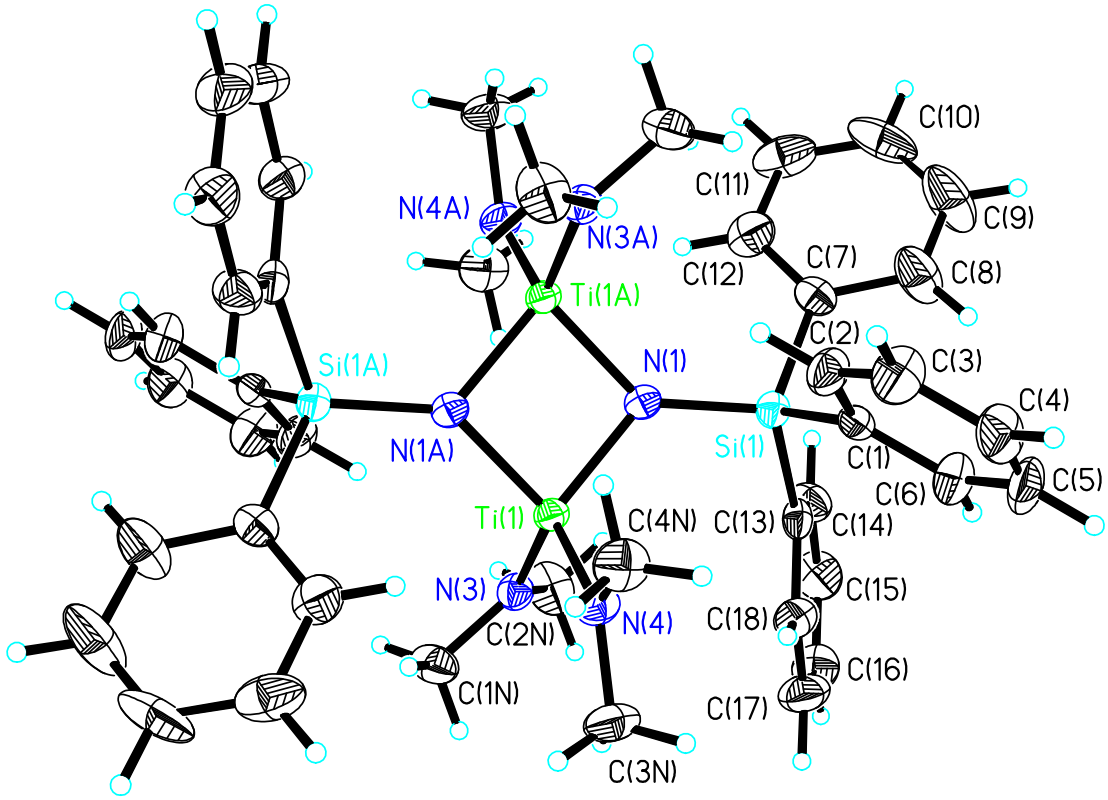

Figure 2.24: Molecular structure of the complex $[\{(Me_2N)_2Ti(\mu_2\text{-}NSiPh_3)\}_2]$, **6**. Thermal ellipsoids are shown at 50 % probability and hydrogen atoms as hollow spheres.

Table 2.2: Selected bond lengths (Å) and bond angles (°) for complex **6**.

Ti(1)-N(1)	1.915 (3)	Ti(1)-N(1A)	1.938 (3)
Ti(1)-N(3)	1.889 (3)	Ti(1)-N(4)	1.899 (3)
Si(1)-N(1)	1.732 (3)		
N(1)-Ti(1)-N(1A)	86.27 (11)	Ti(1)-N(1)-Ti(1A)	93.73 (11)
Ti(1A)-N(1)-Si(1)	137.33 (15)	Ti(1)-N(1)-Si(1)	126.66 (15)
Ti(1)-N(3)-C(1N)	116.6 (2)	Ti(1)-N(3)-C(2N)	131.8 (2)
C(1N)-N(3)-C(2N)	111.6 (3)	Ti(1)-N(4)-C(3N)	127.5 (2)
Ti(1)-N(4)-C(4N)	121.4 (2)	C(3N)-N(4)-C(4N)	111.0 (3)

Analysis of the structure shows the titanium atoms within **6** adopt a four-coordinate, *pseudo* tetrahedral geometry. Each titanium atom is bonded to two $\{NMe_2\}$ amide ligands, with the Ti-N amide bonds [Ti(1)-N(3): 1.889 (3) Å; Ti(1)-N(4): 1.899 (3) Å] coming at the lower end of the range reported for other Ti-N amide complexes (1.85 Å - 2.20 Å) [3, 51] and being similar to those

reported for TDMAT.[52] Additionally the sums of the angles around the amido nitrogen atoms are equal to 360° (3) in both cases [∑ {Ti(1)-N(3)-C(1N), Ti(1)-N(3)-C(2N), C(1N)-N(3)-C(2N)}; ∑ {Ti(1)-N(4)-C(3N), Ti(1)-N(4)-C(4N), C(3N)-N(4)-C(4N)}], thereby indicating planarity at the amido nitrogen centres [N(3), N(4)]. Consequently these observations of planarity and short Ti-N bonds imply that the amide substituents are bonding to the titanium atom in a manner depicted in structure (**IIb**) as displayed earlier in this chapter.

In addition to being bonded to the amide ligands, the two titanium atoms are bridged by two μ_2-$NSiPh_3$ units to create a central $\{Ti_2N_2\}$ four-membered ring [Ti(1), N(1), Ti(1A), N(1A)]. Calculations show the ring to be planar, with the sum of the internal angles equal to 360° (11) [∑ 2{Ti(1)-N(1)-Ti(1A), N(1)-Ti(1)-N(1A)}]. Additionally the sums of the angles around the imido nitrogen atoms [N(1), N(1A)] are calculated as 357.72° (15) [∑ {Ti(1)-N(1)-Ti(1A), Ti(1)-N(1)-Si(1), Ti(1A)-N(1)-Si(1)}], indicating little to no degree of pyramidalisation of the nitrogen and therefore implying an sp^2 hybridisation with the lone pair occupying the p-orbital on the nitrogen.

As discussed earlier in this chapter μ_2-bridging imido ligands, such as those observed in **6**, have been observed bonding in both a symmetrical, delocalised manner or alternatively in an unsymmetrical, localised bonding fashion (figure 2.5, page 60, structure **VII** and **VIII** respectively). Analysis of the Ti-N bond lengths within the $\{Ti_2N_2\}$ ring reveals them to be equivalent within experimental error [Ti(1)-N(1), Ti(1A)-N(1A) = 1.915 (3) Å; Ti(1)-N(1A), Ti(1A)-N(1) = 1.938 (3) Å] and are comparable to those reported for related $\{Ti_2N_2\}$ containing systems in the Cambridge Crystallographic Database,[51] implying a delocalised arrangement within the bonding as depicted in structure (**VII**).

The Si-N bond of the Ph_3SiN moiety [Si(1)-N(1) = 1.732 (3) Å] is comparable to many other Si-N complexes, whilst being shorter than the values estimated from covalent radii (1.82 – 1.87 Å).[3] For reasons discussed earlier in this chapter, the short Si-N bond length is indicative of a degree of multiple bonding occurring involving the nitrogen lone pair.

The analogous zirconium complex [{$(Me_2N)_2Zr(\mu_2\text{-}NSiPh_3)\}_2$], **7**, is found to crystallise in the monoclinic space group ($P2_1/n$) with only one half-dimer forming the asymmetric unit. As found with **6**, the dimer of **7** is situated on a crystallographic inversion centre and subsequently the second half of the molecule is generated by the symmetry operator (1-x, 1-y, 1-z). The molecular structure for **7** is shown in detail in figure 2.25, with selected bond lengths and angles for this complex given in table 2.3.

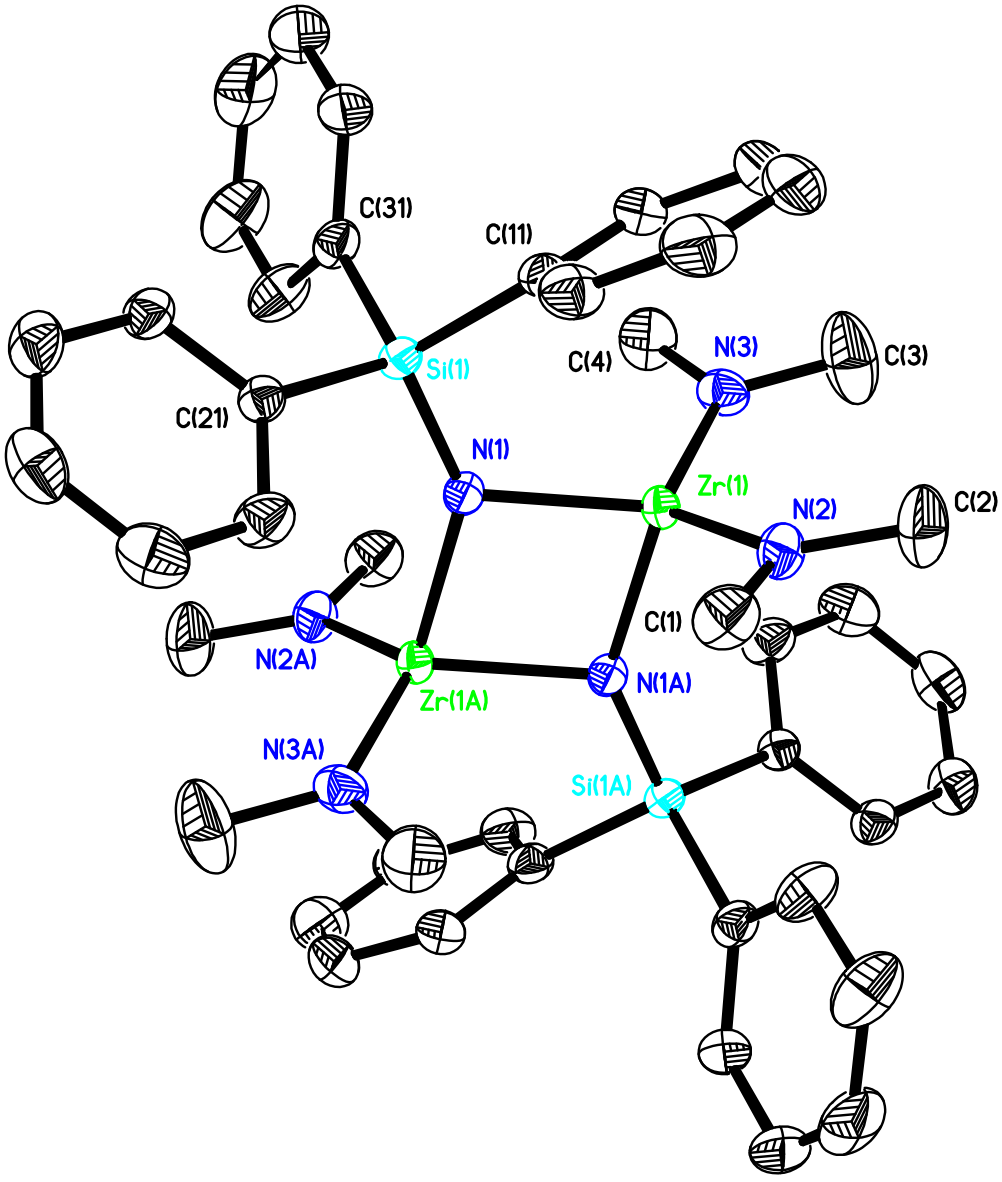

Figure 2.25: Molecular structure of the complex [{$(Me_2N)_2Zr(\mu_2\text{-}NSiPh_3)\}_2$], **7**. Thermal ellipsoids are shown at 50 % probability, with hydrogen atoms omitted for clarity.

Table 2.3: Selected bond lengths (Å) and bond angles (°) for complex **7**.

Zr(1)-N(1)	2.0736 (11)	Zr(1)-N(1A)	2.0784 (11)
Zr(1)-N(2)	2.0548 (13)	Zr(1)-N(3)	2.0453 (13)
Si(1)-N(1)	1.7068 (12)		
N(1)-Zr(1)-N(1A)	81.43 (5)	Zr(1)-N(1)-Zr(1A)	98.57 (5)
Zr(1A)-N(1)-Si(1)	142.98 (7)	Zr(1)-N(1)-Si(1)	118.45 (6)
Zr(1)-N(2)-C(1)	119.50 (11)	Zr(1)-N(2)-C(2)	129.96 (12)
C(1)-N(2)-C(2)	110.52 (15)	Zr(1)-N(3)-C(3)	123.04 (12)
Zr(1)-N(3)-C(4)	125.74 (11)	C(3)-N(3)-C(4)	111.22 (15)

The molecular structure of **7** is found to be isotypic to that observed for **6**, with the dimeric molecule containing two *pseudo* tetrahedral zirconium atoms with two planar NMe_2 amide ligands [N(2) and N(3); N(2A) and N(3A)] bonded to each metal centre and two bridging μ_2-$NSiPh_3$ units creating a four-membered $\{Zr_2N_2\}$ ring [Zr(1), N(1), Zr(1A), N(1A)]. The Zr-N amide bond lengths [Zr(1)-N(2): 2.0548 (13) Å; Zr(1)-N(3): 2.0453 (13) Å] are comparable to other Zr-NMe_2 bond lengths reported within the literature, albeit at the lower end of the range in a manner akin to the Ti-NMe_2 bond lengths observed within **6**.[51]

Additionally, in a similar manner to that observed within **6**, the $\{Zr_2N_2\}$ ring within **7** is planar with the internal angles totalling 360° (5) [∑ 2{Zr(1)-N(1)-Zr(1A), N(1)-Zr(1)-N(1A)}] and the Zr-N bond lengths alternating between 2.0736 (11) Å [Zr(1)-N(1), Zr(1A)-N(1A)] and 2.0784 (11) Å [Zr(1)-N(1A), Zr(1A)-N(1)]. These bond lengths both fall within the range of 2.071 Å to 2.099 Å commonly reported for other $\{Zr_2N_2\}$ ring systems,[51] and are equivalent within experimental error, therefore suggesting that a delocalised arrangement (**VII**) is in effect. Within **7** the imido nitrogen atoms [N(1), N(1A)] also adopt a planar geometry, with the sum of the angles around the nitrogen also equal to 360° (7) [∑ {Zr(1)-N(1)-Zr(1A), Zr(1)-N(1)-Si(1), Zr(1A)-N(1)-Si(1)}], thereby implying an sp^2 hybridisation.

The Si-N bond of the imide ligand within **7** is found to be 1.7068 (12) Å [Si(1)-N(1)] in length, comparable to that observed for the Si-N bond within **6**,

suggesting delocalisation of the nitrogen lone pair and consequently an increase in multiple bond character of the Si-N bond.

Whilst the products obtained from the reaction of **1** with $Ti(NMe_2)_4$ and $Zr(NMe_2)_4$ are structurally analogous, the reaction involving $Hf(NMe_2)_4$ provides a different product, $[\{(Me_2N)_2Hf(\mu_2\text{-}NSiPh_3)\}_2(HNMe_2)]$, **8**. This complex is found to crystallise in the triclinic space group (*P-1*) with two molecules of toluene also present in the asymmetric unit. However, due to the presence of the $HNMe_2$ ligand the molecule does not possess an inversion centre. The molecular structure for **8** is shown in figure 2.26, with toluene solvent molecules omitted for clarity. Additionally, selected bond lengths and angles for this complex given in table 2.4.

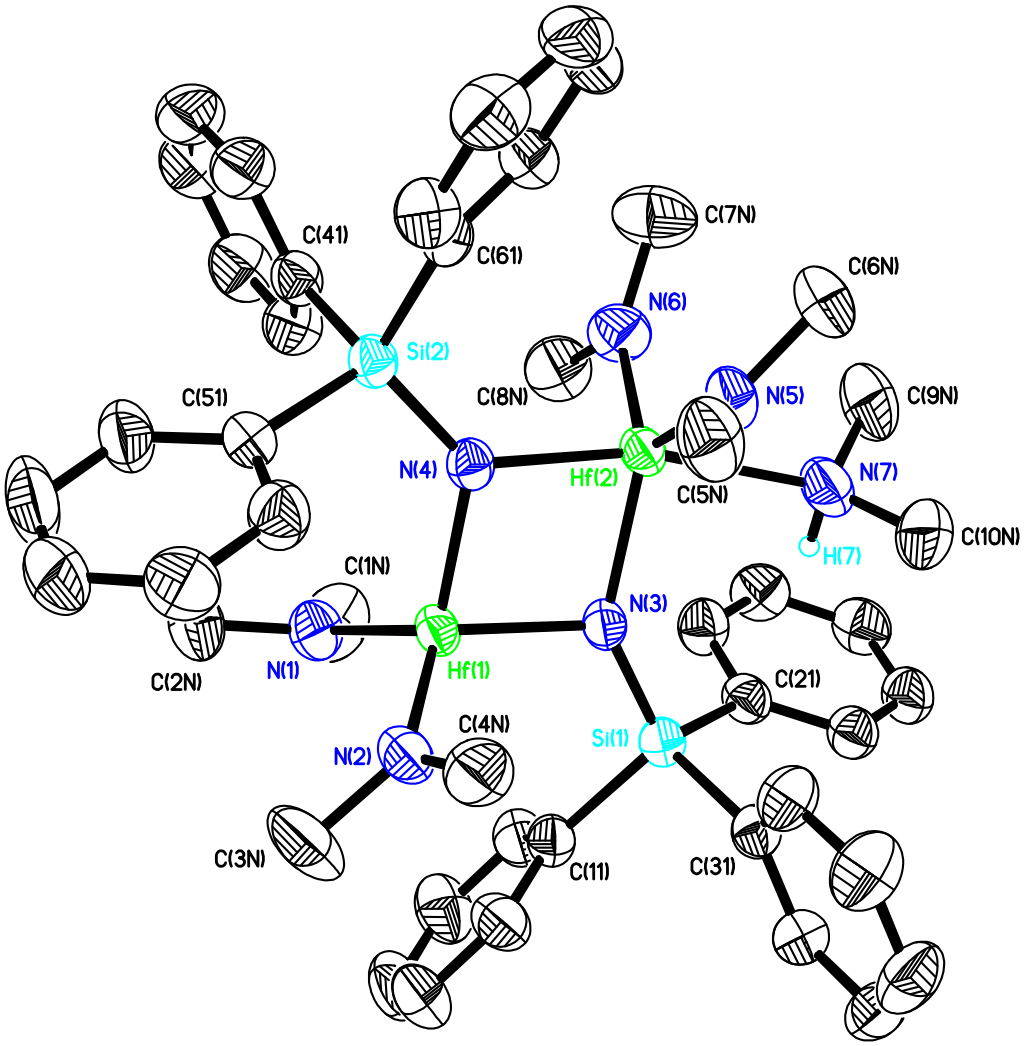

Figure 2.26: Molecular structure of the complex $[\{(Me_2N)_2Hf(\mu_2\text{-}NSiPh_3)\}_2(HNMe_2)]$, **8**. Thermal ellipsoids are shown at 50 % probability, with hydrogen atoms and toluene solvent molecules omitted for clarity.

Table 2.4: Selected bond lengths (Á) and bond angles (°) for complex **8**.

Hf(1)-N(1)	2.041 (3)	Hf(1)-N(2)	2. 042 (3)
Hf(1)-N(3)	2.050 (3)	Hf(1)-N(4)	2.025 (3)
Hf(2)-N(3)	2.121 (3)	Hf(2)-N(4)	2.122 (3)
Hf(2)-N(5)	2.024 (3)	Hf(2)-N(6)	2.030 (3)
Hf(2)-N(7)	2. 442 (3)	Si(1)-N(3)	1.714 (3)
Si(2)-N(4)	1.705 (3)		
N(3)-Hf(1)-N(4)	84.06 (12)	N(3)-Hf(2)-N(4)	80.02 (11)
Hf(1)-N(3)-Hf(2)	97.54 (13)	Hf(1)-N(4)-Hf(2)	98.25 (13)
Hf(1)-N(3)-Si(1)	119.82 (15)	Hf(2)-N(3)-Si(1)	142.59 (17)
Hf(1)-N(4)-Si(2)	128.39 (16)	Hf(2)-N(4)-Si(2)	132.74 (16)
Hf(1)-N(1)-C(1)	128.2 (3)	Hf(1)-N(1)-C(2)	119.1 (3)
C(1)-N(1)-C(2)	112.2 (4)	Hf(1)-N(2)-C(3)	124.8 (3)
Hf(1)-N(2)-C(4)	125.0 (3)	C(3)-N(2)-C(4)	110.2 (4)
Hf(2)-N(5)-C(5)	126.6 (3)	Hf(2)-N(5)-C(6)	123.6 (3)
C(5)-N(5)-C(6)	109.6 (4)	Hf(2)-N(6)-C(7)	133.0 (3)
Hf(2)-N(6)-C(8)	117.4 (3)	C(7)-N(6)-C(8)	109.5 (4)
N(3)-Hf(2)-N(5)	123.98 (13)	N(3)-Hf(2)-N(6)	118.19 (14)
N(3)-Hf(2)-N(7)	85.89 (11)	N(4)-Hf(2)-N(5)	97.90 (12)
N(4)-Hf(2)-N(6)	101.38 (13)	N(4)-Hf(2)-N(7)	165.82 (12)
N(5)-Hf(2)-N(6)	117.05 (15)	N(5)-Hf(2)-N(7)	88.61 (14)
N(6)-Hf(2)-N(7)	86.64 (14)		

Analysis of the structure of **8** by single crystal X-ray diffraction confirms the presence of a single $HNMe_2$ amino ligand within an otherwise dimeric complex, as suggested by analysis of the ^1H NMR spectrum. As a result one hafnium atom, Hf(1), adopts a *pseudo* tetrahedral geometry bonded to two planar NMe_2 amido ligands [N(1) and N(2)] and two N-atoms [N(3) and N(4)] belonging to μ_2-bridging, $\{Ph_3SiN\}$ imido fragments in a comparable manner to that observed for **6** and **7**. However the geometry around the second hafnium atom, Hf(2), is significantly different. Hf(2) adopts a five-coordinate, *pseudo* trigonal bipyramidal geometry in which the amino ligand [$HNMe_2$, N(7)]

occupies an 'axial' position *trans* to a bridging {Ph_3SiN} imido fragment [N(4)]. Whilst relatively few complexes containing the Hf-$NHMe_2$ moiety have been reported, the Hf-N_{amino} bond length calculated for **8** as 2.442 (4) Å [Hf(2)-N(7)] is comparable to the value of 2.462 Å reported by Gao *et*. *al*. for a Hf-N_{amino} bond within a hafnium carborane complex.[49]

Consequently the remaining three 'equatorial' positions about Hf(2) are occupied by two planar NMe_2 amido ligands [N(5) and N(6)] and the second μ_2-bridging {Ph_3SiN} imido fragment [N(3)], which together with the 'axial' imido fragment [N(4)] results in the formation of a planar four-membered {Hf_2N_2} ring [Hf(1), N(3), Hf(2), N(4)].

Due to subsequent geometrical restrictions imparted by the formation of the planar {Hf_2N_2} ring, the N_{amino}-Hf-N_{imido} angle between the 'axial' substituents on Hf(2) is distorted from the ideal angle of 180^o for a trigonal bipyramidal arrangement to 165.82(12)^o [N(7)-Hf(2)-N(4)], although conversely the 'equatorial' substituents exhibit little to no deviation from the expected planar arrangement.

Relatively few complexes have previously been reported which contain a similar {Hf_2N_2} ring.[51, 53 - 55] Nevertheless the Hf-N bond lengths exhibited within the {Hf_2N_2} ring of **8** [Hf(1)-N(3), Hf(1)-N(4), Hf(2)-N(3), Hf(2)-N(4)] are comparable in length to those reported by Castillo (2.050, 2.116 Å) [53] and Bai (2.032, 2.118 Å).[54] The two complexes reported within these references both possess a parallelogram shaped {Hf_2N_2} ring with the Hf-N bond lengths alternating in size around it, in a manner analogous to the rings observed within the {M_2N_2} of **6** and **7**. The {Hf_2N_2} ring within **8** however adopts a different configuration, where the imido ligands are both bonded to Hf(1) through significantly shorter bonds than those to Hf(2). Again, this is consistent with Hf(2) having a higher coordination number.

The four planar NMe_2 amido ligands [N(1), N(2), N(5), N(6)] within **8** all exhibit bonds to the hafnium centres which are comparable in length to those reported in the literature for Hf-NMe_2 bonds (2.001 Å – 2.095 Å).[51] However,

the Hf-N bond lengths for the amido ligands surrounding Hf(2) are marginally shorter than those observed for the amide ligands surrounding Hf(1) - 2.024 (3) Å [Hf(2)-N(5)] and 2.030 (3) Å [Hf(2)-N(6)] versus 2.041 (3) Å [Hf(1)-N(1)] and 2.042 (3) Å [Hf(1)-N(2)] respectively. Whereas the inverse may be expected due greater steric crowding around Hf(2) as a consequence of its greater coordination number, this phenomenon may be explained by the aforementioned steric crowding resulting in the {Ph_3Si} substituents being angled away from Hf(2) and subsequently increasing the steric crowding around Hf(1). This is particularly in evidence for the {Ph_3Si} substituent of the 'equatorial' imido fragment of N(3), i.e. the substituent containing Si(1). Due to a small N(3)-Hf(2)-N(7) angle of 85.89^o (11), the bulky {Ph_3Si} substituent [Si(1)] is held close in space to the amino ligand [N(7)] and therefore requires a greater degree of distortion to lower the steric interactions between the two and subsequently lower the energy of the molecule. Consequently the Hf(2)-N(3)-Si(1) angle of 142.59^o (17) is significantly larger than the angle Hf(1)-N(3)-Si(1) of 119.82^o (15), compared to a smaller difference between the angles Hf(2)-N(4)-Si(2) [132.74^o (16)] and Hf(2)-N(4)-Si(2) [128.39^o (16)] around the nitrogen atom of the 'axial' imido fragement [N(4)].

2.3.2 Bonding within the {M_2N_2} ring

As discussed, a common structural feature of **6**, **7** and **8** is the presence of a planar, four-membered {M_2N_2} ring. This feature is common to many other imido containing complexes of Group 4 metals,[51] including the titanium compound [{$(Me_2N)_2Ti(\mu_2\text{-}N^tBu)\}_2$], **9**, which (as mentioned previously in Chapter 1) has been investigated by Fix *et*. *al*. for its potential as a precursor for TiN films.[56] Complex **9** was first synthesised by Bradley *et*. *al*. in 1963, with the dimeric nature of the complex determined from solution molecular weight measurements.[57] Thorn *et*. *al*. confirmed the structure through single crystal X-ray diffraction in 1981.[11] As part of our investigation into the application of metal complexes synthesised using the silicon amide ligands (**1**-**5**) as CVD single-source precursors, a batch of **9** was prepared through the addition of $^tBuNH_2$ to hexane solution of $Ti(NMe_2)_4$ in a 1:1 ratio with the

evolution of $HNMe_2$ (figure 2.27). Dark red crystals of **9** were then isolated by crystallisation from the reaction solution at –28 °C.

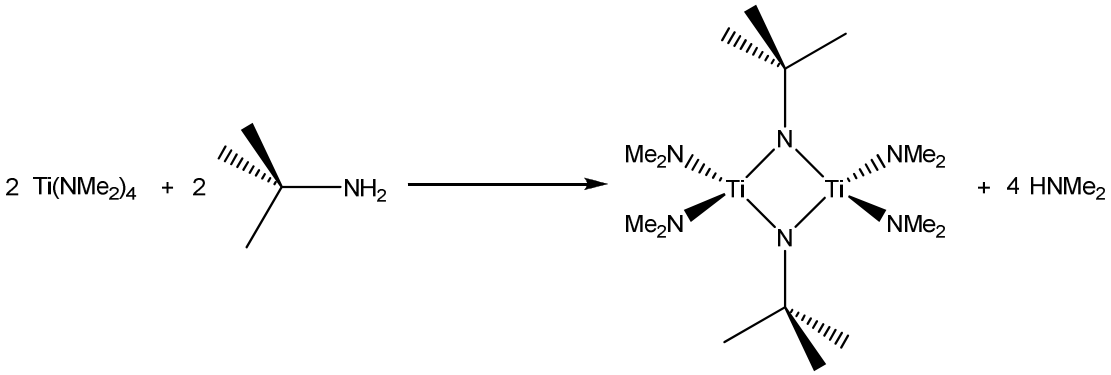

Figure 2.27: Reaction scheme for the reaction of TDMAT and $^{t}BuNH_2$ in a 1:1 ratio.

For completeness, crystals of $[\{(Me_2N)_2Ti(\mu_2\text{-}N^{t}Bu)\}_2]$, **9**, were analysed by single crystal X-ray diffraction. **9** is found to crystallise in the monoclinic space group ($P2_1/n$), with the dimeric molecule situated on a crystallographic inversion centre. Consequently the second half of the molecule containing Ti(1) is generated by the symmetry operator (1-x, -y, 2-z). The molecular structure for **9** is shown in figure 2.28, with selected bond lengths and angles for this complex given in table 2.5.

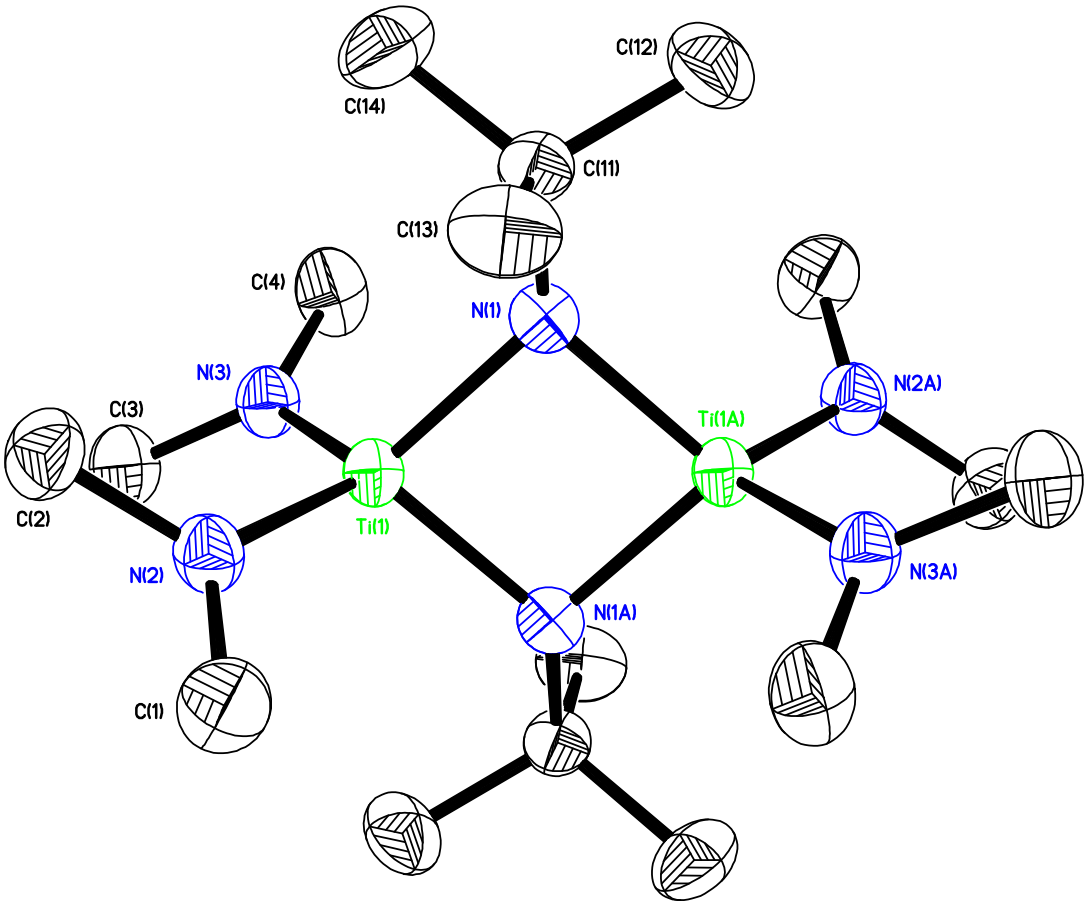

Figure 2.28: Molecular structure of the complex [{$(Me_2N)_2Ti(\mu_2\text{-}N^tBu)\}_2$], **9**. Thermal ellipsoids are shown at 50 % probability, with hydrogen atoms omitted for clarity.

Table 2.5: Selected bond lengths (Å) and bond angles (°) for complex **9**.

Ti(1)-N(1)	1.926 (2)	Ti(1)-N(1A)	1.913 (2)
Ti(1)-N(2)	1.911 (2)	Ti(1)-N(3)	1.916 (2)
N(1)-Ti(1)-N(1A)	86.19 (9)	Ti(1)-N(1)-Ti(1A)	93.81 (9)
Ti(1A)-N(1)-C(11)	129.56 (17)	Ti(1)-N(1)-C(11)	129.95 (17)
Ti(1)-N(2)-C(1)	128.18 (19)	Ti(1)-N(2)-C(2)	120.23 (18)
C(1)-N(2)-C(2)	111.0 (2)	Ti(1)-N(3)-C(3)	124.02 (17)
Ti(1)-N(3)-C(4)	124.74 (18)	C(3)-N(3)-C(4)	111.1 (2)

Complex **9** has been the subject of several studies into the bonding within the $\{M_2N_2\}$ fragment which are particularly relevant to this thesis, in which the symmetrical bonding within this ring system has been rationalised in terms of a delocalised π-bonding system between the vacant d-orbitals of titanium

[Ti(1), Ti(1A)] and the lone pairs on both bridging imido nitrogen atoms [N(1), N(1A)].[11, 58]

Using extended Hückel theory, Thorn *et*. *al*. have described how the π-orbitals of a central $\{Ti_2N_2\}$ core may interact with the π-orbitals of the peripheral ligands.[11] In the absence of peripheral ligands with the ability to form π - bonding interactions the ring system is fully delocalised, involving the d_{xy} and d_{yz} orbitals of the two titanium atoms and the p_y orbitals of the two bridging nitrogen atoms, assuming the $\{Ti_2N_2\}$ ring lies in the *xz* plane. The resultant energy levels obtained for the π-bonding orbitals of this system are shown schematically in figure 2.29.

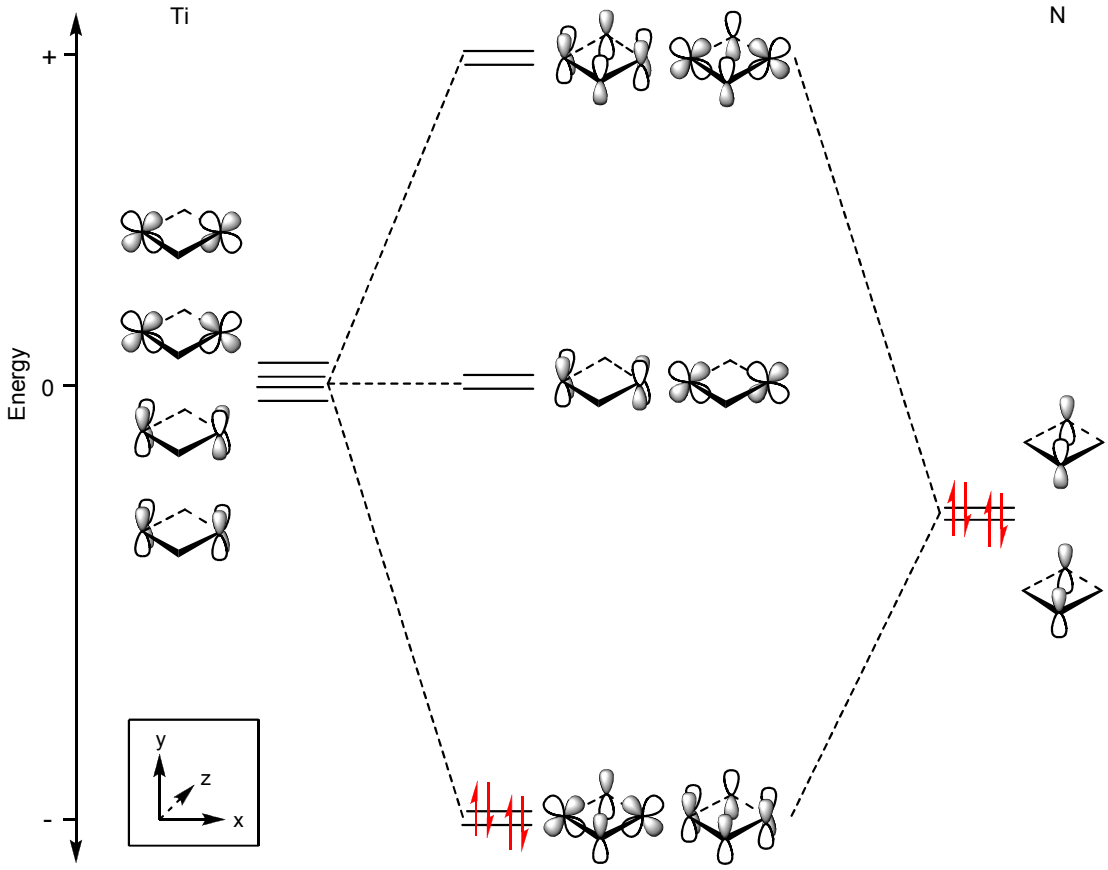

Figure 2.29: Schematic molecular orbital diagram of the Hückel π-orbitals for a $\{Ti_2N_2\}$ ring with no π-interactions from peripheral ligands.

However in the case of **9** the p_z orbitals on the amide nitrogen atoms [N(2), N(3), N(2A), N(3A)] can interact with this system. Of the four possible

symmetry-adapted linear combinations of the p_z orbitals displayed in figure 2.30, only two - (c) and (d) - have the correct symmetry to do so. The remaining two are symmetric to the titanium d_{xz} orbitals and consequently are included within the σ framework of the ring.[11]

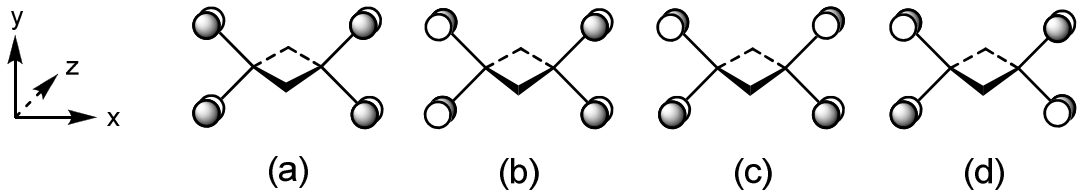

Figure 2.30: The four possible symmetry-adapted linear combinations of p_z orbitals on the amide nitrogen atoms. Only (c) and (d) have the correct symmetry to interact with the π-bonding orbitals of the Ti_2N_2 ring.

Combining these two symmetry combinations with those obtained for the independent ring system results in a change in the pattern of energy levels as shown in figure 2.31.

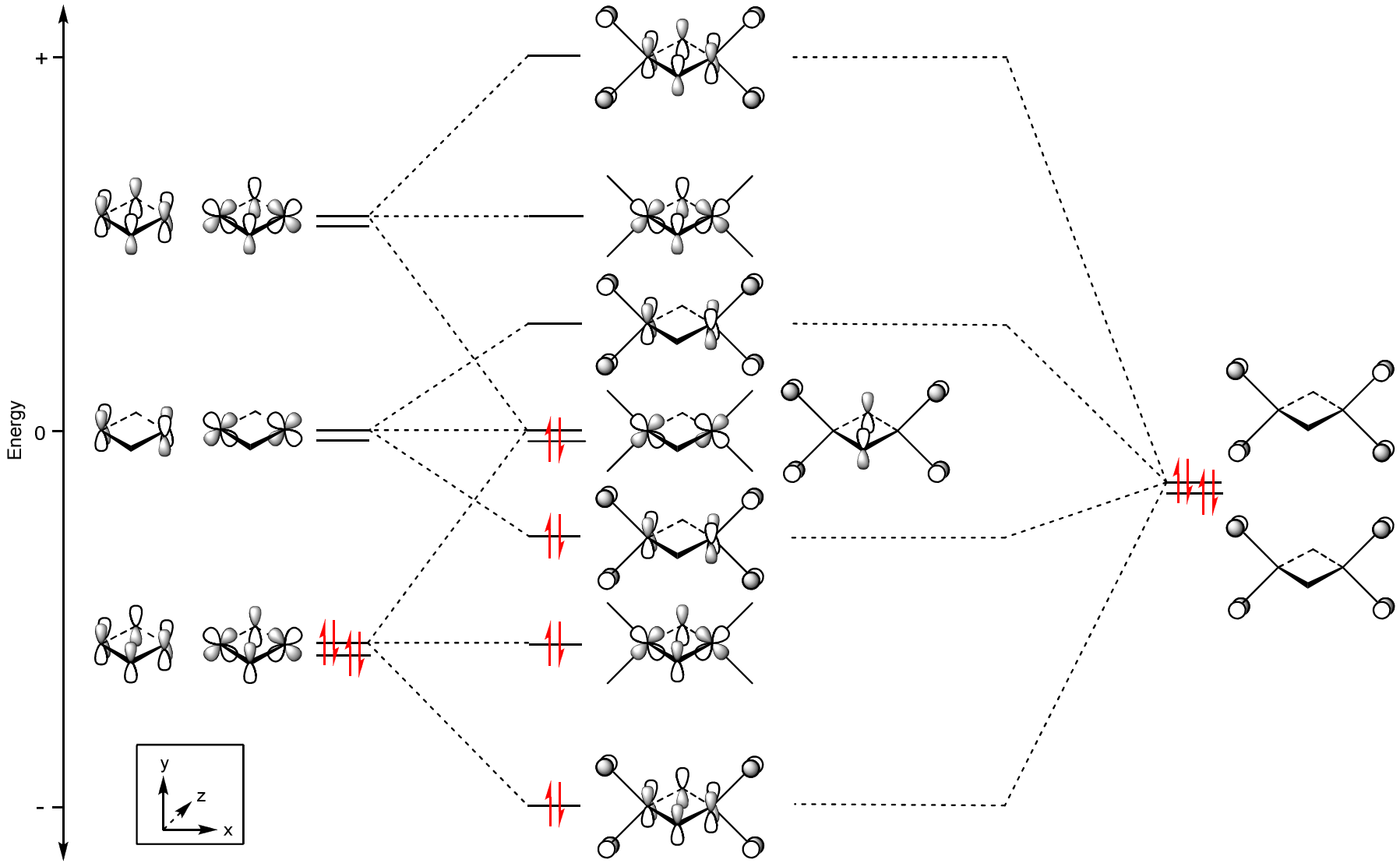
Energy
+
0
-
y
z
x

(Previous page) Figure 2.31: Schematic molecular orbital diagram of the Hückel π-orbitals for the $\{Ti_2N_2\}$ ring with terminal ligand π-interactions included. Two 'non-bonding' symmetry-adapted linear combinations of σ symmetry from the terminal amide ligands are not shown, which contain two additional electron lone pairs.

Into the π-orbitals defined by these energy levels 4 pairs of electrons must be accommodated - the 2 lone pairs from the imido nitrogen atoms [N(1), N(1A)] and 2 pairs from the amido nitrogen atoms [N(2), N(3), N(2A), N(3A)], with the other 2 pairs from the amido nitrogen atoms retained in orbitals of σ-symmetry and therefore discounted. Consequently this results in the apparent half-filling of a degenerate pair of molecular orbitals, implying a potential dissymmetry of the $\{Ti_2N_2\}$ ring due to second-order Jahn-Teller distortions.

Nevertheless analysis by single crystal X-ray diffraction shows the imido Ti-N bond lengths to be equivalent within experimental error [Ti(1)-N(1), Ti(1A)-N(1A) = 1.926 (2) Å; Ti(1)-N(1A), Ti(1A)-N(1) = 1.913 (2) Å]. This can be explained by the assumption for the calculations that the metal d-orbitals and nitrogen p-orbitals have equal ionisation potentials. In reality this is not the case, therefore the degeneracy of these MOs can be broken and a sizeable gap between the HOMO and LUMO generated to lessen the effects of these second-order Jahn-Teller distortions. Due to the difference in ionisation potentials and formal oxidation states the HOMO is consequently confined to the nitrogen atoms and the LUMO to the titanium atoms.[11]

Mountford *et*. *al*. have taken these calculations further, using extended Hückel theory to explain in detail the distortion of groups bonded to the imido nitrogen atom [C(11), ^{t}Bu] out of the plane of the $\{Ti_2N_2\}$ ring,[58] a phenomenon only briefly mentioned by Thorn *et*. *al*.[11] This distortion can potentially be centrosymmetric or non-centrosymmetric, with the centrosymmetric isomer preferred. This phenomenon is a consequence of the second-order Jahn-Teller distortions mentioned above. With the HOMO confined to the nitrogen atoms (figure 2.31), the bridging imido nitrogens should possess "a certain amount of 'lone pair' character". This can result in the nitrogen atoms adopting a pyramidalised geometry, consequently resulting in distortion. Mountford *et*.

al. have gone on to suggest that the extent of pyramidalisation of the bridging imido nitrogen atoms, and the degree of distortion it brings, may give a qualitative indication of the relative π-donating ability of the terminal ligands.[58]

The results from these calculations and the MO digram described in figure 2.31 apply to an ideal system in which certain assumptions have been made. These include the assumption that the p_x orbitals of the amide nitrogens are all perpendicular to the π-orbitals of the central $\{Ti_2N_2\}$ core, and that the metal d-orbitals and the nitrogen p-orbitals have the same ionisation potential.[11, 58] However, as we can see below in figure 2.32, relatively few Group 4 metal complexes exist in which the $\{M_2N_2\}$ fragment is symmetrical.[51]

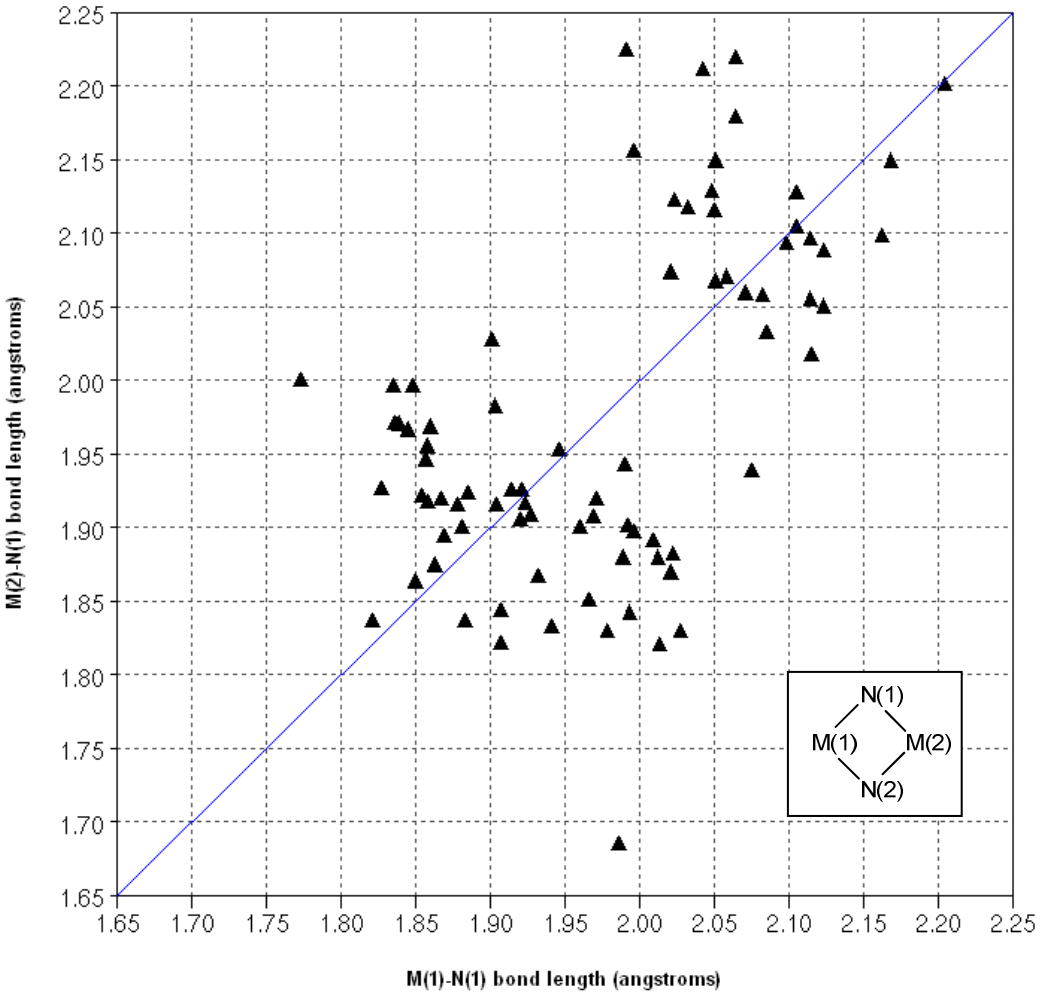

Figure 2.32: Bond lengths within $\{M_2N_2\}$ systems for Group 4 metal complexes.[51]

Although these calculations have been performed with respect to complex **9** in particular, comparable arguments can be made for complexes **6** and **7**, both of which contain the $\{M_2N_2\}$ ring system. However, how much these complexes comply with the molecular orbital (MO) calculations differs by varying degrees. The presence of the silicon atoms in **6** and **7** in particular would be expected to exhibit a significant effect on the MO model. As mentioned previously in this chapter the silicon atom can accept electron density from the imido nitrogen atom to which it is bound [Si(1)-N(1) and Si(1A)-N(1A) within both **6** and **7**], either by d←p π bonding or $n_N \rightarrow \sigma^*_{SiR}$ negative hyperconjugation. Consequently the molecular orbitals depicted in figure 2.31 which possess some contribution from the p_y orbitals of the imido nitrogen atoms [HOMO, HOMO-2, HOMO-3] are likely to be raised in energy, as electron density is withdrawn from these orbitals due to π-bonding interactions with orbitals on the silicon atom. Therefore, the delocalised π-bonding interactions of the $\{M_2N_2\}$ rings within complexes **6** and **7** may be weaker compared to that observed within **9**.

Additionally, as the metal atom is changed from titanium in **6** to zirconium in **7** a greater mismatch in energy between the metal d-orbitals [3d for titanium, 4d for zirconium] and the nitrogen 2p atomic orbitals will occur. This is likely to result in the M-N bonds within the zirconium complex, **7**, becoming increasingly ionic in character compared to that observed within the titanium complex, **6**. Subsequently, the mismatch between the nitrogen 2p atomic orbitals and the hafnium 5d orbitals may be one of many factors why the hafnium complex, **8**, adopts a different structure despite containing the $\{M_2N_2\}$ moiety, although the precise difference is unknown.

2.3.3 Synthesis of Group 4 metal complexes using Ph_2HSiNH_2 (2), Et_3SiNH_2 (3) and $^tBuMe_2SiNH_2$ (4)

As mentioned earlier in this chapter, the use of Ph_2HSiNH_2 (**2**) as a ligand was considered as a viable option to improve the volatility of any resultant complex. However, the reaction of **2** with $Ti(NMe_2)_4$ afforded an intractable yellow-orange solid after the solvent had been removed *in vacuo*. This

intractable solid may be attributed to the formation of a mixture of products, potentially resulting from abstraction of the hydride from the silicon atom by the titanium.[20]

An alternative possibility to improve the volatility of the ligand and any metal complex formed from its reactions is exchanging the aryl substituents for alkyl groups. Therefore a series of reactions were performed with **3** or **4** being refluxed with a Group 4 metal amide, $M(NMe_2)_4$ (M = Ti, Zr, Hf), in a 1:1 ratio in hexane, in an analogous manner to the reaction of $M(NMe_2)_4$ and **1** (figure 2.33, table 2.6).

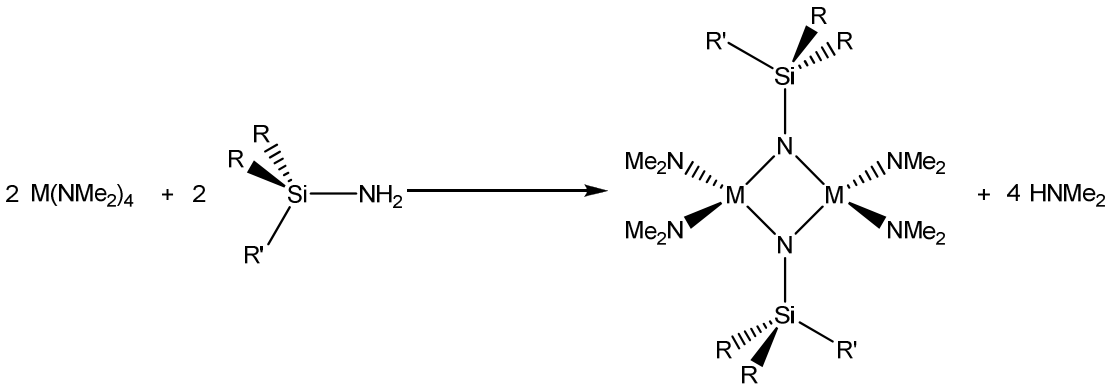

Figure 2.33: Reaction scheme for the reaction of a Group 4 metal amide of the form $M(NMe_2)_4$ and a primary aminosilane containing alkyl substituents (**3** or **4**).

Table 2.6: Group 4 metal amide complexes prepared using aminosilanes **3** and **4**.

Complex	M	R	R'
10	Ti	Et	Et
11	Zr	Et	Et
12	Hf	Et	Et
13	Ti	Me	^{t}Bu
14	Zr	Me	^{t}Bu
15	Hf	Me	^{t}Bu

The reaction of **3** with $Ti(NMe_2)_4$ caused a colour change in the solution from light orange to a deeper shade as the reaction progressed, whilst the analogous reactions with colourless solutions of the zirconium and hafnium derivatives displayed no significant difference in appearance over the course of the reaction. Upon completion the metal complexes were isolated by

crystallisation at –28 ^{o}C from a minimum amount of the reaction solution, with the metal complexes being readily soluble. Consequently, due to the high degree of solubility, the zirconium and hafnium complexes were both isolated by filtering the reaction solution rapidly at 0^{o}C. Subsequently the titanium complex (**10**) was isolated as orange crystals, whilst the zirconium (**11**) and hafnium (**12**) complexes were both isolated as colourless crystals. As with the {$SiPh_3$} derivatives, complexes **10**, **11** and **12** are sensitive to air and moisture.

Analysis of the ^{1}H NMR spectra for **10**, **11** and **12** show them to be comparable, with all three spectra displaying a triplet resonance (1.07 ppm for **10**, 1.10 ppm for **11**, 1.09 ppm for **12**) and a quartet resonance (0.57 ppm for **10**, 0.58 ppm for **11**, 0.56 ppm for **12**) attributed to the CH_3 and CH_2 protons respectively of the {$SiEt_3$} moiety. Additionally the spectra show a single peak (3.30 ppm for **10**, 3.10 ppm for **11**, 3.05 ppm for **12**) that may be assigned to the methyl protons in the {NMe_2} groups. Integration of the resonances attributed to the {$SiEt_3$} and {NMe_2} moieties show them to be present in a 1:2 ratio in both **10** and **11**. This observation is consistent with the elimination of two equivalents of $HNMe_2$ and the formation of an imido species with the empirical formula [$(Me_2N)_2M{=}NSiEt_3$], which is directly comparable to the observations made for the equivalent {$SiPh_3$} containing systems, **6** and **7**. Consequently **10**, **11** and **12** are also likely to exist as the dimeric species [$(Me_2N)_2M(\mu_2\text{-}NSiEt_3)]_2$.

Curiously, analysis of the ^{1}H NMR spectrum for **12** shows no indication of the presence of $HNMe_2$ as observed in the sterically encumbered {$SiPh_3$} system, **8**. Consequently it may be assumed that one molecule of $HNMe_2$ coordinates to a hafnium atom within **8** as a result of electronic rather than steric factors.

Although crystals were obtained for all three metal complexes prepared using **3**, only those isolated for **10** were suitable for single crystal X-ray diffraction. The structure obtained from these studies was consistent with that predicted from observations made through analysis of the ^{1}H NMR spectrum. However, although the crystals of **11** and **12** that were isolated were unsuitable for

single crystal X-ray diffraction, the structures are assumed to be similar to that observed for **10** based on the analysis of the ^{1}H NMR spectra.

The titanium complex [{$(Me_2N)_2Ti(\mu_2\text{-}NSiEt_3)$}$_2$], **10**, is found to crystallise in the monoclinic space group ($P2_1/n$) with half of one dimer molecule occupying the asymmetric unit. As found with **6** and **7**, the dimer of **10** is situated on a crystallographic inversion centre and subsequently the second half of the molecule is generated by the symmetry operator (1-x, -y, 1-z). The molecular structure for **10** is shown in detail in figure 2.34, with selected bond lengths and angles for this complex given in table 2.7.

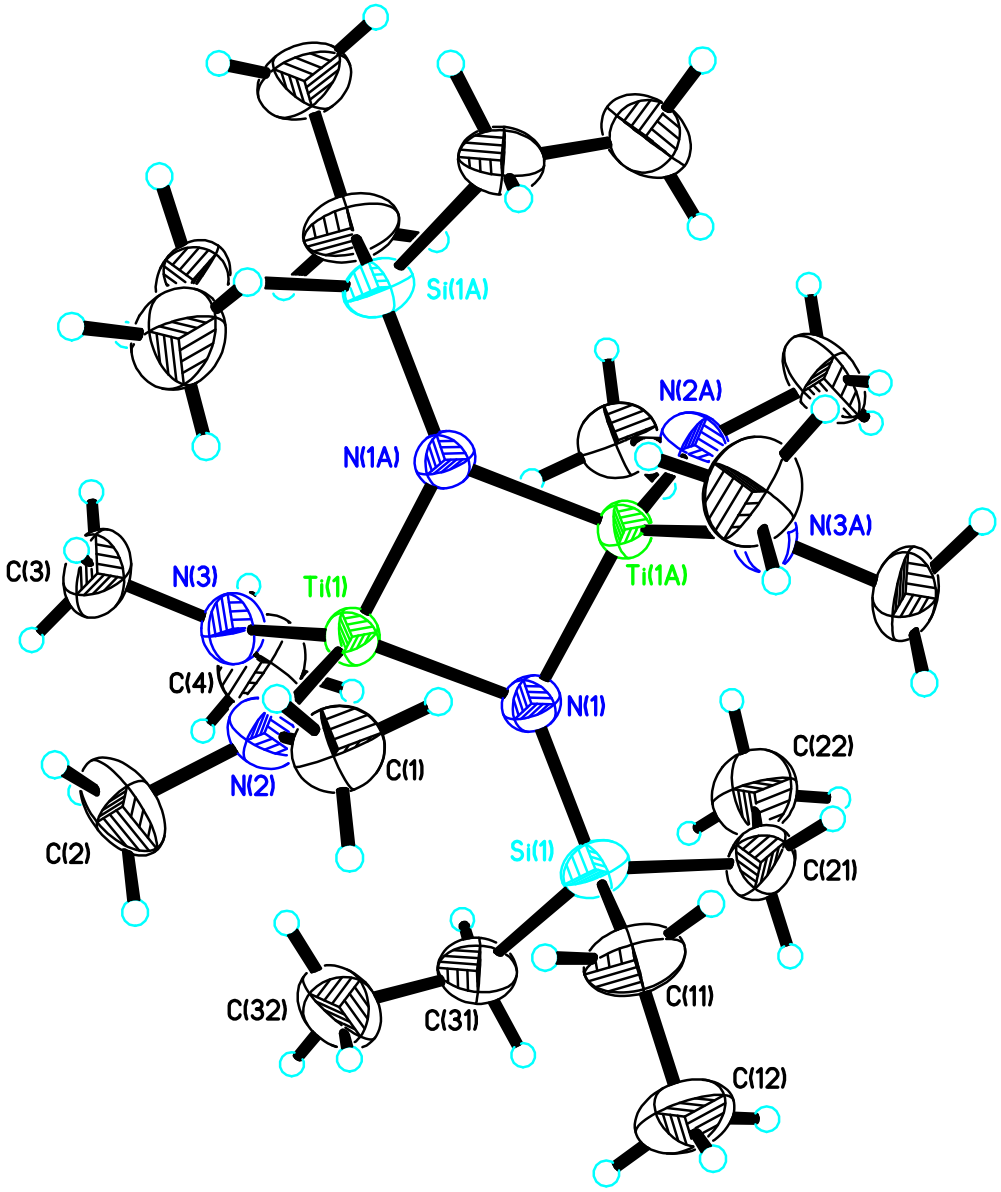

Figure 2.34: Molecular structure of the complex $[\{(Me_2N)_2Ti(\mu_2\text{-}NSiEt_3)\}_2]$, **10**. Thermal ellipsoids are shown at 50 % probability.

Table 2.7: Selected bond lengths (Á) and bond angles (^{o}) for complex **10**.

Ti(1)-N(1)	1.8937 (16)	Ti(1)-N(1A)	1.9448 (16)
Ti(1)-N(2)	1.9086 (18)	Ti(1)-N(3)	1.8955 (18)
Si(1)-N(1)	1.7312 (17)		
N(1)-Ti(1)-N(1A)	86.59 (7)	Ti(1)-N(1)-Ti(1A)	93.41 (7)
Ti(1A)-N(1)-Si(1)	130.98 (9)	Ti(1)-N(1)-Si(1)	131.82 (10)
Ti(1)-N(2)-C(1)	121.87 (16)	Ti(1)-N(2)-C(2)	126.78 (18)
C(1)-N(2)-C(2)	111.3 (2)	Ti(1)-N(3)-C(3)	118.87 (19)
Ti(1)-N(3)-C(4)	129.22 (19)	C(3)-N(3)-C(4)	111.8 (2)

In a similar manner to the equivalent reactions using **1** and **3**, the reaction of **4** with $Ti(NMe_2)_4$ invoked a colour change in the solution from light orange to a deeper shade as the reaction progressed, whilst the analogous reactions with colourless solutions of the zirconium and hafnium derivatives displayed no significant difference in appearance over the course of the reaction. Upon completion the metal complexes were isolated by crystallisation at –28 ^{o}C from the reaction solution. Subsequently the titanium complex (**13**) was isolated as orange crystals, whilst the zirconium (**14**) and hafnium (**15**) were both isolated as colourless crystals. Similarly, these metal complexes have been shown to be sensitive to air and moisture.

Analysis of the ^{1}H NMR spectra for **13**, **14** and **15** show them to be comparable, with all three spectra displaying three distinct resonances. All three show a single peak (3.32 ppm for **13**, 3.11 ppm for **14**, 3.14 ppm for **15**) common to all the spectra for compounds **6** – **12** which may be assigned to the methyl protons in the $\{NMe_2\}$ groups. Additionally the spectra exhibit two singlet resonances further upfield (0.98 ppm and 0.15 ppm for **13**, 1.00 ppm and 0.14 ppm for **14**, 1.00 ppm and 0.12 ppm for **15**) which may be attributed to the butyl and methyl protons respectively of the $\{Si^{t}BuMe_2\}$ moiety. Subsequent integration of the resonances attributed to the $\{Si^{t}BuMe_2\}$ and $\{NMe_2\}$ moieties show them to be present in a 1:2 ratio in all three complexes. Furthermore, in a similar manner to that observed for **12**, analysis of the ^{1}H

NMR spectrum for **15** shows no indication of the presence of $HNMe_2$ as observed in the sterically encumbered {$SiPh_3$} system, **8**.

As before, these observations are consistent with the elimination of two equivalents of $HNMe_2$ and the formation of an imido species with the empirical formula [$(Me_2N)_2M{=}NSi^tBuMe_2$], most likely the dimeric species [$(Me_2N)_2M(\mu_2\text{-}NSi^tBuMe_2)]_2$. Additionally, for reasons stated earlier for compounds **6** and **7**, a high degree of fluxionality may also be assumed to occur for molecules of **13**, **14** and **15** at room temperature in solution.

For all three metal complexes crystals suitable for single crystal X-ray diffraction were isolated. Subsequently the structures obtained from these studies are found to be consistent with those predicted from observations made through analysis of the ^1H NMR spectra and are similar to the structures obtained for complexes **6** – **12**. In a similar manner to the titanium complex **10**, complexes **13** – **15** are all found to crystallise in the monoclinic space group ($P2_1/n$), in which the dimeric molecule is situated on a crystallographic inversion centre. Consequently the second half of the molecule in all three complexes is generated by symmetry operations [**13**: (-x, -y, -z); **14**: (2-x, 1-y, 1-z); **15**: (1-x, 1-y, 1-z)]. The molecular structures along with corresponding selected bond lengths and angles are given below for **13** (figure 2.35, table 2.8), **14** (figure 2.36, table 2.9) and **15** (figure 2.37, table 2.10).

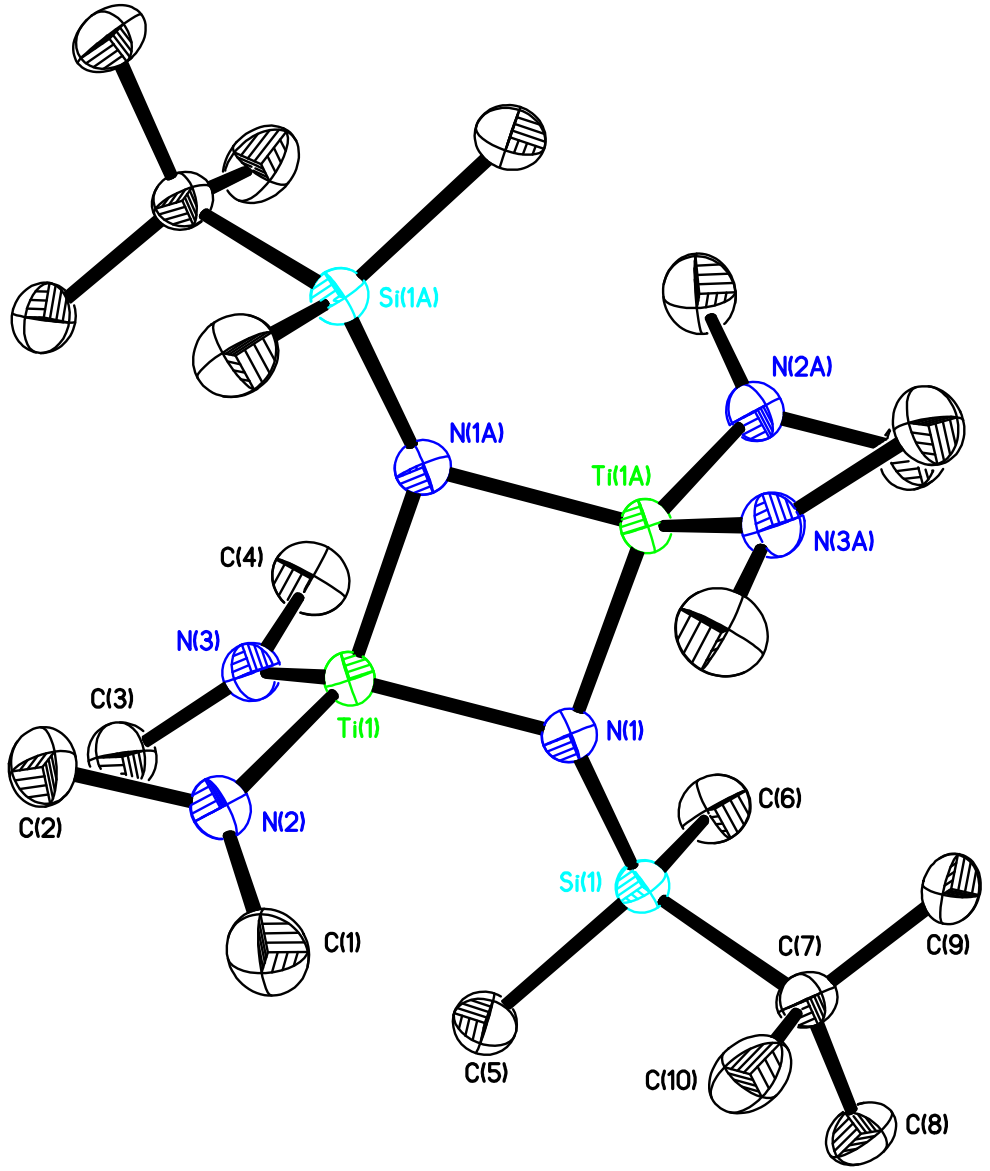

Figure 2.35: Molecular structure of the complex $[\{(Me_2N)_2Ti(\mu_2\text{-}NSi^tBuMe_2)\}_2]$, **13**. Thermal ellipsoids are shown at 50 % probability, with hydrogen atoms omitted for clarity.

Table 2.8: Selected bond lengths (Å) and bond angles (°) for complex **13**.

Ti(1)-N(1)	1.9089 (12)	Ti(1)-N(1A)	1.9365 (12)
Ti(1)-N(2)	1.8984 (13)	Ti(1)-N(3)	1.9096 (13)
Si(1)-N(1)	1.7360 (12)		
N(1)-Ti(1)-N(1A)	86.45 (5)	Ti(1)-N(1)-Ti(1A)	93.55 (5)
Ti(1A)-N(1)-Si(1)	136.14 (7)	Ti(1)-N(1)-Si(1)	126.41 (7)
Ti(1)-N(2)-C(1)	129.82 (11)	Ti(1)-N(2)-C(2)	119.17 (11)
C(1)-N(2)-C(2)	110.95 (14)	Ti(1)-N(3)-C(3)	127.90 (11)
Ti(1)-N(3)-C(4)	120.89 (10)	C(3)-N(3)-C(4)	111.20 (14)

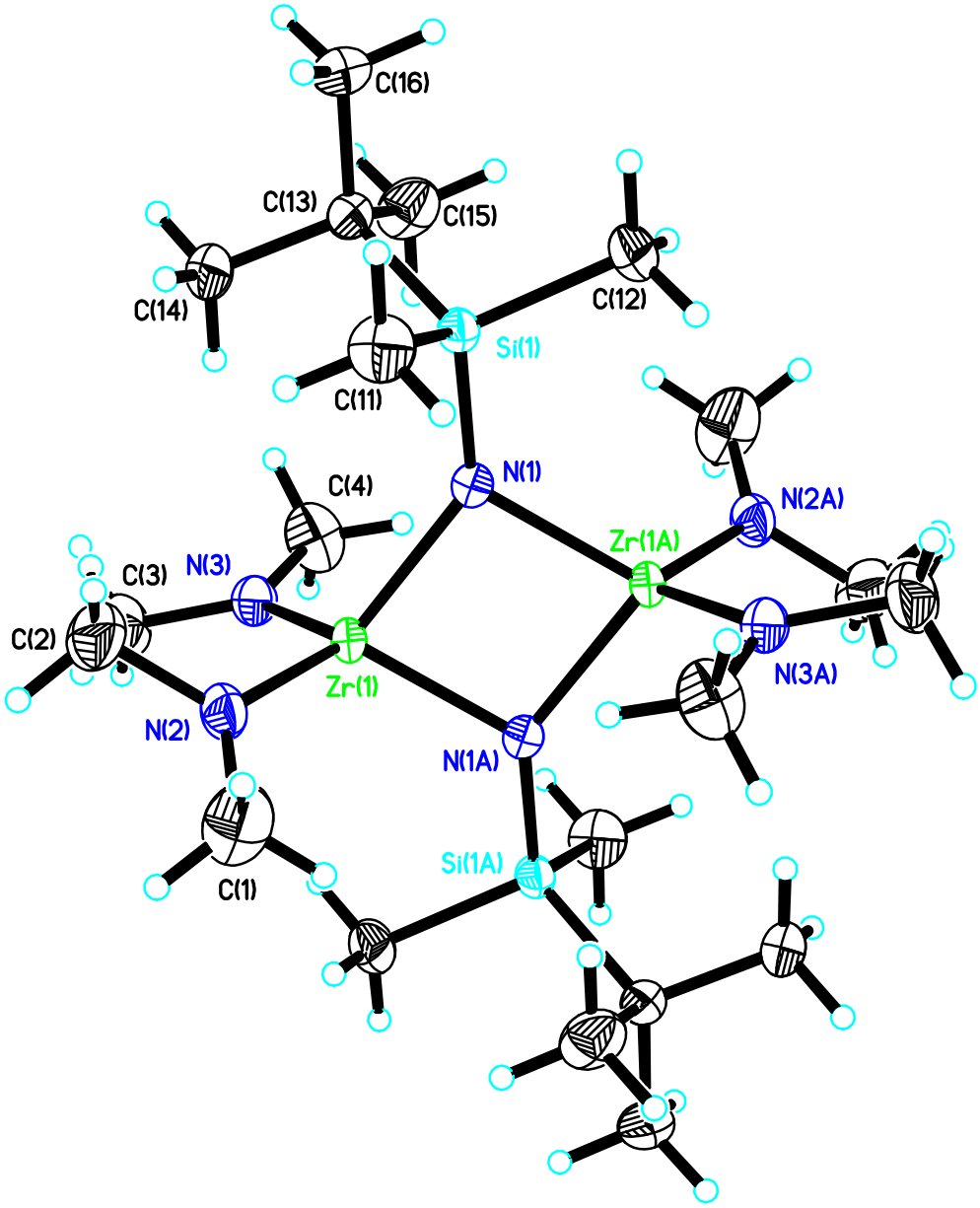

Figure 2.36: Molecular structure of the complex $[\{(Me_2N)_2Zr(\mu_2\text{-}NSitBuMe_2)\}_2]$, **14**. Thermal ellipsoids are shown at 50 % probability.

Table 2.9: Selected bond lengths (Á) and bond angles (^{o}) for complex **14**.

Zr(1)-N(1)	2.0699 (10)	Zr(1)-N(1A)	2.0618 (10)
Zr(1)-N(2)	2.0499 (11)	Zr(1)-N(3)	2.0595 (10)
Si(1)-N(1)	1.7257 (10)		
N(1)-Zr(1)-N(1A)	82.93 (4)	Zr(1)-N(1)-Zr(1A)	97.07 (4)
Zr(1A)-N(1)-Si(1)	123.99 (5)	Zr(1)-N(1)-Si(1)	136.67 (5)
Zr(1)-N(2)-C(1)	132.18 (10)	Zr(1)-N(2)-C(2)	116.43 (10)
C(1)-N(2)-C(2)	111.17 (12)	Zr(1)-N(3)-C(3)	126.82 (10)
Zr(1)-N(3)-C(4)	122.19 (9)	C(3)-N(3)-C(4)	110.90 (12)

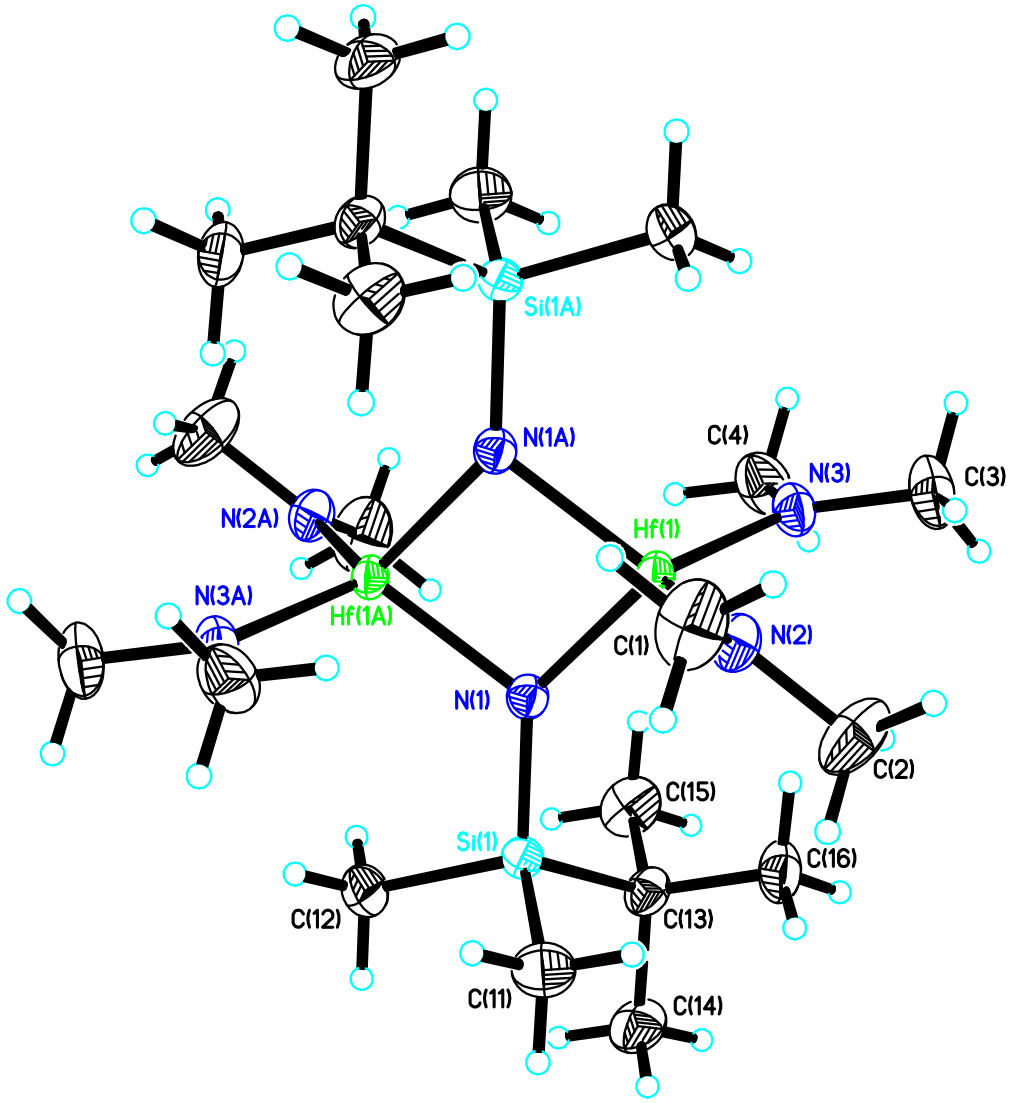

Figure 2.37: Molecular structure of the complex $[\{(Me_2N)_2Hf(\mu_2\text{-}NSi^tBuMe_2)\}_2]$, **15**. Thermal ellipsoids are shown at 50 % probability.

Table 2.10: Selected bond lengths (Å) and bond angles (°) for complex **15**.

Hf(1)-N(1)	2.0550 (18)	Hf(1)-N(1A)	2.0464 (18)
Hf(1)-N(2)	2.033 (2)	Hf(1)-N(3)	2.0405 (19)
Si(1)-N(1)	1.728 (2)		
N(1)-Hf(1)-N(1A)	83.82 (8)	Hf(1)-N(1)-Hf(1A)	96.18 (8)
Hf(1A)-N(1)-Si(1)	125.11 (10)	Hf(1)-N(1)-Si(1)	136.21 (11)
Hf(1)-N(2)-C(1)	131.22 (19)	Hf(1)-N(2)-C(2)	117.58 (19)
C(1)-N(2)-C(2)	111.1 (2)	Hf(1)-N(3)-C(3)	126.23 (19)
Hf(1)-N(3)-C(4)	122.65 (16)	C(3)-N(3)-C(4)	111.1 (2)

Complexes **10**, **13**, **14** and **15** are all found to be isostructural to **6** and **7**. Consequently arguments concerning the $\{M_2N_2\}$ ring made for complexes **6** and **7** may be applied to both the $\{SiEt_3\}$ and the $\{Si^tBuMe_2\}$ containing systems.

However, as mentioned earlier, Mountford *et. al.* have proposed that pyramidalisation of the bridging imido nitrogen atoms will occur, due to the presence of the HOMO being confined to the aforesaid nitrogen atoms.[58] Consequently, this results in distortion of the imido-bound substituents out of the plane of the $\{Ti_2N_2\}$ ring, with the centrosymmetric isomer preferred (figure 2.38). Subsequently complexes **10, 13, 14** and **15** are all found to comply with these observations, with a slight deviation from planarity at the bridging imido nitrogen atoms [N(1), N(1A): ∑ {Ti(1)-N(1)-Ti(1A), Ti(1)-N(1)-Si(1), Ti(1A)-N(1)-Si(1)} = 356.21° (10) for **10**; 356.10 (7) for **13**; 357.73 (5) for **14**; 357.50 (11) for **15**] resulting in the $\{SiEt_3\}$ / $\{Si^tBuMe_2\}$ groups being situated in a *trans* arrangement across the $\{Ti_2N_2\}$ ring.

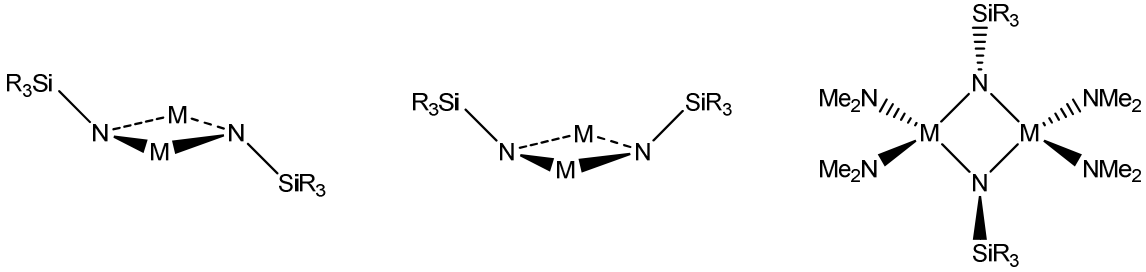

Figure 2.38: Schematic representation of the centrosymmetric (left and right) and non-centrosymmetric (centre) arrangements of the $\{SiR_3\}$ groups across the $\{M_2N_2\}$ ring which may arise from pyramidalisation of the imido nitrogen atoms. The centrosymmetric isomer is observed for complexes **10**, **13**, **14** and **15**.

Interestingly, the structure obtained for the hafnium complex, **15**, proves the absence of $HNMe_2$ as first suggested by analysis of the ^1H NMR spectrum, unlike the $\{SiPh_3\}$ system, **8**. Consequently it may be assumed that **12**, which contains the $\{SiEt_3\}$ moiety, also adopts a similar structure with no $HNMe_2$ present as suggested by analysis of its respective ^1H NMR spectrum.

2.3.4 Synthesis of Group 4 metal complexes using $(Me_2N)_3SiNH_2$ (5)

As discussed in Chapter 1, the properties of a deposited film are significantly affected by its composition, which in turn may be influenced by the precursor used for deposition. Therefore a series of reactions were performed with silicon amide **5** being refluxed in a 1:1 ratio in hexane with a group 4 metal amide, $M(NMe_2)_4$ (M = Ti, Zr, Hf), in an analogous manner to those using **1**, **3** or **4** (figure 2.39). Since **5** contains a higher percentage of nitrogen compared to **1**, **3** and **4**, any film deposited from metal complexes synthesised using **5** may also potentially contain a relatively higher percentage of nitrogen.

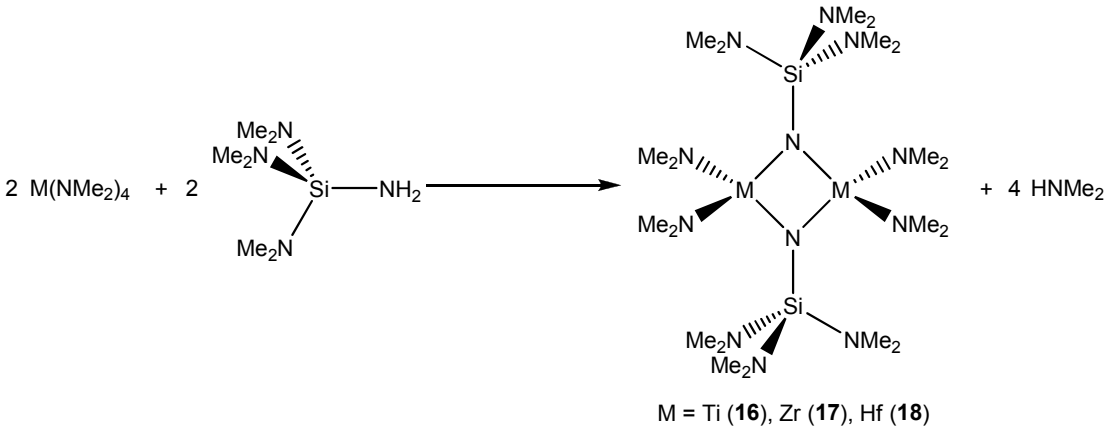

Figure 2.39: Reaction scheme for the reaction of a Group 4 metal amide of the form $M(NMe_2)_4$ and **5** in a 1:1 ratio.

Subsequently the reactions with **5** proceed in a similar manner to the equivalent reactions using **1**, **3** and **4**, with the metal complexes being isolated by crystallisation at –28 ^{o}C from the reaction solution upon completion. The titanium complex (**16**) was isolated as orange crystals, whilst the zirconium (**17**) and hafnium (**18**) were both isolated as colourless crystals. Similarly, these metal complexes have been shown to be sensitive to air and moisture.

Analysis of the ^{1}H NMR spectra for **16**, **17** and **18** show them to be comparable, with all three spectra displaying a single peak (3.29 ppm for **16**, 3.01 ppm for **17**, 3.02 ppm for **18**) common to all the spectra for compounds **6** – **15** which may be assigned to the methyl protons in the $\{NMe_2\}$ groups that are bonded to the metal centre. Additionally the spectra exhibit a singlet

resonance further upfield (2.56 ppm for **16**, 2.62 ppm for **17**, 2.60 ppm for **18**) which may be attributed to the methyl protons of the {NMe_2} groups which are bonded to the silicon atom of the {$Si(NMe_2)_3$} moiety. Subsequent integration of the resonances attributed to the {NMe_2} groups bonded respectively to the metal and silicon atoms show them to be present in a 2:3 ratio in all three complexes. As for complexes **6** – **15**, these observations are consistent with the elimination of two equivalents of $HNMe_2$ and the formation of an imido species with the empirical formula [$(Me_2N)_2M{=}NSi(NMe_2)_3$], most likely the dimeric species [{$(Me_2N)_2M(\mu_2\text{-}NSi(NMe_2)_3)$}$_2$]. Additionally, for reasons stated earlier for compounds **6** and **7**, a high degree of fluxionality may also be assumed to occur for molecules of **16**, **17** and **18** at room temperature in solution.

For all three metal complexes crystals suitable for single crystal X-ray diffraction were isolated. The titanium complex [{$(Me_2N)_2Ti(\mu_2\text{-}NSi(NMe_2)_3)$}$_2$], **16**, is found to crystallise in the triclinic space group (*P-1*) with half of one dimer molecule occupying the asymmetric unit. As before, the dimer of **16** is situated on a crystallographic inversion centre and subsequently the second half of the molecule is generated by the symmetry operator (1-x, -y, 1-z). The molecular structure for **16** is shown in detail in figure 2.40, with selected bond lengths and angles for this complex given in table 2.11. The structure obtained from these studies was consistent with that predicted from observations made through analysis of the ^{1}H NMR spectrum.

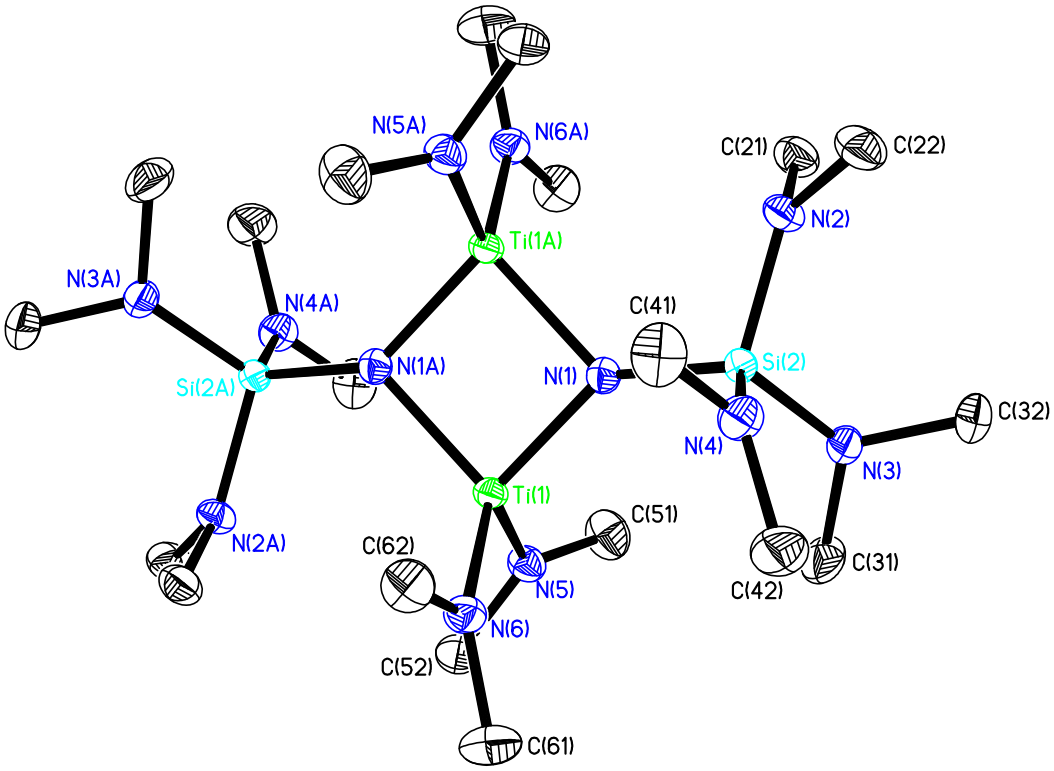

Figure 2.40: Molecular structure of the complex $[\{(Me_2N)_2Ti(\mu_2\text{-}NSi(NMe_2)_3)\}_2]$, **16**. Thermal ellipsoids are shown at 50 % probability, with hydrogen atoms omitted for clarity.

Table 2.11: Selected bond lengths (Å) and bond angles (°) for complex **16**.

Ti(1)-N(1)	1.8992 (13)	Ti(1)-N(1A)	1.9598 (13)
Ti(1)-N(5)	1.9080 (13)	Ti(1)-N(6)	1.9111 (13)
Si(2)-N(1)	1.7315 (13)	Si(2)-N(2)	1.7255 (14)
Si(2)-N(3)	1.7180 (14)	Si(2)-N(4)	1.7187 (14)
N(1)-Ti(1)-N(1A)	86.54 (6)	Ti(1)-N(1)-Ti(1A)	93.46 (6)
Ti(1A)-N(1)-Si(2)	122.93 (7)	Ti(1)-N(1)-Si(2)	136.91 (8)
Ti(1)-N(5)-C(51)	130.15 (12)	Ti(1)-N(5)-C(52)	118.41 (11)
C(51)-N(5)-C(52)	111.32 (14)	Ti(1)-N(6)-C(61)	127.78 (12)
Ti(1)-N(6)-C(62)	121.09 (11)	C(61)-N(6)-C(62)	111.12 (14)
Si(2)-N(2)-C(21)	118.71 (11)	Si(2)-N(2)-C(22)	124.63 (12)
C(21)-N(2)-C(22)	111.46 (13)	Si(2)-N(3)-C(31)	124.64 (12)
Si(2)-N(3)-C(32)	120.42 (11)	C(31)-N(3)-C(32)	111.81 (14)
Si(2)-N(4)-C(41)	121.86 (11)	Si(2)-N(4)-C(42)	122.17 (12)
C(41)-N(4)-C(42)	112.56 (14)		

The structure of complex **16** is observed to be consistent with results previously reported by Wagner *et*. *al*. for the same compound, prepared by the thermolysis of the amide complex [N{B(NMe_2)$_2$}{Si(NMe_2)$_3$}{Ti(NMe_2)$_3$}].[59] In addition, **16** is observed to be isostructural with the {SiE_{t3}} and {$SitBuMe_2$} containing complexes, with slight pyramidalisation of the bridging imido nitrogen atoms [N(1), N(1A): ∑ {Ti(1)-N(1)-Ti(1A), Ti(1)-N(1)-Si(1), Ti(1A)-N(1)-Si(1)} = 353.30^o (8)] again resulting in the {Si(NMe_2)$_3$} groups being ordered in a staggered arrangement across the {M_2N_2} ring to afford the centrosymmetric isomer.

The analogous zirconium complex [{(Me_2N)$_2$Zr(μ$_2$-NSi(NMe_2)$_3$)}$_2$], **17**, is found to crystallise in the monoclinic space group (*C2/c*), whilst the hafnium complex [{(Me_2N)$_2$Hf(μ$_2$-NSi(NMe_2)$_3$)}$_2$], **18**, is found to crystallise in the monoclinic space group (*P2$_1$/n*). In both complexes the dimeric molecule is situated on a crystallographic inversion centre and subsequently the second half of the molecule is generated by symmetry operations [**17**: ($^1/_2$ -x, $^1/_2$ -y, -z); **18**: (1-x, 1-y, 1-z)]. The molecular structures along with corresponding selected bond lengths and angles are given below for **17** (figure 2.41, table 2.12) and **18** (figure 2.42, table 2.13).

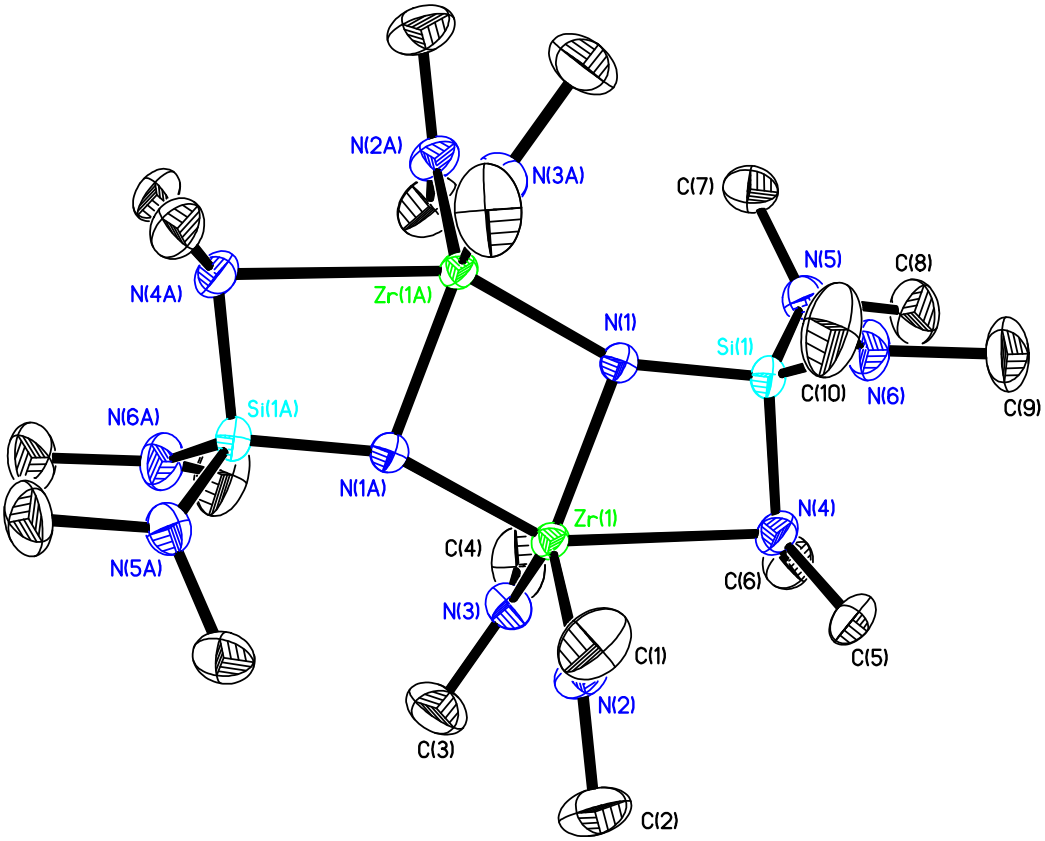

Figure 2.41: Molecular structure of the complex [{$(Me_2N)_2Zr(\mu_2\text{-}NSi(NMe_2)_3)\}_2$], **17**. Thermal ellipsoids are shown at 50 % probability, with hydrogen atoms omitted for clarity.

Table 2.12: Selected bond lengths (Á) and bond angles (^{o}) for complex **17**.

Zr(1)-N(1)	2.0992 (11)	Zr(1)-N(1A)	2.0800 (10)
Zr(1)-N(2)	2.0711 (12)	Zr(1)-N(3)	2.0603 (11)
Zr(1)-N(4)	2.5915 (11)	Si(1)-N(1)	1.6801 (10)
Si(1)-N(4)	1.7985 (12)	Si(1)-N(5)	1.7119 (12)
Si(1)-N(6)	1.7146 (13)		
N(1)-Zr(1)-N(1A)	80.49 (4)	Zr(1)-N(1)-Zr(1A)	99.51 (4)
Zr(1A)-N(1)-Si(1)	155.84 (7)	Zr(1)-N(1)-Si(1)	104.39 (5)
N(1)-Si(1)-N(4)	101.89 (5)	Zr(1)-N(4)-Si(1)	84.04 (4)
N(1)-Zr(1)-N(4)	69.45 (4)	N(1)-Zr(1)-N(3)	122.54 (4)
N(1)-Zr(1)-N(2)	118.75 (5)	N(1A)-Zr(1)-N(4)	149.94 (4)
N(1A)-Zr(1)-N(3)	104.61 (4)	N(1A)-Zr(1)-N(2)	102.35 (4)
N(2)-Zr(1)-N(3)	115.76 (5)	N(2)-Zr(1)-N(4)	92.22 (4)
N(3)-Zr(1)-N(4)	92.07 (4)	Zr(1)-N(2)-C(1)	121.75 (10)
Zr(1)-N(2)-C(2)	127.54 (11)	C(1)-N(2)-C(2)	110.71 (13)
Zr(1)-N(3)-C(3)	112.45 (11)	Zr(1)-N(3)-C(4)	135.34 (12)
C(3)-N(3)-C(4)	111.24 (15)	Si(1)-N(4)-C(5)	118.50 (10)
Si(1)-N(4)-C(6)	120.59 (10)	C(5)-N(4)-C(6)	109.06 (12)
Si(1)-N(5)-C(7)	120.83 (10)	Si(1)-N(5)-C(8)	123.09 (11)
C(7)-N(5)-C(8)	111.74 (12)	Si(1)-N(6)-C(9)	123.34 (12)
Si(1)-N(6)-C(10)	125.09 (11)	C(9)-N(6)-C(10)	111.36 (14)

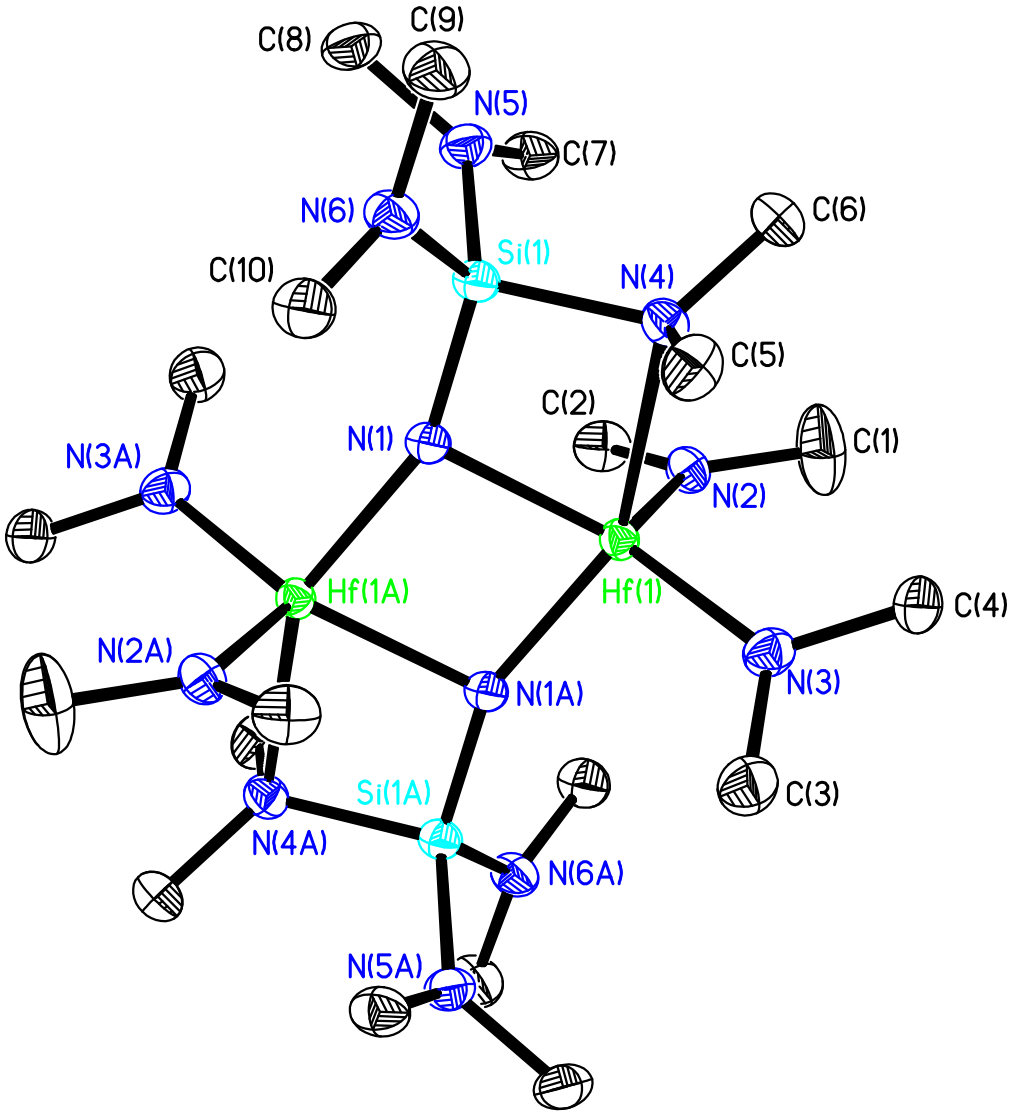

Figure 2.42: Molecular structure of the complex [{$(Me_2N)_2Hf(\mu_2\text{-}NSi(NMe_2)_3)\}_2$], **18**. Thermal ellipsoids are shown at 50 % probability, with hydrogen atoms omitted for clarity.

Table 2.13: Selected bond lengths (Á) and bond angles (^{o}) for complex **18**.

Hf(1)-N(1)	2.139 (2)	Hf(1)-N(1A)	2.037 (2)
Hf(1)-N(2)	2.051 (2)	Hf(1)-N(3)	2.056 (2)
Hf(1)-N(4)	2.486 (2)	Si(1)-N(1)	1.674 (2)
Si(1)-N(4)	1.823 (3)	Si(1)-N(5)	1.719 (2)
Si(1)-N(6)	1.714 (2)		
N(1)-Hf(1)-N(1A)	80.42 (9)	Hf(1)-N(1)-Hf(1A)	99.58 (9)
Hf(1A)-N(1)-Si(1)	156.49 (14)	Hf(1)-N(1)-Si(1)	103.93 (11)
N(1)-Si(1)-N(4)	96.54 (11)	Hf(1)-N(4)-Si(1)	87.45 (9)
N(1)-Hf(1)-N(4)	68.28 (8)	N(1)-Hf(1)-N(3)	130.52 (8)
N(1)-Hf(1)-N(2)	113.79 (8)	N(1A)-Hf(1)-N(4)	145.92 (8)
N(1A)-Hf(1)-N(3)	100.25 (9)	N(1A)-Hf(1)-N(2)	106.12 (8)
N(2)-Hf(1)-N(3)	113.34 (10)	N(2)-Hf(1)-N(4)	98.78 (7)
N(3)-Hf(1)-N(4)	90.56 (8)	Hf(1)-N(2)-C(1)	127.3 (2)
Hf(1)-N(2)-C(2)	122.2 (2)	C(1)-N(2)-C(2)	110.4 (3)
Hf(1)-N(3)-C(3)	126.7 (2)	Hf(1)-N(3)-C(4)	122.83 (18)
C(3)-N(3)-C(4)	110.2 (2)	Si(1)-N(4)-C(5)	108.60 (18)
Si(1)-N(4)-C(6)	121.53 (18)	C(5)-N(4)-C(6)	108.0 (2)
Si(1)-N(5)-C(7)	122.54 (19)	Si(1)-N(5)-C(8)	122.8 (2)
C(7)-N(5)-C(8)	110.5 (2)	Si(1)-N(6)-C(9)	121.6 (2)
Si(1)-N(6)-C(10)	123.53 (18)	C(9)-N(6)-C(10)	111.9 (2)

Complexes **17** and **18** possess many structural features comparable to those observed within the titanium complex, **16**, and the corresponding complexes containing the {Si^{t}BuMe$_2$} moiety, **14** and **15**. These include a central planar {M_2N_2} ring [M(1), N(1), M(1A), N(1A)] and two planar {NMe_2} amide groups bonded to each metal atom [N(2), N(3)], whilst the two bridging μ_2-NSi(NMe_2)$_3$ units [N1, N1A] are also planar. However, the overall structures of both **17** and **18** are significantly different to those observed for **14**, **15** and **16**.

Within **17** the zirconium atoms adopt a five coordinate geometry, with each bonded to the two {NMe_2} amide groups [N(2), N(3)] and the two nitrogen

atoms of the bridging μ_2-NSi(NMe_2)$_3$ units [N1, N1A] in a similar manner to **14** and **16**. Furthermore, the zirconium atoms within **17** are both bonded to a nitrogen atom belonging to a silicon-bound {NMe_2} group [Zr(1)-N(4), Zr(1A)-N(4A)]. This nitrogen atom is bonded to the zirconium centre through a dative bond involving the nitrogen lone pair, with the calculated Zr-N_{amino} bond length of 2.5915 (11) Å [Zr(1)-N(4)] comparable to other Zr-N_{amino} bond lengths which have been reported (2.361 Å – 2.769 Å).[51] As a result of the formation of this Zr-N_{amino} bond the geometry of the nitrogen atom [N(4)] is distorted from a planar arrangement [∑ {Si(1)-N(4)-C(5), Si(1)-N(4)-C(6), C(5)-N(4)-C(6)} = 348.15^o (12)], with the increased pyramidalisation indicating an sp^3 hybridisation of the nitrogen atom. In comparison, the two remaining {NMe_2} groups bonded to the silicon atom [N(5), N(6)] are both observed in a near planar arrangement [∑ {Si(1)-N(5)-C(7), Si(1)-N(5)-C(8), C(7)-N(5)-C(8)} = 355.66^o (12); ∑ {Si(1)-N(6)-C(9), Si(1)-N(6)-C(10), C(9)-N(6)-C(10)} = 359.79^o (14)], therefore implying an sp^2 hybridisation of the two nitrogen atoms.

The formation of the Zr-N_{amino} bonds within the **17** [Zr(1)-N(4), Zr(1A)-N(4A)] also results in the subsequent creation of two additional planar four-membered rings [{Zr(1), N(1), Si(1), N(4)}, {Zr(1A), N(1A), Si(1A), N(4A)}; ∑ {Zr(1)-N(1)-Si(1), N(1)-Si(1)-N(4), Si(1)-N(4)-Zr(1), N(4)-Zr(1)-N(1)} = 359.77^o (5)]. As these four-membered rings both share a common edge [Zr(1)-N(1) and Zr(1A)-N(1A)] with the central {Zr_2N_2} ring, the formation of a planar ladder-like structure within the molecule is observed (figure 2.43).

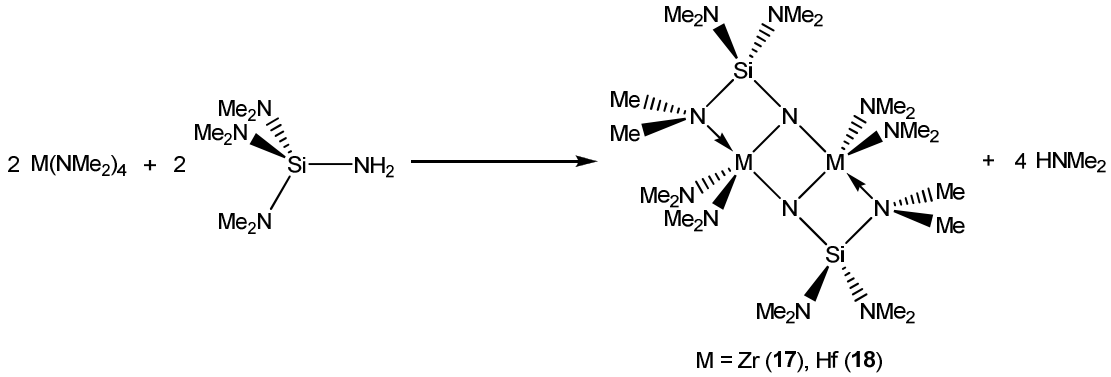

Figure 2.43: Reaction scheme for the reactions Zr(NMe_2)$_4$ and Hf(NMe_2)$_4$ with **5** in a 1:1 ratio. The resulting dimeric metal complexes contain a ladder-like structure created by dative bonds between the metal atom and the lone pair of a nitrogen atom within a {NMe_2} group bonded to the silicon.

The structures obtained for **17** and **18** are consistent to a degree with observations made within the ^{1}H NMR spectra. However, since the {NMe_2} group [N(4)] that is bonded via a dative bond to the metal is in a different environment to the two other {NMe_2} groups [N(5) and N(6)] bonded to the silicon atom, a splitting of the singlet resonance attributed to the protons of these groups may be expected. (Similarly, since the apical {NMe_2} metal amide group [N(2)] is arranged in a different environment and is consequently magnetically inequivalent to the equatorial {NMe_2} metal amide group [N(3)], a splitting of the attributed resonance may also be expected). Attempts to freeze out the complexes and analyse this phenomenon using VT-NMR though proved unsuccessful. Therefore it may be assumed that the structures of both **17** and **18** are fully fluxional in solution (figure 2.44).

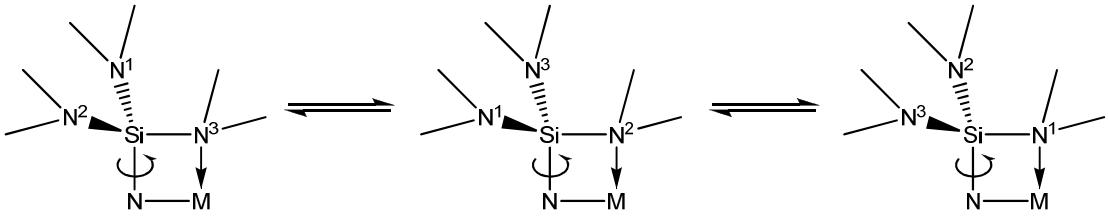

Figure 2.44: Schematic representation of the fluxionality within solution of the {NMe_2} groups bonded to the silicon atom within **17** and **18**.

As mentioned, the zirconium atoms within **17** adopt a five coordinate geometry [N(1), N(1A), N(2), N(3), N(4)]. Using the method reported by Addison *et*. *al*. for determining the geometry within a five coordinate environment (figure 2.45),[60] a value of τ = 0.457 was calculated for **17** [β = N(1A)-Zr(1)-N(4), 149.94^{o} (4); α = N(1)-Zr(1)-N(3), 122.54^{o} (4)]. Therefore, although the value of τ calculated is approximately halfway between the values expected for a tetragonal, square pyramidal structure (τ = 0) and a trigonal bipyramidal structure (τ = 1), the geometry at the zirconium atoms within **17** may be described as tending towards the former.

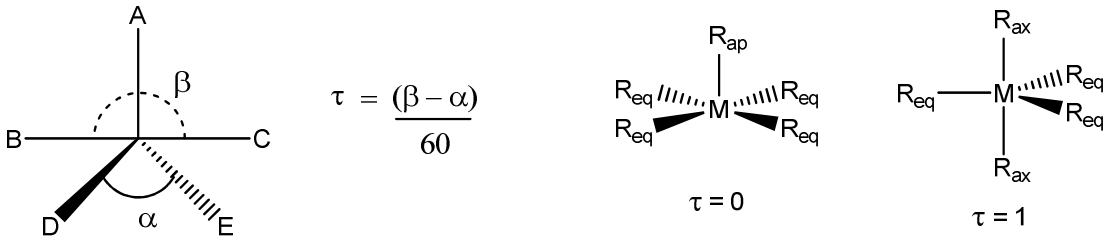

Figure 2.45: The formula reported by Addison *et. al*. for determining the geometry within a five coordinate environment. The geometry may be described between the extremes of a tetragonal, square pyramidal structure ($\tau = 0$) and a trigonal bipyramidal structure ($\tau = 1$).[60]

Within the square pyramidal environment described for the zirconium atoms within **17**, the nitrogen atoms N(1), N(1A), N(3) and N(4) are situated in equatorial positions with the nitrogen atom N(2) occupying the apical position. However, steric restraints imposed on the structure primarily by the fused ring systems [{Zr_2N_2} and {ZrN_2Si}] result in a distortion of the geometry from an idealised square pyramidal system (as indicated by the value of τ for **17**). Consequently the equatorial nitrogen atoms and the central zirconium atom deviate from lying in the same plane.

Interestingly, the Zr-N_{amide} bond length observed for the equatorial amido nitrogen atom [N(3), Zr(1)-N(3) = 2.0603 (11) Å] is comparable within experimental error to that observed for the apical amido nitrogen atom [N(2), Zr(1)-N(2) = 2.0711 (12) Å], despite an inequivalence being expected due to geometrical constraints.

The overall structure of the analogous hafnium complex, **18**, is comparable to the structure of **17**, with the hafnium atoms within **18** adopting a five coordinate geometry. Each hafnium atom is bonded to two {NMe_2} amide groups [N(2), N(3)] and the two nitrogen atoms of the bridging μ_2-N-Si(NMe_2)$_3$ units [N(1), N(1A)], in addition to a single nitrogen atom belonging to a silicon-bound {NMe_2} group [Hf(1)-N(4)] through a dative bond involving the nitrogen lone pair. The length of the Hf-N_{amino} dative bond, calculated as 2.486 (2) Å [Hf(1)-N(4)], is comparable to other Hf-N_{amino} bond lengths which have been reported (2.378 Å – 2.488 Å).[51] As observed within **17**, this results in the formation of three four-membered rings [{Hf(1), N(1), Si(1), N(4)}, {Hf(1), N(1),

Hf(1A), N(1A)}, {Hf(1A), N(1A), Si(1A), N(4A)}] to create a ladder-like structure within the molecule.

As before within the structure of **17**, the formation of the Hf-N_{amino} bond within **18** results in a distortion of the geometry of the nitrogen atom [N(4)] from a planar arrangement [∑ {Si(1)-N(4)-C(5), Si(1)-N(4)-C(6), C(5)-N(4)-C(6)} = 338.13^{o} (18)], with the increased pyramidalisation indicating an sp^3 hybridisation of the nitrogen atom. Equally, the two remaining {NMe_2} groups bonded to the silicon atom [N(5), N(6)] are both observed in a near planar arrangement [∑ {Si(1)-N(5)-C(7), Si(1)-N(5)-C(8), C(7)-N(5)-C(8)} = 355.84^{o} (19); ∑ {Si(1)-N(6)-C(9), Si(1)-N(6)-C(10), C(9)-N(6)-C(10)} = 357.03^{o} (18)], therefore implying an sp^2 hybridisation of the two nitrogen atoms.

However, the hafnium atoms within **18** display a greater degree of square pyramidal character compared to the zirconium atoms within **17**, with a calculated τ value of 0.257 for **18** [β = N(1A)-Zr(1)-N(4), 145.92^{o} (8); α = N(1)-Zr(1)-N(3), 130.52^{o} (8)]. As within the structure of **17**, the nitrogen atoms N(1), N(1A), N(3) and N(4) are situated in equatorial positions with the nitrogen atom N(2) occupying the apical position. The degree of distortion of the equatorial nitrogen atoms and the central metal atom from the same plane though is less for the structure of **18** relative to that observed within **17**. This in part may be due to the greater deviation from planarity of the {HfN_2Si} rings [{Zr(1), N(1), Si(1), N(4)}, {Zr(1A), N(1A), Si(1A), N(4A)}; ∑ {Zr(1)-N(1)-Si(1), N(1)-Si(1)-N(4), Si(1)-N(4)-Zr(1), N(4)-Zr(1)-N(1)} = 356.20^{o} (11)].

The intramolecular donation of electrons from the nitrogen of the silicon bound {NMe_2} group to the metal centre that is observed within the structures of **17** and **18** is comparable to the intermolecular donation observed within the hafnium complex **8**, in which a single molecule of $HNMe_2$ [N(7)] donates electrons to a single hafnium atom [Hf(2)] within the dimeric molecule. However, the τ value of 0.697 calculated for the five coordinate hafnium atom [Hf(2)] within **8** [β = N(4)-Hf(2)-N(7), 165.82^{o} (12); α = N(3)-Hf(2)-N(5), 123.98^{o} (13)] indicates the geometry of this atom is significantly trigonal bipyramidal in

character compared to that of the metal atoms within **17** and **18**. Within this trigonal bipyramidal geometry the $HNMe_2$ nitrogen atom [N(7)] occupies an axial position, as discussed earlier in this chapter.

The geometry adopted by Hf(2) within **8** is distorted from an ideal trigonal bipyramid by steric constraints, imposed by the bulky phenyl substituents and formation of the $\{M_2N_2\}$ ring. Within this geometry the nitrogen atom which is bonded to the metal through a dative bond [N(7)] is a component of the largest angle, β. This phenomenon is also observed within the structures of **17** and **18** [N(4) for **17** and **18**]. Consequently the metal atoms within **17** and **18** may also prefer to adopt a trigonal bipyramidal geometry in which the nitrogen atom bonded to the silicon atom occupies an axial position. However, the greater steric constraints enforced by the formation of the $\{MN_2Si\}$ ring results in a greater deviation from a trigonal bipyramidal geometry to that of a square pyramidal arrangement for these two complexes. Yet why a greater deviation towards a square pyramidal arrangement is observed for **18** compared to **17** is uncertain. Since the covalent radii of zirconium and hafnium are comparable [1.56 Å and 1.57 Å respectively],[51] a similar degree of strain within the $\{MN_2Si\}$ ring and consequently a similar structure would be expected for both.

As described within this chapter, complexes **6** – **8**, **10** and **13** – **18**, prepared using primary aminosilane of the form R_3SiNH_2, are all found to adopt a dimeric bridged-imido structure with subsequent formation of a planar four-membered $\{M_2N_2\}$ ring. As described for complex **9**, $[\{(Me_2N)_2Ti(\mu_2\text{-}N^tBu)\}_2]$, the $\{M_2N_2\}$ ring system may be delocalised with additional π-bonding interactions from the peripheral $\{NMe_2\}$ amide groups. Within complexes **6** – **8**, **10** and **13** – **18** orbitals on the silicon atoms which are bonded to the imido nitrogen atoms may also potentially interact with the $\{M_2N_2\}$ π-bonding system.

The bond lengths involved within the π-bonding interactions in complexes **6** – **8** and **10**– **18** are summarised below in tables 2.14, 2.15 and 2.16.

Table 2.14: M-N imido [M_2N_2] bond lengths (Á) involved within the π-bonding interactions in complexes **6** – **8** and **10**– **18**. Complexes are prepared using primary aminosilanes of the form R_3SiNH_2.

[M-N_{imido}]	M = Ti	M = Zr	M = Hf
$R_3 = Ph_3$	1.915 (3)	2.0736 (11)	2.050 (3) / 2.025 (3)
	1.938 (3)	2.0784 (11)	2.121 (3) / 2.122 (3)
$R_3 = Et_3$	1.8937 (16)	-	-
	1.9448 (16)	-	-
$R_3 = {}^tBuMe_2$	1.9089 (12)	2.0699 (10)	2.0550 (18)
	1.9365 (12)	2.0618 (10)	2.0464 (18)
$R_3 = (NMe_2)_3$	1.8992 (13)	2.0992 (11)	2.139 (2)
	1.9598 (13)	2.0800 (10)	2.037 (2)

Table 2.15: M-N amido [M-NMe_2] bond lengths (Á) involved within the π-bonding interactions in complexes **6** – **8** and **10**– **18**. Complexes are prepared using primary aminosilanes of the form R_3SiNH_2.

[M-N_{amido}]	M = Ti	M = Zr	M = Hf
$R_3 = Ph_3$	1.889 (3)	2.0548 (13)	2.041 (3) / 2.042 (3)
	1.899 (3)	2.0453 (13)	2.024 (3) / 2.030 (3)
$R_3 = Et_3$	1.9086 (18)	-	-
	1.8955 (18)	-	-
$R_3 = {}^tBuMe_2$	1.8984 (13)	2.0499 (11)	2.033 (2)
	1.9096 (13)	2.0595 (10)	2.0405 (19)
$R_3 = (NMe_2)_3$	1.9080 (13)	2.0711 (12)	2.051 (2)
	1.9111 (13)	2.0603 (11)	2.056 (2)

Table 2.16: Si-N imido bond lengths (Á) involved within the π-bonding interactions in complexes **6** – **8** and **10**– **18**. Complexes are prepared using primary aminosilanes of the form R_3SiNH_2.

[Si-N]	M = Ti	M = Zr	M = Hf
$R_3 = Ph_3$	1.732 (3)	1.7068 (12)	1.714 (3) / 1.705 (3)
$R_3 = Et_3$	1.7312 (17)	-	-
$R_3 = {}^tBuMe_2$	1.7360 (12)	1.7257 (10)	1.728 (2)
$R_3 = (NMe_2)_3$	1.7315 (13)	1.6801 (10)	1.674 (2)

Typically, the bond lengths within the titanium complexes [**6**, **10**, **13** and **18**] are found to be comparable within experimental error. However, within the zirconium [**7**, **14** and **17**] and hafnium [**8**, **15** and **18**] complexes a greater variation of the bond lengths shown in tables 2.14 – 2.16 is observed depending on the substituents bonded to the silicon atom.

Most significantly the length of the Si-N_{imido} bond is found to be significantly shorter for complexes **7** and **8** [R_3 = Ph_3], and **17** and **18** [R_3 = $(NMe_2)_3$] compared to complexes **14** and **15** [R_3 = $^tBuMe_2$]. This observation may be attributed to the presence of σ-electron withdrawing groups bonded to the silicon atom within complexes **7**, **8**, **17** and **18** (Ph and NMe_2) lowering the energy of the silicon d-orbitals. Subsequently, π-orbital overlap and d←p π bonding between the silicon and imido nitrogen atoms may be enhanced.[3]

Therefore, this enhanced Si-N_{imido} d←p π bonding and the increasing energy mismatch between the frontier orbitals of the imido nitrogen atoms (2p) and the zirconium and hafnium metal atoms (4d and 5d respectively) may result in significant disruption of the delocalised $\{M_2N_2\}$ π-bonding system. Subsequently, this disruption of the electronic structure may explain the intermolecular and intramolecular donation observed within complex **8** and complexes **17** and **18** respectively in order to stabilise the comparatively electron-deficient metal atoms.

2.4 Summary for Chapter 2

A range of silicon amides of the form R_3SiNH_2 have been prepared from the corresponding chlorosilane with an excess of ammonia. A range of group 4 metal complexes have subsequently been synthesised by reacting the prepared silicon amide with a Group 4 metal amide of the form $M(NMe_2)_4$ in a 1:1 ratio, resulting in the elimination of $HNMe_2$.

In the majority of cases, the reaction affords the dimeric product $[\{(Me_2N)_2M(\mu_2\text{-}NSiR_3)\}_2]$. Within the structure of the dimeric product the metal atoms adopt a *pseudo*-tetrahedral geometry, with the presence of the two

bridging {μ_2-$NSiR_3$} groups resulting in the formation of a planar {M_2N_2} four membered ring.

However, within the hafnium complex **8** (R = Ph) intermolecular donation to one of the two hafnium atoms from an additional molecule of $HNMe_2$ is observed. Subsequently, the five-coordinate hafnium atom is found to adopt a *pseudo*-trigonal bipyramidal geometry.

In addition, within the complexes **17** and **18** intramolecular donation between the nitrogen of a silicon-bonded {NMe_2} group and the metal atom (zirconium and hafnium respectively) is observed. Subsequently, the hafnium atoms within **18** adopt a *pseudo*-square pyramidal, five-coordinate geometry, whilst the zirconium atoms within **17** are found to be within an increasingly *pseudo*-trigonal bipyramidal environment.

The M-N bond lengths around the {M_2N_2} rings have been rationalised in terms of a delocalised π-bonding systems between the vacant d-orbitals of the metal atoms and the lone pairs on both bridging imido nitrogen atoms, with additional π-bonding interactions from peripheral {NMe_2} amido ligands. However, orbitals on the silicon atoms bonded to the imido nitrogen atoms may also interact with the π-bonding system. Subsequently, the lengths of the $Si\text{-}N_{imido}$ bonds and the electronic structure of the molecules have been shown to be dependent on the metal atom present and the nature of the {R} substituents bonded to the silicon.

The reactions and compounds presented in this chapter are shown below in figure 2.46.

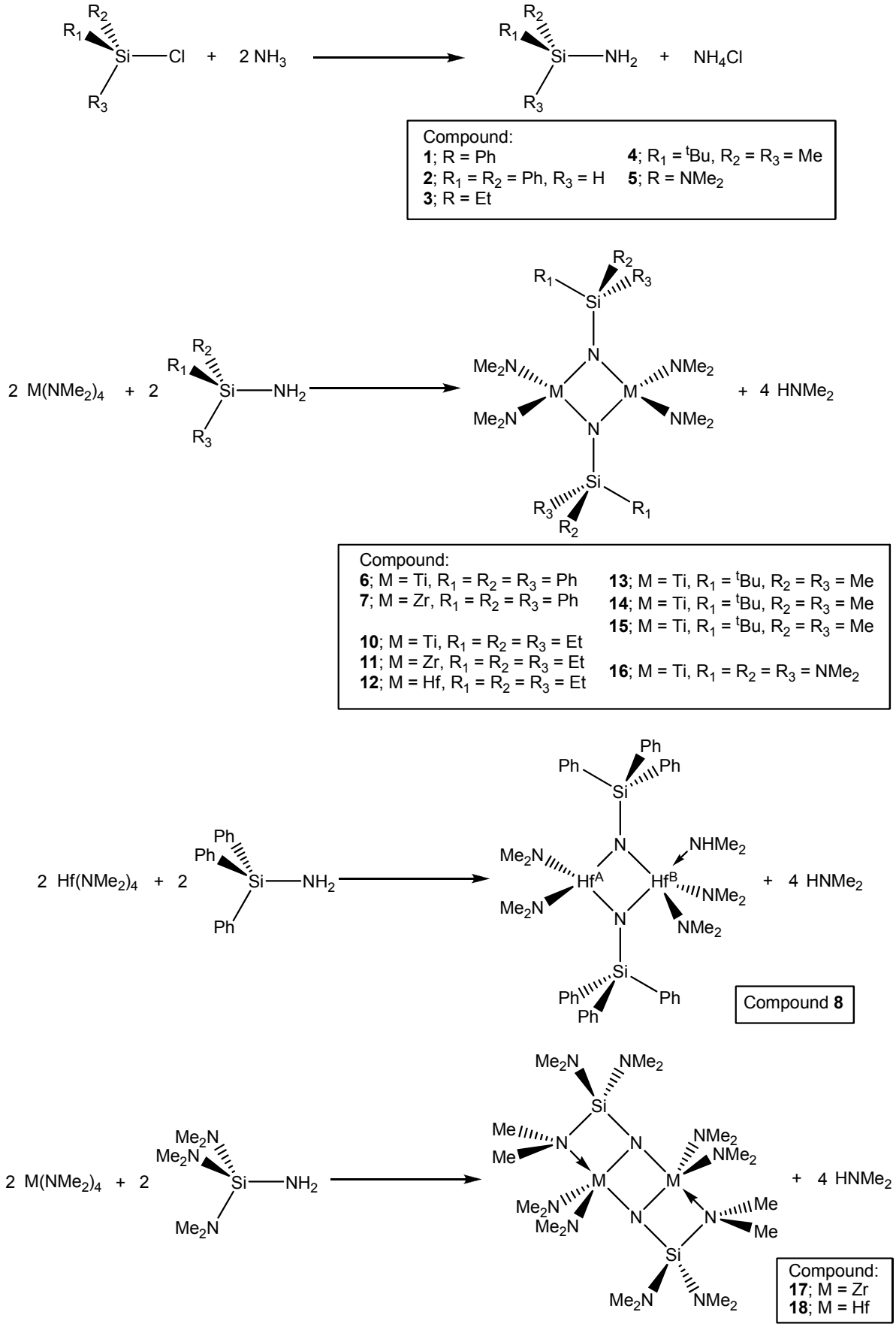

Figure 2.46: Reactions and compounds presented within Chapter 2.

2.5 References for Chapter 2

1. S. Hassan, A. L. Hector, J. R. Hyde, A. Kalaji and D. C. Smith, *Chem. Commun.*, 2008, 5304.
2. R. G. Gordon, D. M. Hoffman and U. Riaz, *Chem. Mater.*, 1990, **2**, 480.
3. M. F. Lappert, P. P. Power, A. R. Sanger and R. C. Srivastava, *"Metal and Metalloid Amides; syntheses, structures, and physical and chemical properties"*, **1980**, Ellis Horwood Ltd., Chichester, UK.
4. M. Lappert, A. Protchenko, P. Power and A. Seeber, *"Metal Amide Chemistry"*, **2009**, John Wiley & Sons, Ltd., Chichester, UK.
5. D. C. Bradley and I. M. Thomas, *J. Chem. Soc.*, 1960, 3857.
6. W. A. Nugent and J. M. Mayer, *"Metal-Ligand Multiple Bonds; The chemistry of transition metal complexes containing oxo, nitrido, imido, alklyidene, or alkylidyne ligands"*, **1988**, John Wiley & Sons, Inc., New York, USA.
7. N. Hazari and P. Mountford, *Acc. Chem. Res.*, 2005, **38**, 839.
8. W. A. Nugent and B. L. Haymore, *Coord. Chem. Rev.*, 1980, **31**, 123.
9. D. E. Wigley, *Prog. Inorg. Chem.*, 1994, **42**, 239.
10. T. R. Cundari, *J. Am. Chem. Soc.*, 1992, **114**, 7879.
11. D. L. Thorn, W. A. Nugent and R. L. Harlow, *J. Am. Chem. Soc.*, 1981, **103**, 357.
12. H. Chen, R. A. Bartlett, H. V. R. Dias, M. M. Olmstead and P. P. Power, *Inorg. Chem.*, 1991, **30**, 3390.
13. C. Lorber, R. Choukroun and L. Vendier, *Inorg. Chem.*, 2007, **46**, 3192.
14. B. C. Bailey, F. Basuli, J. C. Huffman and D. J. Mindiola, *Organometallics*, 2006, **25**, 2725.
15. C. Matthes, M. Noltemeyer, U. Klingebiel and S. Schmatz, *Organometallics*, 2007, **26**, 838.
16. C. J. Carmalt, J. D. Mileham, A. J. P. White and D. J. Williams, *New J. Chem.*, 2000, **24**, 929.
17. R. Bettenhausen, W. Milius and W. Schnick, *Chem. – Eur. J.*, 2006, **3**, 1337.
18. A. Mommertz, R. Leo, W. Massa and K. Dehnicke, *Z. Naturforsch. B*, 1998, **53**, 887.

19. G. Chandra, A. D. Jenkins, M. F. Lappert and R. C. Srivastava, *J. Chem. Soc. A*, 1970, **15**, 2550.
20. P. Braunstein, M. Veith, J. Blin and V. Huch, *Organometallics*, 2001, **20**, 627.
21. Y. Mo, Y. Zhang and J. Gao, *J. Am. Chem. Soc.*, 1999, **121**, 5737.
22. B. L. Kormos and C. J. Kramer, *Inorg. Chem.*, 2003, **42**, 6691.
23. T. Kremer, F. Hampel, F. A. Knoch, W. Bauer, A. Schmidt, P. Gabold, M. Schütz, J. Ellerman and P. Von Ragué Schleyer, *Organometallics*, 1996, **15**, 4776.
24. F. Cheng, S. Clark, S. M. Kelly, J. S. Bradley and F. Lefebvre, *J. Am. Ceram. Soc.*, 2004, **87**, 1413.
25. M. Westerhausen, T. Bollwein, N. Makropoulos and H. Piotrowski, *Inorg. Chem.*, 2005, **44**, 6439.
26. F. Cheng, S. M. Kelly, S. Clark, N. A. Young, S. J. Archibald, J. S. Bradley and F. Lefebvre, *Chem. Mater.*, 2005, **17**, 5594.
27. C. C. Cummins, C. P. Schaller, G. D. van Duyne, P. T. Wolczanski, A. W. E. Chan and R. Hoffmann, *J. Am. Chem. Soc.*, 1991, **113**, 2985.
28. C. Lorber and L. Vendier, *Organometallics*, 2008, **27**, 2774.
29. Y. Li, S. Banerjee and A. L. Odom, *Organometallics*, 2005, **24**, 3272.
30. P. J. Walsh, F. J. Hollander and R. G. Bergman, *Organometallics*, 1993, **12**, 3705.
31. C. C. Cummins, G. D. v. Duyne, C. P. Schaller and P. T. Wolczanski, *Organometallics*, 1991, **10**, 164.
32. C. C. Cummins, S. M. Baxter and P. T. Wolczanski, *J. Am. Chem. Soc.*, 1988, **110**, 8731.
33. J. de With, A. D. Horton and A. G. Orpen, *Organometallics*, 1990, **9**, 2207.
34. C. P. Schaller and P. T. Wolczanski, *Inorg. Chem.*, 1993, **32**, 131.
35. D. F. Schafer II and P. T. Wolczanski, *J. Am. Chem. Soc.*, 1998, **120**, 4881.
36. S. M. Holmes, D. F. Schafer II, P. T. Wolczanski and E. B. Lobkovsky, *J. Am. Chem. Soc.*, 2001, **123**, 10571.
37. M. Westerhausen, T. Bollwein, A. Pfitzner, T. Nilges and H.-J. Deiseroth, *Inorg. Chim. Acta*, 2001, **312**, 239.

38. J. R. Bowser, R. H. Neilson and R. L. Wells, *Inorg. Chem.*, 1978, **17**, 1882.
39. J. S. Bradley, F. Cheng, S. J. Archibald, R. Supplit, R. Rovai, C. W. Lehmann, C. Krüger and F. Lefebvre, *Dalton Trans.*, 2003, 1846.
40. F. Cheng, S. Clark, S. J. Archibald, S. M. Kelly and J. S. Bradley, *J. Organomet. Chem.*, 2005, **690**, 1205.
41. D. M. Choquette, M. J. Timm, J. L. Hobbs, M. M. Rahim, K. J. Ahmed and R. P. Planalp, *Organometallics*, 1992, **11**, 529.
42. D. M. Choquette, M. J. Timm, J. L. Hobbs, T. M. Nicholson, M. M. Olmstead and R. P. Planalp, *Inorg. Chem.*, 1993, **32**, 2600.
43. R. J. Wehmschulte and P. P. Power, *Inorg. Chem.*, 1998, **37**, 6906.
44. B-J. Bae, J. E. Park, Y. Kim, J. T. Park and I-H. Suh, *Organometallics*, 1999, **18**, 2513.
45. F. Cheng, S. M. Kelly, S. Clark, J. S. Bradley and F. Lefebvre, *J. Organomet. Chem.*, 2007, **692**, 3816.
46. R. O. Sauer and R. H. Hasek, *J. Am. Chem. Soc.*, 1946, **68**, 241
47. V. Passarelli, G. Carta, G. Rossetto and P. Zanella, *Dalton Trans.*, 2003, 413.
48. Y. Wan and J. G. Verkade, *Inorg. Chem.*, 1993, **32**, 341.
49. M. Gao, Y. Tang, M. Xie, C. Qian and Z. Xie, *Organometallics*, 2006, **25**, 2578.
50. A. K. Hughes, A. Meetsma and J. H. Teuben, *Organometallics*, 1993, **12**, 1936.
51. F. H. Allen and O. Kennard, *Chemical Design Automation News*, 1993, **8**, 31.
52. M. E. Davie, T. Foerster, S. Parsons, C. Pulham, D. W. H. Rankin and B. A. Smart, *Polyhedron*, 2006, **25**, 923.
53. I. Castillo and T. D. Tilley, *J. Organomet. Chem.*, 2002, **643-644**, 431.
54. Y. N. Bai, H. W. Roesky, M. Noltemeyer and M. Witt, *Chemische Ber.-Recl.*, 1992, **125**, 825.
55. D. J. Arney, M. A. Bruck, S. R. Huber and D. E. Wigley, *Inorg. Chem.*, 1992, **31**, 3749.
56. R. M. Fix, R. G. Gordon and D. M. Hoffman, *Chem. Mater.*, 1990, **2**, 235.

57. W. A. Nugent and R. L. Harlow, *Inorg. Chem.*, 1979, **18**, 2030. Complex **9** originally reported D. C. Bradley and E. G. Torrible, *Can. J. Chem.*, 1963, **41**, 134.
58. P. E. Collier, A. J. Blake and P. Mountford, *J. Chem. Soc., Dalton Trans.*, 1997, 2911.
59. O. Wagner, M. Jansen and H.-P. Baldus, *Z. anorg. Allg. Chem.*, 1994, **620**, 366.
60. A. W. Addison, T. N. Rao, J. Reedijk, J. van Rijn and G. C. Verschoor, *J. Chem. Soc. Dalton Trans.*, 1984, 1349.

Chapter 3

Synthesis and characterisation of titanium complexes prepared using bidentate aminosilanes

3.1 Introduction to Chapter 3

As described in Chapter 2, the zirconium (**17**) and hafnium (**18**) complexes which have been synthesised contain {$NSi(NMe_2)_3$} moieties which are arguably bonded to the metal atom in a bidentate manner. Chelating ligands such as those observed within **17** and **18** have been shown to be advantageous for use within CVD precursors for several reasons.[1, 2] These include potentially improving the volatility of the precursor through a greater saturation of the coordination sphere of the metal atom. Consequently this saturation decreases the possibility of strong interactions with other neighbouring molecules occurring, which may otherwise result in unfavourable agglomeration of the precursor molecules.[1, 2] Additionally, chelating systems may provide an increased degree of stability to the precursor, consequently reducing the possibility of premature deposition within the CVD reactor.[1, 2]

A vast number of silicon amide-metal complexes have been reported in which the silicon amide ligand bonds to the metal centre through multiple atoms, including bidentate diamide ligands of the type $R_2Si(NHR')_2$. As observed for the R_3SiNH_2 systems discussed in Chapter 2, a review of the literature reveals that several main group and transition metal complexes have been obtained from reaction with these silicon amides or their lithiated derivatives.[3 - 22] Again, as observed for the metal complexes synthesised using the R_3SiNH_2 systems, these metal complexes have been investigated primarily as alternative catalytic species to metallocene catalysts in olefin polymerisation reactions.[18 - 25]

Interestingly, comparisons of several spirocyclic metal complexes synthesised using bidentate ligands of the form $X(NR)_2$, where X = Me_2Si, $Me_2SiSiMe_2$ and $Me_2SiZSiMe_2$ (Z = CH_2, NR or O) as shown in figure 3.1, have shown that the four-membered ring species (structure **A**) are more chemically and thermally stable than the five- and six-membered ring equivalents.[26, 27] Furthermore, several known complexes which adopt structure **A** exist as crystalline solids that are sufficiently volatile to be sublimed *in vacuo* without decomposition,[27] properties desirable within precursor compounds for CVD.

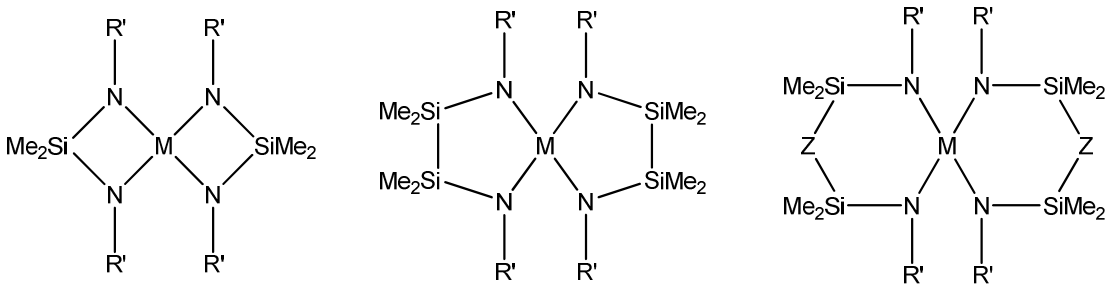

(**A**) (**B**) (**C**)

Figure. 3.1: Various spirocyclic Group 4 metal systems using bidentate ligands of the form $X(NR)_2$.

Consequently, titanium complexes prepared using chelating silicon amides have been investigated for their potential as single-source precursors for TiNSi thin films.

3.2 Synthesis of diaminosilane ligands

A range of symmetrical diaminosilane ligands of the form $R_2Si(NHR')_2$ were prepared using the general synthesis described in figure 3.2. In a similar manner to the synthesis of the R_3SiNH_2 systems described in Chapter 2, on slow addition of an excess of amine to a solution of the dichlorosilane a white precipitate of the equivalent ammonium chloride salt is immediately formed in a highly exothermic reaction. After removal of the precipitate by filtration to yield a colourless solution, the diaminosilane may be isolated by removal of volatiles under reduced pressure.[14 - 16] Consequently, using the general synthesis described in figure 3.2 diaminosilanes **19** – **21** have been prepared, as described in table 3.1.

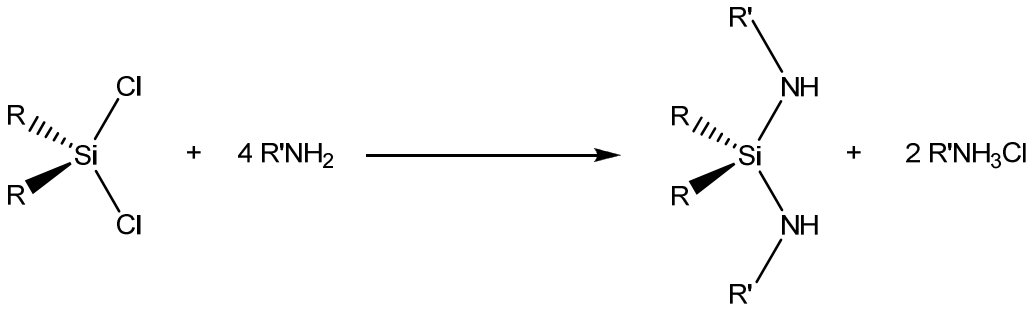

Figure 3.2: Schematic of the reaction of R_2SiCl_2 and a primary amine.

Table 3.1: Ligand systems of the form $R_2Si(NHR')_2$ prepared.

Ligand	R	R'
19	Me	^{t}Bu
20	Me	^{i}Pr
21	Me	$CH_2CH_2NMe_2$
22	Ph	^{t}Bu

As before, a wide range of R and R' groups can potentially be incorporated into the ligand using this procedure, enabling the properties of the metal complex precursor formed using the silicon diamide ligand to be tuned with relative ease. Additionally, **21** has the potential to chelate to a metal atom in a tetradentate fashion through the silicon amide nitrogen atoms and also through the nitrogen atoms of the pendant {NMe_2} groups.[16] This increased chelation ability may potentially further enhance the stability of the metal complex.

However, variation of the R' substiuent is shown to affect the volatility of the molecule, with the volatility of **20** in particular being relatively high. As a result removal of the reaction solvent and other volatiles under reduced pressure subsequently resulted in partial removal of the diaminosilane product and a reduced yield (12 % for **20** compared to 72 % and 81 % for **19** and **21** respectively). Therefore isolation of the diaminosilane by distillation may provide an attractive alternative to reduce the amount of product lost.

The exception to the general synthetic procedure described above in figure 3.2 occurs when particularly bulky substituents are involved,[13, 23, 28 - 31] as with ligand **22** where R = Ph and R' = ^{t}Bu. In the analogous reaction to the formation of the ligand systems **19** - **21** only one of the chlorine atoms on the dichlorodiphenylsilane, Ph_2SiCl_2, is substituted (figure 3.3). This monosubstitution may predominantly be due to the presence of the two phenyl groups along with the first *tert*-butylamine group on the silicon atom resulting in steric hindrance to the second substitution.

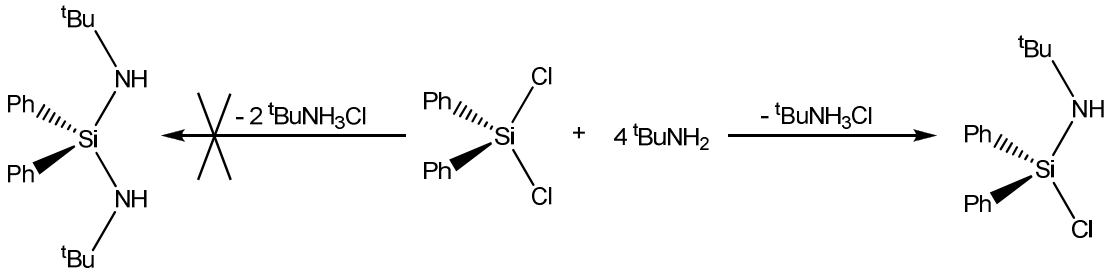

Figure 3.3: Schematic of the reaction of Ph_2SiCl_2 and $^tBuNH_2$. Only monosubstitution of the chlorine atoms is observed, with disubstitution prevented by steric hindrance.

Therefore, to obtain the disubstituted ligand, **22**, harsher reaction conditions are required. Murugavel *et*. *al*. have reported the synthesis of similar diaminosilanes bearing bulky substituents on the nitrogen by reacting Ph_2SiCl_2 with two equivalents of monolithiated amine, RNHLi.[31] Consequently one equivalent of n-butyl lithium, ^nBuLi, is slowly added to a solution of $^tBuNH_2$ at –78 ^oC to prevent abstraction of both protons of the primary amine and afford the monolithiated salt ^tBuNHLi only. After gradual warming of the reaction solution to confirm reaction completion, one half equivalent of Ph_2SiCl_2 is added to the ^tBuNHLi *in situ* at –78 ^oC resulting in the formation of a white precipitate of LiCl (figure 3.4). In a similar manner to the general synthesis for **19** - **21**, the LiCl precipitate may be removed by filtration and **22** isolated as a white solid by drying *in vacuo*.

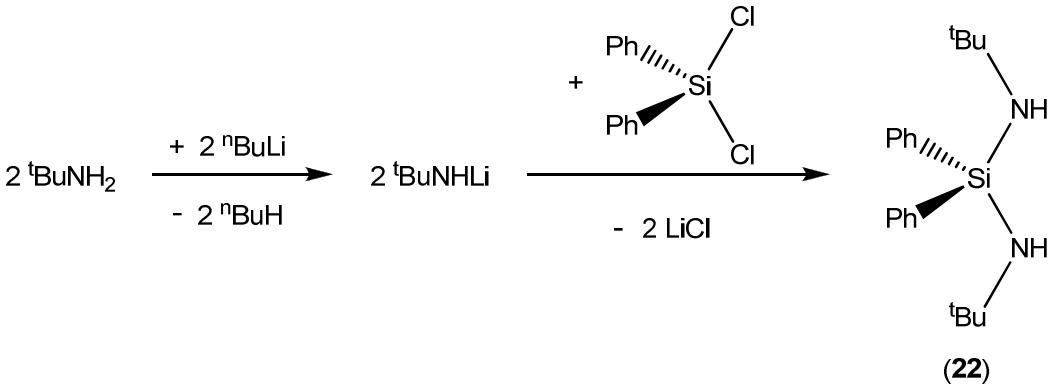

(**22**)

Figure 3.4: Synthesis of $R_2Si(NHR')_2$ ligand systems, with bulky substituents present

In general, the ^1H NMR spectra of diaminosilanes **19** – **22** are as expected. However the singlet peak displayed within the ^1H NMR spectra attributed to the NH proton resonance is relatively broad. In addition, ^3J-coupling is observed within the spectra of **20** and **21** between the NH proton and protons

bonded to the α-carbon atom. Consequently the resonance attributed to the methine protons of the isopropyl substituents of **20** is observed within the ^{1}H NMR spectrum as a doublet of septets, whilst the resonance attributed to the α-{CH_2} moieties within **21** is observed as an apparent quartet.

3.3 Synthesis of titanium complexes using $R_2Si(NHR')_2$ ligands

As mentioned earlier in this chapter, many metal complexes which have been synthesised using diaminosilanes of the form $R_2Si(NHR')_2$ have previously reported. Several of these metal complexes have been prepared from the direct reaction of the diaminosilane with a metal amide in a transamination reaction. Passarelli *et*. *al*. have reported the synthesis of several such complexes from $Zr(NMe_2)_4$ with the elimination of one or two equivalents of $HNMe_2$ (figure 3.5).[14 - 16] Within these complexes the denticity of the diaminosilane ligand is reported to be related to the steric hindrance of the nitrogen substituent, R'.[15]

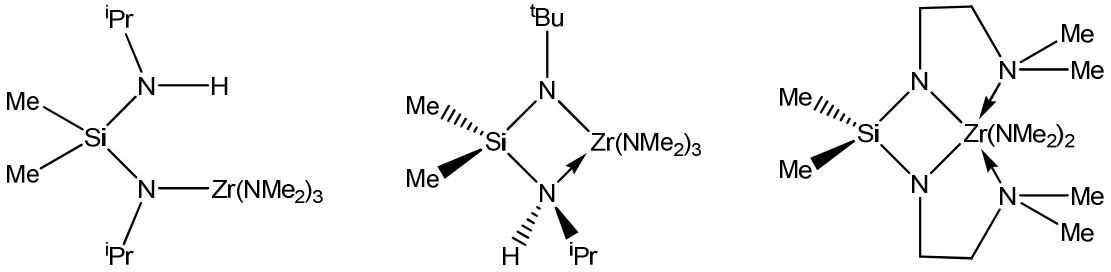

Figure 3.5: Zirconium complexes reported by Passarelli *et*. *al*. containing the ligand fragment {$Me_2Si(NR)(NR')$}. The denticity of the ligand may vary depending on the steric hindrance at the nitrogen atoms.[15, 16]

In addition, Gibson *et*. *al*. have reported the structure of a similar zirconium complex where bulky substituents are present within the diaminosilane ligand,[23] whilst Kim *et*. *al*. have synthesised a range of titanium complexes using cyclic diaminosilane ligands (figure 3.6).[21] In both cases the metal amide, $M(NMe_2)_4$ (M = Ti, Zr), is refluxed in toluene with the diaminosilane ligand, resulting in the elimination of two equivalents of $HNMe_2$ and the formation of a four-membered {MN_2Si} ring due to the bidentate nature of the ligand.

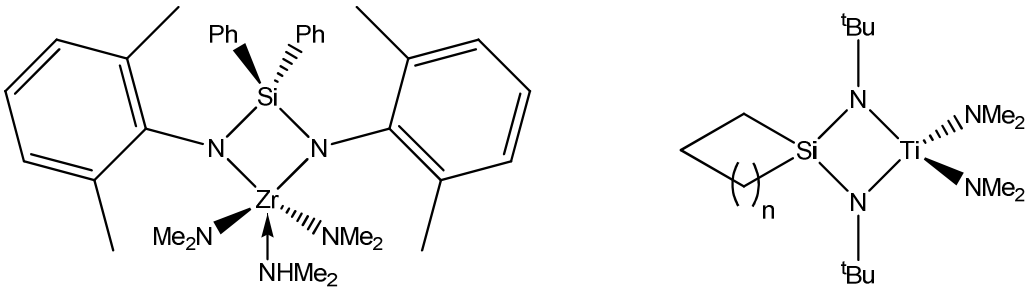

Figure 3.6: Group 4 metal complexes containing bidentate $\{R_2Si(NR')_2\}$ ligand systems.[21, 23]

Consequently, a series of reactions were performed in which the diaminosilanes prepared (**19** - **22**) were refluxed in toluene with $Ti(NMe_2)_4$ in a 1:1 ratio, with the anticipated elimination of $HNMe_2$ and the formation of a titanium complex within which the diaminosilane ligand is bonded to the metal atom in a bidentate fashion (figure 3.7). Unfortunately, in the majority of cases these reactions resulted in the formation of an intractable semi-solid that could not be characterised. However, recrystallisation from hexane at – 28 ^oC of the product obtained from the reaction using **19** resulted in the co-crystallisation of small yellow needles and a small amount of larger red crystals. Subsequent identification of the red crystals by single crystal X-ray diffraction and ^1H NMR spectroscopy reveal them not to be the anticipated product $Me_2Si(N^tBu)_2Ti(NMe_2)_2$ but in fact the dimeric complex $[(Me_2N)_2Ti(\mu\text{-}N^tBu)]_2$ (**9**) reported previously in Chapter 2 (figure 3.7). This observed formation of **9** is driven by the creation of the delocalised $\{Ti_2N_2\}$ ring system described in Chapter 2.

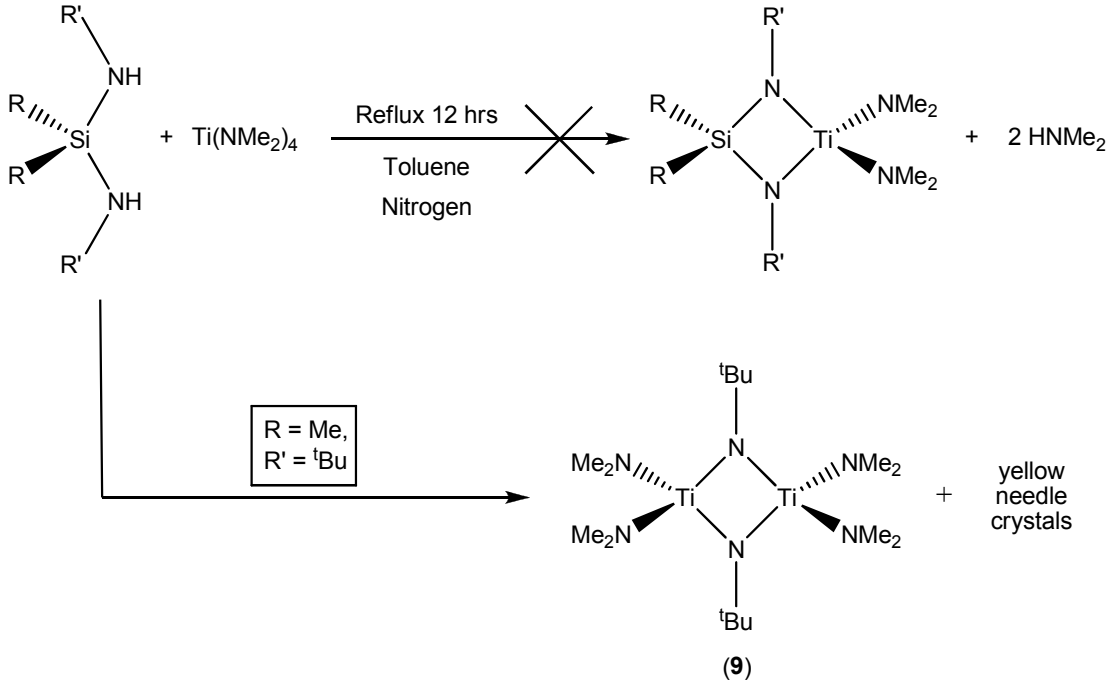

Figure 3.7: The predicted reaction between $R_2Si(NHR')_2$ and $Ti(NMe_2)_4$, and the actual product isolated.

Unfortunately, the nature of the yellow crystals isolated is uncertain. The formation of **9** was initially assumed to proceed via a transamination reaction, with the simultaneous formation of a silicon bisamido or polymeric silicon imido species and elimination of amine (figure 3.8). However, aminosilanes are typically observed as colourless, volatile liquids or solids,[32, 33] with $Me_2Si(NMe_2)_2$ and $Me_2Si(NMe_2)(NH^tBu)$ reported by Passarelli *et. al*. as colourless [14] and pale yellow [15] liquids respectively.

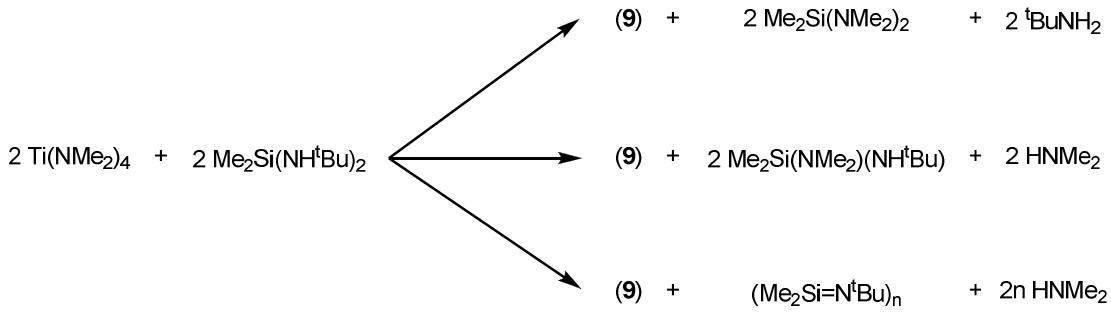

Figure 3.8: Potential transamination reactions between $R_2Si(NHR')_2$ and $Ti(NMe_2)_4$, affording a silicon bisamido or polymeric silicon imido species.

3.4 Synthesis of titanium complexes using $R_2Si(NLiR')_2$ dilithium salt

An alternative approach to coordinate the diaminosilane ligand to titanium is to proceed via the transmetallation (or salt metathesis) reaction, reacting the dilithiated salt of the diaminosilane with titanium(IV) chloride, $TiCl_4$. This approach was initially disfavoured due to the more laborious nature of the reactions and the increased chance of impurities appearing in the final complex as a result of the extra steps required.

Consequently, the dilithiated salt of the diaminosilane may be prepared by the slow addition of two equivalents of ^{n}BuLi to a solution of the corresponding diaminosilane at –78 ^{o}C, resulting in the formation of a white precipitate of the dilithiated salt (figure 3.9). After gradual warming to ensure reaction completion, the salt may be isolated by crystallisation at -28 ^{o}C from the solvent.

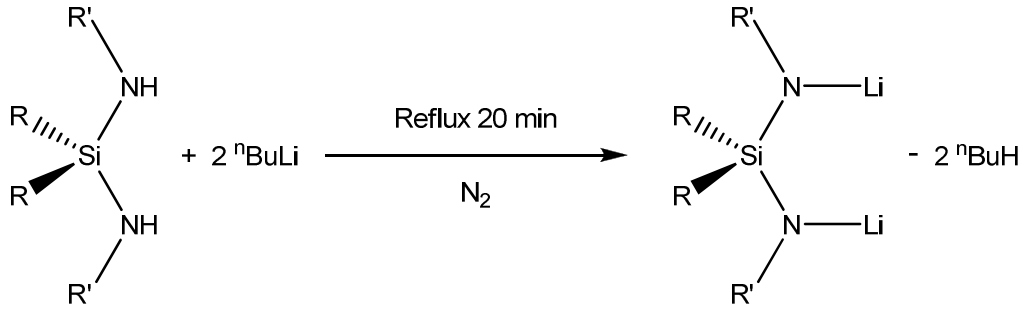

Figure 3.9: Schematic of the reaction of the diaminosilane [$R_2Si(NHR')_2$] with n-butyl lithium to afford the dilithiated salt.

Initial experiments were performed using **19** and **22**, with the respective dilithium salts $Me_2Si\{N(Li)^tBu\}_2$ (**23**) and $Ph_2Si\{N(Li)^tBu\}_2$ (**24**) both isolated as colourless crystals. These salts have been shown to be highly reactive and rapidly turn pink upon exposure to air as exothermic decomposition reactions occur.

For both dilithium salts crystals suitable for single crystal X-ray diffraction were isolated. The structure of **23** was observed to be a dimeric molecule, consistent with results previously reported by Brauer *et. al.* for the same compound.[34] Similarly, the structure of **24**, which has not previously been

reported, was also observed to be a dimeric species analogous to **23**, with a core of four lithium atoms in a bisphenoidal arrangement (figure 3.10). Each of the nitrogen atoms of the two $\{Ph_2Si(N^tBu)_2\}$ fragments are bonded to three of these lithium atoms, essentially capping a Li_3 face to form a rather distorted square antiprism.

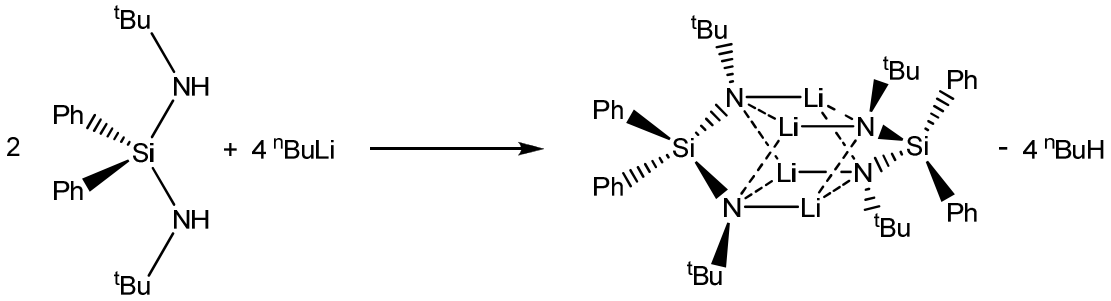

Figure 3.10: Schematic of the formation of the dimer $[Ph_2Si\{N(Li)^tBu\}_2]_2$, **24**.

Despite the fact that the reaction was done in diethyl ether, a Lewis base solvent which favourably coordinates to lithium via the lone pairs on the oxygen, no solvent molecules are observed within the crystal structure. This is possibly due to aggregation of the monomer being favoured over solvation in addition to steric hindrance from peripheral $\{^tBu\}$ groups retarding solvent coordination to the lithium atoms.

The molecular structure for **24** is shown in greater detail in figure 3.11, with selected bond lengths and angles for this complex given in table 3.2.

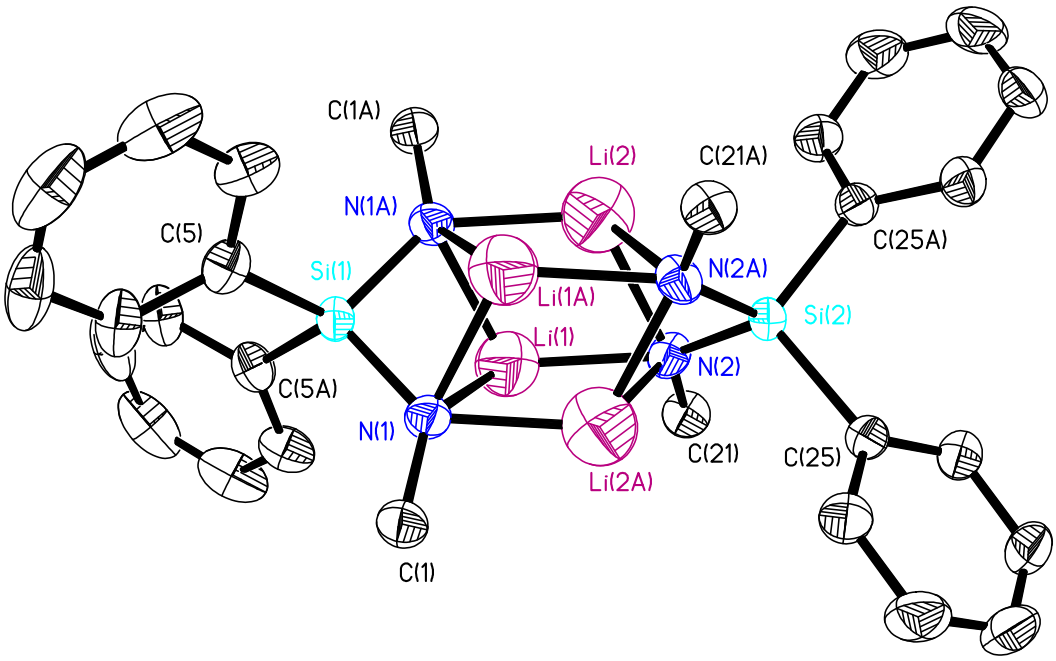

Figure 3.11: The molecular structure of the dimeric complex $[Ph_2Si\{N(Li)^tBu\}_2]_2$, (**24**). Thermal ellipsoids are shown at 50% probability. Hydrogen atoms and methyl groups of the *tert*-butyl substituents are omitted for clarity.

Table 3.2: Selected bond lengths and angles of the molecular structure of complex **24**.

N(1)-Li(1)	2.136 (11)	N(1)-Li(1A)	2.123 (10)
N(1)-Li(2A)	2.059 (12)	N(1A)-Li(1)	2.123 (10)
N(1A)-Li(2)	2.059 (12)	N(2)-Li(2)	2.078 (12)
N(2)-Li(2A)	2.157 (11)	N(2)-Li(1)	2.057 (11)
N(2A)-Li(2)	2.157 (11)	Si(1)-N(1)	1.727 (3)
Si(1)-N(1A)	1.727 (3)	Si(2)-N(2)	1.723 (3)
Si(2)-N(2A)	1.723 (3)	Li(1)-Li(2A)	2.299 (16)
Li(1)-Li(2)	2.303 (15)	Li(2)-Li(1A)	2.299 (16)
N(1)-Si(1)-N(1A)	96.6 (19)	Li(1)-Si(1)-Li(1A)	69.1 (5)
Si(1)-N(1)-Li(2A)	135.0 (4)	Si(1)-N(1)-Li(1)	84.0 (5)
Si(1)-N(1)-Li(1A)	66.8 (4)	Si(2)-N(2)-Li(1)	134.9 (4)
Li(2)-Li(1)-Li(2A)	75.3 (6)	Li(1)-Li(2)-Li(1A)	76.5 (6)

The titanium complex [{$Me_2Si(N^tBu)_2$}$_2$Ti] and its zirconium analogue,[26] as well as the hafnium and vanadium(IV) analogues,[27] have previously been prepared by Brauer *et. al*. through the reaction of the dilithiated ligand (**23**) with the corresponding metal(IV) chloride, MCl_4, in a 2:1 ratio. The reaction of **23** with $TiCl_4$ in a 1:1 ratio has also been used to yield the monosubstituted complex [{$Me_2Si(N^tBu)_2$}$TiCl_2$].[35] However, at the time the work reported here was performed, these complexes had not been tested for their viability as precursors for CVD.

Therefore, a series of reactions were performed in which $TiCl_4$ is slowly added to a diethyl ether solution of the dilithiated diaminosilane salt in a 1:2 ratio, as shown in figure 3.12. Consequently the disubstituted titanium complexes **25** and **26** have been synthesised from the dilithiated salt **23** and **24** respectively (table 3.3).

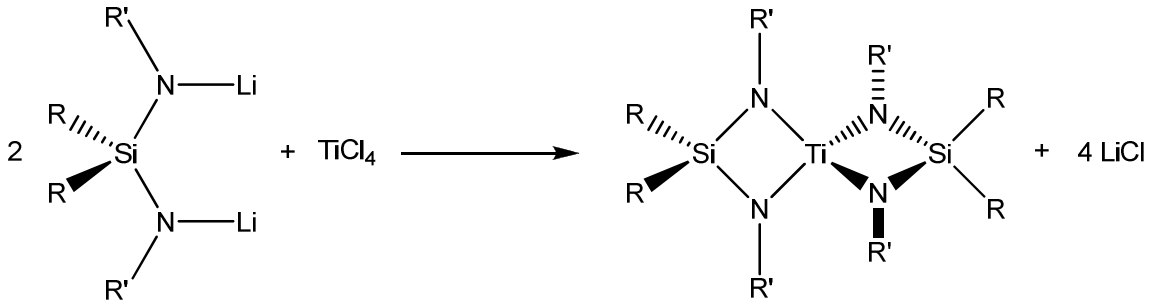

Figure 3.12: Synthesis of titanium complexes **25** and **26,** of the form [{$R_2Si(NR')_2$}$_2$Ti].

Table 3.3: [{$R_2Si(NR')_2$}$_2$Ti] systems synthesised.

Complex	R	R'
25	Me	^{t}Bu
26	Ph	^{t}Bu

The reaction of **23** with $TiCl_4$ at -78 ^oC invoked a colour change in the solution from colourless to dark green upon addition of the colourless metal chloride, with the simultaneous formation of a precipitate of LiCl. Similar observations are displayed within the analogous reaction with **24**. After gradual warming to room temperature to ensure completion, the LiCl precipitate was removed by filtration and all volatiles removed *in vacuo*. From the subsequent residue the

titanium complexes were isolated by recrystallisation at -28 ^{o}C from a toluene solution, with the methyl derivative (**25**) being isolated as green crystals whilst the phenyl derivative (**26**) has been isolated as fine green crystals. Typically for titanium(IV) amide systems, **25** and **26** have been shown to be sensitive to air and moisture.

Analysis of the ^{1}H NMR spectrum for **25** shows it to be comparable to the ^{1}H NMR spectrum for the dilithiated diaminosilane ligand, **23**. Consequently only two resonances are observed, attributed to the ^{t}butyl and silicon-bonded methyl groups (1.34 ppm and 0.50 ppm respectively). Similar observations are made within the ^{1}H NMR spectrum for **26**, with only resonances attributed to the phenyl (8.10 ppm and 7.66 ppm) and ^{t}butyl (1.10 ppm) groups observed.

Due to the symmetry of the titanium complexes and the nature of the chloride groups of the titanium reagent, $TiCl_4$, it is uncertain from ^{1}H NMR spectra of both **25** and **26** as to whether the monosubstituted [{$R_2Si(N^tBu)_2$}$TiCl_2$] or disubstituted [{$R_2Si(N^tBu)_2$}$_2$Ti] complexes are obtained. However, CHN elemental analysis is indicative of the disubstituted complex having been formed for both **25** and **26**.

Curiously, although complex **25** was initially isolated as green crystals, when stored under an atmosphere of nitrogen over a period of several weeks these crystals were observed to turn orange. The cause of this colour change is uncertain. Analysis of the ^{1}H NMR spectrum for the orange crystals shows it to be identical to the initial spectrum for the green crystals, whilst both spectra show no broadening of the resonances due to the presence of $Ti^{(III)}$. Therefore degradation of the complex is unlikely. In addition, the ^{1}H NMR spectrum of the green crystals of **25** showed no trace of resonances attributed to residual solvent. However, it is interesting to note that crystals isolated and characterised by Brauer *et. al.* are reported to be yellow-orange in colour.[26]

For the methyl derivative, **25**, crystals suitable for single crystal X-ray diffraction were isolated, with the structure obtained from these studies consistent with that predicted from observations made through analysis of the

^{1}H NMR spectrum and elemental analysis. In addition, although the crystals of **26** that were isolated were unsuitable for single crystal X-ray diffraction, the structure is assumed to be similar to that observed for **25** based on the data from the ^{1}H NMR spectrum and elemental analysis.

The titanium complex [{$Me_2Si(N^tBu)_2$}$_2$Ti], **25**, is found to crystallise in the monoclinic space group (*C2/c*) with only one half of the molecule forming the asymmetric unit. The dimeric molecule of **25** is situated on a crystallographic inversion centre and subsequently the second half of the molecule is generated by the symmetry operator (-x, y, $^3/_2$-z). In addition, the molecule exhibits disorder within the {^{t}Bu} groups due to rotation about the [N(1)-C(3)] and [N(2)-C(4)] bonds. Consequently the associated methyl groups are refined over two positions [{C(3A), C(3B), C(3C)} and {C(3D), C(3E), C(3F)}; {C(4A), C(4B), C(4C)} and {C(4D), C(4E), C(4F)}], the relative proportions of which are defined by a free variable, the sum of which is equal to 1. The molecular structure for **25** is shown in detail in figure 3.13, with selected bond lengths and angles for this complex given in table 3.4.

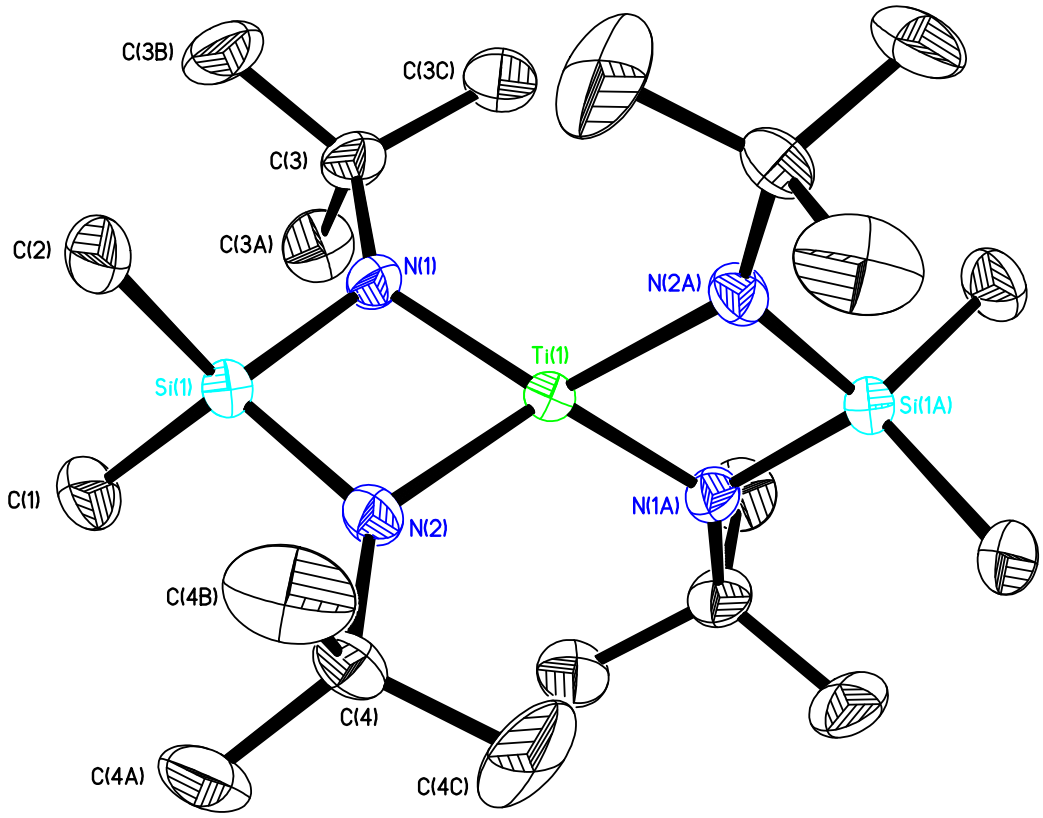

Figure 3.13: Molecular structure of the complex [{$Me_2Si(N^tBu)_2$}$_2$Ti], **25**. Thermal ellipsoids are shown at 50% probability, with hydrogen atoms omitted for clarity.

Table 3.4: Selected bond lengths (Å) and bond angles (°) for complex **25**.

Ti(1)-N(1)	1.9298 (15)	Ti(1)-N(2)	1.9336 (14)
Si(1)-N(1)	1.7462 (16)	Si(1)-N(2)	1.7432 (16)
Si(1)-C(1)	1.866 (2)	Si(1)-C(2)	1.870 (2)
N(1)-C(3)	1.471 (2)	N(2)-C(4)	1.476 (2)
N(1)-Ti(1)-N(2)	81.72 (6)	N(1)-Si(1)-N(2)	92.83 (7)
Ti(1)-N(1)-Si(1)	92.70 (7)	Ti(1)-N(2)-Si(1)	92.67 (7)
Ti(1)-N(1)-C(3)	138.06 (13)	Ti(1)-N(2)-C(4)	137.49 (13)
Si(1)-N(1)-C(3)	129.22 (13)	Si(1)-N(2)-C(4)	129.81 (13)

Analysis of the molecular structure of **25** shows the central titanium atom adopts a four-coordinate, *pseudo*-tetrahedral geometry and is bonded in bidentate manner to the nitrogen atoms of two {$Me_2Si(NtBu)_2$} moieties. Consequently this results in the formation of two planar, four-membered

{TiN_2Si} rings that are conjoined at the titanium atom [{Ti(1), N(1), N(2), Si(1)}, {Ti(1), N(1A), N(2A), Si(1A); ∑ {Ti(1)-N(1)-Si(1), Ti(1)-N(2)-Si(1), N(1)-Ti(1)-N(2), N(1)-Si(1)-N(2)} = 359.92 (7)]. These rings are observed to be perpendicular to one another, with an angle of 89.10^o (5) between the planes of the two {TiN_2Si} rings. The silicon atoms also adopt a four-coordinate *pseudo*-tetrahedral geometry, which results in the methyl groups [C(1), C(2)] bonded to the silicon atom occupying a plane that is perpendicular [89.80^o (8)] to the plane of the {TiN_2Si} ring.

Additionally, the nitrogen atoms [N(1), N(2)] adopt a planar geometry [∑ {Ti(1)-N(1)-Si(1), Ti(1)-N(1)-C(3), Si(1)-N(1)-C(3)} = 359.98^o (13); ∑ {Ti(1)-N(2)-Si(1), Ti(1)-N(2)-C(4), Si(1)-N(2)-C(4)} = 359.97^o (13)], indicating little to no degree of pyramidalisation of the nitrogen and therefore implying an sp^2 hybridisation with the lone pair occupying the p-orbital on the nitrogen. Furthermore the Si-N [Si(1)-N(1), Si(1)-N(2)] and Ti-N [Ti(1)-N(1), Ti(1)-N(2)] bond lengths observed are shorter than the values estimated from the covalent radii (N = 0.68 Å, Si = 1.20 Å, Ti = 1.47 Å),[36] suggestive of a degree of multiple bonding occurring within these bonds. Consequently these observations, along with planarity of the {TiN_2Si} ring, are suggestive of delocalisation of the nitrogen lone pair of electrons into d-orbitals of correct symmetry on the titanium and low energy d-orbitals (or Si-C antibonding orbital, as discussed in Chapter 2) of the silicon.

3.5 Synthesis of titanium complexes using [Ti(N^{t}Bu)Cl$_2$(py)$_2$], 27

As discussed in Chapter 1, the composition and consequently the properties of a TiNSi thin film may be affected by the choice of precursor used to deposit the film. Consequently, alternative titanium reagents have been investigated in order to vary the elemental composition of the titanium complexes synthesised.

As displayed in figure 2.14 of Chapter 2, several metal complexes have been reported within the literature that contain the {$NSiPh_3$} fragment. The majority of the complexes displayed within figure 2.14 are synthesised using the

complex [{Ti(NSiPh$_3$)Cl$_2$(py)$_2$}$_2$], which is initially prepared through the reaction of Ph$_3$SiNH$_2$ with the imido complex [Ti(N^{t}Bu)Cl$_2$(py)$_3$].[37] This imido complex and the related bis(pyridine) complex, [Ti(N^{t}Bu)Cl$_2$(py)$_2$], were first reported by Mountford *et. al*.[38] and have proven to be useful starting reagents for the synthesis of a wide variety of titanium imido complexes.[37, 39 - 41] In addition, [Ti(N^{t}Bu)Cl$_2$(py)$_3$] has been investigated as a potential precursor for the CVD of TiN.[1]

Consequently Mountford's reagent provides an attractive alternative to TiCl$_4$ as a reagent for reaction with the dilithium diaminosilane salts, **23** and **24**, by enabling a greater variation of the precursor properties and reducing the risk of chlorine contamination within the product. A batch of [Ti(N^{t}Bu)Cl$_2$(py)$_2$], **27**, was therefore subsequently prepared and isolated as an orange powder using the procedure reported in the literature (figure 3.14).[38]

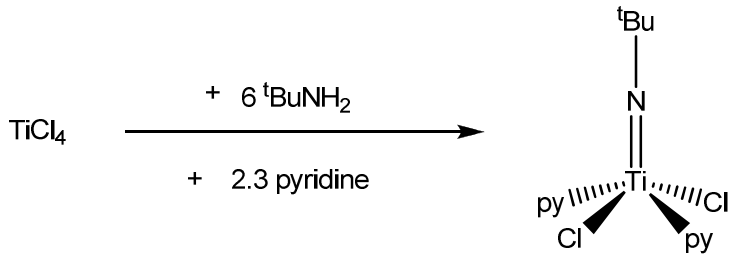

Figure 3.14: Synthesis of titanium imido complex [Ti(N^{t}Bu)Cl$_2$(py)$_2$], (**27**).

A series of reactions were performed in which a solution of **27** is slowly added to a diethyl ether solution of the dilithiated diaminosilane salt in a 1:1 molar ratio, as shown in figure 3.15. Consequently the titanium complexes **28** and **29** have been synthesised from the dilithiated salts **23** and **24** respectively (table 3.5). These complexes may potentially contain between 0 and 2 molecules of pyridine coordinated to the titanium atom.

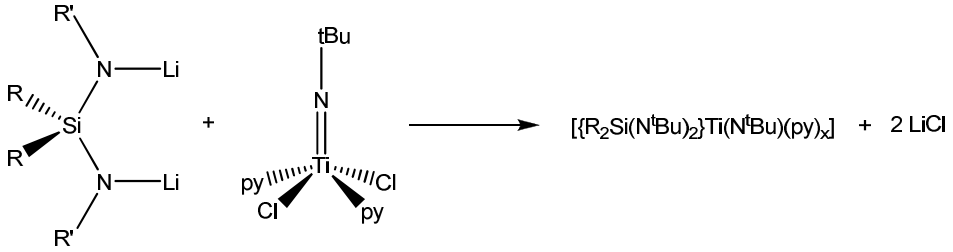

Figure 3.15: Schematic representation of the synthesis of titanium complexes **28** and **29,** prepared using **27**.

Table 3.5 Titanium complexes synthesised using the titanium imido reagent $[Ti(N^tBu)Cl_2(py)_2]$ (**27**).

Complex	R	R'
28	Me	^{t}Bu
29	Ph	^{t}Bu

In a similar manner to the synthesis of **25** and **26**, the addition of an orange solution of **27** to a colourless solution of **23** at -78 ^{o}C invoked a colour change in the solution to dark green, whilst the analogous reaction with **24** invoked a colour change in the solution to dark brown. Within both reactions the simultaneous formation of a precipitate of LiCl is observed. After gradual warming to room temperature to ensure completion, the LiCl precipitate was removed by filtration and all volatiles removed *in vacuo*. From the subsequent residue the titanium complexes were isolated by recrystallisation at -28 ^{o}C from a toluene solution. The methyl derivative, **28**, has been isolated as green crystals whilst the phenyl derivative, **29**, has been isolated as fine orange-brown crystals. Curiously, although **28** has been isolated as green crystals in a similar manner to **25**, the crystals of **28** have not been observed to change colour over time when stored under nitrogen.

Analysis of the ^{1}H NMR spectrum for **28** shows it to be comparable to the ^{1}H NMR spectrum for **25**, although the resonance attributed to the *t*-butyl groups of the diaminosilane is observed to be shifted slightly downfield (1.61 ppm for **28** compared to 1.34 ppm for **25**). Furthermore, an additional singlet resonance is observed (1.32 ppm) that may be assigned to the *t*-butyl protons of the {N^{t}Bu} imido group bonded to the titanium. Integration of the resonance

attributed to the *tert*-butyl groups of the {$Me_2Si(N^tBu)$} and {TiN^tBu} moieties show them to be present in a 2:1 ratio. Similar observations are made within the ^1H NMR spectrum for **29**.

Interestingly no resonances are observed within the ^1H NMR spectra for **28** and **29** that may be attributed to coordinated pyridine molecules. Consequently these observations are consistent with the formation of titanium imido species of **28** and **29** with the empirical formula [{$R_2Si(N^tBu)_2$}$Ti(N^tBu)$]. **28** and **29** may therefore exist as monomeric complexes in which the titanium atom adopts a three coordinate geometry, or alternatively as the coordinatively more satisfied dimeric complex containing the titanium atoms in a more favourable 4-coordinate environment, comparable to the titanium complexes reported in Chapter 2 (figure 3.16).

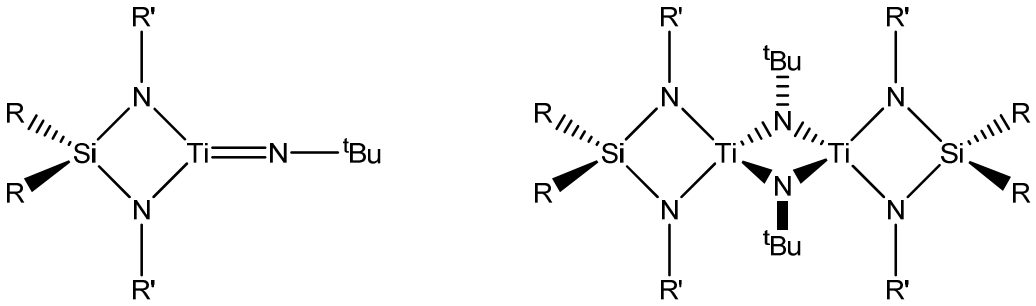

Figure 3.16: The possible products for the reaction scheme shown in figure 3.15 – the 3-coordinate titanium monomeric complex (left), or the 4-coordinate titanium dimeric complex (right).

Crystals of **28** suitable for single crystal X-ray diffraction were isolated, with the structure obtained from these studies consistent with that predicted from observations made through analysis of the ^1H NMR spectrum and confirming the dimeric nature of the molecule. In addition, although the crystals of **29** that were isolated were unsuitable for single crystal X-ray diffraction, the structure is assumed to be similar to that observed for **28** based on the data from the ^1H NMR spectrum.

The titanium complex [{$Me_2Si(N^tBu)_2Ti(\mu_2\text{-}N^tBu)$}$_2$], **28**, is found to crystallise in the triclinic space group (*P-1*) with only one half-dimer forming the asymmetric unit. In a similar manner to that observed for **25**, the dimer of **28** is

situated on a crystallographic inversion centre and subsequently the second half of the molecule is generated by the symmetry operator (-x, 1-y, -z). The molecular structure for **28** is shown in detail in figure 3.17, with selected bond lengths and angles for this complex given in table 3.6.

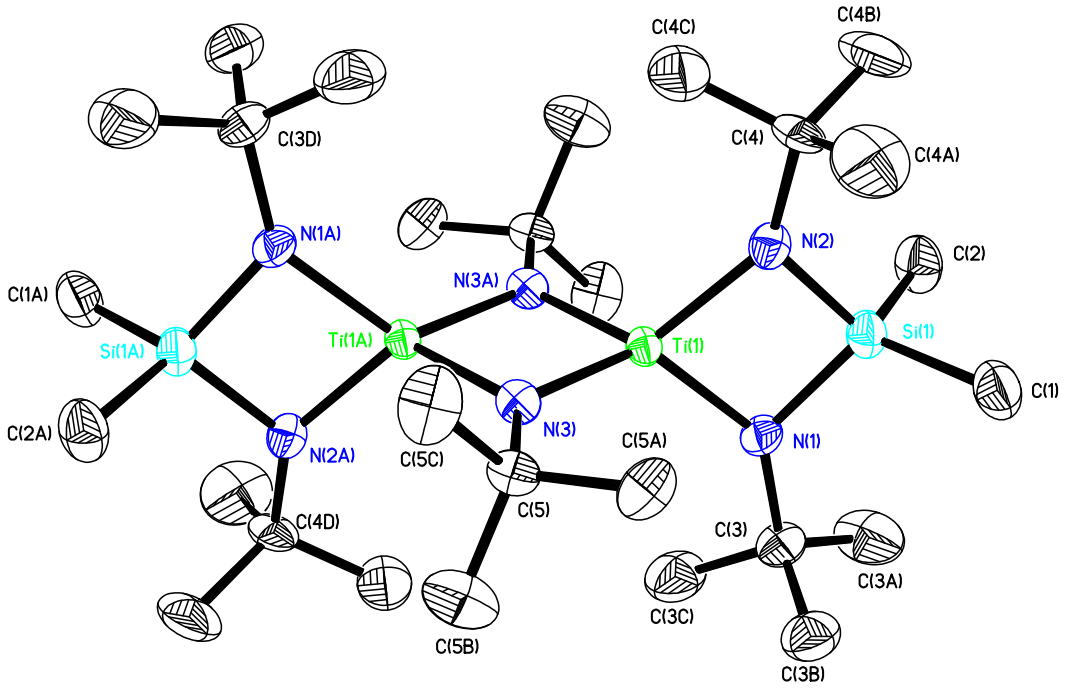

Figure 3.17: Molecular structure of the complex [{$Me_2Si(N^tBu)_2Ti(\mu_2\text{-}N^tBu)\}_2$], **28**. Thermal ellipsoids are shown at 50 % probability, with hydrogen atoms omitted for clarity.

Table 3.6: Selected bond lengths (Å) and bond angles (°) for complex **28**.

Ti(1)-N(1)	1.915 (7)	Ti(1)-N(2)	1.906 (7)
Si(1)-N(1)	1.760 (7)	Si(1)-N(2)	1.757 (7)
Ti(1)-N(3)	1.925 (7)	Ti(1A)-N(3)	1.944 (7)
Si(1)-C(1)	1.859 (10)	Si(1)-C(2)	1.861 (9)
N(1)-C(3)	1.477 (11)	N(2)-C(4)	1.488 (11)
N(3)-C(5)	1.472 (11)		
N(1)-Ti(1)-N(2)	83.9 (3)	N(1)-Si(1)-N(2)	93.2 (3)
Ti(1)-N(1)-Si(1)	91.1 (3)	Ti(1)-N(2)-Si(1)	91.6 (3)
Ti(1)-N(1)-C(3)	141.6 (6)	Ti(1)-N(2)-C(4)	141.2 (5)
Si(1)-N(1)-C(3)	126.5 (5)	Si(1)-N(2)-C(4)	127.1 (5)
N(3)-Ti(1)-N(3A)	86.5 (3)	Ti(1)-N(3)-Ti(1A)	93.5 (3)
Ti(1)-N(3)-C(5)	132.5 (5)	Ti(1A)-N(3)-C(5)	134.0 (5)

The structure of **28** incorporates several different structural features previously observed earlier in this chapter and in Chapter 2. In a similar manner to that observed within **25**, the titanium atoms within **28** occupy a four coordinate *pseudo*-tetrahedral environment with one $\{Me_2Si(N^tBu)_2\}$ moiety bonded to each titanium atom, resulting in the formation of two planar $\{TiN_2Si\}$ rings [{Ti(1), N(1), Si(1), N(2)}; {Ti(1A), N(1A), Si(1A), N(2A)]. Again, as observed within **25** before, the methyl groups bonded to the silicon occupy a plane perpendicular to the plane of the $\{TiN_2Si\}$ ring [89.76^o (31)].

However, unlike within the structure of **25**, the $\{TiN_2Si\}$ rings are not conjoined but rather linked through the titanium atoms via a planar four-membered $\{Ti_2N_2\}$ ring [Ti(1), N(3), Ti(1A), N(3A)] that is observed to be perpendicular [89.95^o (32)] to the plane of the two $\{TiN_2Si\}$ four-membered rings.

This $\{Ti_2N_2\}$ ring is similar to that observed within the crystal structure of **9** as described in Chapter 2. Consequently, comparable arguments made concerning the π-bonding structure of **9** may be applied to the π-bonding structure observed within **28** involving the vacant d-orbitals of titanium [Ti(1), Ti(1A)] and the lone pairs on both bridging imido nitrogen atoms [N(3), N(3A)].

As discussed in Chapter 2, the π-orbitals of a central $\{Ti_2N_2\}$ core may interact with the π-orbitals of the peripheral ligands,[41, 42] although the results discussed apply to an ideal system with certain assumptions being made. These include the assumption that the p_x orbitals of the amide nitrogens are all perpendicular to the π-orbitals of the central Ti_2N_2 core.[41] Complex **28** is more likely to adhere to this assumption compared to **9** due to the chelating Me_2Si- spacer group within **28** restricting rotation around the Ti-N amide bonds [Ti(1)-N(1), Ti(1)-N(2)].

There is the possibility for the two lone pairs of electrons on the nitrogen atoms of the $\{Me_2Si(N^tBu)_2\}$ fragment [N(1), N(2)] to be delocalised around the $\{TiN_2Si\}$ ring as discussed for the structure of **25**. However, since these lone pairs may interact with the π-bonding within the central $\{Ti_2N_2\}$ core,

delocalisation around the {TiN_2Si} ring is likely to be disrupted. Consequently the Ti-N amide bonds display a greater degree of multiple bonding within **28** [Ti(1)-N(1) = 1.915 (7) Å; Ti(1)-N(2) = 1.906 (7) Å] compared to that observed within **25** [Ti(1)-N(1) = 1.9298 (15) Å; Ti(1)-N(2) = 1.9336 (14) Å]. In addition, a concurrent lengthening of the Si-N amide bonds [Si(1)-N(1), Si(1)-N(2)], indicative of a reduction in multiple bond character, is observed within the structure of **28** [1.760 (7) Å and 1.757 (7) Å respectively, compared to 1.7462 (16) Å and 1.7432 (16) Å within **25**].

3.6 Reaction of Mountford's reagent ([Ti(N^{t}Bu)Cl_2(py)$_2$], 27) with LiN(SiMe$_3$)$_2$

As discussed earlier in this chapter, variation of the {N^{t}Bu} imido group within Mountford's reagent, **27**, using silicon amides has previously been reported.[37] As part of our studies into the titanium complexes prepared using **27**, the substitution of the chloride groups using non-chelating silicon amides has been investigated.

The commercially available silicon amide $HN(SiMe_3)_2$ has previously been investigated as a precursor in a dual-source approach for the deposition of MN thin films.[43, 44] In addition, due to the weaker nature of the Ti-$N(SiMe_3)_2$ amido bond caused by the smaller amount of (d←p) π bonding compared to a Ti-NMe_2 bond,[33, 45] the anticipated complex from the reaction of the lithiated amide, $LiN(SiMe_3)_2$, with **27** may provide a useful reagent for transamination reactions to further complexes and potential single-source precursors.

Therefore, a reaction has been performed in which a solution of **27** is slowly added to a diethyl ether solution of $LiN(SiMe_3)_2$ in a 1:2 molar ratio, to obtain a disubstituted titanium imido bis-amido complex as shown in figure 3.18. As mentioned previously for the synthesis of **28** and **29**, the resultant titanium complex may potentially contain between 0 and 2 molecules of pyridine coordinated to the titanium atom.

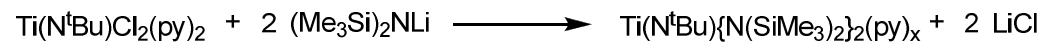

Figure 3.18: Schematic representation of the anticipated reaction of **27** and $LiN(SiMe_3)_2$ in a 1:2 ratio.

The addition of an orange solution of **27** to a colourless solution of $LiN(SiMe_3)_2$ at -78 ^oC invoked a colour change in the solution to dark green, with the simultaneous formation of a precipitate of LiCl. Upon gradual warming to room temperature to ensure completion, the LiCl precipitate was removed by filtration and all volatiles removed *in vacuo* to yield a red solid.

However, analysis of the ^1H and ^{29}Si NMR spectra obtained for the product show multiple peaks which cannot be assigned only to the anticipated product $[Ti(N^tBu)\{N(SiMe_3)_2\}_2(py)_x]$. Therefore it may be possible that multiple competing reactions are occurring, subsequently resulting in the formation of multiple products.

Red crystals suitable for single crystal X-ray diffraction were isolated from the residue by recrystallisation at -28 ^oC from a hexane solution. Subsequently the crystals isolated were determined to be the dimeric titanium complex $[\{(Me_3Si\overline{NSiMe_2CH_2})Ti(\mu_2\text{-}N^tBu)\}_2]$, **30**, by single crystal X-ray diffraction. This complex is found to crystallise in the triclinic space group (*P-1*). The asymmetric unit is observed to contain one half-dimer in which atoms are disordered over two positions as shown in figure 3.19. The dimer of **30** is situated on a crystallographic inversion centre and subsequently the second half of both dimers arising from the disorder are generated by the symmetry operator (1-x, 1-y, 1-z). The two dimeric molecules arising from the disorder within the asymmetric unit are shown separately in greater detail in figures 3.20 and 3.21. The molecular structure for molecule 1 containing Ti(1) is shown in detail in figure 3.20, whilst the molecular structure for molecule 2 containing Ti(2) is shown in detail in figure 3.21. Selected bond lengths and angles for both dimer molecules given in table 3.7.

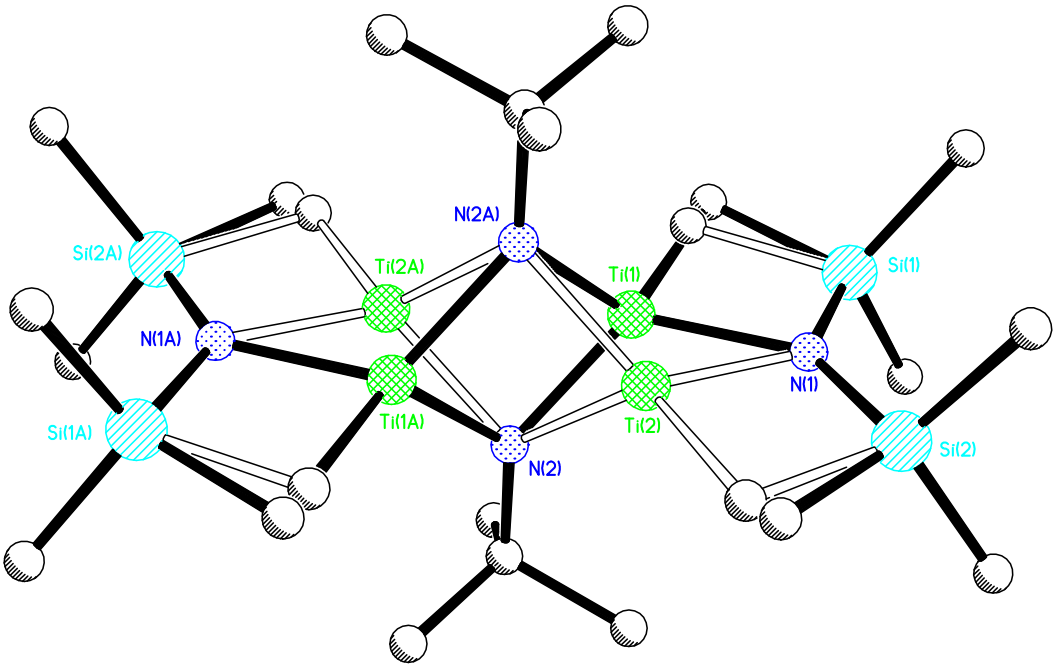

Figure 3.19: Structure of the complex [{($Me_3SiNSiMe_2CH_2$)Ti(μ_2-N^{t}Bu)}$_2$], **30**, in which the atoms are disordered over two positions. Bonds attributed to the crystallographic isomer containing the atom [Ti(1)] are shown in bold, whilst equivalent bonds within the second molecule containing [Ti(2)] are unshaded.

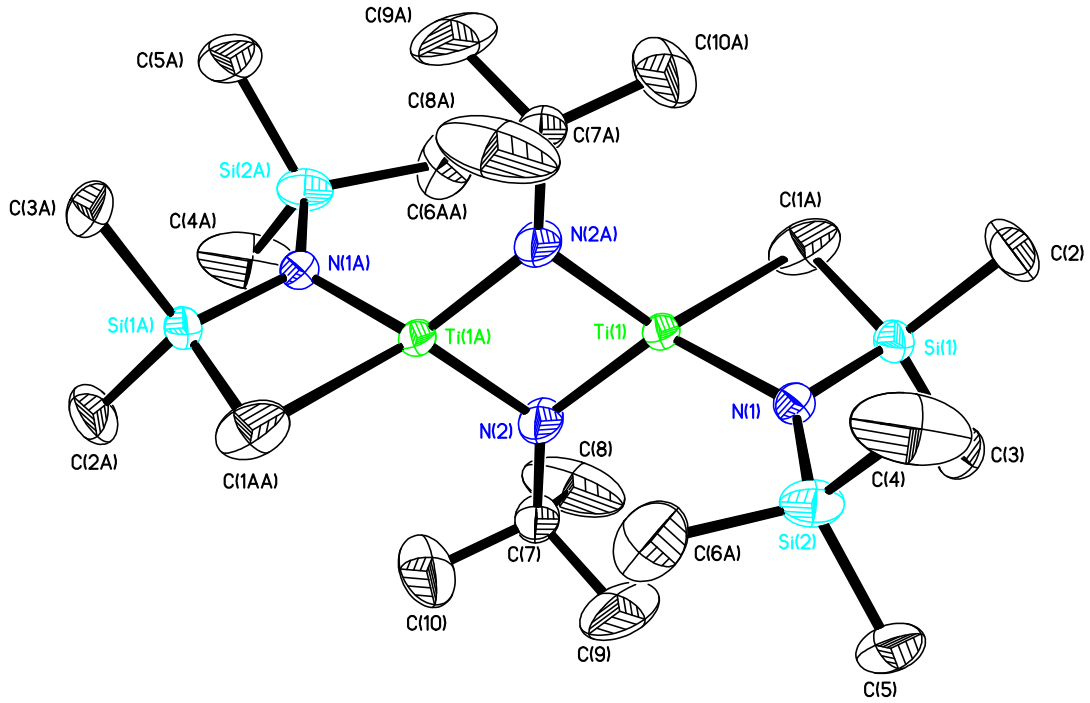

Figure 3.20: Molecular structure of molecule 1 of the complex [{($Me_3SiNSiMe_2CH_2$)Ti(μ$_2$-N^{t}Bu)}$_2$], **30**. Thermal ellipsoids are shown at 30 % probability, with hydrogen atoms omitted for clarity.

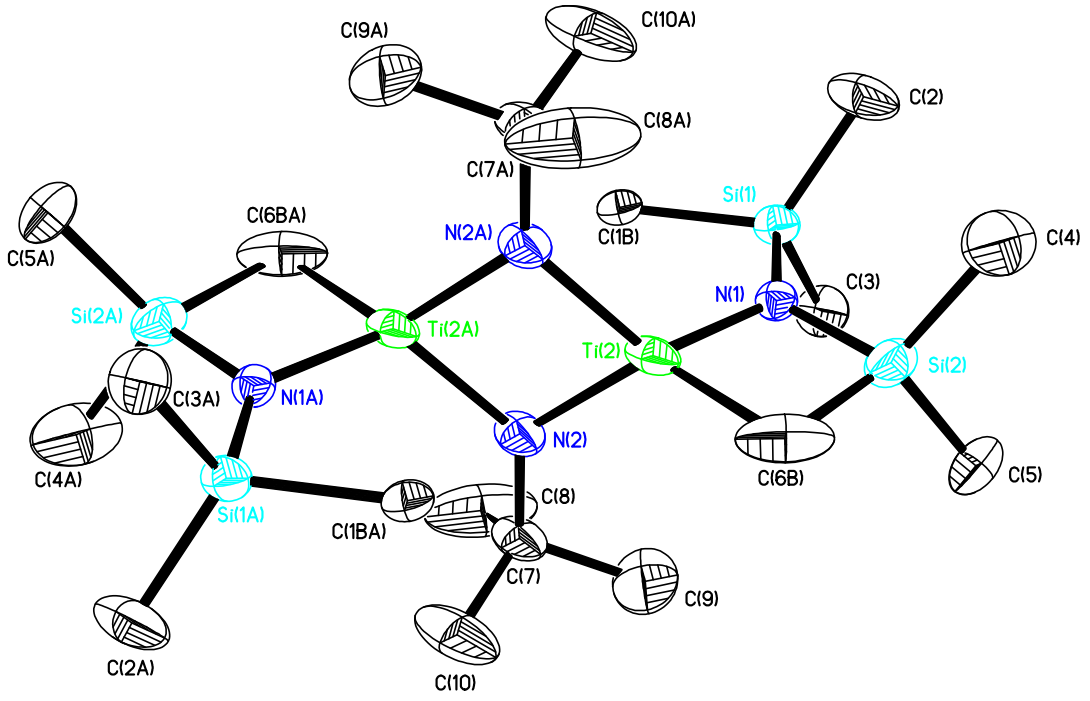

Figure 3.21: Molecular structure of molecule 2 of the complex [{($Me_3SiNSiMe_2CH_2$)Ti(μ$_2$-N^{t}Bu)}$_2$], **30**. Thermal ellipsoids are shown at 30 % probability, with hydrogen atoms omitted for clarity.

Table 3.7: Selected bond lengths (Á) and bond angles (^{o}) for complex **30**.

Molecule 1		Molecule 2	
Ti(1)-N(2)	1.909 (2)	Ti(2)-N(2)	1.964 (3)
Ti(1)-N(2A)	1.939 (2)	Ti(2)-N(2A)	1.984 (3)
Ti(1)-N(1)	1.915 (2)	Ti(2)-N(1)	1.868 (2)
Ti(1)-C(1A)	2.347 (13)	Ti(2)-C(6B)	2.04 (2)
Si(1)-N(1)	1.742 (2)	Si(2)-N(1)	1.731 (2)
Si(1)-C(1A)	1.846 (16)	Si(2)-C(6B)	1.90 (2)
Si(1)-C(2)	1.849 (4)	Si(2)-C(4)	1.859 (5)
Si(1)-C(3)	1.865 (3)	Si(2)-C(5)	1.852 (5)
Si(2)-N(1)	1.731 (2)	Si(1)-N(1)	1.742 (2)
Si(2)-C(4)	1.859 (5)	Si(1)-C(2)	1.849 (4)
Si(2)-C(5)	1.852 (4)	Si(1)-C(3)	1.865 (3)
Si(2)-C(6A)	1.837 (14)	Si(1)-C(1B)	1.91 (2)
N(1)-Si(2)-C(6A)	107.5 (5)	N(1)-Si(1)-C(1B)	94.2 (5)
N(1)-Si(1)-C(1A)	104.0 (4)	N(1)-Si(2)-C(6B)	94.5 (7)
N(1)-Ti(1)-C(1A)	82.5 (4)	N(1)-Ti(2)-C(6B)	86.2 (7)
Ti(1)-C(1A)-Si(1)	78.7 (5)	Ti(2)-C(6B)-Si(2)	84.5 (7)
Ti(1)-N(1)-Si(1)	94.44 (9)	Ti(2)-N(1)-Si(2)	94.82 (10)
Ti(1)-N(1)-Si(2)	132.93 (11)	Ti(2)-N(1)-Si(1)	132.53 (12)
Si(1)-N(1)-Si(2)	132.63 (12)	Si(2)-N(1)-Si(1)	132.63 (12)
N(2)-Ti(1)-N(2A)	86.31 (9)	N(2)-Ti(2)-N(2A)	83.61 (10)
Ti(1)-N(2)-Ti(1A)	93.69 (9)	Ti(2)-N(2)-Ti(2A)	96.39 (10)
Ti(1)-N(2)-C(7)	135.20 (18)	Ti(2)-N(2)-C(7)	129.5 (2)
Ti(1A)-N(2)-C(7)	130.78 (18)	Ti(2A)-N(2)-C(7)	133.7 (2)

The titanium complex **30** is observed to contain many structural features previously observed within the structure of **28**. This includes a central planar four-membered $\{Ti_2N_2\}$ ring [Ti(1), N(2), Ti(1A), N(2A); Ti(2), N(2), Ti(2A), N(2A)] that is conjoined to two other planar four-membered rings through the titanium atoms. However, within **30** these rings are observed to be {TiNSiC} rings [Ti(1), N(1), Si(1), C(1A); Ti(2), N(1), Si(2), C(6B)], compared to the

{TiN_2Si} rings observed within **28**. These {TiNSiC} rings are observed to be arranged in an almost perpendicular [88.21^o (21)] fashion in relation to the {Ti_2N_2} ring.

The {TiNSiC} rings observed arise from the elimination of a single proton from one of the {Me_3Si} groups of a {$N(SiMe_3)_2$} ligand, with the resultant {$Me_3SiNSiMe_2CH_2$} moiety bonding to the titanium in a bidentate manner through the nitrogen and methylene carbon atoms. This γ–hydrogen elimination within {$N(SiMe_3)_2$} ligands and subsequent formation of a {MNSiC} ring has previously been reported for several Group 4 metal complexes, as shown in figure 3.22.[46 - 53]

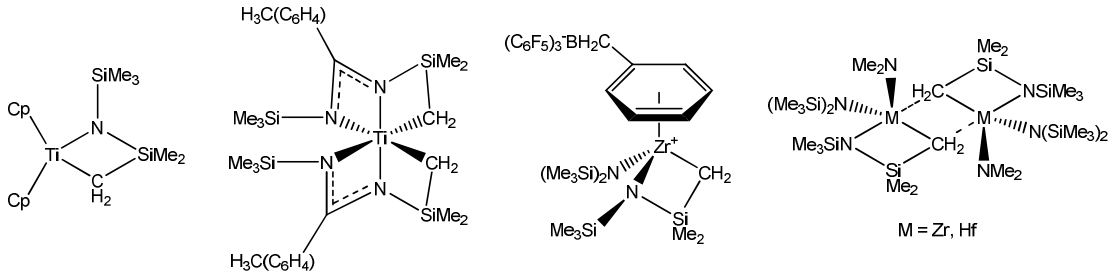

Figure 3.22: Group 4 complexes containing a four-membered {MNSiC} ring.[46 - 53]

The related titanium complex [$Cp_2Ti(CH_2SiMe_2NSiMe_3)$], which has previously been investigated as a potential single–source precursor for TiNSiC ceramic thin films,[54] has been prepared by a similar reaction for the synthesis of **30** through the addition of two equivalents of $LiN(SiMe_3)_2$ to a solution of Cp_2TiCl_2.[46, 47] Within this reaction the mechanism by which the {TiNSiC} ring is formed has been discussed by Andersen *et. al*. (figure 3.23).[46] A possibility is the reaction proceeding via a transient [$Cp_2Ti\{N(SiMe_3)_2\}_2$] species, from which intramolecular elimination of a molecule of $(Me_3Si)_2NH$ may occur. Alternatively, after the first substitution to obtain the intermediate species [$Cp_2Ti\{N(SiMe_3)_2\}(Cl)$], steric effects may favour deprotonation of the coordinated {$N(SiMe_3)_2$} ligand by the second molecule of $LiN(SiMe_3)_2$. This would result in the formation of the lithium salt [$Li\{Cp_2Ti(NSiMe_3SiMe_2CH_2)(Cl)\}$], from which elimination of LiCl may occur to yield the {TiNSiC} ring. However, the precise mechanism remains uncertain.

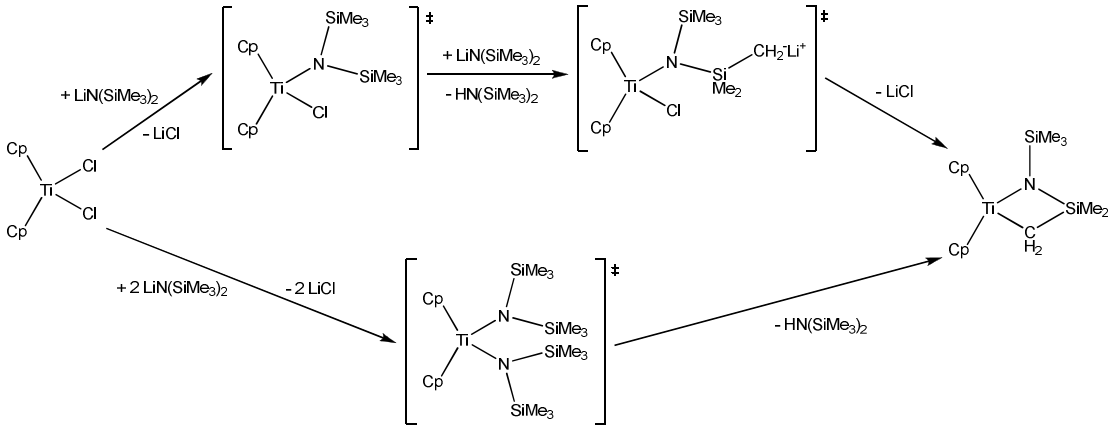

Figure 3.23: The potential mechanisms by which the reaction of Cp_2TiCl_2 and two equivalents of $LiN(SiMe_3)_2$ may proceed.[46]

Similar arguments may be made for the synthesis of **30**. However, as discussed earlier, the presence of multiple peaks within the ^1H and ^{29}Si NMR spectra suggest the occurrence of competing reactions. These include the presence within the ^1H NMR spectrum of several resonances which may be attributed to the presence of pyridine. Unfortunately due to time limitations further elucidation of the reaction products was not possible.

3.7 Summary for Chapter 3

A range of symmetrical diaminosilanes of the form $[R_2Si(NHR')_2]$ have been prepared from the corresponding dichlorosilane with an excess of the relevant primary amine. However, when {R} and {R'} are bulky substituents, only the monosubstituted product, $[R_2Si(Cl)(NHR')]$ is observed due to steric hindrance. Therefore, to obtain the disubstituted product harsher reaction conditions are required, in which the dichlorosilane is treated with a monolithiated primary amide, [R'NHLi], in a 1:2 ratio.

Subsequently, a range of titanium complexes have successfully been prepared from the reactions of the dilithiated diaminosilane salt, $[R_2Si(NLiR')_2]$, with titanium(IV) chloride and the titanium imido complex $[Ti(N^tBu)Cl_2(py)_2]$ in a 1:2 and 1:1 ratio respectively. Within the titanium complexes isolated from the corresponding reactions of the diaminosilane salt $[Me_2S(NLi^tBu)_2]$, the diaminosilane is found to bond to the metal atom in a

bidentate fashion to create a four-membered planar {TiN_2Si} ring. In addition, the reaction of [$Me_2S(NLi^tBu)_2$] and the titanium imido complex [$Ti(N^tBu)Cl_2(py)_2$] affords a dimeric product containing a central four-membered, planar {Ti_2N_2} ring.

The bond lengths within the {TiN_2Si} rings are found to be shorter than the values estimated from the covalent radii, suggesting a degree of multiple bonding is occurring within these bonds. Consequently these observations are suggestive of delocalisation of the nitrogen lone pairs of electrons into d-orbitals of correct symmetry and energy on the titanium and silicon atoms. However, within the complex isolated from the reaction of [$Ti(N^tBu)Cl_2(py)_2$], delocalisation of electrons within the {TiN_2Si} rings may be disrupted by the presence of the delocalised {Ti_2N_2} ring.

In addition, the titanium imido complex [$Ti(N^tBu)Cl_2(py)_2$] has been treated with the non-chelating silicon amide [$LiN(SiMe_3)_2$] in a 1:2 ratio. However, crystals isolated from the reaction were found not to be the anticipated disubstituted titanium imido bis-amido complex. Instead, the isolated dimeric product is found to contain planar, four-membered {TiNSiC} rings. These rings are attributed to the occurrence of γ–hydrogen elimination within the {$N(SiMe_3)_2$} ligands. However, the precise mechanism by which the {TiNSiC} rings are formed is unknown.

Whilst the work presented within this chapter was being performed, several patents were filed by Air Products and Chemicals, Inc., USA, concerning the preparation of metal silicon nitride films using the diaminosilane [$H_2Si(NH^tBu)_2$], the titanium complex [{$H_2Si(N^tBu)_2$}$_2$Ti] and related compounds.[55, 56] Subsequently, detailed investigation into further Group 4 metal complexes containing the bidentate {$R_2Si(NR')_2$} moiety as potential single-source CVD precursors for the deposition of MNSi materials was not performed.

The reactions and compounds presented in this chapter are shown below in figure 3.24.

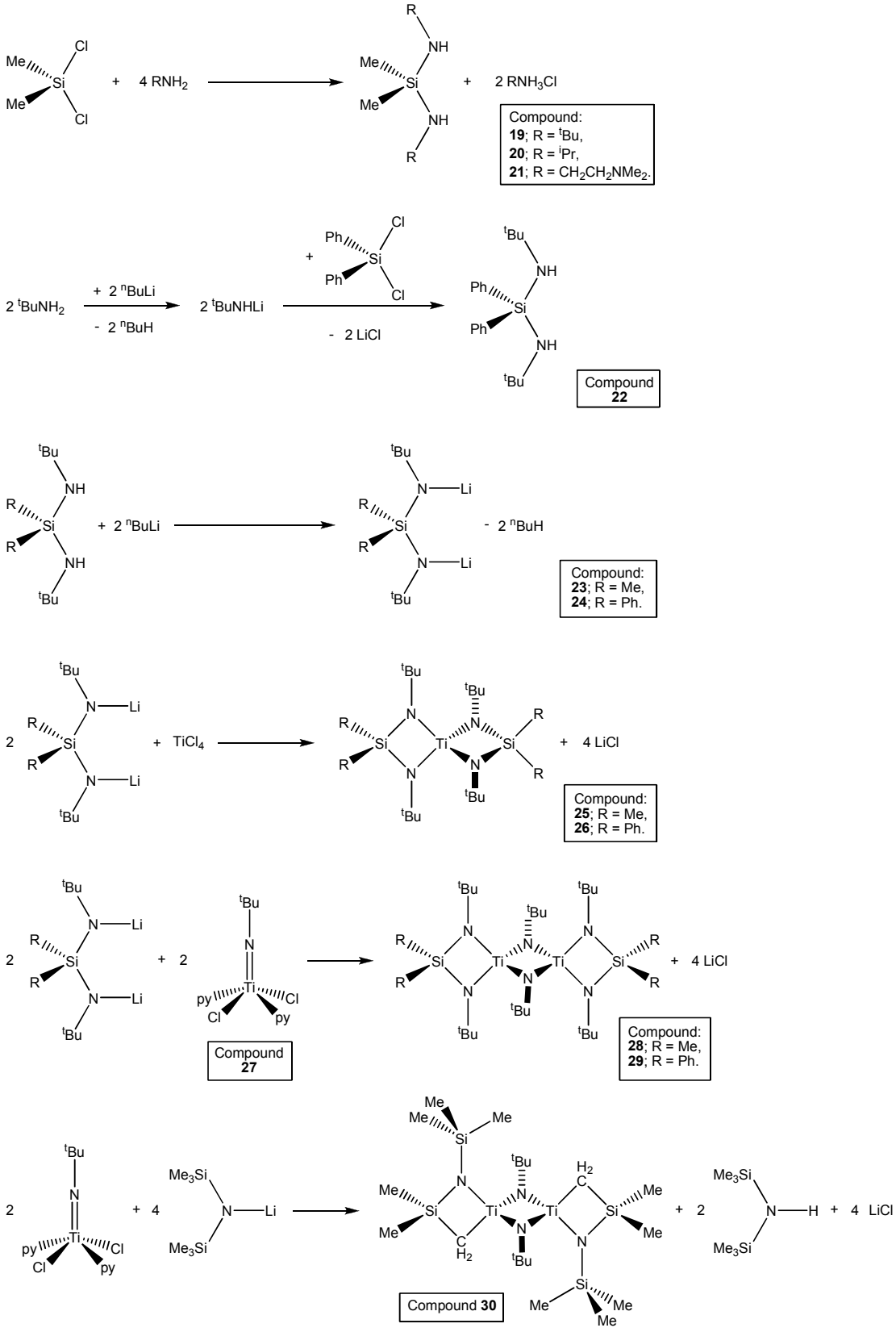

Figure 3.24: Reactions and compounds presented within Chapter 3.

3.8 References for Chapter 3

1. A. C. Jones and M. L. Hitchman, *"Chemical Vapour Deposition; Precursors, Processes and Applications"*, **2009**, RSC Publishing, Cambridge, UK.
2. L. McElwee-White, *Dalton Trans.*, 2006, 5327.
3. M. Veith, M. Opsölder, M. Zimmer and V. Huch, *Eur. J. Inorg. Chem.*, 2000, 1143.
4. M. Veith, A. Müller, L. Stahl, M. Nötzel, M. Jarczyk and V. Huch, *Inorg. Chem.*, 1996, **35**, 3848.
5. K. Sharma, N. Fahmi and R. V. Singh, *Appl. Organometal. Chem.*, 2001, **15**, 221.
6. D. C. Haagenson, D. F. Moser, L. Stahl and R. J. Staples, *Inorg. Chem.*, 2002, **41**, 1245.
7. M. Veith, N. Auvray, V. Huch and P. Braunstein, *C. R. Chimie*, 2005, **8**, 57.
8. C. Jones, P. C. Junk, S. G. Leary and N. A. Smithies, *Inorg. Chem. Commun.*, 2003, **6**, 1126.
9. A. M. Martins, J. R. Ascenso, S. M. B. Costa, A. R. Dias, H. Ferreira and J. A. B. Ferreira, *Inorg. Chem.*, 2005, **44**, 9017.
10. B. D. Ward, G. Orde, E. Clot, A. R. Cowley, L. H. Gade and P. Mountford, *Organometallics*, 2004, **23**, 4444.
11. A. F. Heyduk, K. J. Blackmore, N. A. Ketterer and J. W. Ziller, *Inorg. Chem.*, 2005, **44**, 468.
12. S. Friedrich, L. H. Gade, A. J. Edwards and M. McPartlin, *J. Chem. Soc. Dalton Trans.*, 1993, 2861.
13. M. S. Hill and P. B. Hitchcock, *Organometallics*, 2002, **21**, 3258.
14. V. Passarelli, F. Benetollo, P. Zanella, G. Carta and G. Rossetto, *Dalton Trans.*, 2003, 1411.
15. V. Passarelli and P. Zanella, *Eur. J. Inorg. Chem.*, 2004, 4439.
16. V. Passarelli, F. Benetollo and P. Zanella, *Eur. J. Inorg. Chem.*, 2004, 1714.
17. V. Passarelli, F. Benetollo and P. Zanella, *Dalton Trans.*, 2004, 1424.
18. C. H. Lee, Y-H. La and J. W. Park, *Organometallics*, 2000, **19**, 344.

19. C. Wang, G. Erker, G. Kehr, K. Wedeking and R. Fröhlich, *Organometallics*, 2005, **24**, 4760.
20. A. D. Horton and J. de With, *Organometallics*, 1997, **16**, 5424.
21. S-J. Kim, I. N. Jung, B. R. Yoo, S. H. Kim, J. Ko, D. Byun and S. O. Kang, *Organometallics*, 2001, **20**, 2136.
22. R. M. Gauvin, C. Lorber, R. Choukroun, B. Donnadieu and J. Kress, *Eur. J. Inorg. Chem.*, 2001, 2337.
23. V. C. Gibson, B. S. Kimberley, A. J. P. White, D. J. Williams and P. Howard, *Chem. Commun.*, 1998, 313.
24. T. Dall'Occo, A. D. Horton, B. J. Ruisch, K. L. Hebel, A. van Zon, H. H. Deuling and E. J. M. de Boer, *US Pat.*, 0097668, 2004.
25. E. J. M. de Boer, H. H. Deuling, K. L. von Hebel, B. J. Ruisch and A. van Zon, *World Intellectual Property Organization*, WO 03/000628 A1, 2003.
26. D. J. Brauer, H. Burger, E. Essig and W. Geschwandtner, *J. Organomet. Chem.*, 1980, **190**, 343.
27. D. J. Brauer, H. Bürger, G. R. Liewald and J. Wilke, *J. Organomet. Chem.*, 1986, **310**, 317.
28. C. Jones, P. C. Junk, S. G. Leary, N. A Smithies and J. W. Stead, *Inorg. Chem. Commun.*, 2002, **5**, 533.
29. P. C. Junk and S. G. Leary, *Inorg. Chim. Acta*, 2004, **357**, 2195.
30. C. Jones, P. C. Junk and N. A. Smithies, *J. Organomet. Chem.*, 2000, **607**, 105.
31. R. Murugavel, N. Palanisami and R. J. Butcher, *J. Organomet. Chem.*, 2003, **675**, 65.
32. W. Fink, *Angew. Chem. Int. Ed.*., 1966, **5**, 760.
33. M. F. Lappert, P. P. Power, A. R. Sanger and R. C. Srivastava, *"Metal and Metalloid Amides; syntheses, structures, and physical and phemical properties"*, **1980**, Ellis Horwood Ltd., Chichester, UK.
34. D. J. Brauer, H. Bürger and G. R. Liewald, *J. Organomet. Chem.*, 1986, **308**, 119.
35. R. A. Jones, M. H. Seeberger, J. L. Atwood and W. E. Hunter, *J. Organomet. Chem.*, 1983, **247**, 1.
36. F. H. Allen and O. Kennard, *Chemical Design Automation News*, 1993, **8**, 31.

37. Y. Li, S. Banerjee and A. L. Odom, *Organometallics*, 2005, **24**, 3272.
38. A. J. Blake, P. E. Collier, S. C. Dunn, W.-S. Li, P. Mountford and O. V. Shishkin, *J. Chem. Soc., Dalton Trans.*, 1997, 1549.
39. N. Hazari and P. Mountford, *Acc. Chem. Res.*, 2005, **38**, 839.
40. P. E. Collier, S. M. Pugh, H. S. C. Clark, J. B. Love, A. J. Blake, F. G. N. Cloke and P. Mountford, *Inorg. Chem.*, 2000, **39**, 2001.
41. P. E. Collier, A. J. Blake and P. Mountford, *J. Chem. Soc., Dalton Trans.*, 1997, 2911.
42. D. L. Thorn, W. A. Nugent and R. L. Harlow, *J. Am. Chem. Soc.*, 1981, **103**, 357.
43. A. C. Newport, J. E. Bleau, C. J. Carmalt, I. P. Parkin and S. A. O'Neill, *J. Mater. Chem.*, 2004, **14**, 3333.
44. A. Newport, C. J. Carmalt, I. P. Parkin and S. A. O'Neill, *Eur. J. Inorg. Chem.*, 2004, 4286.
45. M. Lappert, A. Protchenko, P. Power and A. Seeber, *"Metal Amide Chemistry"*, **2009**, John Wiley & Sons, Ltd., Chichester, UK.
46. S. J. Simpson and R. A. Andersen, *Inorg. Chem.*, 1981, 20, 3627.
47. C. R. Bennett and D. C. Bradley, *J. C. S. Chem. Comm.*, 1974, 29.
48. V. Volkis, E. Nelkenbaum, A. Lisovskii, G. Hasson, R. Semiat, M. Kapon, M. Botoshansky, Y. Eishen and M. S. Eisen, *J. Am. Chem. Soc.*, 2003, **125**, 2179.
49. X. Yu, S. Bi, I. A. Guzei, Z. Lin and Z.-L., Xue, *Inorg. Chem.*, 2004, **43**, 7111.
50. J. M. Wright, C. R. Landis, M. A. M. P. Ros and A. D. Horton, *Organometallics*, 1998, **17**, 5031.
51. A. D. Horton and J. de With, *Chem. Commun.*, 1996, 1375.
52. R. P. Planalp and R. A. Andersen, *Organometallics*, 1983, **2**, 1675.
53. R. P. Planalp, R. A. Andersen and A. Zalkin, *Organometallics*, 1983, **2**, 16.
54. B. Chansou, R. Choukroun and L. Valade, *Appl. Organomet. Chem.*, 1997, **11**, 195.
55. X. Lei, H. Thridandam, K. S. Cuthill and A. K. Hochberg, *Eur. Pat.*, EP 1 691 400 A1, 2006.
56. J. A. T. Norman and X. Lei, *Eur. Pat.*, EP 1 772 460 A1, 2007.

Chapter 4

Synthesis and characterisation of tantalum, zinc and manganese complexes prepared using R_3SiNH_2 ligands

4.1 Introduction to Chapter 4

As discussed in Chapter 2, several Group 4 metal complexes have been prepared using aminosilanes **1** – **5**. As part of a wider study into the chemistry of these aminosilanes their reaction with tantalum, zinc and manganese organometallic reagents has been investigated.

4.2 Tantalum complexes

As discussed in Chapter 1, TaNSi thin films have been investigated as an alternative material to TiNSi films for use within IC diffusion barriers. However, as with the latter, effective single-source precursors for the deposition of TaNSi thin films by CVD are unknown.[1]

The tantalum complex [(^{t}Bu$_3$SiNH)Me$_2$TaNSi^{t}Bu$_3$] has previously been prepared by Schaller *et*. *al*. through the reaction of Me_3TaCl_2 and the monolithiated aminosilane salt ^{t}Bu$_3$SiNHLi in a 1:2 ratio.[2] However, the direct reaction of the parent aminosilane, ^{t}Bu$_3$SiNH$_2$, with tantalum organometallic reagents has not been reported. Therefore, in order to investigate the interaction of aminosilanes with tantalum amide reagents, a range of reactions were performed using the tantalum amide $Ta(NMe_2)_5$. In a comparable manner to the reactions described in Chapter 2 for the Group 4 amides, $M(NMe_2)_4$, aminosilanes **1**, **3**, **4** and **5** were refluxed in solution with one equivalent of $Ta(NMe_2)_5$. The analogous reaction with **2** was discounted due the multiple products observed within the related reaction of $Ti(NMe_2)_4$.

In all cases no significant change in the colour of the pale yellow solution was observed as the reaction progressed. After refluxing for 24 hr tantalum complexes from the reactions of **1** and **5** with $Ta(NMe_2)_5$ were isolated as colourless crystals by crystallisation at -28 ^{o}C from the reaction solution. However, from the reactions of **3** and **4** with $Ta(NMe_2)_5$ only starting reagents could be isolated from the reaction solution.

It is possible the presence of the electron-withdrawing groups bonded to the silicon atoms within **1** and **5** ({Ph} and {NMe_2} respectively) increases the acidity of the {NH} protons compared to within **3** and **4** which contain alkyl groups bonded to the silicon. Consequently the reactions of $Ta(NMe_2)_5$ with **1** and **5** are more facile compared to the equivalent reactions involving **3** and **4**.

Analysis of the ^1H NMR spectra for the complexes isolated from the reactions with **1** and **5** shows them to contain resonances consistent with {NMe_2} and {R_3SiN} groups present in a 3:1 ratio. Consequently these observations are consistent with the elimination of two equivalents of $HNMe_2$ and formation of the imido-containing complexes $[(Me_2N)_3TaNSiPh_3]$ (**31**) and $[(Me_2N)_3TaNSi(NMe_2)_3]$ (**32**) respectively as shown in figure 4.1.

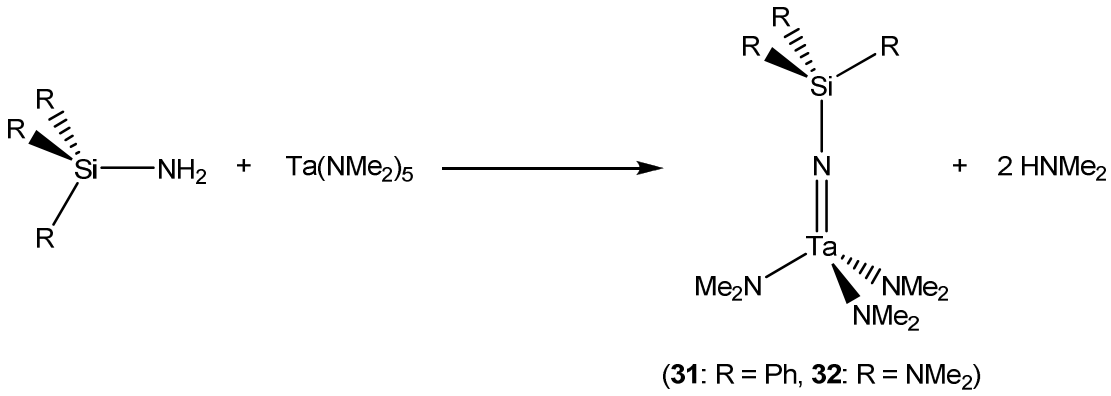

Figure 4.1. Reaction of $Ta(NMe_2)_5$ with one equivalent of a silicon amide of the form R_3SiNH_2.

For complexes **31** and **32** crystals suitable for single crystal X-ray diffraction were isolated, with the structures obtained from these studies are consistent with those predicted from observations made through analysis of the ^1H NMR spectra.

The tantalum complex $[(Me_2N)_3TaNSiPh_3]$, **31**, is found to crystallise in the trigonal space group (*R-3*), with a third of a molecule occupying the asymmetric unit. In addition, within the asymmetric unit the atoms are disordered over two positions, equivalent to two chiral rotamers that are present in a 70:30 ratio. Consequently the major isomer is anisotropic and the minor isomer is isotropic. Equivalent atoms within the molecules are generated by the symmetry operators (1-x+y, 1-x, z) and (1-y, x-y, z).

Furthermore a molecule of toluene is present that is disordered over three positions and is observed within the asymmetric unit as a third of a molecule.

The structure of **31** containing both isomers is shown below in figure 4.2, with the toluene molecule omitted for clarity.

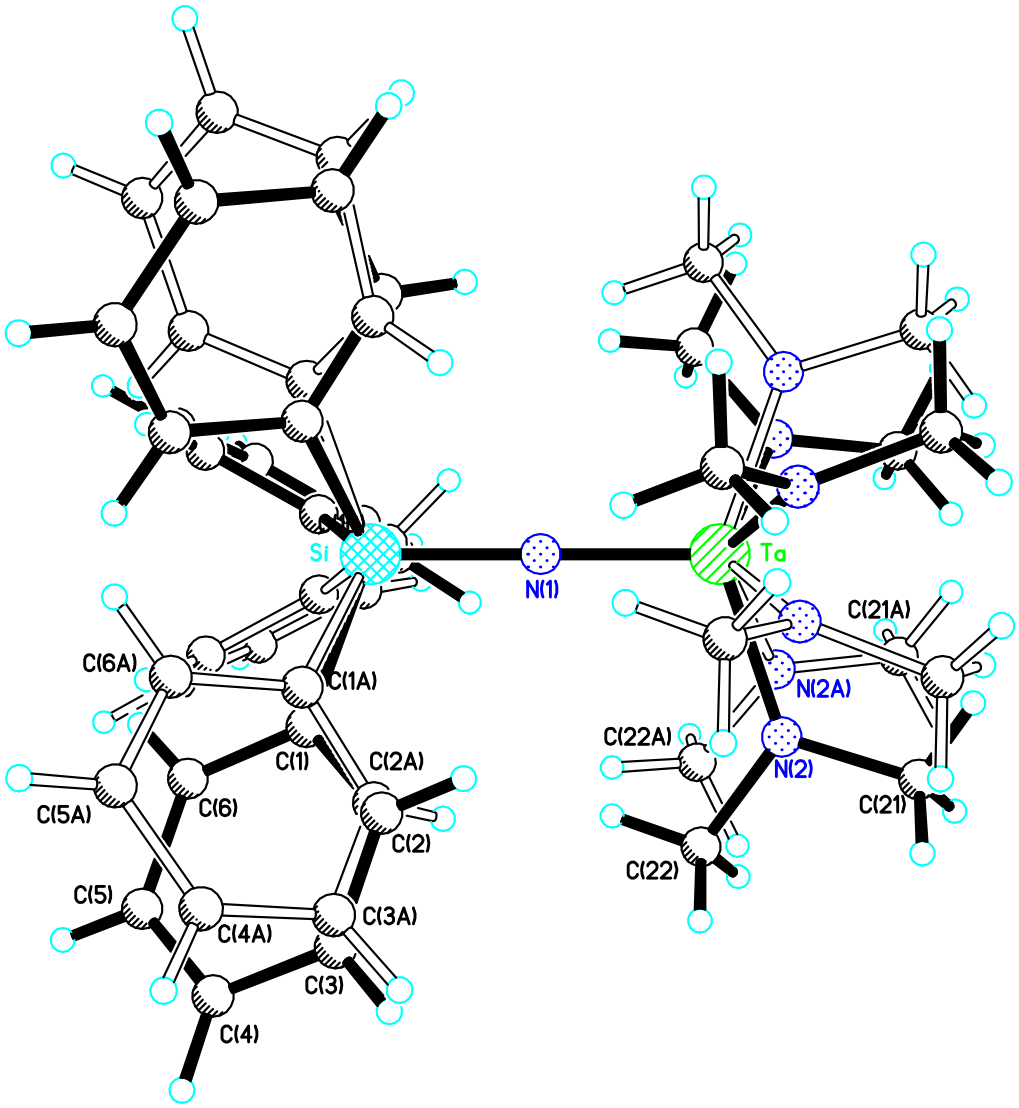

Figure 4.2. Structure of the complex $[(Me_2N)_3TaNSiPh_3]$, **31**, with atoms disordered over two positions. Bonds attributed to the major rotamer are shown in bold, with bonds attributed to the minor rotamer shown unshaded.

The following discussion of the structure of **31** will focus on the major isomer as an example case, with bond lengths and angles in both the major and minor rotamers identical within experimental error. The molecular structure for

the major isomer of **31** is shown in greater detail in figure 4.3, with selected bond lengths and angles for this complex given in table 4.1.

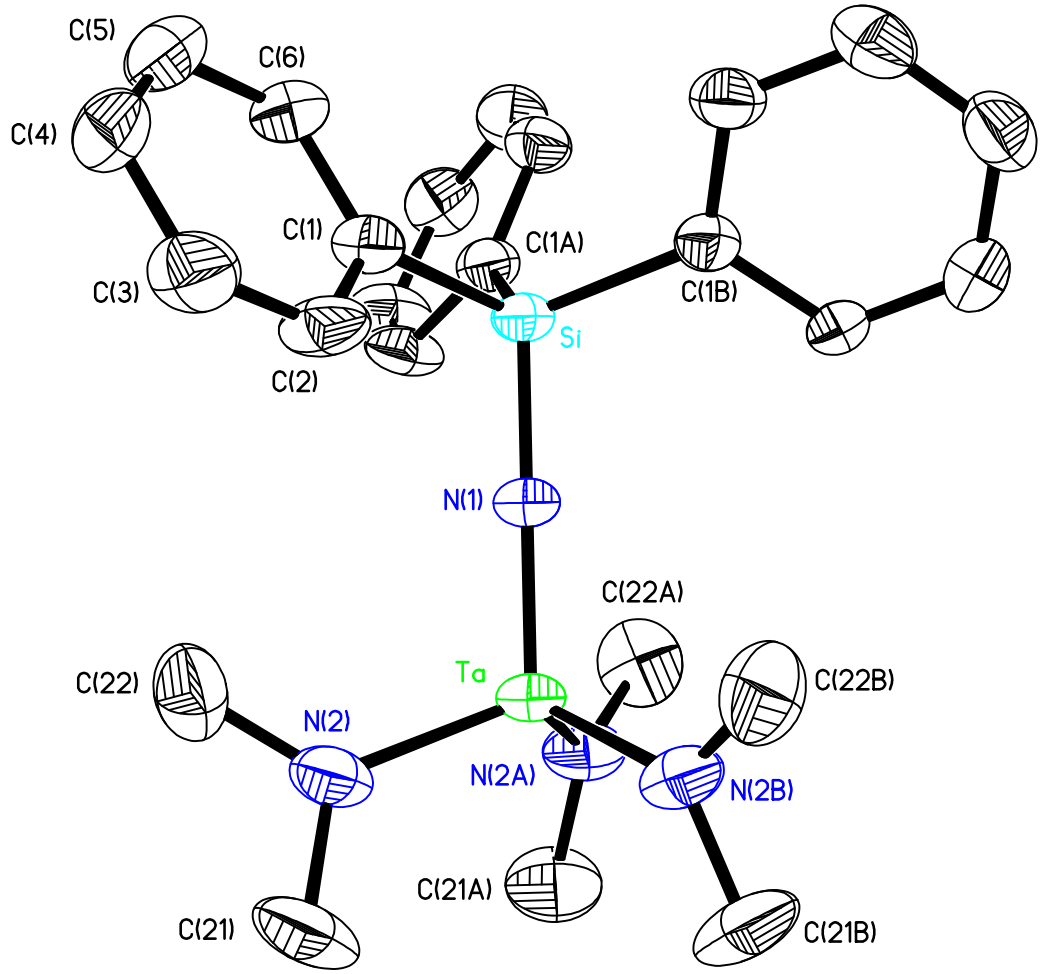

Figure 4.3. The molecular structure of the complex $[(Me_2N)_3TaNSiPh_3]$, (**31**). Thermal ellipsoids are shown at 50% probability. Hydrogen atoms are omitted for clarity.

Table 4.1. Selected bond lengths (Å) and angles (°) of the molecular structure of complex **31**. No error is displayed for the angle [Ta-N(1)-Si] due to symmetry within the molecule.

Ta-N(1)	1.793 (5)	Ta-N(2)	1.982 (7)
Si-N(1)	1.701 (6)	Si-C(1)	1.878 (6)
Ta-N(1)-Si	180.0	N(1)-Ta-N(2)	109.02 (18)
N(1)-Si-C(1)	108.98 (18)	Ta-N(2)-C(21)	121.5 (6)
Ta-N(2)-C(22)	127.1 (5)	C(21)-N(2)-C(22)	111.1 (7)

Complex **31** is found to be isostructural to the tantalum complex $[(Me_2N)_3TaN^tBu]$,[3] which has previously been investigated for its potential as a precursor for TaN films.[1, 4] Within the molecular structure of complex **31** the tantalum atom adopts a four-coordinate *pseudo* tetrahedral geometry in which the tantalum atom is bonded to three planar $\{NMe_2\}$ amide groups [N(2), N(2A), N(2B); ∑ {Ta-N(2)-C(21), Ta-N(2)-C(22), C(21)-N(2)-C(22)} = 359.7° (7)]. The Ta-N amide bonds are observed as 1.982 (7) Å [Ta-N(2)], comparable to values reported for other Ta-NMe_2 amide complexes (1.87 Å - 2.44 Å).[5]

In addition to the three amide groups, the tantalum atom is also bonded to a terminal $\{Ph_3SiN\}$ imido group [N(1)]. This imido group is observed in a linear arrangement [Ta-N(1)-Si = 180.0°], in which the atoms occupy a C_3 rotation axis through the molecule. Subsequently the {Ph} and $\{NMe_2\}$ groups are arranged around the C_3 axis in a slightly staggered conformation.

The tantalum complex $[(Me_2N)_3TaNSi(NMe_2)_3]$, **32**, is found to crystallise in the monoclinic space group ($P2_1/n$). The molecular structure for **32** is shown in detail in figure 4.4, with selected bond lengths and angles for this complex given in table 4.2.

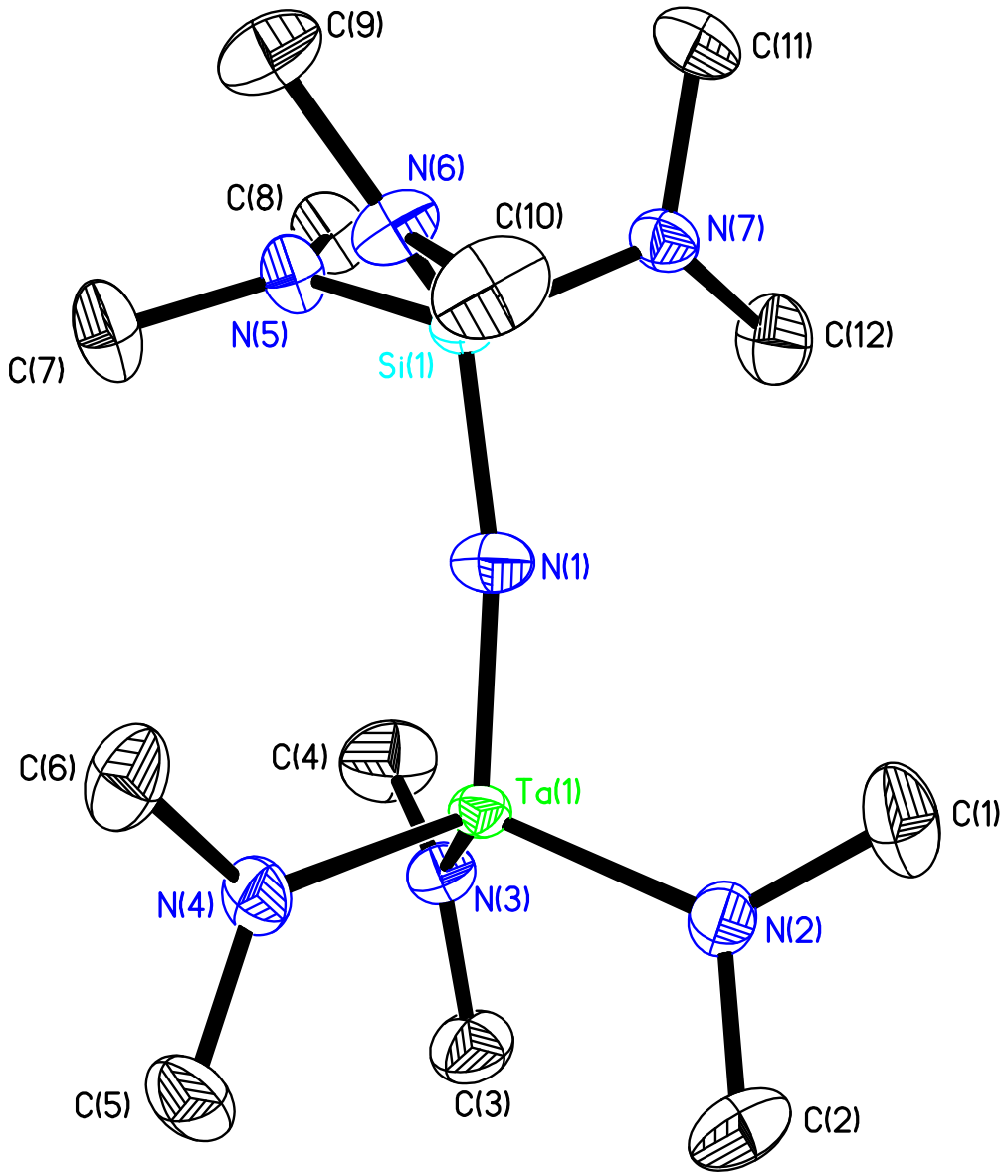

Figure 4.4. The molecular structure of the complex $[(Me_2N)_3TaNSi(NMe_2)_3]$, (**32**). Thermal ellipsoids are shown at 50% probability. Hydrogen atoms are omitted for clarity.

Table 4.2. Selected bond lengths (Á) and angles (^{o}) of the molecular structure of complex **32**.

Ta(1)-N(1)	1.779 (3)	Ta(1)-N(2)	1.979 (3)
Ta(1)-N(3)	1.996 (2)	Ta(1)-N(4)	1.982 (2)
Si(1)-N(1)	1.712 (3)	Si(1)-N(5)	1.714 (3)
Si(1)-N(6)	1.704 (3)	Si(1)-N(7)	1.713 (3)
Ta(1)-N(1)-Si(1)	169.43 (19)	N(1)-Ta(1)-N(2)	108.25 (12)
N(1)-Ta(1)-N(3)	107.54 (11)	N(1)-Ta(1)-N(4)	107.27 (12)
N(2)-Ta(1)-N(3)	112.39 (11)	N(2)-Ta(1)-N(4)	110.26 (11)
N(3)-Ta(1)-N(4)	110.92 (11)	N(1)-Si(1)-N(5)	113.05 (14)
N(1)-Si(1)-N(6)	108.46 (13)	N(1)-Si(1)-N(7)	107.10 (13)
N(5)-Si(1)-N(6)	105.95 (13)	N(5)-Si(1)-N(7)	109.31 (12)
N(6)-Si(1)-N(7)	113.08 (13)	Ta(1)-N(2)-C(1)	129.5 (3)
Ta(1)-N(2)-C(2)	119.6 (2)	C(1)-N(2)-C(2)	110.5 (3)
Ta(1)-N(3)-C(3)	121.4 (2)	Ta(1)-N(3)-C(4)	127.7(2)
C(3)-N(3)-C(4)	110.9 (3)	Ta(1)-N(4)-C(5)	119.9 (2)
Ta(1)-N(4)-C(6)	128.4 (2)	C(5)-N(4)-C(6)	111.8 (3)
Si(1)-N(5)-C(7)	120.9 (2)	Si(1)-N(5)-C(8)	123.4 (2)
C(7)-N(5)-C(8)	112.5 (3)	Si(1)-N(6)-C(9)	125.7 (2)
Si(1)-N(6)-C(10)	121.1 (2)	C(9)-N(6)-C(10)	112.3 (3)
Si(1)-N(7)-C(11)	120.6 (2)	Si(1)-N(7)-C(12)	123.8 (2)
C(11)-N(7)-C(12)	112.5 (3)		

Not unexpectedly, complex **32** is found to be structurally similar to **31**, with the molecule containing a four coordinate, *pseudo* tetrahedral tantalum atom that is bonded to three planar {NMe_2} amide ligands [N(2), N(3) and N(4)] and a terminal {$NSi(NMe_2)$} imido unit [N(1)]. This imido group is observed in a near-linear arrangement [Ta(1)-N(1)-Si(1) = 169.43^{o} (19)]. In addition the {NMe_2} units bonded to the silicon atom [N(5), N(6) and N(7)] are observed in a near planar arrangement.

Within the structures of **31**, **32** and the tantalum complex $[(Me_2N)_3TaN^tBu]$ the amide substituents adopt a planar geometry with a comparatively short Ta-N amide bond length. These observations imply that the amide substituents are bonded to the metal centre in a manner depicted earlier in structure (**IIb**) [Chapter 2, figure 2.1, page 56]. Within structure (**IIb**) the amide substituent acts as a three-electron donor. In addition, due to the linearity of the Ta-N-Si bond within these complexes the imido group may act as a four-electron donor as described earlier in structure (**VI**) [Chapter 2, figure 2.4, page 58]. Therefore, upon first inspection these complexes appear to behave as 18 electron complexes, as shown in figure 4.5.

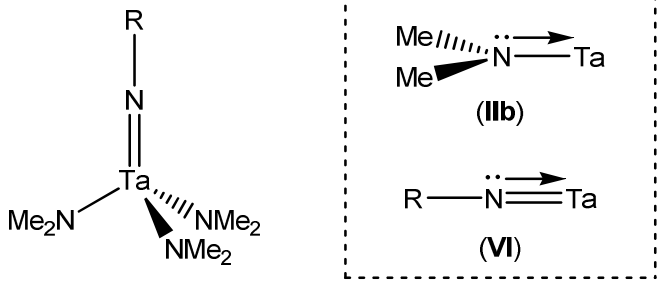

3 {NMe_2}	3 x $3e^-$
{RN}	$4e^-$
Ta	$5e^-$
Total	$18e^-$

Figure 4.5. Electron count for tantalum imido-containing complexes of the form $[(Me_2N)_3Ta(NR)]$. Complexes appear on first inspection to behave as 18 electron complexes.

For all four groups (3 x {NMe_2} amido groups and 1 x {NR} imido group) to bond to their full potential to the tantalum centre would require 9 orbitals on the metal to accept the electron donation (4 of σ-symmetry and 5 possessing π-symmetry). However, although the tantalum possesses 9 vacant frontier orbitals (1 x s-, 3 x p- and 5 x d-orbitals), the amount of π-donation to the metal atom is restricted by the number of d-orbitals of the tantalum that possess the correct symmetry to accept donation.

Within these tantalum complexes the nitrogen and carbon atoms of each {NMe_2} group are observed to occupy a plane with the nitrogen atom [N(1)] of the imido group. Consequently, this orientation of the {NMe_2} amide groups implies the π-donation is likely to be dominated by the {NR} imido group,[6] which may act as a four-electron donor as described in structure (**VI**).

However, within **31** the length of the Ta-N imido bond [Ta-N(1), 1.793 (5) Å] is observed to be comparatively long with respect to other Ta-N imido complexes (1.736 Å - 1.804 Å).[5] This may be indicative of the Ta-N imido bond possessing lower bond order. Therefore, rather than bonding to the tantalum in the manner depicted in structure (**VI**), the {Ph_3SiN} imido group may be bonded to the metal atom through a Ta-N double bond as depicted in structure (**V**) [Chapter 2, figure 2.4, page 58]. Consequently, the imido nitrogen atom [N(1)] is likely to act as only a two electron donor to the metal centre, which may be due in part to a mismatch in the energies of the nitrogen 2p and tantalum 5d orbitals. The imido nitrogen [N(1)] lone pair is instead likely to be involved in multiple bonding to the silicon atom as observed in the comparatively short Si-N bond [1.701 (6) Å]. In this instance the structure of **31** and the linearity of the {Ph_3SiN} imido bond may be influenced more by electrostatic and crystal packing effects.

4.3 Zinc complexes

The focus of this body of work has primarily been the formation of early transition metal nitrides and their use as diffusion barrier materials within integrated circuits. However, due to their diverse properties, metal nitride materials have been investigated for a variety of applications.[7, 8]

Zinc oxide, ZnO, has been reported to be a viable candidate for use in UV optoelectronic devices due to a large bandgap of 3.3 eV.[9] The fabrication of such devices, including light-emitting diodes (LEDs) and laser diodes (LDs), requires both n-type and p-type ZnO. However, the reproducible formation of reliable p-type ZnO has proven to be difficult.[9, 10] Recently, the formation of p-type ZnO by thermal oxidation of zinc nitride, Zn_3N_2, has attracted increasing interest.[9 - 12] In addition, the electrical and optical properties of Zn_3N_2 itself have been investigated to determine its potential use within optoelectronic devices.[9 – 11, 13, 14]

Typically, Zn_3N_2 thin films have been prepared using PVD techniques.[10 - 13] However, Maile and Fischer have reported the MOCVD of Zn_3N_2 using

ammonia and the zinc amide complex bis[bis(trimethylsilyl)amido]zinc, $Zn[N(SiMe_3)_2]_2$, as the precursors.[9]

The first zinc amide complex, $Zn(NEt_2)_2$, was first synthesised by Frankland in 1856. Since then the reaction of zinc complexes with secondary amines has been systematically investigated in greater detail.[15 - 17] In comparison, studies into the reaction of organozinc reagents with primary amines are far less extensive.[17, 18]

The direct reaction of the primary aminosilane $^{i}Pr_3SiNH_2$ and the commercially available organometallic reagents $ZnMe_2$ and $ZnEt_2$ with the subsequent elimination of alkane has been reported by Westerhausen *et*. *al*. [17] From these reactions the dimeric zinc amide complexes $[\{MeZn(\mu_2\text{-}NHSi^{i}Pr_3)\}_2]$ and $[\{EtZn(\mu_2\text{-}NHSi^{i}Pr_3)\}_2]$ have been isolated. Within these two complexes and other related zinc amide complexes, the degree of oligomerization is determined to be dependant on the steric demand of the substituents bonded to the zinc and nitrogen atoms.[17]

However, unlike within the comparable reactions with $Ti(NMe_2)_4$ and $Ta(NMe_2)_5$ described in Chapter 2 and this chapter respectively, further deprotonation of the amide and subsequent formation of zinc imido complexes is not observed even under forcing conditions (figure 4.5).[17 - 21]

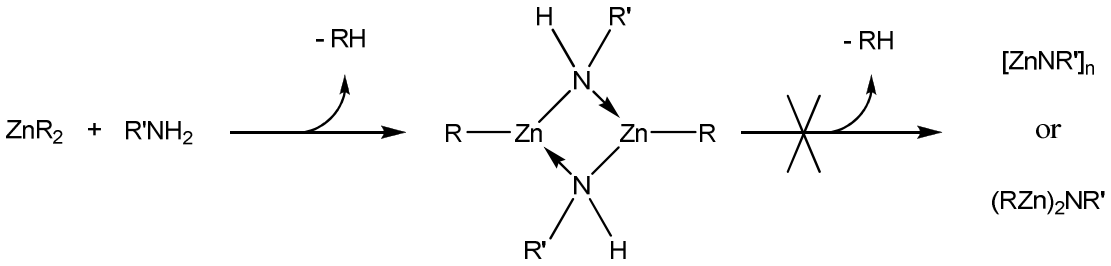

Figure 4.5: Schematic of the reaction of an organozinc reagent with a primary amine, resulting in the formation of a bridged amido species. Further reaction and subsequent formation of a zinc imido species is not observed.

Interestingly, within similar zincated primary phosphane and arsane complexes, $[\{RZn(\mu_2\text{-}EHR')\}_2]$ (E = P, As), the increased acidic nature of the

{E-H} moieties results in the self-condensation of the complex and subsequent formation of bridging phosphanediide and arsanediide species (figure 4.6).[20, 21]

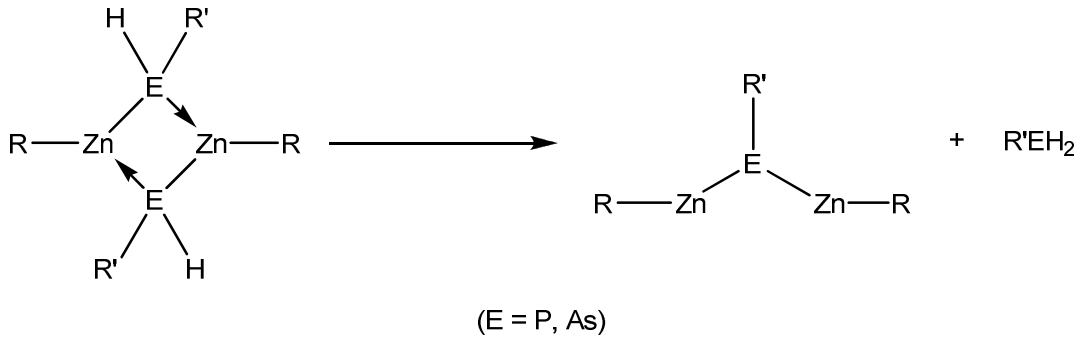

Figure 4.6: Schematic of self-condensation of zincated primary phosphane and arsane complexes.

As discussed earlier in this chapter, the reaction of $Ta(NMe_2)_5$ with **1** and **5** was attributed to the presence of electron-withdrawing groups bonded to the silicon atoms within the aminosilanes increasing the acidity of the {N-H} protons. Therefore the increased acidity of the {N-H} protons within **1** and **5** may promote the formation of imido species in their reaction with organozinc reagents.

To investigate this, a series of reactions were performed in which colourless hexane solutions of aminosilanes **1** and **5** were treated with a toluene solution of $ZnMe_2$ in a 1:1 ratio and gently refluxed. Within the reaction with **1** the formation of a white precipitate was observed as the reaction progressed, whilst the colourless reaction solution with **5** displayed no significant difference in appearance over the course of the reaction. After 24 hr all volatiles were removed *in vacuo*. From the subsequent residue from the reaction solution of **1** the zinc complex **33** has been isolated by recrystallisation at room temperature from a hexane solution, whilst from the residue from the reaction solution of **5** the zinc complex **34** was isolated by recrystallisation at -28 ^{o}C from a hexane solution. Subsequently, both **33** and **34** were isolated as colourless crystals.

Analysis of the ^{1}H NMR spectra of **33** and **34** show them to be comparable. Both spectra display expected resonances attributed to the substituents bonded to the silicon atoms ({Ph} and {NMe_2} for **33** and **34** respectively). Additionally both spectra show a single resonance [δ = - 0.31 ppm (**33**), δ = - 0.25 ppm (**34**)] that may be assigned to a methyl group bonded to the zinc atom. Furthermore, both spectra display a broad singlet peak [δ = 0.01 ppm (**33**), δ = 0.16 ppm (**34**)] that may be attributed to {NH} protons. Integration of these resonances show the {R_3Si}, {ZnMe} and {NH} moieties to be present in a 1:1:1 ratio. Consequently, these observations are consistent with the formation of a zinc amido species with the empirical formula [MeZn{$N(H)SiR_3$}] rather than a zinc imido species.

For both **33** and **34** crystals suitable for single crystal X-ray diffraction were isolated, with the structures obtained from these studies consistent with those predicted from observations made through analysis of the ^{1}H NMR spectra.

The zinc complex [{$MeZn(\mu_2\text{-}NHSiPh_3)\}_2$], **33**, is found to crystallise in the monoclinic space group (*Cc*), with two dimer molecules and one molecule of toluene occupying the asymmetric unit as shown in figure 4.7.

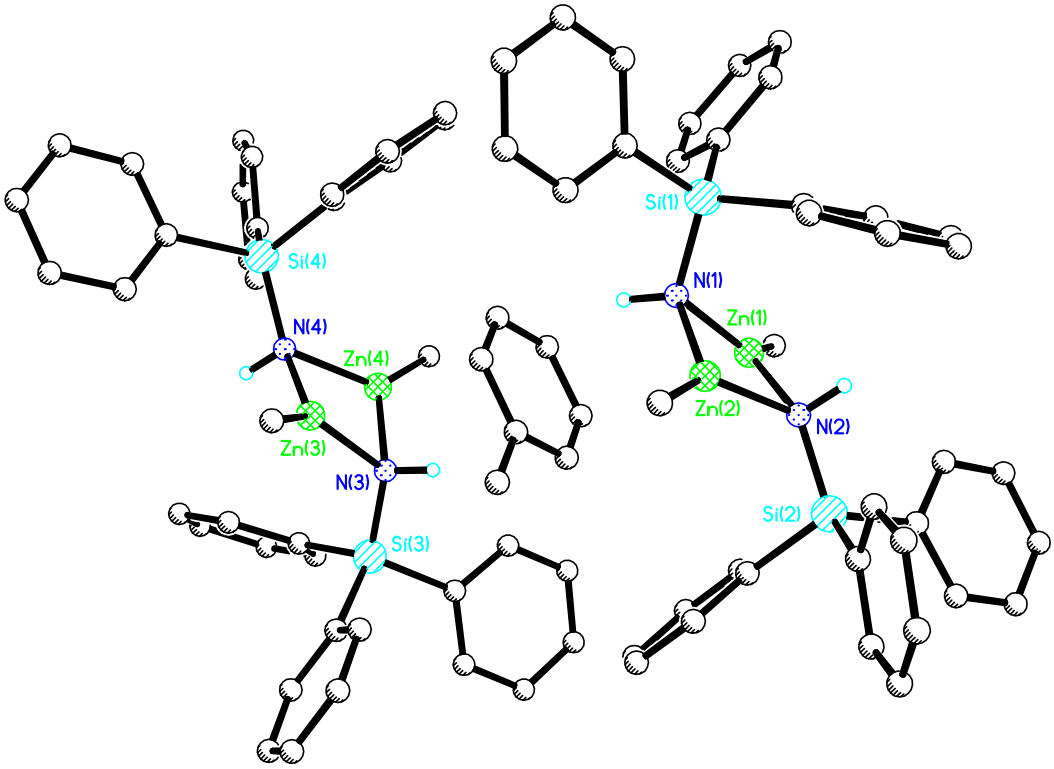

Figure 4.7 Asymmetric unit for the complex [{MeZn(μ_2-NHSiPh$_3$)}$_2$], **33**, containing two dimers and one molecule of toluene. Hydrogen atoms except for amido protons are omitted for clarity.

The molecular structure for molecule 1 containing Zn(1) and Zn(2) is shown in detail in figure 4.8, whilst the molecular structure for molecule 2 containing Zn(3) and Zn(4) is shown in detail in figure 4.9. Selected bond lengths and angles for both dimer molecules given in table 4.3.

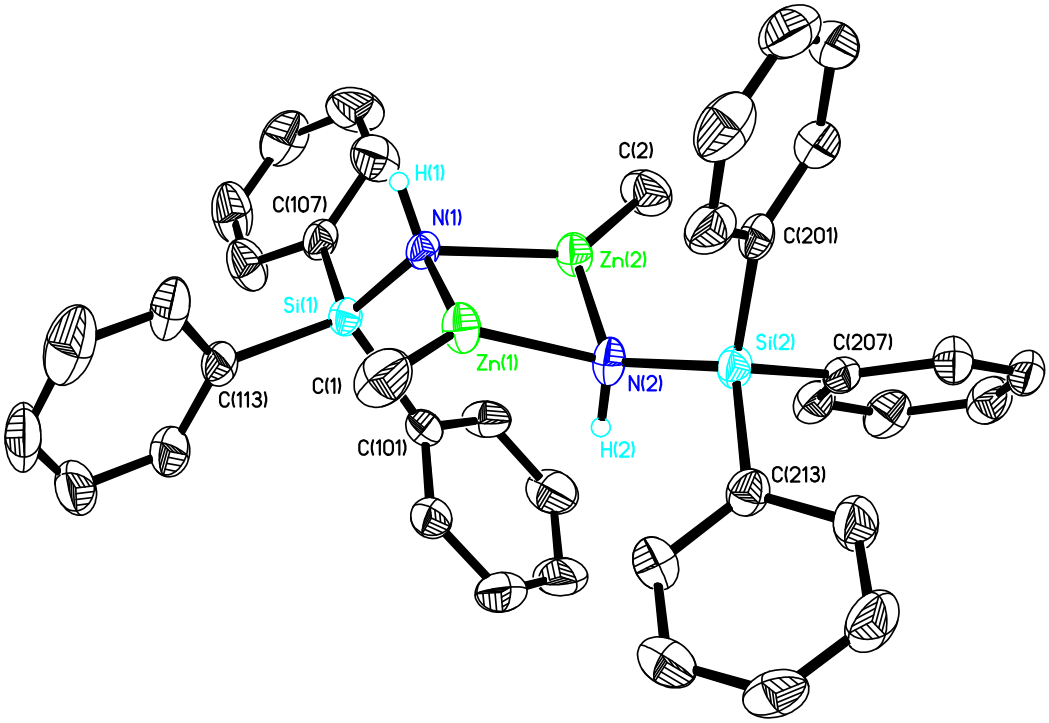

Figure 4.8 Molecular structure of molecule 1 of the complex [{MeZn(μ_2-NHSiPh$_3$)}$_2$], **33**. Thermal ellipsoids are shown at 50% probability. Hydrogen atoms except for {ZnNH} amide protons are omitted for clarity.

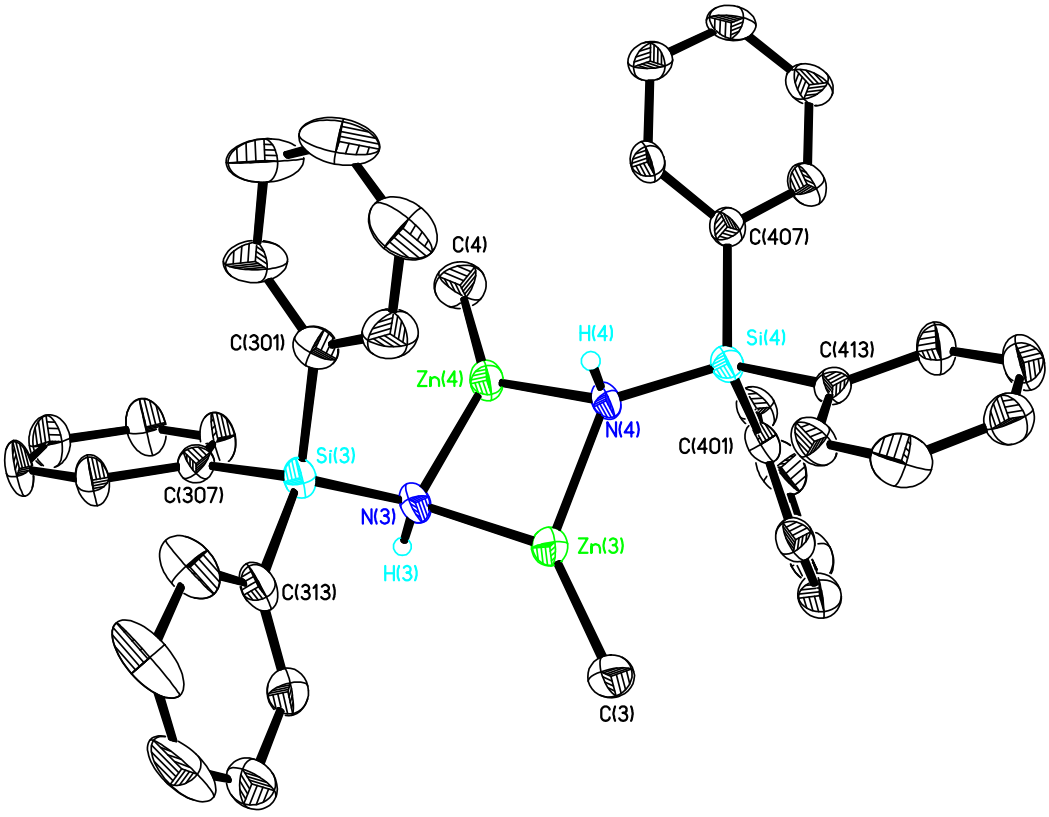

Figure 4.9 Molecular structure of molecule 2 of the complex [{MeZn(μ_2-NHSiPh$_3$)}$_2$], **33**. Thermal ellipsoids are shown at 50% probability. Hydrogen atoms except for {ZnNH} amide protons are omitted for clarity.

Table 4.3 Selected bond lengths (Á) and angles (^{o}) of the molecular structure of complex **33**. The positions of the {NH} protons [H(1), H(2), H(3) and H(4)] are modelled. Consequently, the bond lengths and angles associated with these atoms have no error values.

Molecule 1		Molecule 2	
Zn(1)-N(1)	2.015 (4)	Zn(3)-N(3)	2.024 (4)
Zn(1)-N(2)	2.048 (4)	Zn(3)-N(4)	2.039 (4)
Zn(2)-N(1)	2.036 (4)	Zn(4)-N(3)	2.029 (4)
Zn(2)-N(2)	2.037 (4)	Zn(4)-N(4)	2.046 (4)
Zn(1)-C(1)	1.935 (6)	Zn(3)-C(3)	1.942 (5)
Zn(2)-C(2)	1.939 (5)	Zn(4)-C(4)	1.953 (6)
Si(1)-N(1)	1.733 (4)	Si(3)-N(3)	1.728 (4)
Si(2)-N(2)	1.726 (4)	Si(4)-N(4)	1.725 (4)
N(1)-H(1)	0.9300	N(3)-H(3)	0.9300
N(2)-H(2)	0.9300	N(4)-H(4)	0.9300
Zn(1)-N(1)-Zn(2)	89.40 (15)	Zn(3)-N(3)-Zn(4)	88.81 (15)
Zn(1)-N(2)-Zn(2)	88.47 (16)	Zn(3)-N(4)-Zn(4)	87.94 (15)
N(1)-Zn(1)-N(2)	89.77 (16)	N(3)-Zn(3)-N(4)	89.81 (16)
N(1)-Zn(2)-N(2)	89.48 (15)	N(3)-Zn(4)-N(4)	89.48 (15)
N(1)-Zn(1)-C(1)	136.6 (2)	N(3)-Zn(3)-C(3)	137.3 (2)
N(2)-Zn(1)-C(1)	133.1 (2)	N(4)-Zn(3)-C(3)	132.9 (2)
N(1)-Zn(2)-C(2)	134.5 (2)	N(3)-Zn(4)-C(4)	137.1 (2)
N(2)-Zn(2)-C(2)	136.0 (2)	N(4)-Zn(4)-C(4)	133.4 (2)
Zn(1)-N(1)-Si(1)	115.97 (19)	Zn(3)-N(3)-Si(3)	124.1 (2)
Zn(2)-N(1)-Si(1)	112.71 (19)	Zn(4)-N(3)-Si(3)	114.9 (2)
Zn(1)-N(1)-H(1)	112.3	Zn(3)-N(3)-H(3)	109.1
Zn(2)-N(1)-H(1)	112.3	Zn(4)-N(3)-H(3)	109.1
Si(1)-N(1)-H(1)	112.3	Si(3)-N(3)-H(3)	109.1
Zn(1)-N(2)-Si(2)	125.8 (2)	Zn(3)-N(4)-Si(4)	129.4 (2)
Zn(2)-N(2)-Si(2)	123.0 (2)	Zn(4)-N(4)-Si(4)	120.8 (2)
Zn(1)-N(2)-H(2)	105.7	Zn(3)-N(4)-H(4)	105.3
Zn(2)-N(2)-H(2)	105.7	Zn(4)-N(4)-H(4)	105.3
Si(2)-N(2)-H(2)	105.7	Si(4)-N(4)-H(4)	105.3

The following discussion of the structure of **33** will focus on molecule 1 containing Zn(1) and Zn(2) as an example case, with bond lengths and angles in both molecule 1 and molecule 2 not too dissimilar.

Complex **33** is found to be isostructural to the zinc complex [{MeZn(μ_2-NHSi^{i}Pr$_3$)}$_2$] previously reported by Westerhausen *et*. *al*. [17] Within **33** the zinc atoms [Zn(1), Zn(2)] adopt a three-coordinate, *pseudo* trigonal planar geometry in which each zinc atom is bonded to a single methyl group [Zn(1)-C(1), Zn(2)-C(2)].

In addition the two zinc atoms are bridged by two {μ_2-NHSiPh$_3$} amide units [N(1), N(2)] to create a central {Zn_2N_2} four-membered ring which exhibits a slight distortion from planar [$\sum$ {Zn(1)-N(1)-Zn(2), Zn(1)-N(2)-Zn(2), N(1)-Zn(1)-N(2), N(1)-Zn(2)-N(2)} = 357.12^o (16)]. Analysis of the Zn-N bond lengths within the {Zn_2N_2} ring [Zn(1)-N(1), Zn(1)-N(2), Zn(2)-N(1), Zn(2)-N(2)] reveal them to be comparable to those reported for related {Zn_2N_2} containing systems in the Cambridge Crystallographic Database (1.997 Å - 2.109 Å).[5]

Due to the bridging nature of the {NHSiPh$_3$} amide unit [structure (**III**), Chapter 2, figure 2.2, page 57], the nitrogen atoms [N(1), N(2)] adopt a four-coordinate, *pseudo*-tetrahedral geometry. Subsequently, the {SiPh$_3$} units [Si(1), Si(2)] are observed in an *anti*- arrangement across the {Zn_2N_2} ring.

The zinc complex [{MeZn(μ_2-NHSi{NMe$_2$}$_3$)}$_2$], **34**, is found to crystallise in the monoclinic space group (*P2$_1$/c*), with one half of a dimer molecule occupying the asymmetric unit. Each dimer is situated on a crystallographic inversion centre. Consequently the second half of the molecule containing Zn(1) is generated by the symmetry operator (1-x, -y, -z). The molecular structure for **34** is shown in figure 4.10, with selected bond lengths and angles for this complex given in table 4.4.

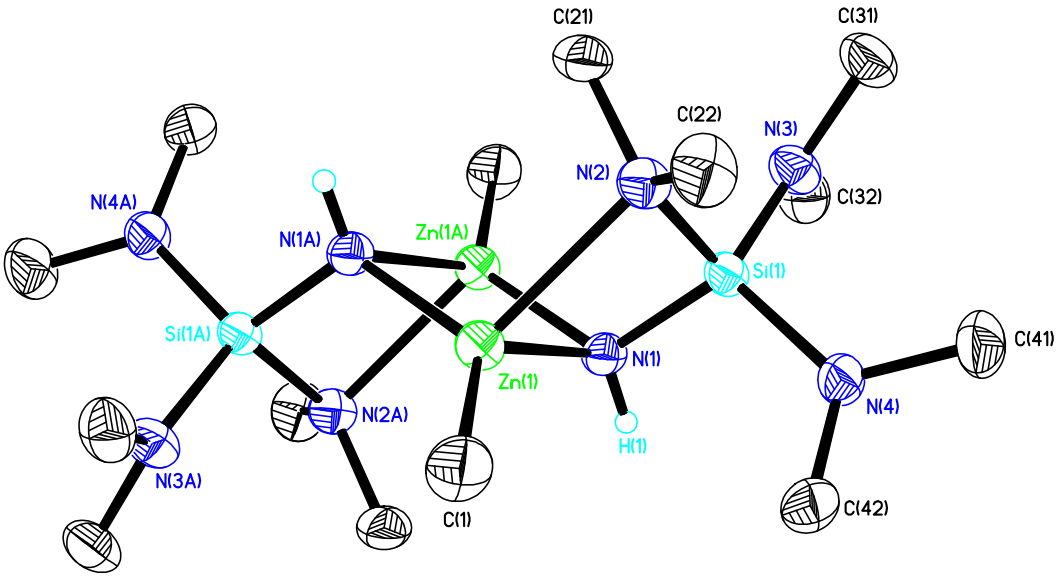

Figure 4.10 The molecular structure of the complex [MeZn{NHSi(NMe_2)$_3$}], (**34**). Thermal ellipsoids are shown at 50% probability. Hydrogen atoms except for {NH} amide protons are omitted for clarity.

Table 4.4 Selected bond lengths (Å) and angles (°) of the molecular structure of complex **34**.

Zn(1)-N(1)	2.1422 (14)	Zn(1)-N(1A)	2.0165 (13)
Zn(1)-N(2)	2.3377 (14)	Zn(1)-C(1)	1.9734 (18)
N(1)-H(1)	0.87 (3)	Si(1)-N(1)	1.7023 (14)
Si(1)-N(2)	1.7769 (15)	Si(1)-N(3)	1.7056 (14)
Si(1)-N(4)	1.7131 (14)		
Zn(1)-N(1)-Zn(1A)	89.35 (5)	N(1)-Zn(1)-N(1A)	90.65 (5)
N(1)-Zn(1)-C(1)	131.24 (7)	N(1A)-Zn(1)-C(1)	131.37 (7)
Zn(1A)-N(1)-Si(1)	121.21 (8)	N(1A)-Zn(1)-N(2)	103.02 (5)
N(1)-Zn(1)-N(2)	73.23 (5)	N(1)-Si(1)-N(2)	100.57 (7)
Zn(1)-N(1)-Si(1)	93.82 (6)	Zn(1)-N(2)-Si(1)	85.52 (5)
Si(1)-N(2)-C(21)	118.57 (12)	Si(1)-N(2)-C(22)	119.48 (12)
C(21)-N(2)-C(22)	110.25 (14)	Si(1)-N(3)-C(31)	123.51 (13)
Si(1)-N(3)-C(32)	122.61 (12)	C(31)-N(3)-C(32)	112.91 (15)
Si(1)-N(4)-C(41)	122.87 (13)	Si(1)-N(4)-C(42)	123.94 (12)
C(41)-N(4)-C(42)	111.33 (15)		

Complex **34** possesses several structural features comparable to those observed within **33** and the zinc complex [{MeZn(μ_2-NHSi^{i}Pr$_3$)}$_2$].[17] These include a central, planar {Zn_2N_2} ring [Zn(1), Zn(1A), N(1), N(1A)], in which the nitrogen atoms [N(1), N(1A)] of the bridging {NHSi(NMe_2)$_3$} amide units adopt a four-coordinate, *pseudo*-tetrahedral geometry. In addition the {Si(NMe_2)$_3$} units [Si(1), Si(1A)] are observed in an *anti*- arrangement across the {Zn_2N_2} ring. However, the overall structure of **34** is significantly different to that observed for **33** and [{MeZn(μ_2-NHSi^{i}Pr$_3$)}$_2$].

Within **34** the zinc atoms adopt a four-coordinate, *pseudo*-tetrahedral geometry, with each zinc atom bonded to a methyl group [C(1)] and the two nitrogen atoms of the bridging {NHSi(NMe_2)$_3$} amide units [N(1), N(1A)] in a similar manner to within **33**. Furthermore, the zinc atoms within **34** are both bonded to a nitrogen atom belonging to a silicon-bound {NMe_2} group [Zn(1)-N(2), Zn(1A)-N(2A)]. This nitrogen atom is bonded to the zinc centre through a dative bond involving the nitrogen lone pair in a similar manner to the intramolecular donation observed within the zirconium and hafnium complexes **17** and **18** described in Chapter 2. Consequently, the geometry of the {NMe_2} nitrogen atom [N(2)] is significantly distorted from a planar arrangement [∑ {Si(1)-N(2)-C(21), Si(1)-N(2)-C(22), C(21)-N(2)-C(22)} = 348.30^o (14)] in comparison to the nitrogen atoms of the two remaining {NMe_2} groups bonded to the silicon atom [N(3), N(4); ∑ {Si(1)-N(3)-C(31), Si(1)-N(3)-C(32), C(31)-N(3)-C(32)} = 359.03^o (15); ∑ {Si(1)-N(4)-C(41), Si(1)-N(4)-C(42), C(41)-N(4)-C(42)} = 358.14^o (15)].

The formation of the Zn-N_{amino} bonds within the **34** [Zn(1)-N(2), Zn(1A)-N(2A)] also results in the subsequent creation of two additional {ZnN_2Si} four-membered rings [{Zn(1), N(1), Si(1), N(2)}, {Zn(1A), N(1A), Si(1A), N(2A)}] which exhibit a distortion from a planar geometry [∑ {Zn(1)-N(1)-Si(1), Zn(1)-N(2)-Si(1), N(1)-Zn(1)-N(2), N(1)-Si(1)-N(2)} = 353.14^o (7)].

The {ZnN_2Si} four-membered rings both share a common edge with the central {Zn_2N_2} ring [Zn(1)-N(1), Zn(1A)-N(1A)]. In addition to the *pseudo*-tetrahedral geometry adopted by the zinc and nitrogen atoms within the

{Zn_2N_2} ring, this structural feature results in the formation of a puckered ladder-like structure within the molecule.

4.4 Manganese complexes

Manganese nitride materials are of increasing interest due to their unique magnetic properties. Such materials have been investigated for their potential use in a number of applications, including spintronics and within electronic memory devices. However, to our knowledge, manganese nitride has only been reported to have been deposited using PVD techniques.[22 - 26]

Manganese(II) amides may potentially act as CVD precursors for the deposition of manganese nitride materials. Most structurally characterised Mn(II) amido complexes contain secondary-amido ligands and have typically been prepared by the reaction of a manganese halide complex and the relevant lithium amide.[27 - 29] However, as observed previously in this chapter for zinc amides, relatively few Mn(II) amido complexes containing primary-amido ligands are known.[30]

Wright and coworkers have reported the preparation of several Mn(II) primary-amido complexes by the direct reactions of several heterocyclic primary amines and the commercially available organometallic reagent manganocene [Cp_2Mn, $(C_5H_5)_2Mn$] as shown below in figure 4.11. These complexes have been investigated for their potential as molecular magnets.[30 - 33]

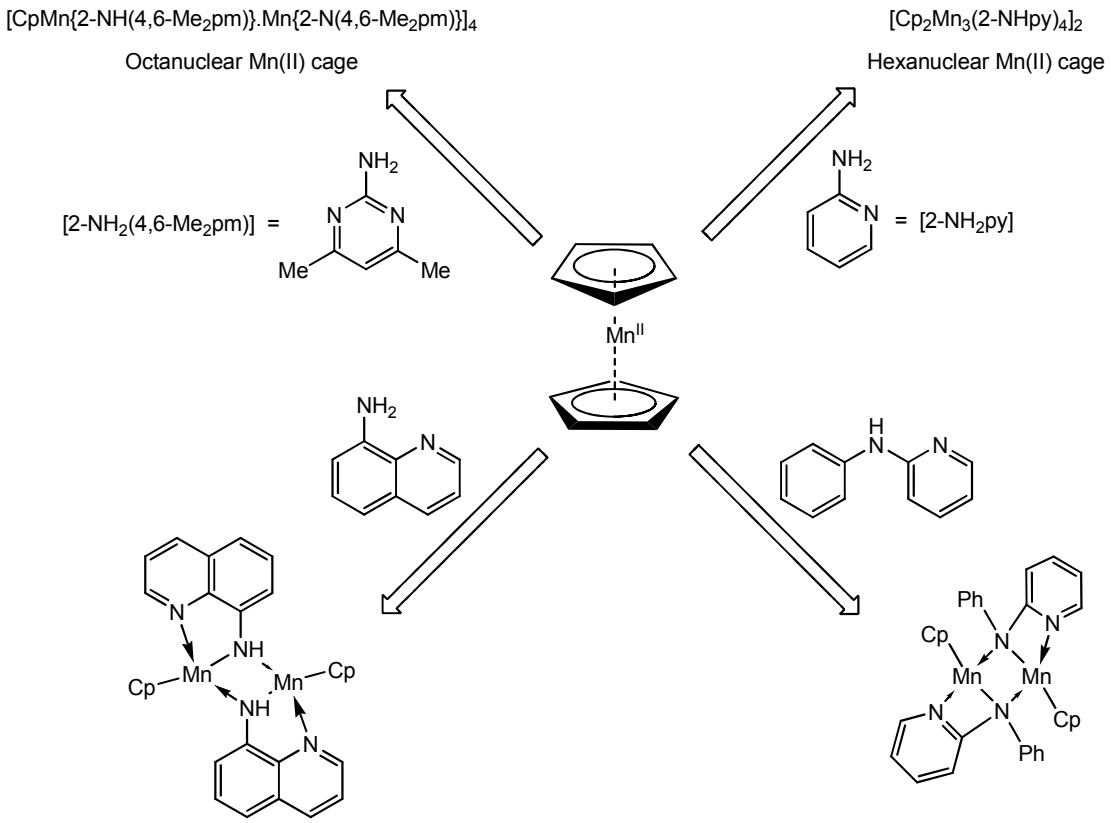

Figure 4.11: Manganese(II) primary-amido complexes prepared from the organometallic reagent manganocene, Cp_2Mn.

In these reactions substitution of the cyclopentadienyl ($C_5H_5^-$, Cp) ligands and formation of an oligomeric species is observed. However, the nature of the oligomeric species formed is dependant on the acidity of the amino protons within the amine. In particular, double deprotonation of the amine and subsequent formation of mixed amido-imdo complexes is observed for relatively acidic 2-aminopyrimidine based ligands.[30] In contrast, only single deprotonation and the formation of an amido complex is observed for less acidic 2-aminopyridines and 8-aminoquinoline under similar conditions.[30, 31]

Typically, relatively little information may be gained from the ^{1}H NMR spectra of the complexes reported by Wright *et*. *al*. due to the paramagnetic nature of the manganese atoms. However, variable-temperature magnetic susceptibility studies have been performed using these complexes to investigate the potential as molecular magnets. The data obtained from these magnetic studies show the occurrence of antiferromagnetic interactions between neighbouring Mn(II) atoms. Consequently, the magnitudes of the observed

interactions are found to be dependent on the geometry and covalency of the {Mn-N-Mn} bridging units.[31]

Therefore, in order to investigate the structure and potential magnetic susceptibility of Mn(II) amido complexes prepared using aminosilanes, a colourless hexane solution of **1** was treated with a hexane solution of $(MeCp)_2Mn$ in a 1:1 ratio and gently refluxed. Due to solvachromic effects, the reaction solution was observed to be either orange or green in appearance depending on the angle of observation. After 24 hr the manganese complex **35** was isolated as brown crystals by crystallisation at -28 ^oC from the reaction solution.

Unfortunately, due to the paramagnetic nature of **35** and its high sensitivity to air, characterisation by spectroscopic and analytical techniques has proven to be difficult. However, crystals of **35** suitable for single crystal X-ray diffraction were isolated.

The manganese complex $[\{(MeCp)Mn(\mu_2\text{-}NHSiPh_3)\}_2]$, **35**, is found to crystallise in the triclinic space group (*P-1*), with a dimeric molecule occupying the asymmetric unit as shown in figure 4.12. The molecular structure for **35** is shown in greater detail in figure 4.13, with selected bond lengths and angles for this complex given in table 4.5.

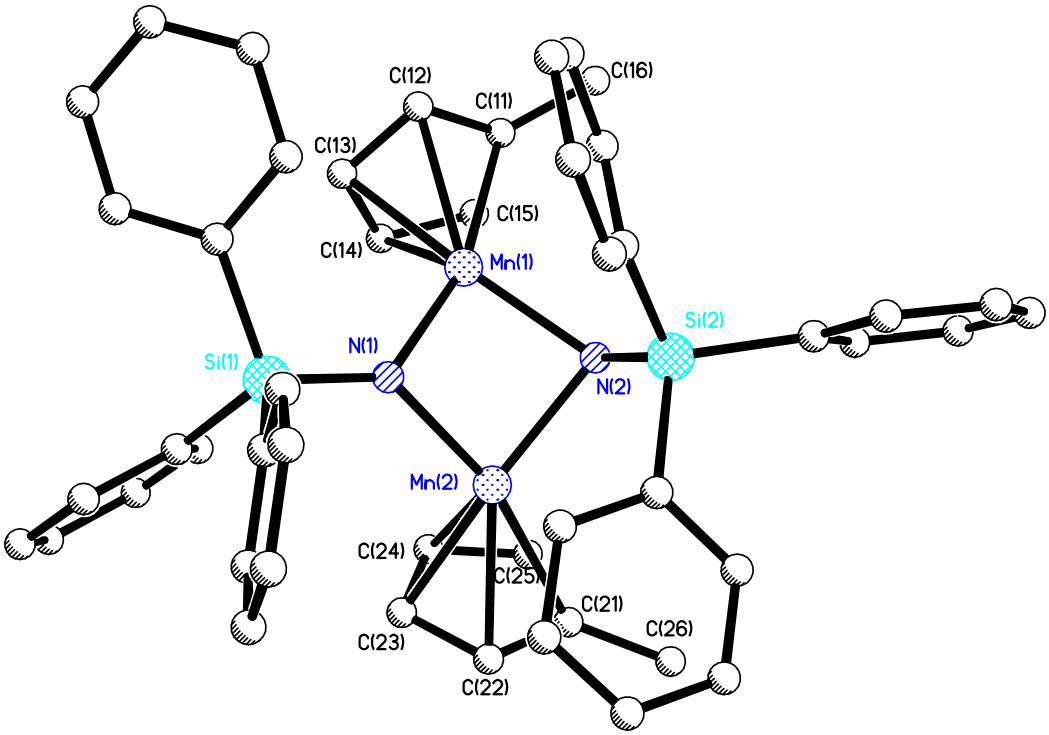

Figure 4.12: Asymmetric unit of the complex [(MeCp)Mn(NHSiPh$_3$)], (**35**). Hydrogen atoms are omitted for clarity.

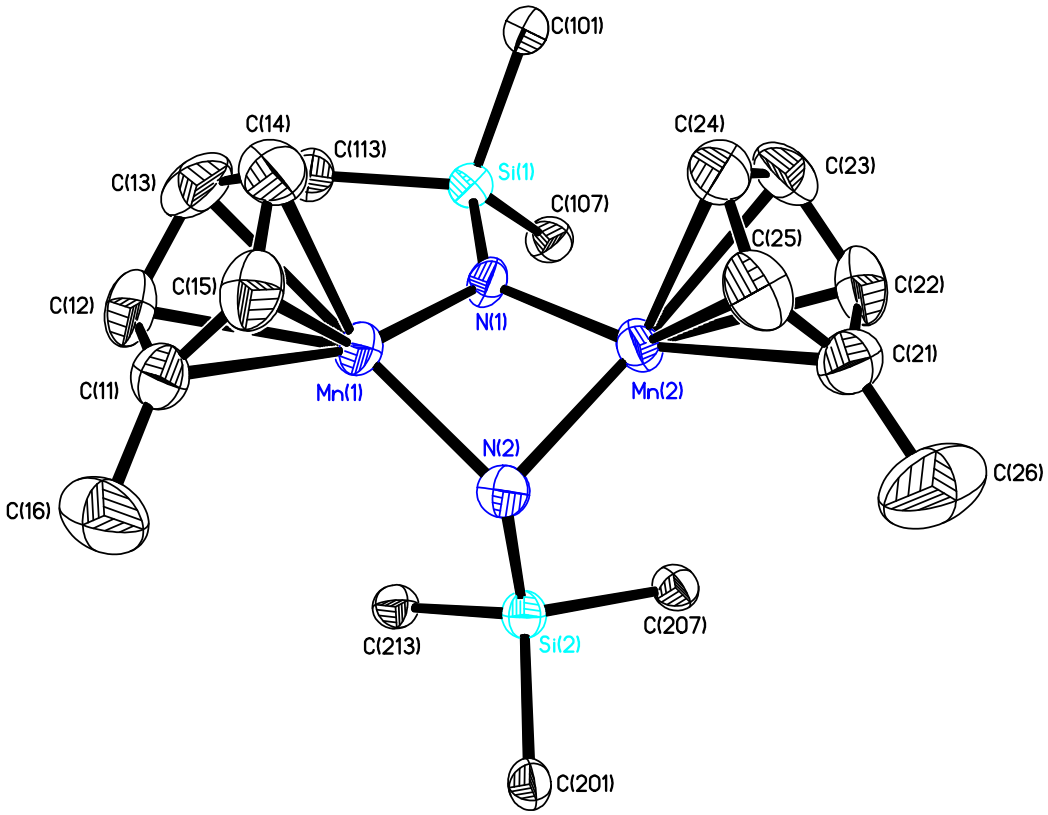

Figure 4.13. The molecular structure of the complex [(MeCp)Mn(NHSiPh$_3$)], (**35**). Thermal ellipsoids are shown at 50% probability. Hydrogen atoms are omitted and only *ipso*- carbon atoms displayed for the phenyl groups for clarity.

Table 4.5. Selected bond lengths (Á) and angles (°) of the molecular structure of complex **35**.

Mn(1)-N(1)	2.0989 (17)	Mn(1)-N(2)	2.1254 (18)
Mn(2)-N(1)	2.1148 (17)	Mn(2)-N(2)	2.1666 (18)
Si(1)-N(1)	1.6707 (17)	Si(2)-N(2)	1.7250 (19)
Si(1)-C(101)	1.871 (2)	Si(1)-C(107)	1.879 (2)
Si(1)-C(113)	1.879 (2)	Si(2)-C(201)	1.871 (2)
Si(2)-C(207)	1.891 (2)	Si(1)-C(213)	1.876 (2)
Mn(1)-C(11)	2.457 (2)	Mn(1)-C(12)	2.373 (2)
Mn(1)-C(13)	2.356 (3)	Mn(1)-C(14)	2.399 (3)
Mn(1)-C(15)	2.452 (2)	Mn(2)-C(21)	2.508 (3)
Mn(2)-C(22)	2.372 (3)	Mn(2)-C(23)	2.332 (3)
Mn(2)-C(24)	2.408 (3)	Mn(2)-C(25)	2.514 (3)
N(2)-H(2)	1.01 (4)		
N(1)-Mn(1)-N(2)	86.07 (7)	N(1)- Mn(2)-N(2)	84.64 (7)
Mn(1)-N(1)-Mn(2)	87.91 (6)	Mn(1)-N(2)-Mn(2)	85.90 (7)
Mn(1)-N(1)-Si(1)	132.08 (9)	Mn(1)-N(2)-Si(2)	120.34 (10)
Mn(2)-N(1)-Si(1)	136.36 (10)	Mn(2)-N(2)-Si(2)	105.44 (9)
Mn(1)-N(2)-H(2)	114 (2)	Mn(2)-N(2)-H(2)	117 (2)
Si(2)-N(2)-H(2)	112 (2)		

Within the molecular structure of **35** the manganese atoms [Mn(1), Mn(2)] adopt a geometry with a nominal coordination number of three. Each manganese atom is bonded to a single {MeCp} group, with the Mn-C_{Cp} bond lengths observed [Mn(1)-C(11) to Mn(1)-C(15) inclusive and Mn(2)-C(21) to Mn(2)-C(25) inclusive; range 2.332 (3) – 2.508 (3) Á] within a range typical of high spin Mn(II) Cp complexes [2.33 – 2.65 Á].[30] The Mn-C_{Cp} bond lengths observed also suggest the {MeCp} group adopts an η^5-bonding mode. However, the hapticity of {Cp} rings within high-spin manganocene derivatives is known to be highly flexible and may be significantly affected by crystal-packing effects.[31]

In addition, the two manganese atoms are bridged by two {μ_2-$NHSiPh_3$} amide units [N(1), N(2)] to create a central {Mn_2N_2} four-membered ring, which exhibits a significant distortion from planar [∑ {Mn(1)-N(1)-Mn(2), Mn(1)-N(2)-Mn(2), N(1)-Mn(1)-N(2), N(1)-Mn(2)-N(2)} = 344.52^o (7)]. Similar {Mn_2N_2} rings have been observed within related manganese(II) amide complexes, including those reported by Wright *et*. *al*. [27 - 31]

Due to the bridging nature of the amide groups, the nitrogen atoms exist in a four-coordinate geometry, Subsequently, the amide unit containing [N(2)] adopts a *pseudo*-tetrahedral geometry as anticipated, with the {$SiPh_3$} moiety observed in an *anti*- arrangement to both {MeCp} groups across the {Mn_2N_2} ring. However, within the second amide unit the atoms [N(1), Mn(1), Mn(2) and Si(1)] are observed in near-planar arrangement [∑ {Mn(1)-N(1)-Mn(2), Mn(1)-N(1)-Si(1), Mn(2)-N(1)-Si(1)} = 356.35^o (10)].

Consequently, due to the ‘planar’ nature of the amido group and the presence of the two manganese atoms, it was not possible to find the proton bonded to the ‘planar’ amido nitrogen atom [N(1)] within the electron density difference map. Although two amide protons [{N-H}; N(1), N(2)] are included in the unit cell contents [$C_{48}H_{46}Mn_2N_2Si_2$], only the proton bonded to the pyramidal amido nitrogen atom [N(2)] could be observed.

Interestingly, the bridging amido groups within structurally related manganese(II) complexes typically adopt a *pseudo*-tetrahedral geometry comparable to that observed for the amido nitrogen atom [N(2)].[30, 31] Therefore, the geometry of the ‘planar’ amido nitrogen atom [N(1)] within the molecular structure **35** may instead be defined by steric and crystal packing effects, with the methyl substituents of the {MeCp} groups orientated away from the ‘planar’ amido group [N(1)] to minimize unfavourable steric interactions.

Unfortunately, attempts to determine the magnetic moment of **35** were unsuccessful. It is feasible to assume that the magnetic susceptibility of **35** is

comparable to the dimeric manganese(II) complexes reported by Wright *et*. *al*. due to similarities within the respective molecular structures.[30, 31] However, the magnitude of any magnetic exchange interactions within **35** may potentially be affected by the observed distortion from planar of the $\{Mn_2N_2\}$ ring.[31]

4.5 Summary for Chapter 4

Transition metal nitride materials are of interest for a variety of applications due to their diverse properties.[7, 8] Therefore, as part of a wider study into their chemistry, the reactions of aminosilanes **1** [Ph_3SiNH_2], **3** [Et_3SiNH_2], **4** [$^tBuMe_2SiNH_2$] and **5** [$(Me_2N)_3SiNH_2$] with tantalum, zinc and manganese organometallic reagents have been investigated. Subsequently several transition metal complexes have successfully been prepared from the direct reaction of aminosilane and organometallic reagent in a 1:1 ratio.

The reactions of aminosilanes **1** and **5** with the tantalum organometallic reagent pentakis(dimethylamido)tantalum [$Ta(NMe_2)_5$, PDMAT] afford the terminal imido species of the form $[(Me_2N)_3TaNSiR_3]$ (**31** and **32** respectively). However, no reaction is observed for the analogous reactions of aminosilanes **3** and **4**. This may be attributed to the presence of electron-withdrawing groups bonded to the silicon atoms within **1** and **5** increasing the acidity of the amino {NH} protons. Therefore the reactivity of the aminosilanes appears dependant on the substituents bonded to the silicon.

Complexes **31** and **32** are found to be isostructural with the tantalum complex $[(Me_2N)_3TaN^tBu]$, which has previously been investigated as a single-source precursor for the deposition of TaN films.[1, 3, 4]

The reactions of aminosilanes **1** and **5** with dimethylzinc, $ZnMe_2$, afford dimeric zinc amido species (**33** and **34** respectively), rather than a zinc imido species. Complex **33** is found to be isostructural with the known complex $[\{MeZn(NHSi^iPr_3)\}_2]$. In addition, complex **34** exhibits intramolecular donation between a silicon-bonded $\{NMe_2\}$ group and a zinc atom, affording a four-

membered {MN_2Si} ring comparable to that observed within the zirconium and hafnium complexes **17** and **18** reported within Chapter 2.

The reaction of **1** with the manganese(II) reagent $(MeCp)_2Mn$ has been performed. Unfortunately, due to its paramagnetic nature and high sensitivity to air, characterisation of the reaction product has proven to be difficult. However, a dimeric bridged amido structure found by single crystal X-ray diffraction is consistent with the structures reported by Wright *et*. *al*. for several related manganese(II) amido species.[30, 31]

The reactions and compounds presented in this chapter are shown below in figure 4.14.

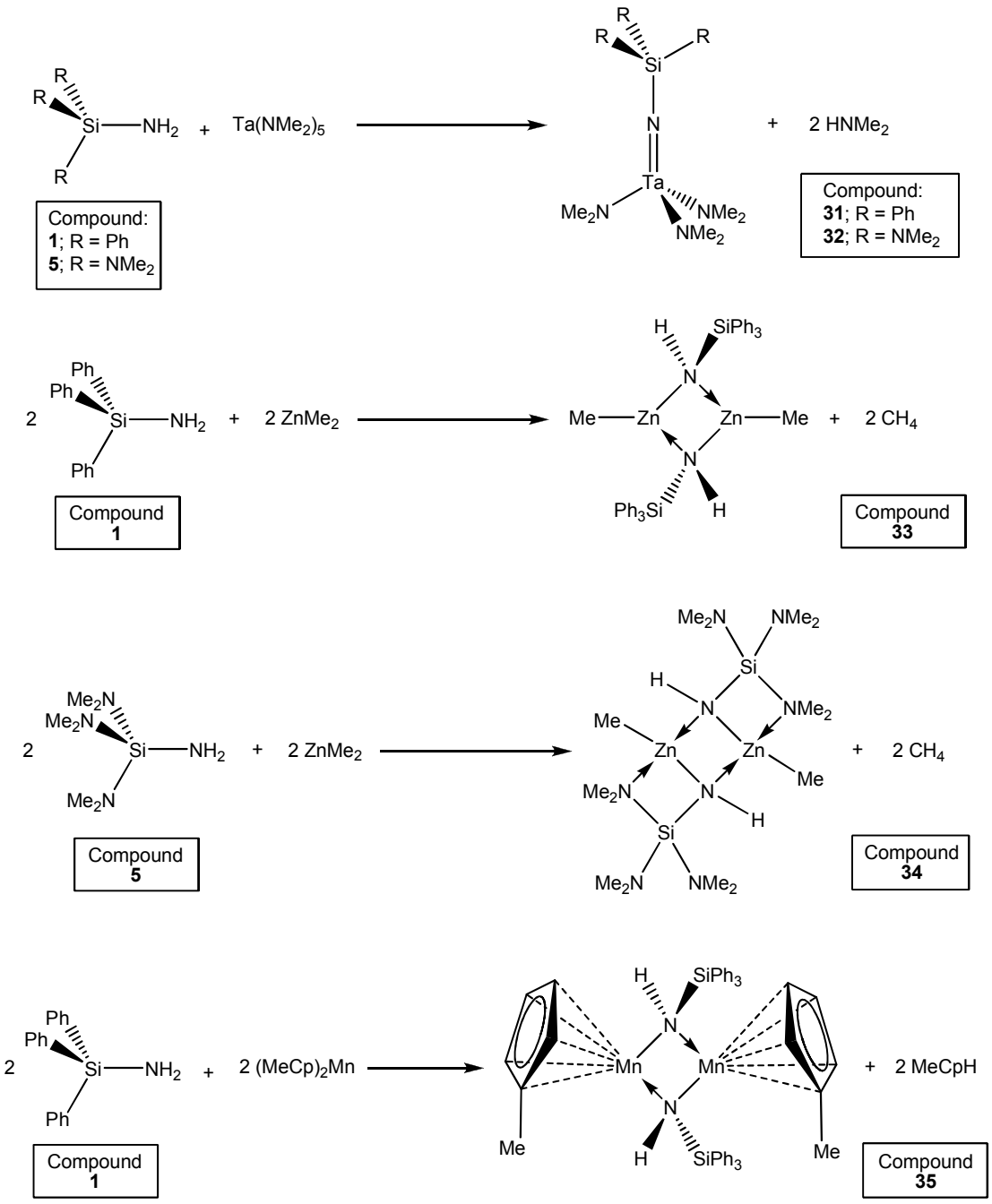

Figure 4.14: Reactions and compounds presented within Chapter 4.

4.6 References for Chapter 4

1. C. H. Winter, *Aldrichim. Acta*, 2000, **33**, 3.
2. C. P. Schaller and P. T. Wolczanski, *Inorg. Chem.*, 1993, **32**, 131.
3. W. A. Nugent and R. L. Harlow, *J. Chem. Soc. Chem. Comm.*, 1978, 579.

4. A. Baunemann, *"Precursor Chemistry of Tantalum and Niobium Nitride for MOCVD and ALD Applications"*, **2006**, Dissertation, Ruhr-Universität Bochum.
5. F. H. Allen and O. Kennard, *Chemical Design Automation News*, 1993, **8**, 31.
6. V. C. Gibson, *J. Chem. Soc. Dalton Trans.*, 1994, 1607.
7. A. C. Jones and M. L. Hitchman, *"Chemical Vapour Deposition; Precursors, Processes and Applications"*, **2009**, RSC Publishing, Cambridge, UK.
8. S. T. Oyama, *"The Chemistry of Transition Metal Carbides and Nitrides"*, **1996**, Chapman and Hall, London, UK.
9. E. Maile and R. A. Fischer, *Chem. Vapor Depos.*, 2005, **11**, 409.
10. T. Yang, Z. Zhang, Y. Li, M. Lv, S. Song, Z. Wu, J. Yan and S. Han, *Appl. Surf. Sci.*, 2009, **255**, 3544.
11. P. Voulgaropoulou, S. Dounis, V. Kambilafka, M. Androulidaki, M. Ružinský, M. Šály, P. Prokein, Z. Viskadourakis, K. Tsagaraki and E. Aperathitis, *Thin Solid films*, 2008, **516**, 8170.
12. V. Kambilafka, P. Voulgaropoulou, S. Dounis, E. Iliopoulos, M. Androulidaki, K. Tsagaraki, V. Šály, M. Ružinský, P. Prokein and E. Aperathitis, *Thin Solid films*, 2007, **515**, 8573.
13. W. Du, F. Zong, H. Ma, J. Ma, M. Zhang, X. Feng, H. Li, Z. Zhang and P. Zhao, *Cryst. Res. Technol*., 2006, **41**, 889.
14. T. Suda and K. Kakishita, *J. Appl. Phys.*, 2006, **99**, 076101.
15. M. F. Lappert, P. P. Power, A. R. Sanger and R. C. Srivastava, *"Metal and Metalloid Amides; syntheses, structures, and physical and chemical properties"*, **1980**, Ellis Horwood Ltd., Chichester, UK.
16. M. Lappert, A. Protchenko, P. Power and A. Seeber, *"Metal Amide Chemistry"*, **2009**, John Wiley & Sons, Ltd., Chichester, UK.
17. M. Westerhausen, T. Bollwein, A. Pfitzner, T. Nilges and H-J. Deiseroth, *Inorg. Chim. Acta*, 2001, **312**, 239.
18. M. M. Olmstead, W. J. Grigsby, D. R. Chacon, T. Hascall and P. P. Power, *Inorg. Chim. Acta*, 1996, **251**, 273.
19. M. G. Davidson, D. Elilio, S. L. Less, A. Martin, P. R. Raithby, R. Snaith and D. S. Wright, *Organometallics*, 1993, **12**, 1.

20. M. Westerhausen, M. Wieneke and W. Schwarz, *J. Organomet. Chem.*, 1999, **572**, 249.
21. M. Westerhausen, T. Bollwein, N. Makropoulos and H. Piotrowski, *Inorg. Chem.*, 2005, **44**, 6439.
22. E. Céspedes, E. Román, Y. Huttel, J. Chaboy, J. García-López, A. de Andrés and C. Prieto, *J. Appl. Phys.*, 2009, **106**, 043912.
23. H. Yang, H. Al-Brithen, A. R. Smith, J. A. Borchers, R. L. Cappelletti and M. D. Vaudin, *Appl. Phys. Lett.*, 2001, **78**, 3860.
24. B. Lu, X. Liu, K. Nakatsuji, T. Iimori and F. Komori, *Phys. Rev. B*, 2007, **76**, 245433.
25. H. Yang, H. Al-Brithen, E. Trifan, D. C. Ingram and A. R. Smith, *J. Appl. Phys.*, 2002, **91**, 1053.
26. W. J. Feng. N. K. Sun, J. Du, Q. Zhang, X. G. Liu, Y. F. Deng and Z. D. Zhang, *Solid State Commun.*, 2008, **148**, 199.
27. B. D. Murray and P. P. Power, *Inorg. Chem.*, 1984, **23**, 4584.
28. J. Chai, H. Zhu, Q. Ma, H. W. Roesky, H-G. Schmidt and M. Noltemeyer, *Eur. J. Inorg. Chem.*, 2004, 4807.
29. A. Belforte, F. Calderazzo, U. Englert, J. Strähle and K. Wurst, *J. Chem. Soc. Dalton Trans.*, 1991, 2419.
30. C. S. Alvarez, A. Bashall, A. D. Bond, D. Cave, E. A. Harron, R. A. Layfield, M. E. G. Mosquera, M. McPartlin, J. M. Rawson, P. T. Wood and D. S. Wright, *Dalton Trans.*, 2003, 3002.
31. C. S. Alvarez, S. R. Boss, J. C. Burley, S. M. Humphry, R. A. Layfield, R. A. Kowenicki, M. McPartlin, J. M. Rawson, A. E. H. Wheatley, P. T. Wood and D. S. Wright, *Dalton Trans.*, 2004, 3481.
32. C. S. Alvarez, A. D. Bond, D. Cave, M. E. G. Mosquera, E. A. Harron, R. A. Layfield, M. McPartlin, J. M. Rawson, P. T. Wood and D. S. Wright, *Chem. Commun.*, 2002, 2980.
33. C. S. Alvarez, A. D. Bond, E. A. Harron, R. A. Layfield, J. A. McAllister, C. M. Pask, J. M. Rawson and D. S. Wright, *Organometallics*, 2001, **20**, 4135.

Chapter 5

CVD of thin films using Group 4 and tantalum organometallic precursors

5.1 Introduction

As discussed in Chapter 1, ternary metal nitride thin films, including TiNSi and TaNSi thin films, have been used as diffusion barrier materials in integrated circuits. However, at present, efficient single-source CVD precursors for the deposition of these materials are unknown. Therefore, the Group 4 and tantalum metal complexes described in Chapters 2, 3 and 4 have been investigated for their potential as single-source CVD precursors for the deposition of MNSi thin films.

5.2 Thermal profiling

As discussed in Chapter 1, for a compound to potentially be used as a precursor for the CVD of thin films there are several properties it ideally has to possess. These include stability at relatively low temperatures to enable volatilisation and reduce premature decomposition of the precursor in the vapour phase, whilst decomposing at a temperature that is high enough to ensure complete decomposition but that is not detrimental to the substrate. In addition, decomposition of the precursor should ideally occur via a clean decomposition pathway in order to minimize contamination of the deposited film. Therefore, studying the thermal profile of a compound is essential to ensure the efficient deposition of thin films when using it as a CVD precursor.

One technique for studying the thermal profile of a compound is thermogravimetric analysis (TGA). TGA involves measuring the change in the mass of a sample as the sample is heated.[1, 2] Consequently the thermal stability of the compound may be observed, with the sample displaying a constant mass as it is heated (M_i, figure 5.1) until decomposition and subsequent loss of mass occurs. This will continue until a second plateau indicating a constant mass is observed, corresponding to the mass of the residue (M_f). Depending on the mechanism by which decomposition occurs, several of these constant mass plateaus may be observed.

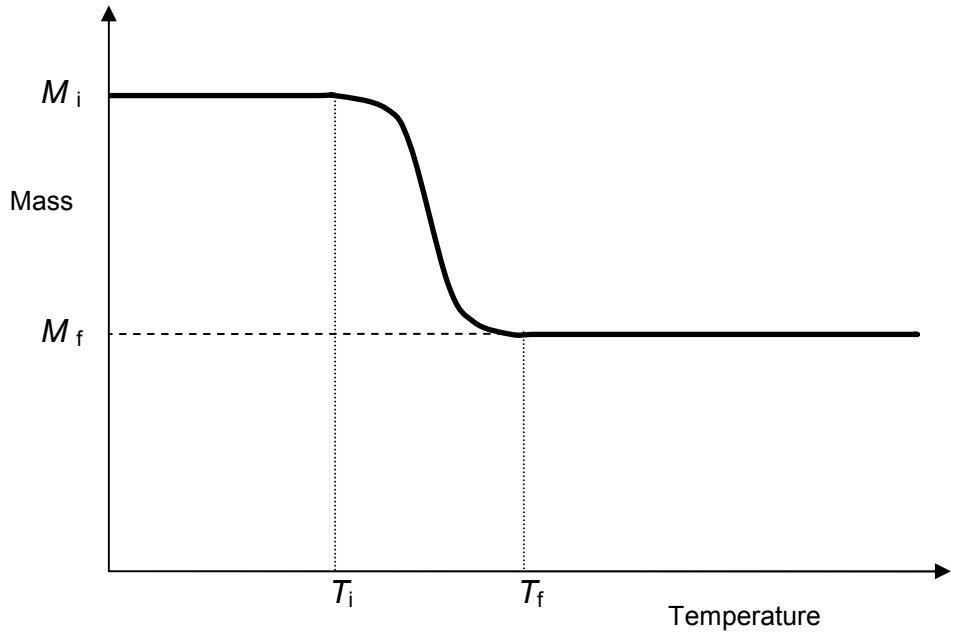

Figure 5.1: Schematic of a TGA graph, showing the change in mass of the sample (M_i to M_f) as the temperature is increased.

The sample may be heated at a constant temperature with the change in mass measured as a function of time. Alternatively, under dynamic heating conditions the change in mass is measured as a function of temperature. Under these conditions decomposition will not occur until the temperature T_i is reached, with decomposition occurring between T_i and T_f. This range of temperatures over which decomposition occurs (T_i to T_f) may be dependent on several factors including the nature of the sample, the atmosphere above the sample and the rate at which heating occurs.[1]

Above T_f the mass may remain constant, corresponding to the formation of a stable decomposition product. Consequently, the change in mass observed, ΔM, may be used to study the compositional change of the sample, with M_f indicating the mass of the decomposition product. In addition, the thermal stability of the compound and the temperatures over which decomposition occurs may be determined, although this data is appropriate only to the specific conditions under which the TGA is performed.[1]

The Group 4 and tantalum metal complexes previously described in Chapters 2 (complexes **6** – **18**), 3 (**25**, **26**, **28** and **29**) and 4 (**31** and **32**), shown below

in table 5.1, have been studied under dynamic TGA conditions. The TGA curve for **30** was not obtained due to the potentially low purity of the sample as discussed in Chapter 3. Analysis of the complexes was performed at SAFC Hitech, Bromborough, UK, using a Shimadzu TGA-51 Thermogravimetric Analyzer with the parameters detailed below in table 5.2. Data points were collected every second.

Table 5.1: Compounds analysed by TGA.

<table>
<tr><th colspan="4">Chapter 2 compounds</th></tr>
<tr><td> 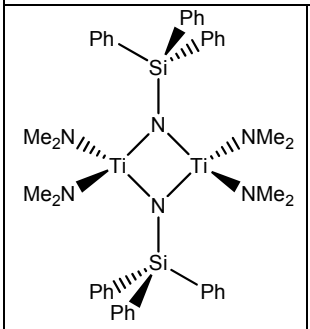
(6)</td><td> 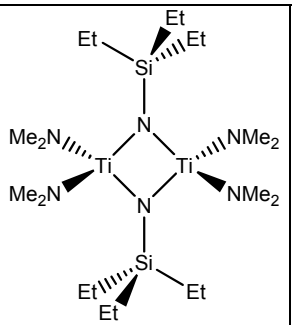
(10)</td><td> 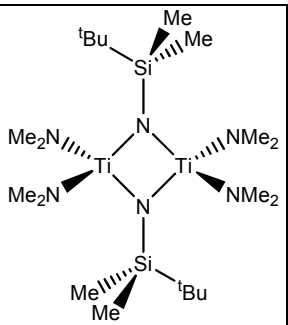
(13)</td><td> 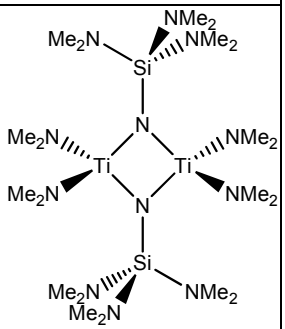
(16)</td></tr>
<tr><td> 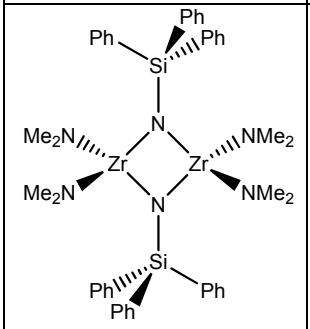
(7)</td><td> 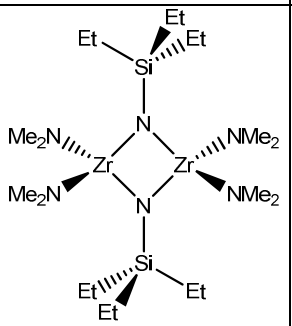
(11)</td><td> 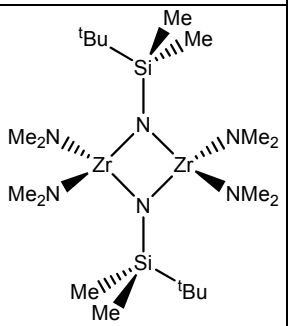
(14)</td><td> 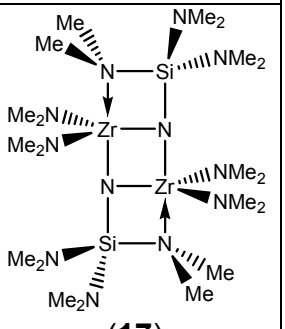
(17)</td></tr>
<tr><td> 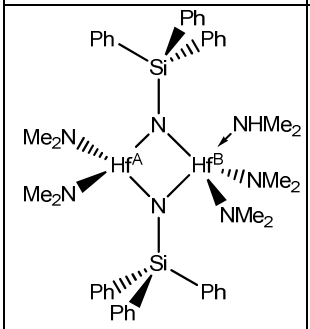
(8)</td><td> 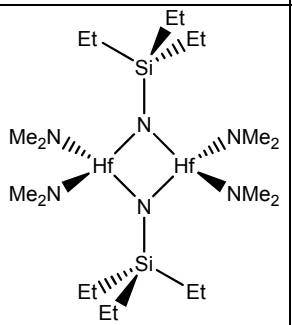
(12)</td><td> 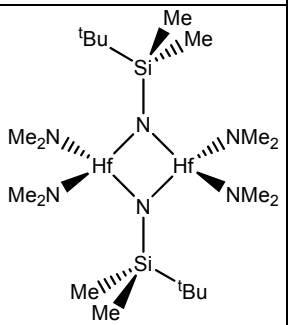
(15)</td><td> 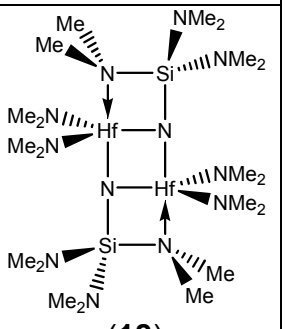
(18)</td></tr>
<tr><td></td><td colspan="2">Chapter 3 compounds</td><td>Chapter 4 compounds</td></tr>
<tr><td> 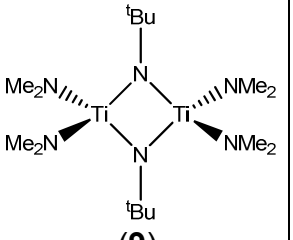
(9)</td><td> 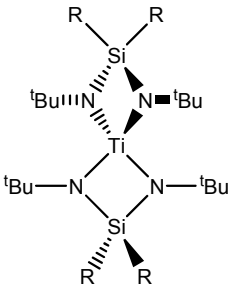
(25): R = Me
(26): R = Ph</td><td> 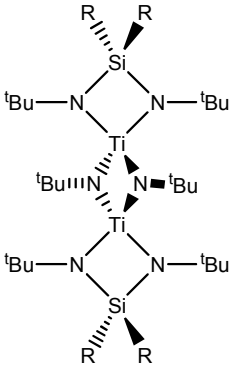
(28): R = Me
(29): R = Ph</td><td> 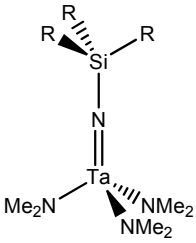
(31): R = Ph
(32): R = NMe₂</td></tr>
</table>

Table 5.2: TGA parameters

Start temperature	30 ^{o}C
Ramping temperature	20 ^{o}C / min
End temperature	600 ^{o}C
Hold time	0 min
Atmosphere	N_2
Flow rate	50 mL / min
Sample boat	Platinum
Maximum weight (sensitivity)	200 mg

Typical TGA curves for the complexes depicted in table 5.1 are shown below in figures 5.2 – 5.5, with the data from all the TGA curves obtained summarised in tables 5.3 – 5.5. Unfortunately, due to lack of precursor and time constraints, TGA curves for the hafnium complexes **12** and **15** were not obtained. However, it is feasible to expect that these two complexes would behave in a similar manner to the analogous zirconium complexes **11** and **14**.

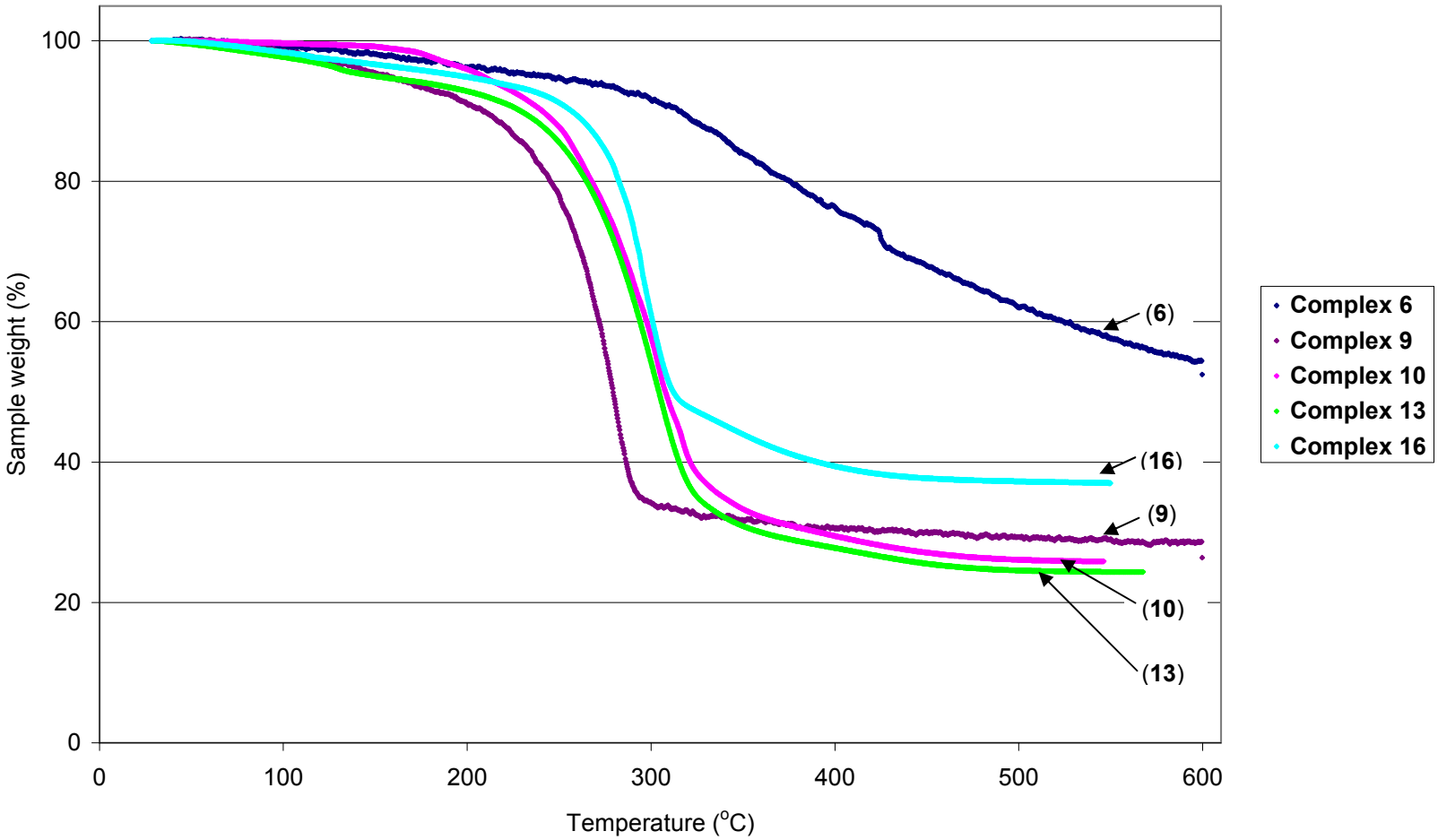

Figure 5.2: Comparison of TGA curves obtained for dimeric titanium complexes of the form $[(Me_2N)_2Ti(NR)]_2$, where R is $\{SiPh_3\}$ (**6**), $\{^tBu\}$ (**9**), $\{SiEt_3\}$ (**10**), $\{SiBuMe_2\}$ (**13**) or $\{Si(NMe_2)_3\}$ (**16**).

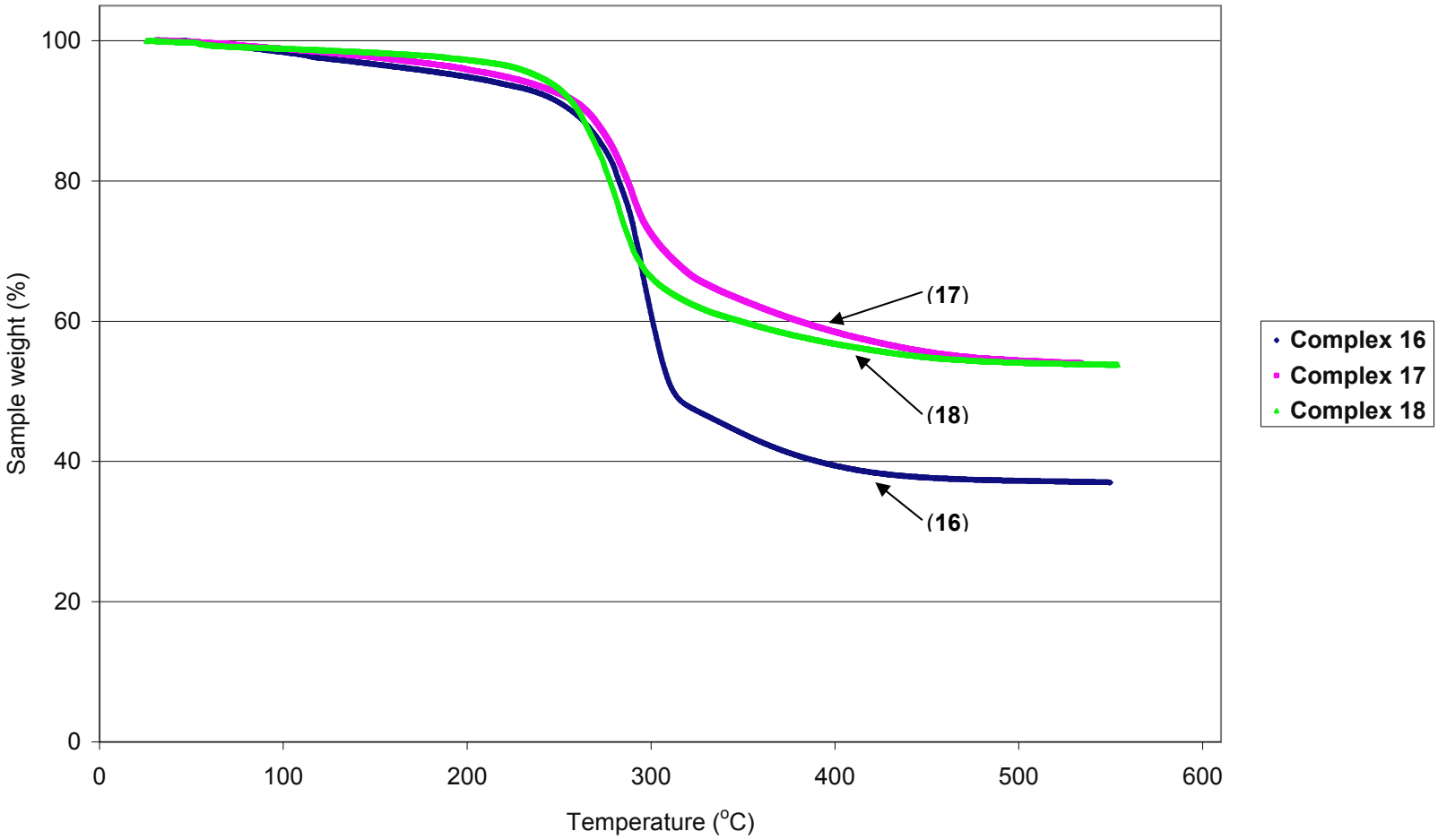

Figure 5.3: Comparison of TGA curves obtained for Group 4 metal complexes of the form $[(Me_2N)_2M(NSi\{NMe_2\}_3)]_2$, where M is Ti (**16**), Zr (**17**) or Hf (**18**).

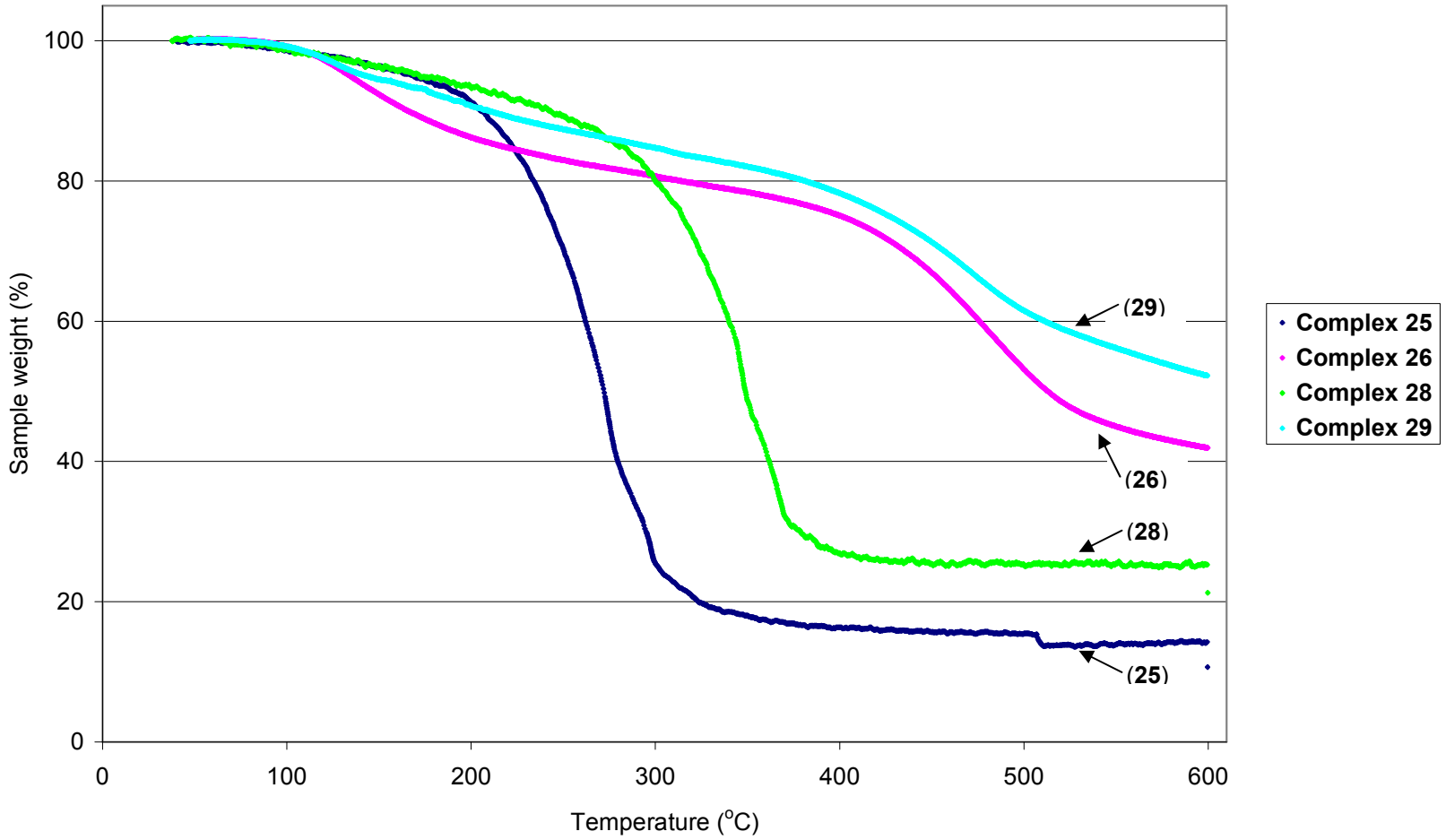

Figure 5.4: Comparison of TGA curves obtained for titanium complexes containing the bidentate fragment $\{R_2Si(N^tBu)_2\}$.

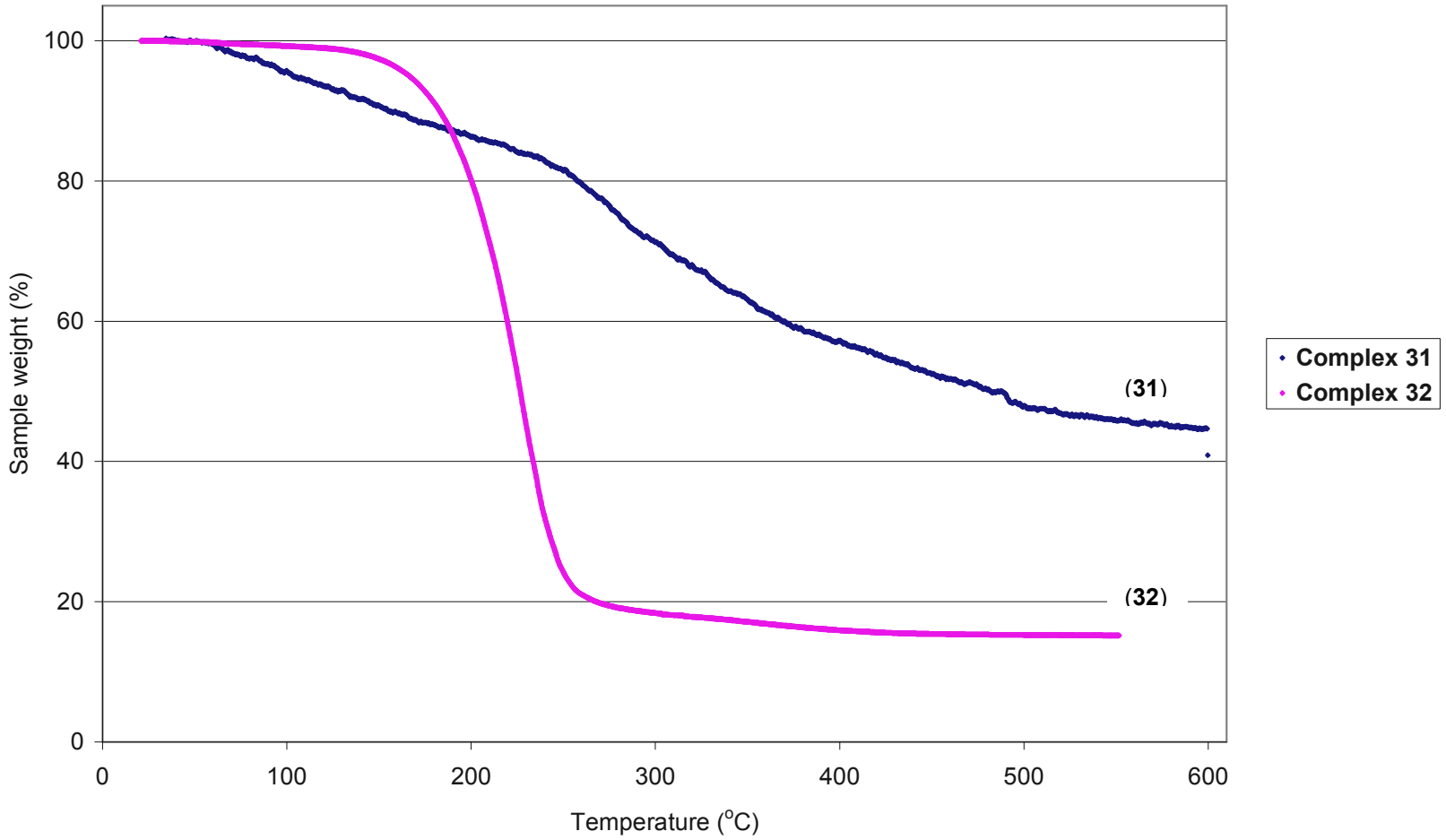

Figure 5.5: Comparison of TGA curves obtained for tantalum complexes **31**, $[(Me_2N)_3TaNSiPh_3]$, and **32**, $[(Me_2N)_3TaNSi(NMe_2)_3]$.

Table 5.3: Summary of the TGA data obtained for the Group 4 metal complexes of the general form $[(Me_2N)M(NSiR_3)]_2$ (**6** – **18**). The structures of these complexes have previously been described in Chapter 2.

	Experimental values			Calculated values			
Comp. No.	Onset temp. (^oC)	Plateau temp. (^oC)	Final mass (%)	M (%)	MN (%)	MNSi (%)	3MN: Si_3N_4 (%)
Titanium complexes							
9	80	194	(92)				
	194	302	28.7	23.2	29.9	-	-
6	100	280	(93)				
	280	-	(54.4)	11.7	15.1	22.0	26.6
10	180	372	25.9	18.1	23.4	33.9	41.0
13	60	156	(95)				
	210	353	24.4	18.1	23.4	33.9	41.0
16	70	240	(92)				
	240	392	37.0	15.5	20.0	29.0	35.0
Zirconium complexes							
7	100	250	(93)				
	250	-	(47.5)	20.2	23.3	29.5	33.6
11	-	-	49.5	29.6	34.1	43.2	49.3
14	-	-	54.5	29.6	34.1	43.2	49.3
17	80	246	(93)				
	246	414	54.0	25.8	29.8	37.7	43.0
Hafnium complexes							
8	105	135	(96)				
	320	-	(60.8)	31.8	34.3	39.2	42.6
18	220	374	53.8	40.5	43.7	50.1	54.3

Table 5.4: Summary of the TGA data obtained for the titanium complexes **25**, **26**, **28** and **29**. The structures of these complexes contain the bidentate fragment $\{R_2Si(N^tBu)_2\}$ and have previously been described in Chapter 3.

	Experimental values			Calculated values		
Compound No.	Onset temp. (^oC)	Plateau temp. (^oC)	Final mass (%)	Ti (%)	TiN (%)	TiNSi (%)
9	80	194	(92)			
	194	302	28.7	23.2	29.9	-
25	85	197	(92)			
	197	340	14.3	10.7	13.8	20.1
26	85	250	(83)			
	330	-	(42.0)	6.9	8.9	12.9
28	85	270	(87)			
	270	395	25.3	15.0	19.4	28.2
29	85	370	(81)			
	370	-	(52.3)	10.8	14.0	20.3

Table 5.5: Summary of the TGA data obtained for the tantalum complexes **31** and **32**. The structures of these complexes have previously been described in Chapter 4.

	Experimental values			Calculated values		
Compound No.	Onset temp. (^oC)	Plateau temp. (^oC)	Final mass (%)	Ta (%)	TaN (%)	TaNSi (%)
31	65	-	(44.7)	30.9	33.3	38.1
32	150	275	15.2	37.2	40.0	45.8

Analysis of the Group 4 metal complexes (**6** – **18**, **25** - **29**) TGA curves shows several common features. Typically, a gradual loss of mass of approximately 10 % or less observed at the lower end of the temperature range analysed. This observation may potentially be attributed to several factors. These include loss of residual solvent molecules trapped within the crystal lattice or unfavourable premature decomposition of the complex.

Alternatively, the gradual loss of mass observed may potentially be attributed to volatilization of the complex. However, Fix *et*. *al*. have reported the volatility of **9** to be comparatively poor, with sublimation of the complex occurring at elevated temperatures only under reduced pressure (140 ^{o}C/ 0.1 mmHg).[3] In addition, Brauer *et*. *al*. have reported the sublimation of **25** occurring under similar conditions (70 ^{o}C/ 0.08 mmHg).[4] Curiously, a patent filed by Air Products and Chemicals Inc. reports the structurally similar complex [{$H_2Si(N^tBu)$}$_2$Ti] to be volatile, with a residual mass of 1.64 % observed within the TGA being less than may be expected for titanium metal alone (12.2 %).[5]

In general, a single significant loss of mass is observed within the temperature range 200 ^{o}C – 350 ^{o}C which may be attributed to decomposition of the compound. At higher temperatures minimal loss of mass is observed, indicating the formation of a thermally stable decomposition product. Interestingly, decomposition of **28** is observed occurring at a significantly higher temperature in relation to complexes **9** – **18** and **25**. This observation may potentially be attributed to the combination of the bidentate {$Me_2Si(N^tBu)_2$} moieties and the delocalised {Ti_2N_2} ring within **28** affording the complex a comparatively greater stability, as described in Chapter 3.

In addition, it is interesting to note that the TGA curves for both the initial green crystals and the orange crystals of **25**, as described in Chapter 3, are identical within experimental error.

An exception to this general observation is the TGA curves for the complexes containing phenyl groups (**6** – **8**, **26**, **29**; the TGA curves for complexes **7** and **8**, not shown here, are found to be comparable to the TGA curve obtained for **6**). Within these TGA curves a loss of mass attributed to decomposition is observed over a significantly wider temperature range. Subsequently the formation of a stable decomposition product is not observed within the temperature range analysed. This observation may be due to unfavourable, gradual decomposition of the phenyl groups via several competing mechanisms. Consequently this may result in incomplete decomposition of the complex and increased contamination of the product.

Interestingly, the TGA curves obtained for the zirconium complexes containing the {$SiEt_3$} (**11**) and {Si^tBuMe_2} (**14**) moieties are significantly different to those obtained for the analogous titanium complexes (**10** and **13** respectively). The TGA curves for both **11** and **14** (not shown here) are consistent with the apparent occurrence of multiple thermal events over a wide temperature range. Therefore, in a similar manner to the complexes containing phenyl groups, decomposition of **11** and **14** may occur by several mechanisms. However, due to a limited amount of compound, both TGAs for **11** and **14** were performed using smaller samples compared to **10** and **13**. Consequently, the TGA curves obtained for **11** and **14** may display a greater sensitivity and be subject to external vibrations.

Analysis of the residual mass obtained for **9** (28.7 %) shows it to be just below what may be expected for TiN (29.9 %). Therefore, it is feasible to suggest that the decomposition product of **9** is TiN, with the discrepancy in masses potentially attributed to partial volatilisation of the complex. In comparison, with the exception of the complexes containing phenyl groups for reasons described above, analysis of the residual masses obtained for the titanium complexes **10**, **13**, and **25** show them to be slightly above the value expected for TiN. This may potentially suggest that for these complexes TiN containing only a small amount of silicon atoms is formed, a situation that is desirable for diffusion barrier materials as discussed in Chapter 1.

In addition, analysis of the residual mass obtained for complex **28** (25.3 %) shows it to be closer to what may be expected for TiNSi (28.2 % vs 19.4 % for TiN). This may potentially be attributed to the presence of a {Ti_2N_2} imido ring within **28** promoting the incorporation of nitrogen within the decomposition product.

However, the residual mass observed for **16** is significantly higher than may be expected for TiNSi. This may potentially be due to the increased nitrogen content within **16**, in particular the larger number of nitrogen atoms bonded only to silicon atom within the {$Si(NMe_2)_3$} moiety. Subsequently, this may

promote the formation of higher amounts of silicon nitride, Si_3N_4. Comparable observations are made for the analogous zirconium and hafnium complexes, **17** and **18**.

Analysis of the TGA curves obtained for the tantalum complexes **31** and **32** show several observations previously seen for the group 4 metal complexes. The TGA curve for **31** shows a loss of mass occurring continuously for the temperature range analysed, whilst the TGA curve for **32** shows a single significant loss of mass attributed to decomposition and the subsequent formation of a thermally stable product. Interestingly, the percentage of mass remaining after the decomposition of **32** (15.2 %) is less than may be expected for the percentage of tantalum metal alone (37.2 %). Consequently, this suggests that **32** is to a certain extent volatile.

5.3 CVD of diffusion barrier materials

Analysis of the TGA data obtained for the group 4 and tantalum metal complexes described in Chapters 2, 3 and 4 shows that the decomposition of complexes **9** – **18**, **25**, **28** and **32** occurs over a narrow temperature range compared to those complexes containing phenyl groups (complexes **6** – **8**, **26**, **29** and **31**). In addition, decomposition of these complexes results in the formation of a thermally stable product, with no further weight loss observed. Therefore complexes **9** – **18**, **25**, **28** and **32** may potentially be used as CVD precursors for the deposition of diffusion barrier materials.

However, as discussed in Chapter 1, for a compound to be used as a precursor for CVD it ideally has to possess a high volatility to readily enable transport of the precursor vapour to the CVD reactor. Whilst TGA may indicate the volatility of potential precursor compounds in addition to their thermal stability, the results are not quantitative. Alternatively, the volatility of a compound may be quantified by measuring its vapour pressure (VP). Accurate determination of the VP of a compound is often difficult though, with a large variation in VP data commonly reported for well-known precursors.[6]

VP studies performed at SAFC Hitech, Bromborough, UK, for the titanium complex **10** show a low volatility for this compound. This data, in addition to the comparatively poor volatility reported for **9**,[3] suggests the volatility of these and related group 4 complexes prepared from silicon amides of the form R_3SiNH_2 may not be suitable to promote efficient film growth.

Several techniques are commonly used to overcome the issue of poor precursor volatility. These include Direct Liquid Injection (DLI) and Aerosol-Assisted CVD (AACVD), where the precursor may be dissolved in a solvent. The solution may then be used to generate an aerosol to transport the precursor to the reactor chamber.[7]

Due to their potentially poor volatility, the compounds identified by TGA were used as precursors to deposit a series of thin films by AACVD. To minimize oxygen and halogen contamination of the deposited film by decomposition of the solvent, the precursors were dissolved in a hydrocarbon solvent.

Depositions were carried out at atmospheric pressure in a laminar flow, cold-wall reactor containing a graphite heating block on which the substrate is situated. The precursors were injected as a solution into a glass flask sat in an ultrasonic nebulizer, located just before the reactor chamber (figure 5.6). Prior to injecting the precursor, the chamber was loaded with the glass substrate and heated under a flow of nitrogen (1.2 L/min) to the required temperature at a rate of 10 ^{o}C/min before allowing to equilibrate for at least 30 min. The precursor was then injected and the nebulizer started to begin the deposition. After each deposition the films were allowed to cool slowly at a rate of 1 ^{o}C/min under a flow of nitrogen. The glass substrates used were glass microscope slides. These were etched for 24 hr in H_2SO_4:HNO_3 (1:1) and then rinsed with deionised water and acetone before loading into the chamber.

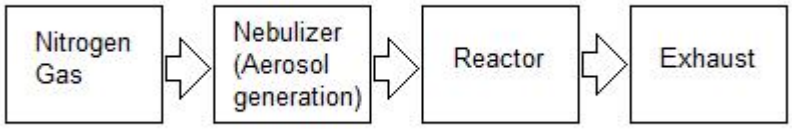

Figure 5.6a: General schematic of AACVD apparatus.

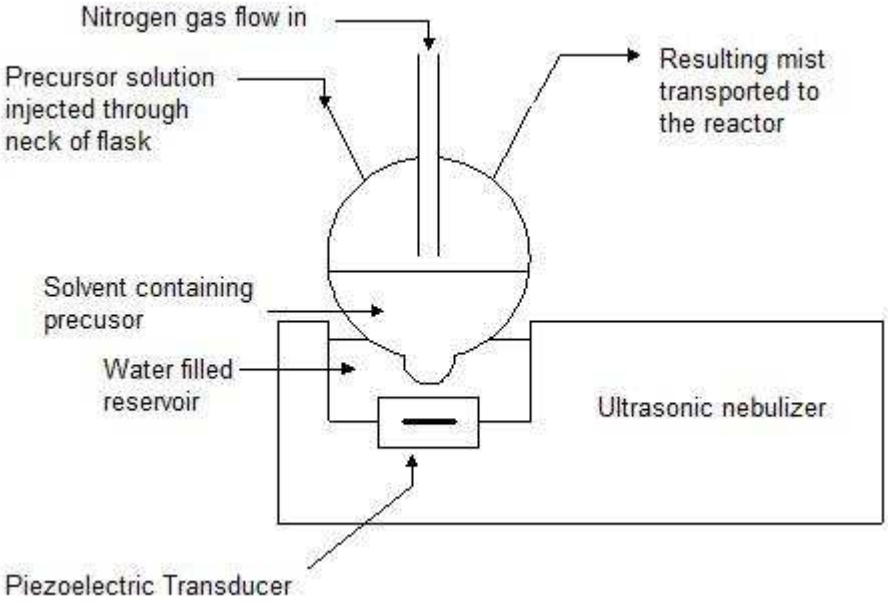

Figure 5.6b: Schematic representation of the nebulizer.

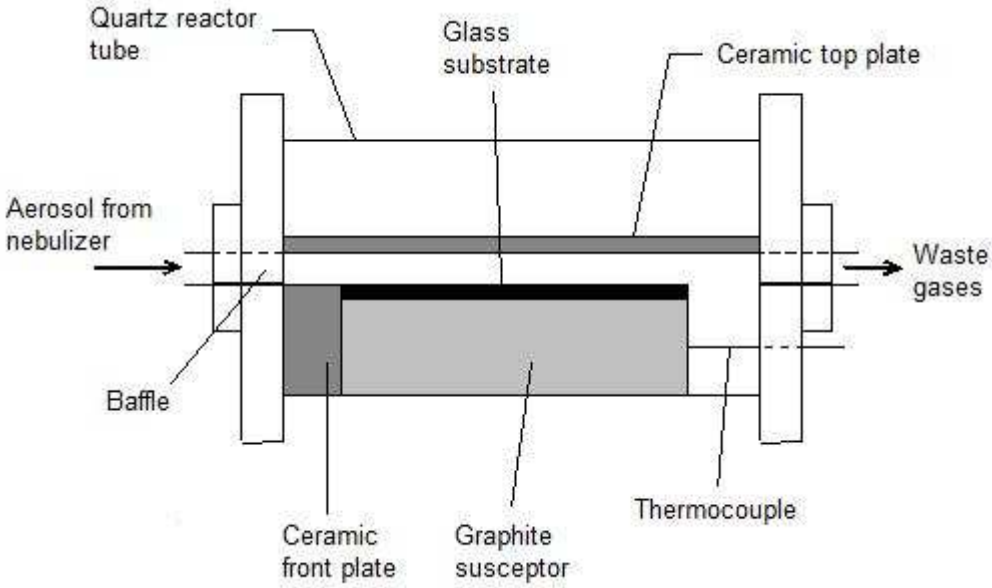

Figure 5.6c: Schematic representation of the CVD reactor chamber.

Films deposited have been characterised by X-Ray diffraction (XRD), scanning electron microscopy (SEM), energy-dispersive X-Ray spectroscopy (EDX) and X-Ray photoelectron spectroscopy (XPS) techniques. XRD, SEM and EDX studies were performed at the University of Bath, whilst XPS studies were performed at Cardiff University.

5.3.1 Deposition of thin films using [{$(Me_2N)_2M(NSiRR'_2)\}_2$] systems

As mentioned earlier in this chapter, the deposition of TiN films by AACVD using **9** as the precursor has previously been reported by Fix *et*. *al*.[3] However, as part of our studies into the deposition of thin films using the Group 4 metal complexes described in Chapter 2, in addition to testing the integrity of our reactor, a series of depositions were performed using **9** as the precursor. The precursor was injected as a hexane solution, with a film successfully deposited using a substrate temperature of 400 ^{o}C. The film deposited is shown below in figure 5.7. Depositions performed at lower temperatures resulted in lower growth rates and highly powdery films with poor adhesion.

Figure 5.7: Film deposited on glass slides by AACVD using the titanium complex [{$(Me_2N)_2Ti(\mu^2\text{-}N^tBu)\}_2$], **9**, as the precursor. The direction of the vapour flow is from left to right as depicted.

A series of depositions were performed using the titanium complexes **10**, **13** and **16**, the zirconium complexes **11** and **14** and the hafnium complexes **12**, **15** and **18**. Unfortunately, due to time constraints and insufficient amount of precursor, comparable deposition using the zirconium complex **17** was not possible. The precursors were injected as a hexane solution, with films successfully deposited using a substrate temperature of 500 ^{o}C. The films deposited are shown below in figure 5.8. As observed for **9**, depositions

performed at lower temperatures resulted in lower growth rates and highly powdery films with poor adhesion.

Complex	M = Ti
10 {Et_3}	
13 {$^tBuMe_2$}	
16 {$(NMe_2)_3$}	
	M = Zr
11 {Et_3}	
14 {$^tBuMe_2$}	
	M = Hf
12 {Et_3}	
15 {$^tBuMe_2$}	
18 {$(NMe_2)_3$}	

Figure 5.8: Films deposited on glass slides by AACVD using group 4 metal complexes of the form [{$(Me_2N)_2M(NSiR_3)$}$_2$] as the precursor. The direction of the vapour flow is from left to right as depicted.

In general, the films deposited using complexes **9** – **18** are golden in appearance, typical of Group 4 MN and MNSi materials.[6] These films have

been characterised by XRD, SEM, EDX and XPS. Due to time constraints, these techniques have only been used to characterize the films at the point where they visibly appear thickest, with the results from these analyses assumed to be representative of the deposited film in general.

Analysis by SEM of the films deposited using complexes **9** – **18** as the precursor shows them to be smooth with no significant surface features, with a typical surface shown below in figure 5.9. In addition, the films are found to be amorphous by XRD. A film thickness of approximately 2 μm has also observed by SEM for the film deposited using **10** as the precursor, as shown in figure 5.10.

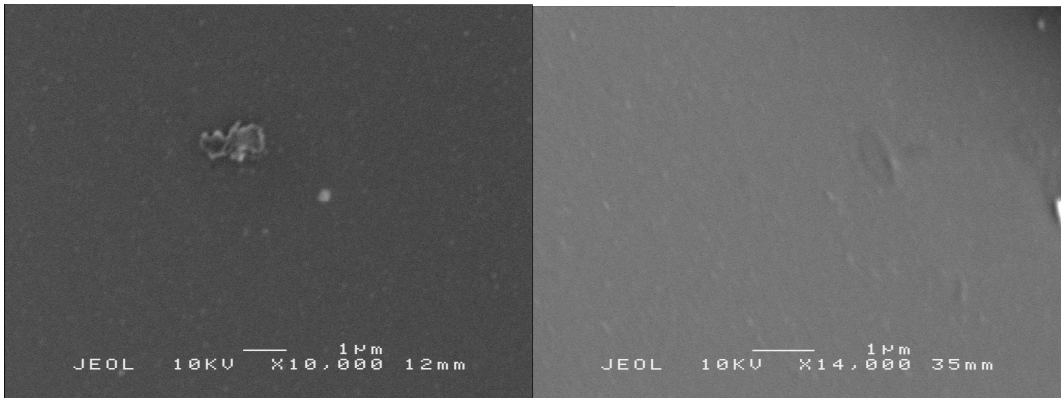

Figure 5.9: Surface images obtained by SEM typical of the film deposited using AACVD with complex **9** as the precursor. Left image is of the film as deposited, whilst the right image shows the film sputter-coated with gold.

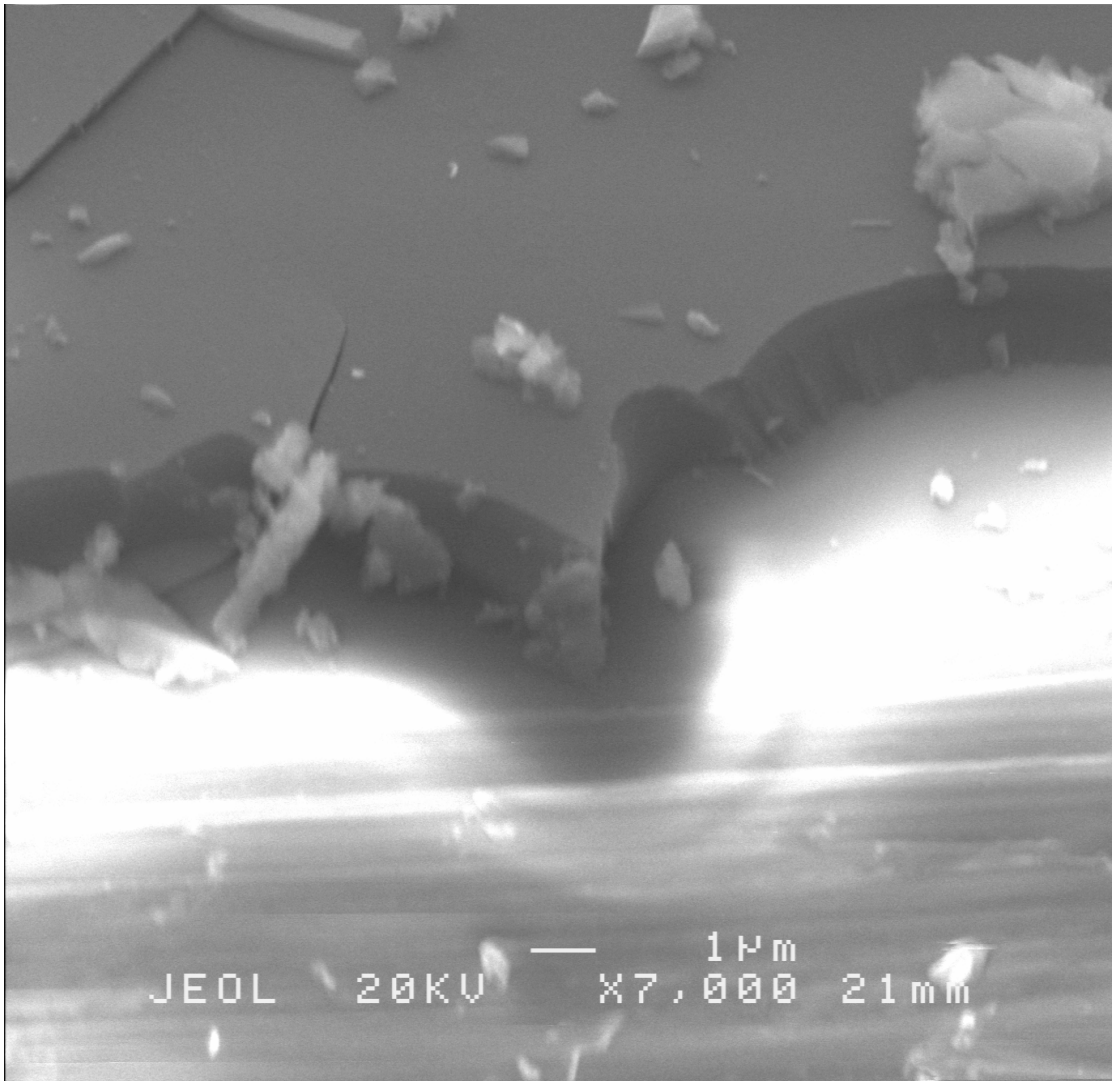

Figure 5.10: SEM image of the film deposited using AACVD with complex **10** as the precursor, showing a scratch in the deposited film to reveal the glass substrate. The dark grey surface at the top of the image is the deposited film whilst the light area at the bottom of the image is the glass substrate. Slight distortion of the image is observed due to surface charge on the uncoated glass substrate. A film thickness of up to 2 μm is observed.

EDX studies of the deposited films, performed in tandem with analysis by SEM, show large peaks attributed to the relevant group 4 metal (Ti within films deposited using **9**, **10**, **13** and **16**; Zr within films from **11** and **14**; Hf within films from **12**, **15** and **18**). However, due to the inherent problems in detecting lighter elements, no signal attributed to the presence of nitrogen could be observed, although emissions attributed to the presence of carbon and oxygen are shown within the spectra.

In addition, the EDX spectra obtained for the deposited films show a strong signal attributed to the presence of silicon (figure 5.11). However, it is not possible to determine whether the observed signal is due to the presence of silicon within the deposited films, as desired, rather than due to the presence of silicon within the glass substrate below. This is emphasised by the observation of an emission attributed to silicon within the spectrum for the film deposited using **9** as the precursor, when the structure of **9** does not contain any silicon atoms (figure 5.12).

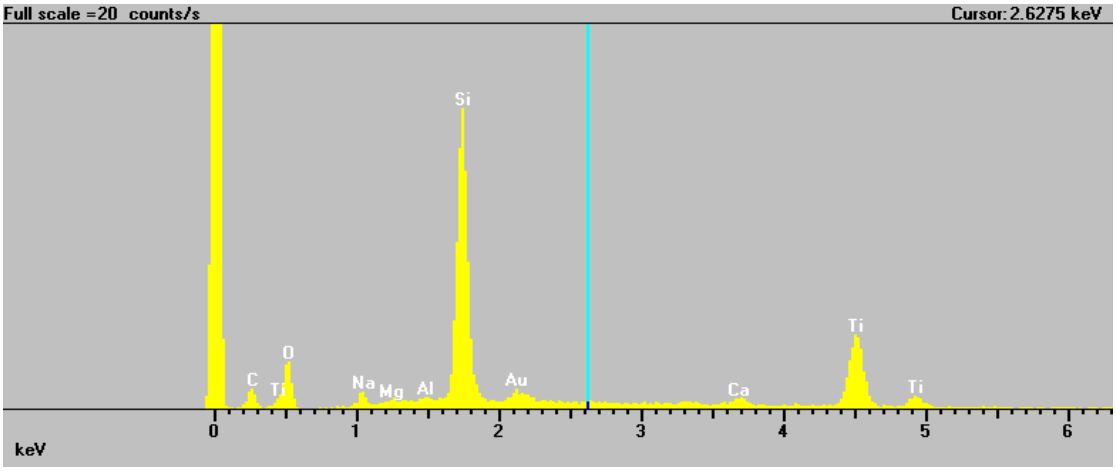

Figure 5.11: EDX spectrum for the film deposited using **13** as the precursor. Spectrum is typical for the films deposited using complexes **10** – **16** and **18** as the precursor, with significant emissions observed for the relevant group 4 metal and silicon.

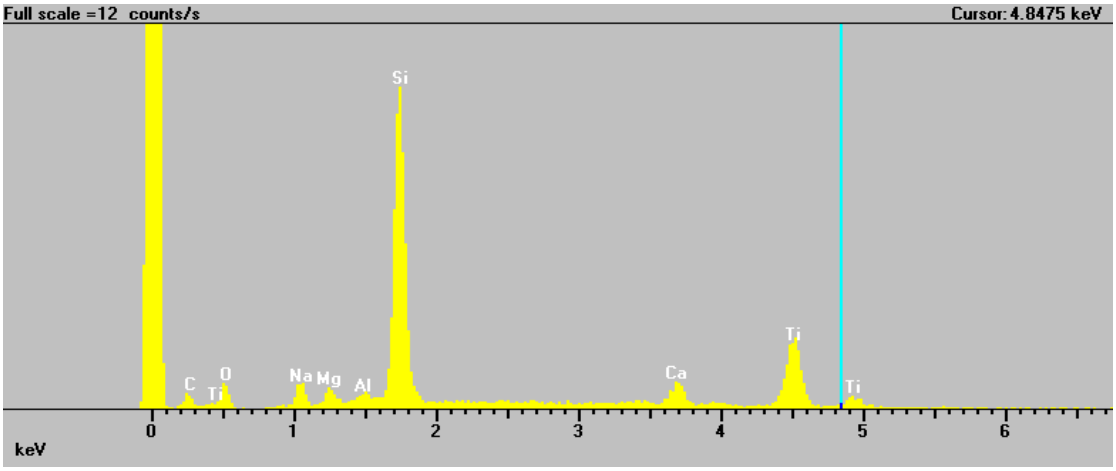

Figure 5.12: EDX spectrum for the film deposited using **9** as the precursor. A signal attributed to silicon is observed despite the absence of silicon within the precursor. The presence of silicon within the spectrum may be attributed to the glass substrate.

The elemental compositions of the films deposited using **9** – **16** and **18** as the precursors have been quantitatively determined by XPS, with sputter etching of the films to achieve a qualitative depth profile. The film is sputter etched over a 2 mm^2 area, with the centre of this area analysed using a 100 micron spot. Typical XPS spectra obtained for the films deposited using **9** - **16** and **18** as the precursor are shown in figures 5.13 and 5.14, with the atomic percentage composition of the deposited films displayed in tables 5.6 – 5.13.

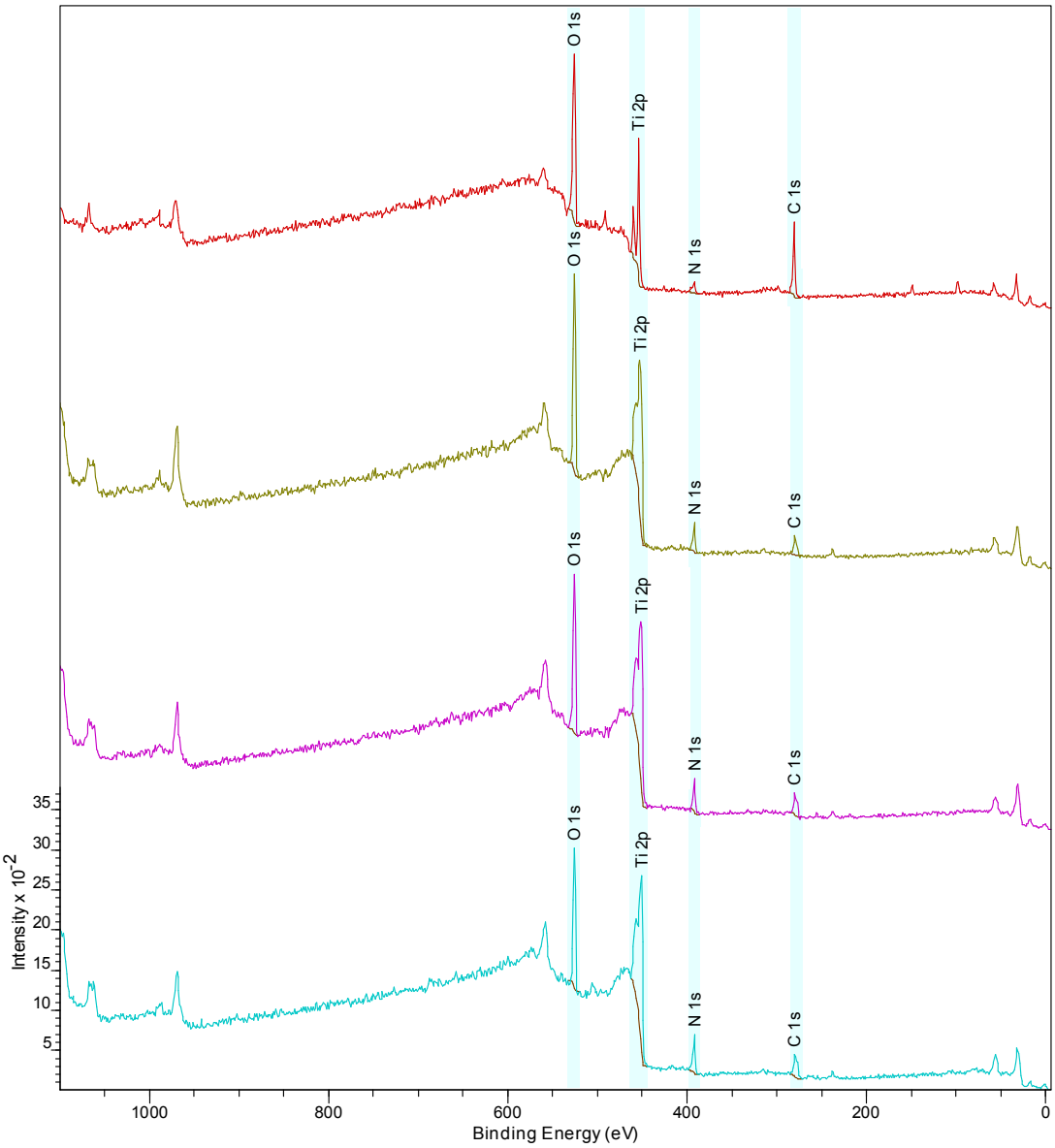

Figure 5.13: X-ray photoelectron spectra for film deposited on glass at 400 ^oC using **9** as the precursor. From top to bottom; spectrum for the film as-deposited (red) and after sputter-etching for 30 s (gold), 60 s (purple) and 90 s (light blue) respectively.

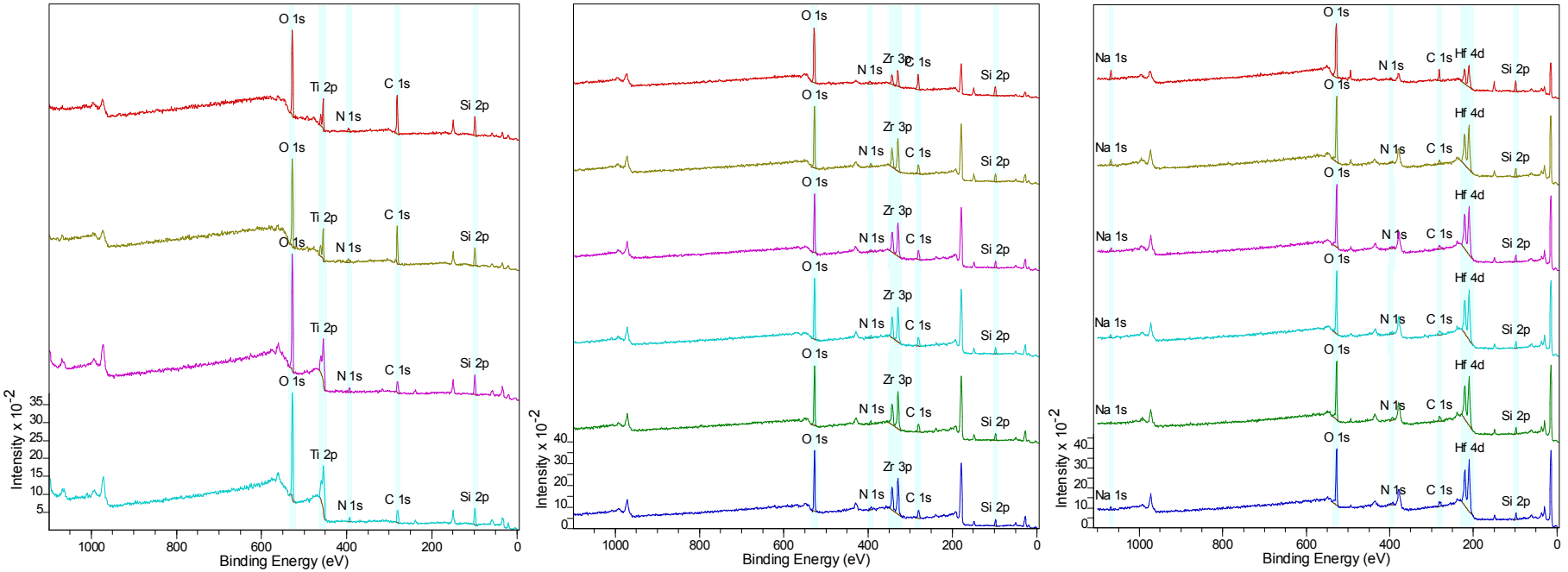

Figure 5.14. Typical X-ray photoelectron spectra for the films deposited on glass at 500 ^{o}C using complexes **10, 11** and **12** as the precursor from left to right respectively. From top to bottom; spectrum for the film as-deposited (red) and after sputter-etching for 30 s (gold), 60 s (purple) and 90 s (light blue) respectively. In addition, the spectra for **11** and **12** show those obtained after sputter-etching for 120 s (green) and 150 s (dark blue).

Table 5.6: Atomic percent composition from XPS analysis of film deposited using **9** as the precursor.

Sputter Time (s)	Ti (at. %)	N (at. %)	C (at. %)	O (at. %)	N / Ti	C / Ti	O / Ti
0	14.60	5.37	40.62	39.42	0.37	2.78	2.70
30	31.21	10.99	14.68	43.12	0.35	0.47	1.38
60	31.93	12.90	18.78	36.38	0.40	0.59	1.14
90	33.67	15.73	22.51	28.09	0.47	0.67	0.83

Table 5.7: Atomic percent composition from XPS analysis of film deposited using **10** as the precursor.

Sputter Time (s)	Ti (at. %)	N (at. %)	Si (at. %)	C (at. %)	O (at. %)	N / Ti	Si / Ti	C / Ti	O / Ti
0	6.04	3.08	13.61	39.82	37.45	0.51	2.25	6.59	6.20
30	6.99	4.57	12.81	34.57	41.07	0.65	1.83	4.95	5.88
60	14.90	2.72	14.79	14.67	52.92	0.18	0.99	0.98	3.55
90	17.32	2.90	14.57	17.12	48.09	0.17	0.83	0.99	2.78

Table 5.8: Atomic percent composition from XPS analysis of film deposited using **13** as the precursor.

Sputter Time (s)	Ti (at. %)	N (at. %)	Si (at. %)	C (at. %)	O (at. %)	N / Ti	Si / Ti	C / Ti	O / Ti
0	6.00	2.35	13.02	42.15	36.48	0.39	2.17	7.03	6.08
30	15.24	3.89	17.17	15.24	48.46	0.26	1.13	1.00	3.18
60	17.57	4.99	16.53	12.38	48.52	0.28	0.94	0.70	2.76

Table 5.9: Atomic percent composition from XPS analysis of film deposited using **16** as the precursor.

Sputter Time (s)	Ti (at. %)	N (at. %)	Si (at. %)	C (at. %)	O (at. %)	N / Ti	Si / Ti	C / Ti	O / Ti
0	3.82	0.62	14.02	47.66	33.88	0.16	3.67	12.48	8.87
30	13.93	3.92	16.51	12.06	53.58	0.28	1.19	0.87	3.85
60	18.26	4.42	14.90	9.92	52.50	0.24	0.82	0.54	2.88

Table 5.10: Atomic percent composition from XPS analysis of film deposited using **11** as the precursor.

Sputter Time (s)	Zr (at. %)	N (at. %)	Si (at. %)	C (at. %)	O (at. %)	N / Zr	Si / Zr	C / Zr	O / Zr
0	6.56	6.01	12.64	30.33	44.46	0.92	1.93	4.62	6.78
30	15.05	5.13	11.57	22.07	46.17	0.34	0.77	1.47	3.07
60	18.42	4.13	10.14	22.47	44.83	0.22	0.55	1.22	2.43
90	18.31	3.91	8.90	22.96	45.92	0.21	0.49	1.25	2.51
120	19.51	5.73	9.20	21.21	44.36	0.29	0.47	1.09	2.27
150	18.77	5.88	9.65	22.38	43.33	0.31	0.51	1.19	2.31

Table 5.11: Atomic percent composition from XPS analysis of film deposited using **12** as the precursor.

Sputter Time (s)	Hf (at. %)	N (at. %)	Si (at. %)	C (at. %)	O (at. %)	N / Hf	Si / Hf	C / Hf	O / Hf
0	7.94	4.58	13.87	21.61	48.92	0.58	1.75	2.72	6.16
30	17.77	3.22	14.60	8.59	53.91	0.18	0.82	0.48	3.03
60	20.34	5.84	9.59	12.45	50.75	0.29	0.47	0.61	2.50
90	19.87	5.84	8.64	14.19	50.17	0.29	0.43	0.71	2.52
120	20.68	6.27	8.99	13.80	49.32	0.30	0.43	0.67	2.38
150	20.58	5.09	11.26	15.13	46.84	0.25	0.55	0.74	2.28

Table 5.12: Atomic percent composition from XPS analysis of film deposited using **15** as the precursor.

Sputter Time (s)	Hf (at. %)	N (at. %)	Si (at. %)	C (at. %)	O (at. %)	N / Hf	Si / Hf	C / Hf	O / Hf
0	6.44	1.75	12.61	39.75	39.45	0.27	1.96	6.17	6.13
30	17.59	5.53	11.35	16.90	48.64	0.31	0.65	0.96	2.77
60	19.97	3.77	13.90	16.30	46.07	0.19	0.70	0.82	2.31
90	21.08	3.21	9.41	22.04	44.27	0.15	0.45	1.05	2.10
120	23.42	5.58	10.38	14.84	45.78	0.24	0.44	0.63	1.95
150	23.44	4.64	10.88	14.51	46.53	0.20	0.46	0.62	1.99

Table 5.13: Atomic percent composition from XPS analysis of film deposited using **18** as the precursor.

Sputter Time (s)	Hf (at. %)	N (at. %)	Si (at. %)	C (at. %)	O (at. %)	N / Hf	Si / Hf	C / Hf	O / Hf
0	6.85	5.37	13.99	28.13	45.65	0.78	2.04	4.11	6.66
30	18.56	4.15	10.26	13.10	53.92	0.22	0.55	0.71	2.91
60	20.13	6.07	10.92	14.45	48.45	0.30	0.54	0.72	2.41
90	23.31	3.03	10.57	16.51	46.58	0.13	0.45	0.71	2.00
120	21.98	5.06	11.04	13.65	48.27	0.23	0.50	0.62	2.20
150	22.65	4.14	12.11	11.72	49.38	0.18	0.53	0.52	2.18

Analysis of the XPS data for the films deposited using complexes **9** – **16** and **18** shows that in all cases the percentage of nitrogen within the film is comparatively low in relation to the percentage of metal atoms, with a N:M ratio of approximately 1:3 generally observed. This observation is found to be inconsistent with the N:Ti ratio of 1:1 reported by Fix *et*. *al*. for films deposited using comparable conditions with **9** as the precursor.[3] The percentage of titanium in relation to the percentage of atoms of lighter elements is, however, reported to always be higher when determined by XPS, potentially due to preferential sputtering.[3] However, the relatively high percentage of titanium compared to nitrogen is also observed at the surface of the film before any sputter etching has been performed. Therefore the high Ti:N ratio observed for the film deposited using **9** compared to that reported by Fix *et*. *al*. may not be explained by preferential sputtering alone.

The films deposited using **10** – **16** and **18** are also observed to contain silicon in a consistent atomic percentage throughout. The silicon present is likely to be a result of the decomposition of the precursor. Alternatively, the presence of silicon within the film may be attributed to diffusion of silicon atoms from the glass substrate. However, due to the consistent spread of silicon throughout the film this is unlikely.

In general, the films deposited using titanium-containing precursors (**10**, **13** and **16**) contain silicon and titanium atoms in an approximately 1:1 ratio, except at the surface of the film where the metal content is typically observed
as being lower. However, within the films deposited using zirconium (**11** and **14**) and hafnium- (**12**, **15** and **18**) containing precursors a silicon to metal ratio of approximately 1:2 is generally observed.

Additionally, a significant amount of carbon and oxygen contamination is observed within the all the films deposited. Similar observations have been reported by Fix *et*. *al*. [3] This contamination is particularly prevalent at the surface of the film in relation to the amount of metal atoms present.

The presence of carbon within the deposited film may be attributed to decomposition of the precursor or alternatively to decomposition of molecules of the hexane aerosol. Analysis of the XPS carbon 1s region of the spectra in all cases shows a peak at a binding energy of 280.9 eV (figure 5.15). This binding energy implies that the carbon present within the films is bonded to the metal (TiC = 281.7 eV; ZrC = 281.10 eV; HfC = 280.8 eV) rather than being organic carbon, where the carbon is attached only to oxygen, nitrogen and other carbon atoms (284.6 eV).[8] Therefore, the formation of metal-bound carbon is likely to result from the mechanism by which decomposition of the precursor occurs.

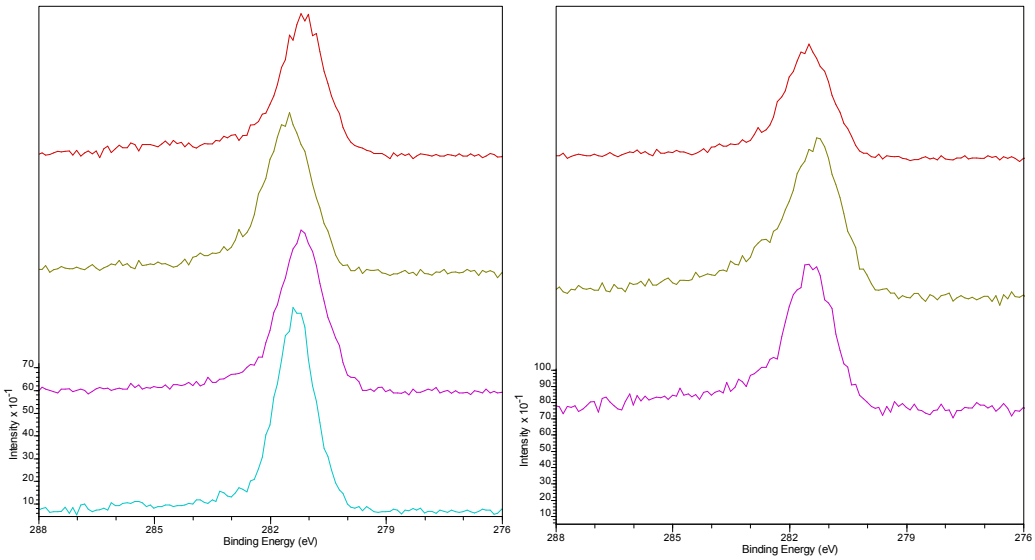

Figure 5.15: Typical carbon 1s regions of the XPS spectra obtained. In all cases a peak at binding energy of 280.9 eV is observed. Left; From top to bottom the as-deposited spectra for the Ti complexes **9** (red), **10** (gold), **13** (purple) and **16** (light blue). Right; From top to bottom the as-deposited spectra for films containing Ti (**10**, red), **Zr** (11, gold) and **Hf** (12, purple).

Interestingly, analysis of the XPS spectra for the films deposited using the three precursors containing titanium (**10**, **13** and **16**) shows a comparable amount of carbon contamination in all cases. This observation may suggest that all three titanium precursor complexes potentially decompose through a mechanism involving a common intermediate. Similar observations are also made for the carbon contamination within films deposited using the precursors containing zirconium (**11**) and hafnium (**12**, **15** and **18**) respectively.

Upon first inspection, the reason why oxygen atoms are observed within the deposited films is not readily apparent. In contrast to the carbon contamination observed, an absence of oxygen atoms precludes the precursor molecules from being the source.

Deposited Group 4 metal nitride films, in particular TiN, are commonly reported to contain large amounts of oxygen, either due to incorporation of residual oxygen and water vapour within the reaction chamber or oxidation of the film post-deposition.[3, 9 - 11] This may be attributed to

oxidation of the metal being thermodynamically favourable compared to nitridation.[9] Consequently, Group 4 metal amide precursors, in tandem with water, O_2, O_3 or an alternative oxidant, have successfully been used for MOCVD and ALD of the corresponding metal oxide, MO_2.[6, 12 - 16]

However, by limiting the amount of oxidant within the reactor chamber the metal oxynitride, MN_xO_y, may instead be deposited. The properties of these oxynitride films have been reported to be dependant on the N/O atomic ratio, with films containing an increased percentage of nitrogen typically deposited at higher temperatures.[13, 14, 17] Subsequently, Group 4 metal oxynitride materials have been used for a wide range of applications, with nitrogen-rich films investigated for their use as diffusion barrier materials.[9, 11, 13, 14]

Futhermore, quaternary titanium silicon oxynitride thin films, TiSiNO, have been investigated as promising candidates for next-generation diffusion barrier materials,[18] whilst the use of hafnium silicon oxynitride, HfSiNO, as a potential gate material in n-MOSFETs has been reported by Kamiyama *et*. *al*. [12]

5.3.2 Deposition of thin films from precursors containing the bidentate {$Me_2Si(N^tBu)_2$} fragment

As discussed earlier in this chapter, TGA analysis of the titanium complexes described in Chapter 3 shows that the complexes **25** and **28** may potentially be used as single-source precursors for the CVD of TiNSi thin films. However, as discussed earlier in Chapter 3, Air Products and Chemicals, Inc. have filed a patent concerning the deposition of MNSi thin films by ALD or CVD using Group 4 metal complexes containing a {$R_2Si(NR'_2)_2$} fragment as the precursor.[5]

The focus of the patent primarily concerns the deposition of TiNSi films by CVD using the titanium complex [{$H_2Si(\mu_2\text{-}N^tBu)_2$}$_2$Ti] as an

organometallic precursor. However, the deposition of TiNSi films using related titanium complexes as the precursor is not described.

Therefore, a series of depositions were performed using **25** and **28** as the precursor. Depositions were performed using AACVD in a comparable manner to the deposition of Group 4 MNSi thin films described earlier in this chapter.

The precursors **25** and **28** were injected as hexane solutions. Depositions performed at 500 ^{o}C resulted in no significant growth as observed with the naked eye. A thin film was successfully deposited using **28** as the precursor at 550 ^{o}C. The film deposited is shown below in figure 5.16. Unfortunately due to time constraints and lack of precursor a film could not be obtained using **25** under the same conditions.

Figure 5.16: Film deposited on glass slides by AACVD using a hexane solution of the titanium complex [{$Me_2Si(N^tBu)_2Ti(N^tBu)\}_2$], **32**, as the precursor. The direction of the vapour flow is from left to right as depicted.

As observed for the films deposited using the titanium complexes **10**, **13** and **16**, the film deposited using **28** is golden in appearance the film and is observed to be amorphous by XRD. In addition, analysis of the films using SEM shows it to be smooth with no significant surface features, whilst the EDX spectrum shows peaks which may be attributed to the presence of titanium and silicon.

The elemental compositions of the film deposited using **28** as the precursor has also been determined by XPS, with sputter etching of the film to achieve a qualitative depth profile. The film is sputter etched over a 2 mm^2 area, with the centre of this area analysed using a 100 micron

spot. The atomic percentage composition obtained from the XPS spectra for the film deposited using **28** as the precursor is displayed in table 5.14.

Table 5.14: Atomic percent composition from XPS analysis of film deposited using **28** as the precursor.

Sputter Time (s)	Ti (at. %)	N (at. %)	Si (at. %)	C (at. %)	O (at. %)	N / Ti	Si / Ti	C / Ti	O / Ti
0	4.81	0.71	14.53	45.43	34.52	0.15	3.02	9.44	7.18
30	17.42	3.33	15.37	9.79	54.10	0.19	0.88	0.56	3.11
60	20.12	2.20	12.81	6.15	58.72	0.11	0.64	0.31	2.92

Analysis of the XPS data for the film deposited using **28** as the precursor shows similar observations to those made for the films deposited using **10, 13** and **16**. Subsequently comparable arguments concerning the composition of the deposited films may be made.

Within the film deposited using **28** the percentage of nitrogen is comparatively low in relation to the percentage of metal atoms, whilst the presence of silicon is observed in a consistent atomic percentage throughout the film. A significant amount of oxygen contamination is also observed throughout the film, whilst carbon contamination is prevalent at the surface of the film. Analysis of the XPS carbon 1s region in all cases shows a peak at a binding energy of approximately 281 eV and may therefore be attributed to carbon bonded directly to titanium and silicon atoms.[8]

However, although the composition of the film deposited using **28** is comparable to those deposited using **10**, **13** and **16**, a higher substrate temperature is required for the deposition of the former (550 ^{o}C vs 500 ^{o}C). As described earlier in this chapter through analysis of the TGA data, this observation may be attributed to the increased stability of **28** due to the presence of the bidentate $\{Me_2Si(N^tBu)_2\}$ fragment.

Interestingly, the deposition of TiNSi films using the titanium complex $[\{H_2Si(\mu_2\text{-}N^tBu)_2\}_2Ti]$ as the precursor is reported to occur at significantly

lower temperatures (400 ^{o}C).[5] In addition, the rate of deposition is reported to be promoted when NH_3 is used as a nitrogen-containing source.[5] Consequently, the deposition of TiNSi thin films using **28** (and **25**) may be more effective when used in conjunction with NH_3 in a dual-source precursor approach rather than as a single-source precursor.

5.3.3 Deposition of thin films using the tantalum precursor [$(Me_2N)_3TaNSi(NMe_2)_3$], 32

As discussed earlier in this chapter, TGA analysis of the tantalum complexes described in Chapter 4 shows that the complex [$(Me_2N)_3TaNSi(NMe_2)_3$] (**32**) may potentially be used as a single-source precursor for the CVD of TaNSi thin films. Therefore, to investigate this potential a series of depositions were performed using **32** as the precursor. Depositions were performed using AACVD in a comparable manner to the deposition of Group 4 MNSi thin films described earlier in this chapter.

The precursor was initially injected as a hexane solution, with a film successfully deposited using a substrate temperature of 550 ^{o}C. The film deposited is shown below in figure 5.17. Depositions performed at 500 ^{o}C resulted in no significant growth as observed with the naked eye.

Figure 5.17: Film deposited on glass slides by AACVD using a hexane solution of the tantalum complex [{$(Me_2N)_3TaNSi(NMe_2)$}$_3$], **32**, as the precursor. The direction of the vapour flow is from left to right as depicted.

However, a high amount of residue is observed within the nebulizer flask post-deposition. This may be attributed to **32** having a lower solubility in hexane compared to the group 4 metal complexes previously described

in this chapter. Subsequently, this may result in the low growth rates observed.

Therefore **32** was injected as a toluene solution, with a film successfully deposited using a substrate temperature of 550 ^{o}C. The film deposited is shown below in figure 5.18. In addition, a significantly smaller amount of residue is observed within the nebulizer flask post-deposition.

Figure 5.18: Film deposited on glass slides by AACVD using a toluene solution of the tantalum complex [{$(Me_2N)_3TaNSi(NMe_2)$}$_3$], **32**, as the precursor. The direction of the vapour flow is from left to right as depicted.

In both cases the films are golden in appearance, although the film deposited using toluene as the solvent appears visibly darker. This phenomenon is assumed to be due to the deposition of a film with increased thickness as a result of greater transport of the precursor molecules using a toluene aerosol. However, the darker appearance may also potentially be attributed to differences in the film composition.

Interestingly, a film exhibiting a lower degree of adhesion is observed when a toluene solution of **32** is used as the precursor instead of a hexane solution, as shown below in figure 5.19. This observation may again potentially be due to differences in the film compositions. Alternatively, the increased transport of precursor to the reactor chamber when using the toluene solution may result in the formation of a different film microstructure. However, the precise reason for this observation is unknown.

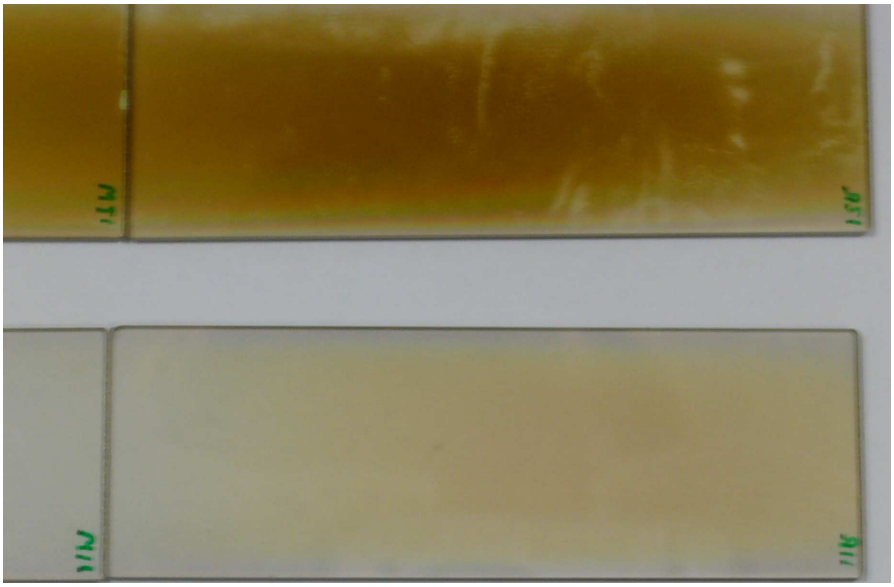

Figure 5.19: Enlarged image of films deposited on glass slides by AACVD using toluene (top) and hexane (bottom) solutions of the tantalum complex [{$(Me_2N)_3TaNSi(NMe_2)$}$_3$], **32**, as the precursor. The direction of the vapour flow is from left to right as depicted. The film deposited using the toluene solution of **32** displays significant damage from minor wear.

Analysis of the films using XRD shows them to be amorphous. In addition, the elemental compositions of the films deposited using **32** as the precursors have been determined by XPS, with sputter etching of the films to achieve a qualitative depth profile. The film is sputter etched over a 2 mm^2 area, with the centre of this area analysed using a 100 micron spot. A typical XPS spectrum for the films deposited using **32** as the precursor is shown in figure 5.20. The subsequent atomic percentage compositions obtained from the XPS spectra of the films deposited using hexane and toluene as the solvent are displayed in tables 5.15 and 5.16 respectively.

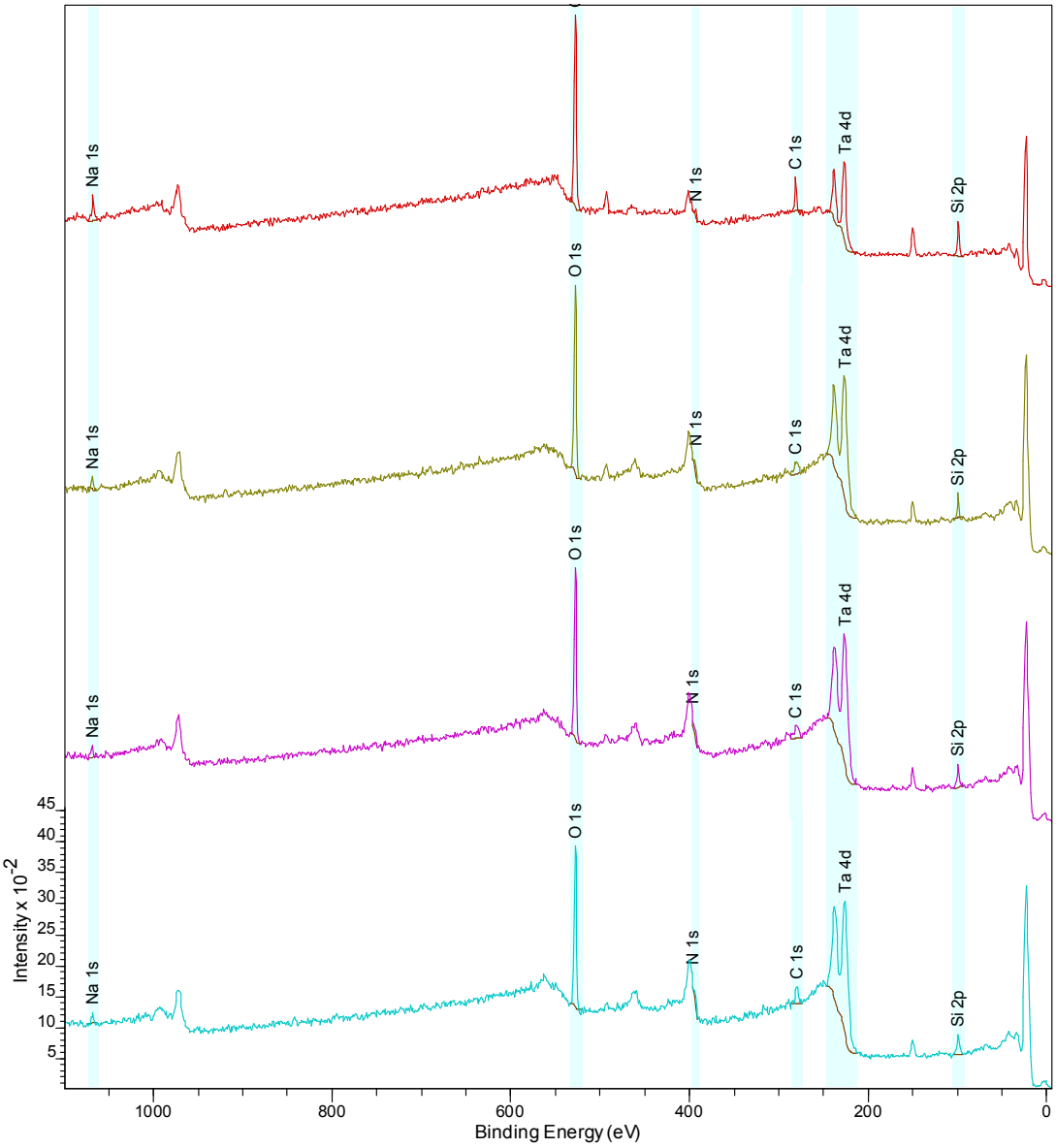

Figure 5.20: X-ray photoelectron spectra for film deposited on glass at 550 °C using a hexane solution of **32** as the precursor. From top to bottom; spectrum for the film as-deposited and after sputter-etching for 30 s, 60 s and 90 s respectively.

Table 5.15: Atomic percent composition from XPS analysis of film deposited using a hexane solution of **32** as the precursor.

Sputter Time (s)	Ta (at. %)	N (at. %)	Si (at. %)	C (at. %)	O (at. %)	N / Ta	Si / Ta	C / Ta	O / Ta
0	7.37	1.00	17.59	16.65	53.31	0.14	2.39	2.26	7.23
30	17.34	3.77	7.76	17.21	52.08	0.22	0.45	0.99	3.00
60	18.23	5.08	13.07	17.69	43.78	0.28	0.72	0.97	2.40
90	20.74	4.77	13.55	16.39	43.52	0.23	0.65	0.79	2.10

Table 5.16 Atomic percent composition from XPS analysis of film deposited using a toluene solution of **32** as the precursor.

Sputter Time (s)	Ta (at. %)	N (at. %)	Si (at. %)	C (at. %)	O (at. %)	N / Ta	Si / Ta	C / Ta	O / Ta
0	5.23	-	17.37	30.21	47.19	-	3.32	5.78	9.02
30	17.02	-	13.66	14.46	54.85	-	0.80	0.85	3.22
60	19.78	-	14.03	8.57	57.62	-	0.71	0.43	2.91
90	21.16	-	13.75	9.38	55.71	-	0.65	0.44	2.63

Analysis of the XPS data shows the films deposited using hexane and toluene solutions of **32** both contain tantalum and silicon, with comparable amounts observed in both. Unfortunately the presence of nitrogen within both films cannot be reliably detected by XPS due to significant overlap of the nitrogen 1s peak (398.4 eV) and the tantalum $4p^3$ peak (400.6 eV).[8]

In addition, a significant amount of surface carbon and oxygen contamination is observed within both films.

In general, comparable amounts of oxygen contamination are observed throughout both films. As discussed previously within this chapter for the formation of Group 4 metal oxynitride films, the formation of Ta-O bonds is favoured over the formation of Ta-N. Consequently, TaN precursors may be oxidised by residual oxygen and water within the reactor chamber with the subsequent formation of tantalum oxynitride, TaN_xO_y, materials.[6, 19 - 21]

In contrast, the carbon contamination observed is significantly different between the two films. Within the film deposited using hexane-based aerosol a consistent percentage of carbon atoms is observed spread throughout the film. However, when the toluene-based aerosol is used the resulting film shows a significantly higher level of carbon contamination at the surface. This contamination is also observed to decrease further from the surface rather than remaining consistent. As

discussed earlier in this chapter, the differences in appearance and adhesion of the two films may potentially be attributed to this difference in the level of carbon contamination within the film composition.

As for the films deposited using the Group 4 metal complexes **9** – **18** described earlier in this chapter, analysis of the XPS carbon 1s region for both the films deposited using **32** shows a peak at a binding energy of 280.9 eV. This implies the carbon present within the film is bonded to tantalum (TaC = 281.9 eV) or silicon (SiC = 281.5 – 283.4 eV) rather than organic carbon (284.6 eV).[8] Therefore, the carbon within both films may be attributed to decomposition of the precursor rather than the hydrocarbon solvent.

However, how the solvent interacts with the precursor must be considered, both in solution and during deposition.[16] In addition, if complete evaporation of the solvent and vaporisation of the precursor does not occur before the aerosol droplets reach the heated substrate, a spray pyrolysis process may occur rather than a true CVD process.[7] Consequently, these factors may affect the mechanism by which deposition occurs and therefore result in the observed differences in the film compositions.

5.4 Summary for Chapter 5

The Group 4 and tantalum metal complexes described in Chapters 2, 3 and 4 have been investigated for their potential use as single-source CVD precursors for the deposition of MNSi thin films. The thermal profiling of these complexes has been performed using TGA. Analysis of the TGA data obtained shows that the decomposition of complexes **9** – **18**, **25**, **28** and **32** occurs over a narrower temperature range compared to those complexes containing phenyl groups (complexes **6** – **8**, **26**, **29** and **31**). In addition, decomposition of these complexes results in the formation of a thermally stable product, with no further weight loss observed.

Subsequently, films have successfully been deposited by AACVD on glass substrates using complexes **9** – **18**, **25**, **28** and **32** as the precursor. The deposited films have been analysed using XRD, SEM, EDX and XPS techniques and are shown to typically be smooth and amorphous. In addition, the compositions of the deposited films, in addition to the anticipated metal, silicon and nitrogen atoms, are also shown to contain significantly high levels of oxygen and carbon. The presence of oxygen may be attributed to residual oxygen within the reaction chamber and the thermodynamically favourable formation of the metal oxide. The carbon present is shown to be bonded to the metal atom and is attributed to the mechanism by which decomposition of the precursor occurs.

Therefore, depending on the parameters and conditions within the reactor chamber, complexes **9** – **18**, **25**, **28** and **32** may potentially be used as single-source precursors for the deposition of ternary MNSi, MSiO and quaternary MNSiO materials. Alternatively, a dual-source approach may be preferred, using a secondary precursor such as ammonia, in order to minimise carbon contamination of the deposited films.[3]

5.5 References for Chapter 5

1. A.R. West, *"Basic Solid State Chemistry Second Edition",* **2000**, John Wiley & Sons, Ltd., Chichester, UK.
2. D. Dollimore and S. Lerdkanchanaporn, *Anal. Chem.*, 1998, **70**, 27R.
3. R. M. Fix, R. G. Gordon and D. M. Hoffman, *Chem. Mater.*, 1990, **2**, 235.
4. D. J. Brauer, H. Bürger, E. Essig and W. Geschwandtner, *J. Organomet. Chem.*, 1980, **190**, 343.
5. J. A. T. Norman and X. Lei, *Eur. Pat.*, EP 1 772 460 A1, 2007.

6. A. C. Jones and M. L. Hitchman, *"Chemical Vapour Deposition; Precursors, Processes and Applications"*, 2009, RSC Publishing, Cambridge, UK..
7. X. H. Huo and K. L. Choy, *Chem. Vapor Depos.*, 2006, **12**, 583.
8. NIST X-ray Photoelectron Spectroscopy Database, Version 3.5 (National Institute of Standards and Technology, Gaithersburg, 2003); http://srdata.nist.gov/xps/.
9. X. Song, D. Gopireddy and C. G. Takoudis, *Thin Solid Films*, 2008, **516**, 6330.
10. G. Hyett, R. Binions and I. P. Parkin, *Chem. Vapor Depos.*, 2007, **13**, 675.
11. M. A. Signore, A. Rizzo, L. Tapfer, E. Piscopiello, L. Capodieci and A. Cappello, *Thin Solid Films*, 2010, **518**, 1943.
12. S. Kamiyama, E. Kurosawa and Y. Nara, *J. Electrochem. Soc.*, 2008, **155**, H373.
13. F. Fabreguette, L. Imhoff, M. Maglione, B. Domenichini, M. C. Marco de Lucas, P. Sibillot, S. Bourgeois and M. Sacilotti, *Chem. Vapor Depos.*, 2000, **6**, 109.
14. I. Polrelyuk, O. Yaskiv, O. Tkachuk and D. B. Lee, *Met. Mater. Int.*, 2009, **15**, 949.
15. M. Cho, D. S. Jeong, J. Park, H. B. Park, S. W. Lee, T. J. Park, C. S. Hwang, G. H. Jang and J. Jeong, *Appl. Phys. Lett.*, 2004, **85**, 5953.
16. R. Thomas, R. Bhakta, A. Milanov, A. Devi and P Ehrhart, *Chem. Vapor Depos.*, 2007, **13**, 98.
17. S. K. Pradhan and P. J. Reucroft, *J. Cryst. Growth*, 2003, **250**, 588.
18. L. García-González, J. Hernández-Torres, C. Mendoza-Barrera, M. Meléndez-Lira, P. J. García-Ramírez, J. Martínez-Castillo, Á. Sauceda, A. L. Herrera-May, J. M. Saldaña and F. J. Espinoza-Beltrán, *J. Mater. Eng. Perform.*, 2008, **17**, 580.
19. C. H. Winter, *Aldrichim. Acta*, 2000, **33**, 3.
20. M. Ritala, P. Kalsi, D. Riihelä, K. Kukli, M. Leskelä and J. Jokinen, *Chem. Mater.*, 1999, **11**, 1712.

21. J. H. Hsieh, C. C. Chang, J. S. Cherng and F. Y. Hsu, *Thin Solid Films*, 2009, **517**, 4711.

Chapter 6

Experimental data

6.1 General Experimental

All operations were carried out under an atmosphere of dry dinitrogen or argon using standard Schlenk and glove-box techniques. Hexane, toluene, pentane, dichloromethane and diethyl ether solvents were dried using an Innovative Technology, Inc. Solvent Purification System (SPS) system and degassed under dinitrogen or argon prior to use. Deuterated benzene (C_6D_6) NMR solvent was purchased from Aldrich and dried by refluxing over potassium before isolating by vacuum distillation. All dry solvents were stored under dinitrogen or argon in Young's flasks over 4 Å molecular sieves.

Chlorotriphenylsilane [Ph_3SiCl], chlorodiphenylsilane [$Ph_2(H)SiCl$], chlorotriethylsilane [Et_3SiCl], tert-butyldimethylchlorosilane [$^tBuMe_2SiCl$], silicon tetrachloride [$SiCl_4$], dichlorodimethylsilane [Me_2SiCl_2], dichlorodiphenylsilane [Ph_2SiCl_2], iso-propylamine [$^iPrNH_2$], N,N-dimethylethylenediamine [$Me_2NCH_2CH_2NH_2$] and lithium bis(trimethylsilyl)amide [$LiN(SiMe_3)_2$, LiHMDS] were purchased from commercial sources and used as supplied, as were 2.5M n-butyl lithium in hexanes, titanium(IV) tetrachloride [$TiCl_4$] and titanium(IV) tetrachloride tetrahydrofuran complex [$TiCl_4.2thf$]. Tert-butylamine [$^tBuNH_2$] and pyridine [C_5H_5N, py] were purchased from commercial sources and dried by refluxing over calcium hydride. Dimethylamine was purchased from commercial sources as a 40 % wt. Me_2NH in H_2O solution and dried by refluxing over sodium hydroxide. Tetrakis(dimethylamino)titanium [$Ti(NMe_2)_4$, TDMAT], tetrakis(dimethylamino)zirconium [$Zr(NMe_2)_4$, TDMAZr], tetrakis(dimethylamino)hafnium [$Hf(NMe_2)_4$, TDMAHf], Pentakis(dimethylamino)tantalum [$Ta(NMe_2)_5$, PDMAT], dimethylzinc [$ZnMe_2$] and bis(methylcyclopentadienyl)manganese [$(MeCp)_2Mn$] were used as supplied by SAFC HiTech.

Solution ^1H and ^{13}C NMR experiments were performed at ambient temperature using a Bruker Avance-300, whilst solution ^7Li and ^{29}Si NMR experiments were performed at ambient temperature using a Bruker

Avance-500. ^{1}H and ^{13}C NMR chemical shifts are referenced internally to residual non-deuterated solvent resonances.[1] All chemical shifts are reported in δ (ppm) and coupling constants in Hz. All spectra were recorded at ambient temperature. The following abbreviations have been used for multiplicities: s (singlet), d (doublet), t (triplet), q (quartet), sept (septet), br (broad), m (unresolved multiplet), ap (apparent).

Elemental analyses were performed externally by Elemental Microanalysis Ltd., Okehampton, UK.

X-ray Crystallography: The solid state molecular structures were obtained using a Nonius Kappa CCD diffractometer fitted with an area detector and Oxford Cryostream. All structural data were obtained by Dr. Andrew Johnson.

Thermogravimetric analyses (TGA) were performed externally at SAFC HiTech, Bromborough, UK.

X-ray Photoelectron Spectroscopy analyses were performed at the Wolfson Nanoscience Laboratory, Cardiff University by Dr. David Morgan and funded by the EPSRC.

6.2 Experimental for Chapter 2

6.2.1 Synthesis of [Ph_3SiNH_2] (1)

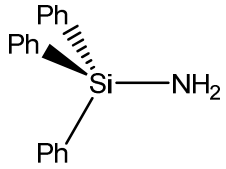

Compound was prepared according to a published procedure.[2]

Slow addition of an Et_2O (200 ml) solution of Ph_3SiCl (29.35 g, 100 mmol) to a stirred Et_2O (300 ml) solution of NH_3 (30ml) at –78 ^oC afforded a white precipitate. The solution was allowed to warm to room temperature and stirred for 48 hr. The solution was filtered and dried *in vacuo* to yield [Ph_3SiNH_2], **1**, as a white powder.
Yield 24.93 g, 91 %.

^1H NMR (300 MHz, $CDCl_3$):
δ_H 7.66-7.60 (m, 6H, meta-C_6H_5), 7.47-7.34 (br m, 9H, ortho- and para-C_6H_5), 1.29 (br s, 2H, NH).

$^{13}C\{^1H\}$ NMR (75.5 MHz, $CDCl_3$):
δ_C 136.4 (ipso C), 135.1 (s, 2C, meta), 129.6 (s, 1C, para), 127.8 (s, 2C, ortho)

Analysis:
Calc.: C%, 78.50; H%, 6.22; N%, 5.09 and found: C%, 77.32; H%, 6.09; N%, 4.21.

6.2.2 Synthesis of [Ph_2HSiNH_2] (2)

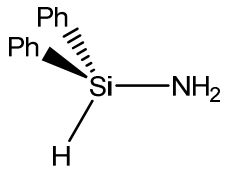

Compound was prepared according to a published procedure for the synthesis of [$^tBu_2HSiNH_2$].[2]

Slow addition of a Et_2O (50 ml) solution of Ph_2HSiCl (9.78 ml, 50 mmol) to a stirred Et_2O (50 ml) solution of NH_3 (15ml) at –78 ^oC afforded a white precipitate. The solution was allowed to warm to room temperature and stirred for 48 hr. The solution was filtered and dried *in vacuo* to yield a pale yellow oil. Distillation of the oil under reduced pressure at 110^oC yielded [Ph_2HSiNH_2], **2**, as a colourless liquid.
Yield 2.69 g, 27 %.

^1H NMR (300 MHz, $CDCl_3$):
δ_H 7.62-7.49 (br m, 4H, meta-C_6H_5), 7.35-7.24 (br m, 6H, ortho- and para-C_6H_5), 5.27 (s, 1H, SiH), 0.94 (br s, 2H, NH).

$^{13}C\{^1H\}$ NMR (75.5 MHz, $CDCl_3$):
δ_C 136.6 (ipso C), 135.0 (s, 2C, meta), 130.4 (s, 1C, para), 128.4 (s, 2C, ortho).

6.2.3 Synthesis of [Et_3SiNH_2] (3)

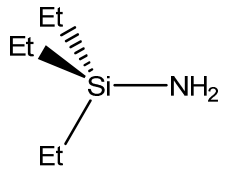

Compound was prepared according to a published procedure.[2]

Through a stirred benzene (100 ml) solution of Et_3SiCl (17 ml, 101 mmol) NH_3 was slowly bubbled for 1 hr at 0^oC, affording a white precipitate. The solution was filtered and the solvent distilled off under nitrogen to yield a colourless liquid. Further distillation of this liquid under nitrogen yielded a colourless liquid of [Et_3SiNH_2], **3**, at 135-136^oC.
Yield 4.18 g, 31 %

^1H NMR (300 MHz, $CDCl_3$):
δ_H 0.94 (t, 9H, $CH_2C\underline{H}_3$, $^3J_{\underline{CH}2\text{-}CH3}$ 8.0), 0.50 (q, 6H, $C\underline{H}_2CH_3$, $^3J_{CH2\text{-}CH3}$ 8.0), 0.30 (br s, 2H, NH_2).

$^{13}C\{^1H\}$ NMR (75.5 MHz, $CDCl_3$):

δ_C 6.93 (s, 1C, $CH_2\underline{CH_3}$), 5.76 (s, 1C, $\underline{CH_2}CH_3$,).

^{29}Si NMR (99.35 MHz, C_6D_6):

δ_{Si} 7.06

Analysis:

Calc.: C%, 54.96; H%, 12.98; N%, 10.69 and found: C%, 56.70; H%, 12.90; N%, 10.80.

6.2.4 Synthesis of [^{t}BuMe$_2$SiNH$_2$] (4)

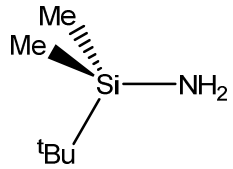

Compound was prepared according to a published procedure.[3]

Slow addition of a pentane (20 ml) solution of ^{t}BuMe$_2$SiCl (7.53 g, 50 mmol) to a stirred pentane (100 ml) solution of NH_3 (15ml) at –78 ^{o}C afforded a white precipitate. The solution was allowed to warm to room temperature and stirred for 24 hr. The solution was filtered and the solvent distilled off under nitrogen to yield a colourless liquid. Further distillation of this liquid under nitrogen yielded a colourless liquid of [^{t}BuMe$_2$SiNH$_2$], **4**, which crystallised to a white solid upon cooling

Yield 5.02 g, 76 %.

^1H NMR (300 MHz, $CDCl_3$):

δ_H 0.88 (s, 9H, Si^{t}Bu), 0.34 (br s, 2H, NH), 0.01 (s, 6H, SiMe).

$^{13}C\{^1H\}$ NMR (75.5 MHz, C_6D_6):

δ_C 26.2(s, 3C, C($\underline{Me}$)$_3$), 17.9 (s, 1C, $\underline{C}$(Me)$_3$), -3.51 (s, 2C, SiMe).

^{29}Si NMR (99.35 MHz, C_6D_6):

δ_{Si} 8.02

Analysis:

Calc.: C%, 54.96; H%, 12.98; N%, 10.69 and found: C%, 54.85; H%, 13.05; N%, 10.75.

6.2.5 Synthesis of $[(Me_2N)_3SiNH_2]$ (5)

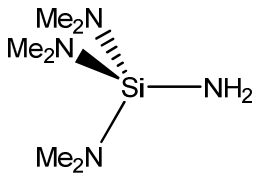

Compound was prepared according to a published procedure.[4]

Slow addition of $SiCl_4$ (32 ml, 280 mmol) to a stirred Et_2O (1000 ml) solution of anhydrous Me_2NH (130ml) at –78 ^oC afforded a white precipitate. The solution was allowed to warm to room temperature and stirred for 24 hr. The white precipitate of was removed by filtration to yield a colourless liquid. Through the colourless liquid NH_3 was slowly bubbled with stirring for 1 hr at 0^oC, affording a white precipitate. The solution was filtered at room temperature and the solvent distilled off under nitrogen to yield a colourless liquid. Further distillation of this liquid under nitrogen yielded a colourless liquid of $[(Me_2N)_3SiNH_2]$, **5**, at 170-180^oC.

Yield 28.69 g, 58 %.

^1H NMR (300 MHz, C_6D_6):

δ_H 2.51 (s, 9H, NMe_2), 0.25 (br s, 2H, NH).

$^{13}C\{^1H\}$ NMR (75.5 MHz, C_6D_6):

δ_C 37.9.

^{29}Si NMR (99.36 MHz, C_6D_6):

δ_{Si} –34.1.

Analysis:

Calc.: C%, 40.91; H%, 11.36; N%, 31.82 and found: C%, 40.05; H%, 11.10; N%, 32.05.

6.2.6 Synthesis of [{$(Me_2N)_2Ti(\mu_2\text{-}NSiPh_3)\}_2$] (6)

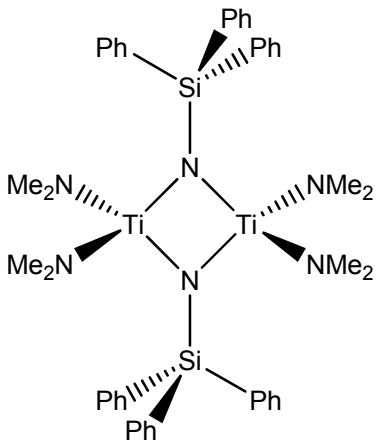

A stirred toluene (20 ml) solution of Ph_3SiNH_2, **1**, (1.11 g, 4 mmol) was treated with a toluene solution (30 ml) of $Ti(NMe_2)_4$ (0.90 g, 4 mmol). Solution was refluxed for 24 h, and the volume then halved under reduced pressure. Crystallisation from the reaction solution at –28 ^oC afforded [{$(Me_2N)_2Ti(\mu_2\text{-}NSiPh_3)\}_2$], **6**, as orange crystals.

Yield 0.69 g, 45 %.

^1H NMR (300 MHz, C_6D_6):

δ_H 7.72-7.63 (br m, 6H, meta-C_6H_5), 7.17-7.03 (br m, 9H, ortho- and para-C_6H_5), 2.92 (s, 12H, NMe_2).

$^{13}C\{^1H\}$ NMR (75.5 MHz, C_6D_6):

δ_C 139.2, 137.2, 136.0, 135.6, 129.7, 129.2, 45.0.

Analysis:

Calc.: C%, 64.57; H%, 6.60; N%, 10.27 and found: C%, 61.36; H%, 5.78; N%, 5.71.

6.2.7 Synthesis of [{$(Me_2N)_2Zr(\mu_2\text{-}NSiPh_3)\}_2$] (7)

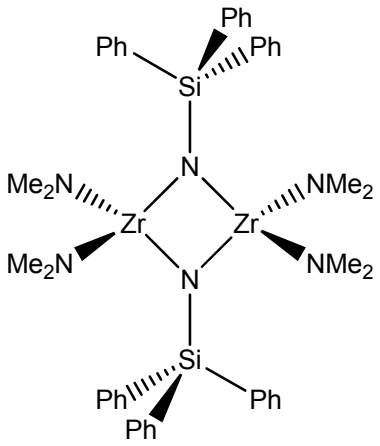

A stirred toluene (30ml) solution of Ph_3SiNH_2, **1**, (2.75 g, 10 mmol) was treated with a toluene (20ml) solution of $Zr(NMe_2)_4$ (2.67 g, 10 mmol). Solution was refluxed at 70°C for 24 h, and the volume then reduced under reduced pressure. Crystallisation from the reaction solution at –28°C affords [{$(Me_2N)_2Zr(\mu_2\text{-}NSiPh_3)\}_2$], **7**, as white crystals.
Yield 2.48 g, 55 %.

^{1}H NMR (300 MHz, C_6D_6):
δ_H 7.87-7.83 (m, 6H, meta-C_6H_5), 7.27-7.17 (br m, 9H, ortho- and para-C_6H_5), 2.72 (s, 12H, NMe_2).

$^{13}C\{^1H\}$ NMR (75.5 MHz, C_6D_6):
δ_C 140.2, 135.9, 129.2, 127.9, 42.2.

Analysis:
Calc.: C%, 58.38; H%, 5.97; N%, 9.29 and found: C%, 54.05; H%, 5.39; N%, 7.61.

6.2.8 Synthesis of [{$(Me_2N)_2Hf(\mu_2\text{-}NSiPh_3)\}_2(HNMe_2)$] (8)

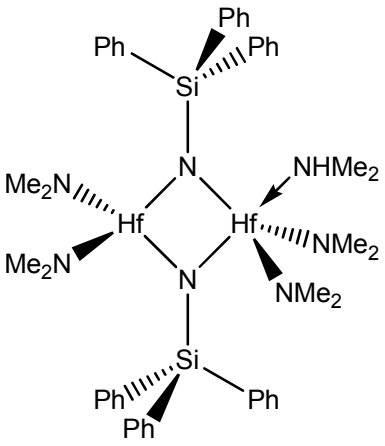

A stirred toluene (30ml) solution of Ph_3SiNH_2, **1**, (2.75g, 10mmol) was treated with a toluene (20ml) solution of $Hf(NMe_2)_4$ (3.56g, 10mmol). Solution was refluxed at 70°C for 24 h, and the volume then reduced under reduced pressure. Crystallisation from the reaction solution at –28°C afforded [{$(Me_2N)_2Hf(\mu_2\text{-}NSiPh_3)\}_2(HNMe_2)$], **8**, as white crystals.
Yield 3.20g, 57 %.

^1H NMR (300 MHz, C_6D_6):
δ_H 8.01-7.96 (m, 12H, meta-C_6H_5), 7.39-7.25 (br m, 18H, ortho- and para-C_6H_5), 2.86 (s, 24H, $HfNMe_2$), 1.60 (s, 6H, $HNMe_2$).

$^{13}C\{^1H\}$ NMR (75.5 MHz, C_6D_6):
δ_C 140.5, 139.5, 136.1, 136.0, 129.5, 129.3, 129.0, 128.6, 127.9, 127.7, 43.7, 42.4, 42.1.

^{29}Si NMR (99.35 MHz, C_6D_6):
δ_{Si} –31.83

Analysis:
Calc.: C%, 49.10; H%, 5.46; N%, 8.71 and found: C%, 47.16; H%, 5.44; N%, 8.05.

6.2.9 Synthesis of [{$(Me_2N)_2Ti(\mu_2\text{-}N^tBu)\}_2$] (9)

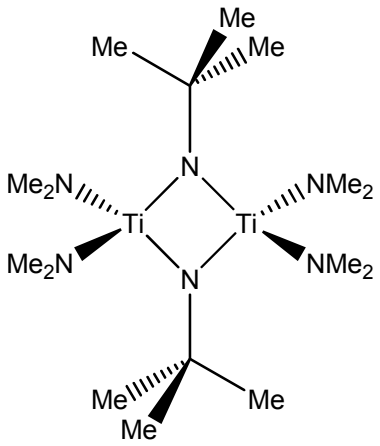

Complex was prepared according to a published procedure.[5]

A stirred hexane (60ml) solution of $Ti(NMe_2)_4$ (22.42g, 100mmol) was treated with $^tBuNH_2$ (10.51ml, 100mmol), affording a dark red solution. After stirring for 24 h volatiles were removed *in vacuo*. Recrystallisation of the residue from hexane at –28°C yielded [{$(Me_2N)_2Ti(\mu_2\text{-}N^tBu)\}_2$], **9**, as dark red crystals.
Yield 13.52 g, 65 %.

^1H NMR (300 MHz, C_6D_6):
δ_H 3.39 (s, 4H, NMe_2), 1.21 (s, 3H, N^tBu).

$^{13}C\{^1H\}$ NMR (75.5 MHz, C_6D_6):
δ_C 69.6 (s, 1C, $\underline{C}(Me)_3$), 45.8 (s, 4C, NMe_2), 34.6 (s, 3C, $C(\underline{Me})_3$).

Analysis:
Calc.: C%, 46.40; H%, 10.15; N%, 20.30 and found: C%, 46.20; H%, 10.10; N%, 20.20.

6.2.10 Synthesis of [{$(Me_2N)_2Ti(\mu_2\text{-}NSiEt_3)\}_2$] (10)

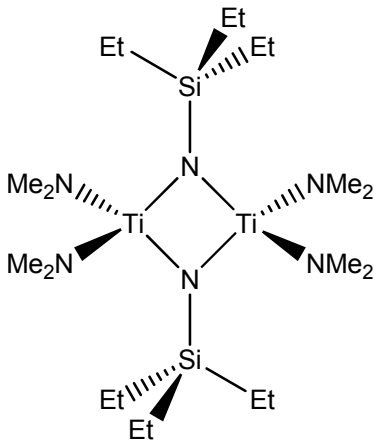

A stirred hexane (20 ml) solution of Et_3SiNH_2, **3**, (9.96 g, 76 mmol) was treated with a hexane (30 ml) solution of $Ti(NMe_2)_4$ (17.04 g, 76 mmol). After stirring for 24 h volatiles were removed *in vacuo*. Recrystallisation of the residue from hexane at –28 ^oC yielded [{$(Me_2N)_2Ti(\mu_2\text{-}NSiEt_3)\}_2$], **10**, as orange crystals.

Yield 10.92 g, 54 %.

^1H NMR (300 MHz, C_6D_6):

δ_H 3.30 (s, 4H, NMe_2), 1.07 (t, 3H, $CH_2C\underline{H}_3$, $^3J_{\underline{CH}2\text{-}CH3}$ 7.8), 0.57 (q, 2H, $C\underline{H}_2CH_3$, $^3J_{CH2\text{-}CH3}$ 7.8).

$^{13}C\{^1H\}$ NMR (75.5 MHz, C_6D_6):

δ_C 45.6 (s, 4C, NMe_2), 8.27 (s, 3C, $CH_2\underline{C}H_3$), 7.45 (s, 3C, $\underline{C}H_2CH_3$,).

^{29}Si NMR (99.35 MHz, C_6D_6):

δ_{Si} –0.71

Analysis:

Calc.: C%, 45.30; H%, 10.19; N%, 15.86 and found: C%, 45.31; H%, 9.88; N%, 14.84.

6.2.11 Synthesis of [{$(Me_2N)_2Zr(\mu_2\text{-}NSiEt_3)\}_2$] (11)

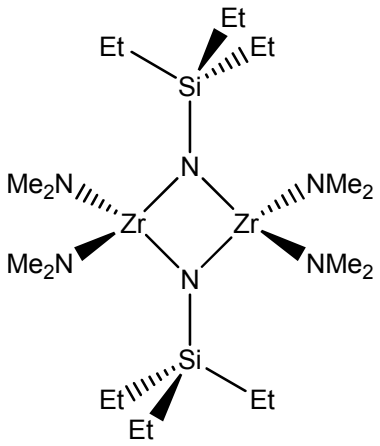

A stirred toluene (20 ml) solution of Et_3SiNH_2, **3**, (0.66 g, 5 mmol) was treated with a toluene (30 ml) solution of $Zr(NMe_2)_4$ (1.34 g, 5 mmol). After stirring for 24 h volatiles were removed *in vacuo*. Recrystallisation of the residue from hexane at –28°C afforded [{$(Me_2N)_2Zr(\mu_2\text{-}NSiEt_3)\}_2$], **11**, as pale yellow crystals. Due to an observed high solubility of **11** within hexane at room temperature crystals were isolated at –20°C using a NaCl ice bath.

Yield 0.33 g, 21 %.

^{1}H NMR (300 MHz, C_6D_6):

δ_H 3.10 (s, 4H, NMe_2), 1.10 (t, 3H, $CH_2C\underline{H}_3$, $^3J_{\underline{CH}2\text{-}CH3}$ 7.8), 0.58 (q, 2H, $C\underline{H}_2CH_3$, $^3J_{CH2\text{-}CH3}$ 7.8).

$^{13}C\{^1H\}$ NMR (75.5 MHz, C_6D_6):

δ_C 42.5 (s, 4C, NMe_2), 8.61 (s, 3C, $CH_2\underline{CH}_3$), 7.68 (s, 3C, $\underline{CH}_2CH_3$,).

Analysis:

Calc.: C%, 38.93; H%, 8.76; N%, 13.63 and found: C%, 33.84; H%, 7.56; N%, 10.46.

6.2.12 Synthesis of [{$(Me_2N)_2Hf(\mu_2\text{-}NSiEt_3)\}_2$] (12)

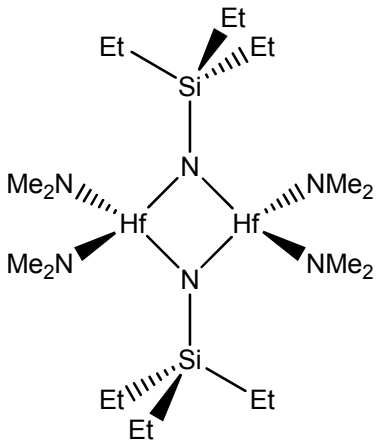

A stirred toluene (20 ml) solution of Et_3SiNH_2, **3**, (0.52 g, 4 mmol) was treated with a toluene (30 ml) solution of $Hf(NMe_2)_4$ (1.42g, 4 mmol). After stirring for 24 h volatiles were removed *in vacuo*. Recrystallisation of the residue from hexane at –28°C afforded [{$(Me_2N)_2Hf(\mu_2\text{-}NSiEt_3)\}_2$], **12**, as colourless crystals. Due to an observed high solubility of **12** within hexane at room temperature crystals were isolated at –20°C using a NaCl ice bath.

Yield 0.30 g, 19 %.

^{1}H NMR (300 MHz, C_6D_6):

δ_H 3.05 (s, 4H, NMe_2), 1.09 (t, 3H, $CH_2C\underline{H_3}$, $^3J_{\underline{CH2}\text{-}CH3}$ 7.5), 0.56 (q, 2H, $C\underline{H_2}CH_3$, $^3J_{CH2\text{-}CH3}$ 7.5).

$^{13}C\{^1H\}$ NMR (75.5 MHz, C_6D_6):

δ_C 42.1 (s, 4C, NMe_2), 8.74 (s, 3C, $CH_2\underline{CH_3}$), 7.58 (s, 3C, $\underline{CH_2}CH_3$,).

^{29}Si NMR (99.35 MHz, C_6D_6):

δ_{Si} –4.87

Analysis:

Calc.: C%, 30.34; H%, 6.83; N%, 10.62 and found: C%, 29.42; H%, 6.80; N%, 9.80.

6.2.13 Synthesis of [{$(Me_2N)_2Ti(\mu_2\text{-}NSi^tBuMe_2)\}_2$] (13)

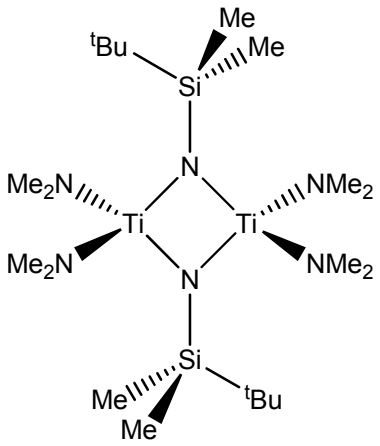

A stirred hexane (40 ml) solution of $^tBuMe_2SiNH_2$, **4**, (1.60 g, 12.2 mmol) was treated with a hexane (60 ml) solution of $Ti(NMe_2)_4$ (2.74 g, 12.2 mmol). After stirring for 24 h volatiles were removed *in vacuo*. Recrystallisation of the residue from hexane at –28°C yielded [{$(Me_2N)_2Ti(\mu_2\text{-}NSi^tBuMe_2)\}_2$], **13**, as orange crystals.
Yield 2.23 g, 69 %.

^{1}H NMR (300 MHz, C_6D_6):
δ_H 3.32 (s, 4H, NMe_2), 0.98 (s, 3H, Si^tBu), 0.15 (s, 2H, SiMe).

$^{13}C\{^1H\}$ NMR (75.5 MHz, C_6D_6):
δ_C 45.6 (s, 4C, NMe_2), 26.5 (s, 3C, $C(\underline{Me})_3$), 18.6 (s, 1C, $\underline{C}(Me)_3$), -0.70 (s, 2C, SiMe).

^{29}Si NMR (99.35 MHz, C_6D_6):
δ_{Si} –1.07

Analysis:
Calc.: C%, 45.30; H%, 10.19; N%, 15.86 and found: C%, 45.41; H%, 9.92; N%, 14.96.

6.2.14 Synthesis of [{$(Me_2N)_2Zr(\mu_2\text{-}NSi^tBuMe_2)\}_2$] (14)

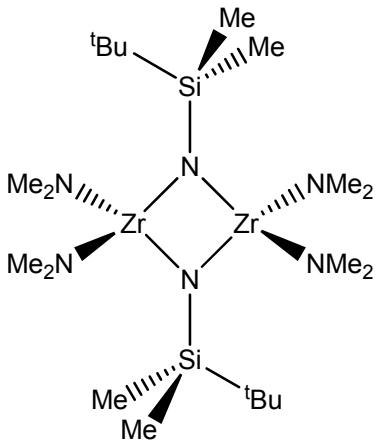

A stirred hexane (15 ml) solution of $^tBuMe_2SiNH_2$, **4**, (0.52 g, 4 mmol) was treated with a hexane (25 ml) solution of $Zr(NMe_2)_4$ (1.07 g, 4 mmol). After stirring for 24 h volatiles were removed *in vacuo*. Recrystallisation of the residue from hexane at –28°C yielded [{$(Me_2N)_2Zr(\mu_2\text{-}NSi^tBuMe_2)\}_2$], **14**, as colourless crystals.
Yield 0.83 g, 67 %.

^{1}H NMR (300 MHz, C_6D_6):
δ_H 3.10 (s, 4H, NMe_2), 1.00 (s, 3H, Si^tBu), 0.14 (s, 2H, SiMe).

$^{13}C\{^1H\}$ NMR (75.5 MHz, C_6D_6):
δ_C 42.39 (s, 4C, NMe_2), 26.21 (s, 3C, $C(\underline{Me})_3$), 18.04 (s, 1C, $\underline{C}(Me)_3$), -0.89 (s, 2C, SiMe).

^{29}Si NMR (99.35 MHz, C_6D_6):
δ_{Si} –7.03

Analysis:
Calc.: C%, 38.93; H%, 8.76; N%, 13.63 and found: C%, 38.42; H%, 8.46; N%, 12.75.

6.2.15 Synthesis of [{$(Me_2N)_2Hf(\mu_2\text{-}NSi^tBuMe_2)\}_2$] (15)

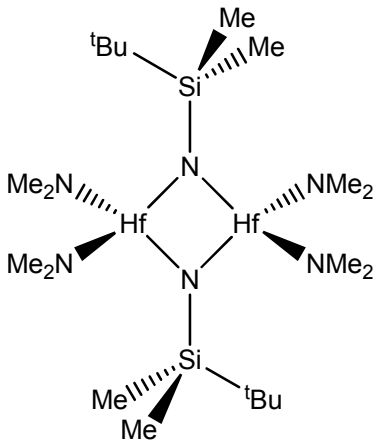

A stirred hexane (15 ml) solution of $^tBuMe_2SiNH_2$, **4**, (0.26 g, 2 mmol) was treated with a hexane (25 ml) solution of $Hf(NMe_2)_4$ (0.71 g, 2 mmol). After stirring for 24 h volatiles were removed *in vacuo*. Recrystallisation of the residue from hexane at –28 ^oC yielded [{$(Me_2N)_2Hf(\mu_2\text{-}NSi^tBuMe_2)\}_2$], **15**, as colourless crystals.
Yield 0.27 g, 34 %.

^1H NMR (300 MHz, C_6D_6):
δ_H 3.14 (s, 4H, NMe_2), 1.00 (s, 3H, Si^tBu), 0.12 (s, 2H, SiMe).

$^{13}C\{^1H\}$ NMR (75.5 MHz, C_6D_6):
δ_C 42.04 (s, 4C, NMe_2), 26.14 (s, 3C, $C(\underline{Me})_3$), 18.20 (s, 1C, $\underline{C}(Me)_3$), -0.75 (s, 2C, SiMe).

^{29}Si NMR (99.35 MHz, C_6D_6):
δ_{Si} –5.02

Analysis:
Calc.: C%, 30.34; H%, 6.83; N%, 10.62 and found: C%, 29.69; H%, 6.56; N%, 9.52.

6.2.16 Synthesis of [{$(Me_2N)_2Ti(\mu_2\text{-}NSi[NMe_2]_3)\}_2$] (16)

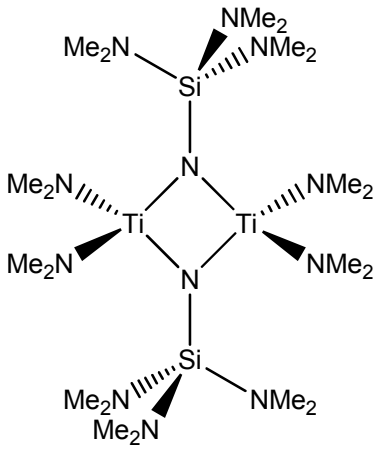

A stirred hexane (60 ml) solution of $(Me_2N)_3SiNH_2$, **5**, (11.26 g, 64 mmol) was treated with a hexane (40 ml) solution of $Ti(NMe_2)_4$ (14.35 g, 64 mmol). After stirring for 24 h volatiles were removed *in vacuo*. Recrystallisation of the residue from hexane at –28°C yielded [{$(Me_2N)_2Ti(\mu_2\text{-}NSi^tBuMe_2)\}_2$], **16**, as orange crystals.
Yield 10.95 g, 55 %.

^{1}H NMR (300 MHz, C_6D_6):
δ_H 3.29 (s, 2H, $Ti(NMe_2)_2$), 2.56 (s, 3H, $Si(NMe_2)_3$).

$^{13}C\{^1H\}$ NMR (75.5 MHz, C_6D_6):
δ_C 45.0 (s, 2C, $Ti(N\underline{Me}_2)_2$), 38.1 (s, 3C, $Si(N\underline{Me}_2)_3$).

^{29}Si NMR (99.35 MHz, C_6D_6):
δ_{Si} -49.46

Analysis:
Calc.: C%, 38.72; H%, 9.68; N%, 27.11 and found: C%, 36.88; H%, 8.10; N%, 24.54.

6.2.17 Synthesis of [{$(Me_2N)_2Zr(\mu_2\text{-}NSi[NMe_2]_3)\}_2$] (17)

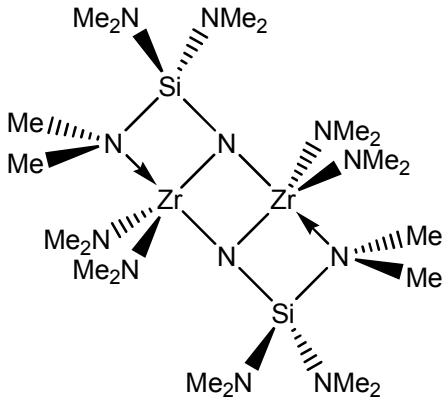

A stirred hexane (20 ml) solution of $(Me_2N)_3SiNH_2$, **5**, (0.88 g, 5 mmol) was treated with a hexane (20 ml) solution of $Zr(NMe_2)_4$ (1.34 g, 5 mmol). After stirring for 24 h the volume was then reduced under reduced pressure. Crystallisation from the reaction solution at –28°C yielded [{$(Me_2N)_2Zr(\mu_2\text{-}NSi^tBuMe_2)\}_2$], **17**, as colourless crystals.
Yield 1.10 g, 62 %.

^{1}H NMR (300 MHz, C_6D_6):
δ_H 3.01 (s, 2H, $Zr(NMe_2)_2$), 2.62 (s, 3H, $Si(NMe_2)_3$).

$^{13}C\{^1H\}$ NMR (75.5 MHz, C_6D_6):
δ_C 42.7 (s, 2C, $Zr(N\underline{Me}_2)_2$), 40.0 (s, 3C, $Si(N\underline{Me}_2)_3$).

^{29}Si NMR (99.35 MHz, C_6D_6):
δ_{Si} –48.03

Analysis:
Calc.: C%, 33.97; H%, 8.49; N%, 23.78 and found: C%, 33.82; H%, 8.78; N%, 22.94.

6.2.18 Synthesis of [{$(Me_2N)_2Hf(\mu_2\text{-}NSi[NMe_2]_3)\}_2$] (18)

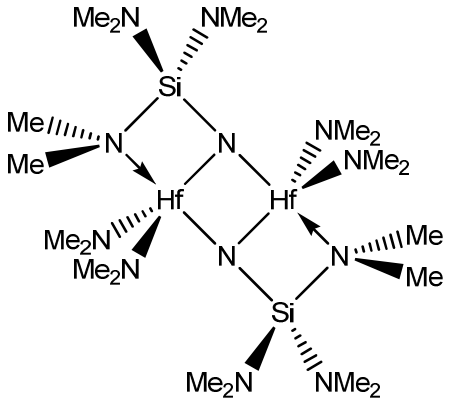

A stirred hexane (20 ml) solution of $(Me_2N)_3SiNH_2$, **5**, (0.88 g, 5 mmol) was treated with a hexane (20 ml) solution of $Hf(NMe_2)_4$ (1.77 g, 5 mmol). After stirring for 24 h the volume was then reduced under reduced pressure. Crystallisation from the reaction solution at –28°C yielded [{$(Me_2N)_2Hf(\mu_2\text{-}NSi^tBuMe_2)\}_2$], **18**, as colourless crystals.
Yield 1.48 g, 67 %.

^{1}H NMR (300 MHz, Tol):
δ_H 3.02 (s, 2H, $Hf(NMe_2)_2$), 2.60 (s, 3H, $Si(NMe_2)_3$).

$^{13}C\{^1H\}$ NMR (75.5 MHz, Tol):
δ_C 43.6 (s, 2C, $Hf(NMe_2)_2$), 40.9 (s, 3C, $Si(NMe_2)_3$).

^{29}Si NMR (99.35 MHz, C_6D_6):
δ_{Si} –44.96

Analysis:
Calc.: C%, 27.24; H%, 6.81; N%, 19.07 and found: C%, 27.10; H%, 6.80; N%, 18.14.

6.3 Experimental for Chapter 3

6.3.1 Synthesis of [$Me_2Si(NH^tBu)_2$] (19)

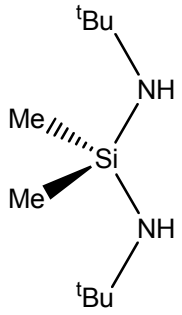

Compound was prepared according to a published procedure.[6]

Slow addition of $^tBuNH_2$ (42.0 ml, 0.4 mol) to a stirred hexane (250 ml) solution of Me_2SiCl_2 (12.0 ml, 0.1 mol) afforded a white precipitate. After stirring for 12 h the solution was filtered and washed with hexane. The filtrate was dried *in vacuo* to yield [$Me_2Si(NH^tBu)_2$], **19**, as a viscous colourless liquid.
Yield 14.47 g, 72 %.

^1H NMR (300 MHz, C_6D_6):
δ_H 1.18 (s, 9H, N^tBu), 0.52 (br s, 1H, NH), 0.17 (s, 3H, SiMe).

$^{13}C\{^1H\}$ NMR (75.5 MHz, C_6D_6):
δ_C 49.2 (s, 1C, $\underline{C}(Me)_3$), 33.8 (s, 3C, $C(\underline{Me})_3$), 3.70 (s, 1C, SiMe).

^{29}Si NMR (99.35 MHz, C_6D_6):
δ_{Si} –17.48

Analysis:
Calc.: C%, 59.41; H%, 12.87; N%, 13.86 and found: C%, 57.50; H%, 12.50; N%, 13.75.

6.3.2 Synthesis of $[Me_2Si(NH^iPr)_2]$ (20)

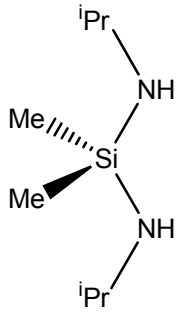

Compound was prepared according to a published procedure.[6]

Slow addition of $^iPrNH_2$ (34.3 ml, 0.4 mol) to a stirred hexane (250 ml) solution of Me_2SiCl_2 (12.0 ml, 0.1 mol) afforded a white precipitate. After stirring for 12 h the solution was filtered and washed with hexane. The filtrate was dried *in vacuo* to yield $[Me_2Si(NH^iPr)_2]$, **20**, as a volatile colourless liquid.
Yield 2.93 g, 12 %.

^1H NMR (300 MHz, C_6D_6):
δ_H 3.09 (d of sept, 1H, C<u>H</u>$(Me)_2$, $^3J_{C\underline{H}\text{-}N\underline{H}}$ 10.5, $^3J_{C\underline{H}\text{-}\underline{Me}}$ 6.3), 1.02 (d, 6H, CH($\underline{Me}$)$_2$, $^3J_{C\underline{H}\text{-}\underline{Me}}$ 6.3), 0.29 (br s, 1H, NH), 0.06 (s, 3H, SiMe).

$^{13}C\{^1H\}$ NMR (75.5 MHz, C_6D_6):
δ_C 42.5 (s, 1C, <u>C</u>H$(Me)_2$), 28.1 (s, 2C, CH($\underline{Me}$)$_2$), -0.07 (s, 1C, SiMe).

6.3.3 Synthesis of $[Me_2Si(NHCH_2CH_2NMe_2)_2]$ (21)

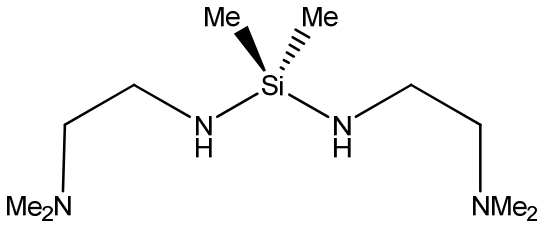

Compound was prepared according to a published procedure.[7]

Slow addition of $Me_2NCH_2CH_2NH_2$ (44.1 ml, 0.4 mol) to a stirred hexane (250 ml) solution of Me_2SiCl_2 (12.0 ml, 0.1 mol) afforded a white precipitate. After stirring for 12 h the solution was filtered and washed

with hexane. The filtrate was dried *in vacuo* to yield $[Me_2Si(NHCH_2CH_2NMe_2)_2]$, **21**, as a viscous colourless liquid.
Yield 18.81 g, 81 %.

^1H NMR (300 MHz, C_6D_6):
δ_H 2.87 (ap q, 2H, $NHC\underline{H}_2CH_2$, $^3J_{NH\text{-}\underline{CH2}\text{-}CH2}$ 6.3), 2.23 (t, 2H, $CH_2C\underline{H}_2NMe_2$, $^3J_{CH2\text{-}CH2}$ 6.3), 2.09 (s, 6H, NMe_2), 1.16 (br s, 1H, NH), 0.10 (s, 3H, SiMe).

$^{13}C\{^1H\}$ NMR (75.5 MHz, C_6D_6):
δ_C 63.5 (s, 1C, $NH\underline{C}H_2$), 45.5 (s, 2C, NMe_2), 39.2 (s, 1C, $\underline{C}H_2NMe_2$), -1.23 (s, 1C, SiMe).

6.3.4 Synthesis of $[Ph_2Si(NH^tBu)_2]$ (22)

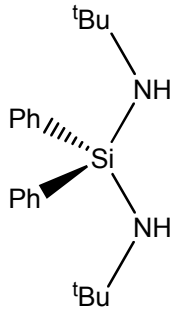

Compound was prepared according to a published procedure for the synthesis of $[(2,6\text{-}^iPr_2C_6H_3NH)_2SiPh_2]$.[8]

A stirred hexane (250 ml) solution of $^tBuNH_2$ (10.5 ml, 100 mmol) was treated with ^{n}Buli (2.5 M, 40 ml, 100 mmol) at –78 ^oC. The solution was allowed to warm to room temperature, then slowly refluxed for 30 min. Slow addition of Ph_2SiCl_2 (10.5 ml, 50 mmol) at –78 ^oC afforded a white precipitate. After allowing to warm to room temperature the solution was filtered and washed with hexane. The filtrate was dried *in vacuo* to yield $[Ph_2Si(NH^tBu)_2]$, **22**, as a colourless liquid.
Yield 11.07 g, 68 %.

^1H NMR (300 MHz, C_6D_6):

δ_H 7.76-7.69 (br m, 2H, meta-C_6H_5), 7.20-7.08 (br m, 3H, ortho- and para-C_6H_5), 1.34 (s, 1H, NH), 1.16 (s, 9H, N^{t}Bu).

$^{13}C\{^1H\}$ NMR (75.5 MHz, C_6D_6):
δ_C 140.4 (s, 1C), 135.3 (s, 2C), 129.1 (s, 1C), 127.9 (s, 2C), 50.0 (s, 1C, $\underline{C}(Me)_3$), 33.7 (s, 3C, $C(\underline{Me})_3$).

Analysis:
Calc.: C%, 73.56; H%, 9.26; N%, 8.58 and found: C%, 73.44; H%, 9.15; N%, 8.33.

6.3.5 Synthesis of [$Me_2Si(N[Li]^tBu)_2$] (23)

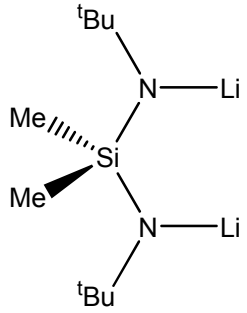

Complex was prepared according to a published procedure.[9]

A stirred hexane (150 ml) solution of [$Me_2Si(NH^tBu)_2$], **19**, (10.11 g, 50 mmol) was treated with ^{n}Buli (2.5 M, 40 ml, 100 mmol) at –78 ^{o}C. The solution was allowed to warm to room temperature, then slowly refluxed for 30 min. Volatiles were then removed *in vacuo*. Recrystallisation of the residue from hexane at –28 ^{o}C yielded [$Me_2Si(N[Li]^tBu)_2$], **23**, as colourless crystals.
Yield 8.46 g, 79 %.

^1H NMR (300 MHz, C_6D_6):
δ_H 1.23 (s, 3H, N^{t}Bu), 0.41 (s, 1H, SiMe).

$^{13}C\{^1H\}$ NMR (75.5 MHz, C_6D_6):
δ_C 51.5 (s, 1C, $\underline{C}(Me)_3$), 36.7 (s, 3C, $C(\underline{Me})_3$), 11.3 (s, 1C, SiMe).

^{29}Si NMR (99.35 MHz, C_6D_6):

δ_{Si} –15.39

^{7}Li NMR (194.37 MHz, C_6D_6):

δ_{Li} 1.67 (s)

6.3.6 Synthesis of [$Ph_2Si(N[Li]^tBu)_2$] (24)

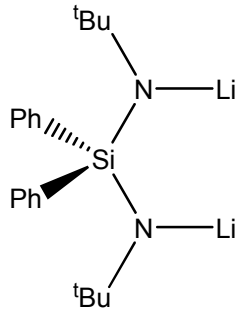

A stirred hexane (100 ml) solution of [$Ph_2Si(NH^tBu)_2$], **22**, (9.78 g, 30 mmol) was treated with ^{n}Buli (2.5 M, 24 ml, 60 mmol) at –78 ^{o}C. The solution was allowed to warm to room temperature, then slowly refluxed for 30 min. Volatiles were then removed *in vacuo*. Recrystallisation of the residue from hexane at –28 ^{o}C yielded [$Ph_2Si(N[Li]^tBu)_2$], **24**, as colourless crystals.

Yield 7.72 g, 76 %.

^{1}H NMR (300 MHz, C_6D_6):

δ_H 8.14 (m, 2H, meta-C_6H_5), 7.47-7.27 (br m, 3H, ortho- and para-C_6H_5), 1.25 (s, 9H, N^{t}Bu).

^{13}C{^{1}H} NMR (75.5 MHz, C_6D_6):

δ_C 145.8, 136.2, 135.3, 128.7, 51.9, 37.1.

6.3.7 Synthesis of [{$Me_2Si(N^tBu)_2$}$_2$Ti] (25)

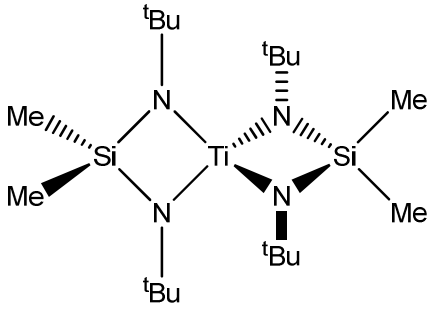

Slow addition of a Et_2O (20 ml) solution of $TiCl_4.2THF$ (3.34 g, 10 mmol) to a stirred Et_2O (60 ml) solution of [$Me_2Si(N[Li]^tBu)_2$], **23**, (4.29 g, 20 mmol) at –78 ^oC afforded a precipitate. After stirring for 24 h the solution was filtered and dried *in vacuo*. Recrystallisation of the residue from toluene at –28 ^oC yielded [{$Me_2Si(N^tBu)_2$}$_2$Ti], **25**, as green crystals.
Yield 1.32 g, 30 %.

^1H NMR (300 MHz, C_6D_6):
δ_H 1.34 (s, 3H, N^tBu), 0.50 (s, 1H, SiMe).

$^{13}C\{^1H\}$ NMR (75.5 MHz, C_6D_6):
δ_C 58.9 (s, 1C, $\underline{C}(Me)_3$), 35.7 (s, 3C, $C(\underline{Me})_3$), 5.80 (s, 1C, SiMe).

^{29}Si NMR (99.35 MHz, C_6D_6):
δ_{Si} -45.66

Analysis:
Calc.: C%, 53.59; H%, 10.72; N%, 12.50 and found: C%, 50.92; H%, 10.24; N%, 11.07.

6.3.8 Synthesis of [{$Ph_2Si(N^tBu)_2$}$_2$Ti] (26)

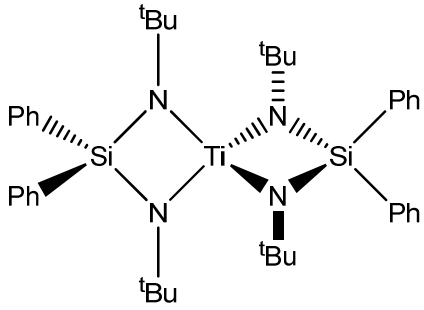

Slow addition of $TiCl_4$ (0.54 ml, 5 mmol) to a stirred Et_2O (60 ml) solution of [$Ph_2Si(N[Li]^tBu)_2$], **24**, (3.38g, 10 mmol) at –78 ^oC afforded a precipitate. After stirring for 24 h the solution was filtered and dried *in vacuo*. Isolation from toluene at –28 ^oC yielded [{$Ph_2Si(N^tBu)_2$}$_2$Ti], **26**, as a green powder.

Yield 0.11 g, 3 %.

^1H NMR (300 MHz, C_6D_6):

δ_H 8.10 (m, 2H, meta-C_6H_5), 7.66 (m, 3H, ortho- and para-C_6H_5), 1.32 (s, 9H, N^tBu).

$^{13}C\{^1H\}$ NMR (75.5 MHz, C_6D_6):

δ_C 138.0, 135.7, 130.2, 129.5, 61.0, 36.8.

Analysis:

Calc.: C%, 68.93; H%, 8.10; N%, 8.04 and found: C%, 57.34; H%, 5.68; N%, 3.02.

6.3.9 Synthesis of [Ti(N^tBu)Cl_2($py)_2$] (27)

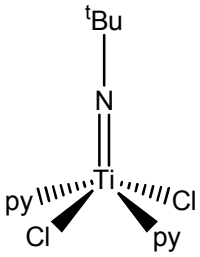

Complex was prepared according to a published procedure.[10]

Slow addition of $^{t}BuNH_2$ (20 ml, 190 mmol) to a stirred DCM (80 ml) solution of $TiCl_4$ (3.50 ml, 31.6 mmol) at –50 ^{o}C afforded an orange precipitate. After stirring for 2 h the solution was filtered. Pyridine (6.0 ml, 74.2 mmol) was added to the filtrate, and after stirring for 3 h volatiles were removed *in vacuo*. The residue was extracted into a 10:1 toluene: DCM (50 ml) solution, filtered, then dried *in vacuo* to yield the crude product. The residue was washed with hexane (2 x 20 ml) then dried *in vacuo* to yield pure $[Ti(N^{t}Bu)Cl_2(py)_2]$, **27**, as an orange powder.
Yield 8.68 g, 79 %.

^{1}H NMR (300 MHz, C_6D_6):
δ_H 9.53 (ap d, 4H, NC_5H_5), 8.87 (br s, 2H, NC_5H_5), 6.77 (ap t, 4H, NC_5H_5), 1.13 (s, 9H, $N^{t}Bu$).

$^{13}C\{^{1}H\}$ NMR (75.5 MHz, C_6D_6):
δ_C 152.2, 137.9, 123.6, 123.2, 30.8.

6.3.10 Synthesis of $[\{[Me_2Si(N^{t}Bu)_2]Ti(\mu_2\text{-}N^{t}Bu)\}_2]$ (28)

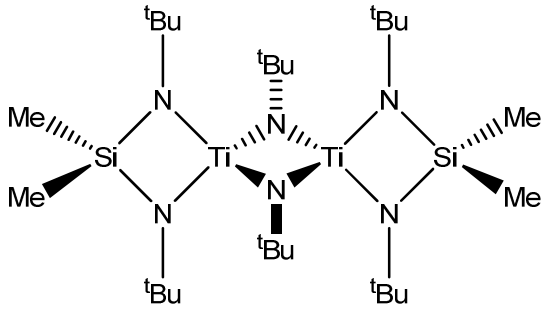

Slow addition of a Et_2O (20 ml) solution of $[Ti(N^{t}Bu)Cl_2(py)_2]$, **27**, (3.50 g, 10 mmol) to a stirred Et_2O (60 ml) solution of $[Me_2Si(N[Li]^{t}Bu)_2]$, **23**, (2.17 g, 10 mmol) at –78 ^{o}C afforded a precipitate. After stirring for 24 h the solution was filtered and dried *in vacuo*. Recrystallisation of the residue from toluene at –28 ^{o}C yielded $[\{[Me_2Si(N^{t}Bu)_2]Ti(\mu_2\text{-}N^{t}Bu)\}_2]$, **28**, as green crystals.
Yield 0.860 g, 27.0%.

^{1}H NMR (300 MHz, C_6D_6):
δ_H 1.61 (s, 6H, $N^{t}Bu$) 1.32 (s, 3H, $\mu_2\text{-}N^{t}Bu$), 0.46 (s, 2H, SiMe).

$^{13}C\{^1H\}$ NMR (75.5 MHz, C_6D_6):

δ_C 69.0, 59.8, 36.4, 6.36, 1.36.

^{29}Si NMR (99.35 MHz, C_6D_6):

δ_{Si} –45.89

Analysis:

Calc.: C%, 52.68; H%, 10.35; N%, 13.17 and found: C%, 51.34; H%, 9.49; N%, 12.76.

6.3.11 Synthesis of [{[$Ph_2Si(N^tBu)_2$]Ti(μ_2-N^tBu)}$_2$] (29)

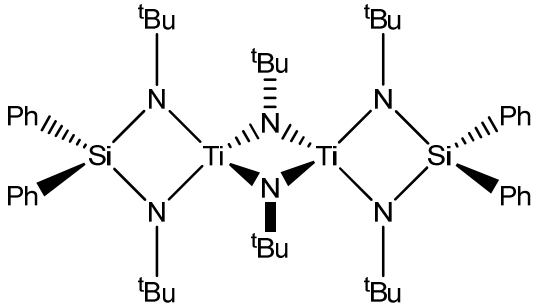

Slow addition of a Et_2O (20 ml) solution of [Ti(N^tBu)$Cl_2(py)_2$], **27**, (1.74 g, 5 mmol) to a stirred Et_2O (50 ml) solution of [$Ph_2Si(N[Li]^tBu)_2$], **24**, (1.69 g, 5 mmol) at –78 ^oC afforded a precipitate. After stirring for 24 h the solution was filtered and dried *in vacuo*. Isolation of the residue from toluene at –28^oC yielded [{[$Ph_2Si(N^tBu)_2$]Ti(μ_2-N^tBu)}$_2$], **29**, as an orange-brown powder.

Yield 0.196 g, 8.9%.

^1H NMR (300 MHz, C_6D_6):

δ_H 8.12 (m, 4H, meta-C_6H_5), 7.25-7.14 (br m, 6H, ortho- and para-C_6H_5), 1.28 (s, 18H, N^tBu), 1.10 (s, 9H, μ_2-N^tBu).

$^{13}C\{^1H\}$ NMR (75.5 MHz, C_6D_6):

δ_C 136.2, 133.9, 128.4, 126.5, 59.3, 35.0, 32.4.

Analysis:

Calc.: C%, 65.00; H%, 8.41; N%, 9.47 and found: C%, 56.32; H%, 5.96; N%, 2.98.

6.3.12 Synthesis of [{(Me$_3$SiNSiMe$_2$CH$_2$)Ti(N^{t}Bu)}$_2$] (30)

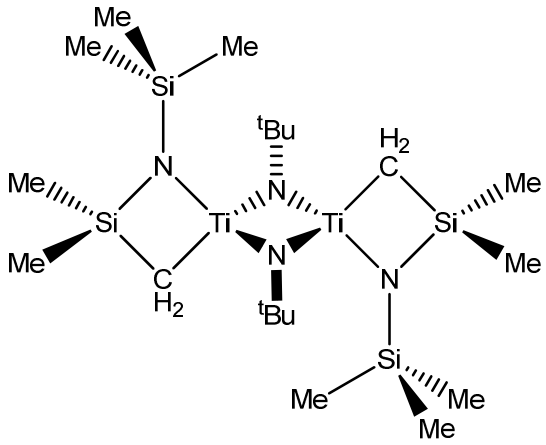

Slow addition of an orange Et_2O (20 ml) solution of [Ti(N^{t}Bu)Cl$_2$(py)$_2$], **27**, (1.74 g, 5 mmol) to a stirred colourless Et_2O (30 ml) solution of [LiN(SiMe$_3$)$_2$] (1.67 g, 10 mmol) at –78 ^oC afforded a dark green solution and a precipitate. After stirring for 24 h the solution was filtered and dried *in vacuo*. Recrystallisation of the residue from hexane at –28 ^oC yielded [{(Me$_3$SiNSiMe$_2$CH$_2$)Ti(N^{t}Bu)}$_2$], **30**, as red crystals.
Yield 0.34 g, 24 %.

Analysis:
Calc.: C%, 43.15; H%, 9.41; N%, 10.06 and found: C%, 41.86; H%, 9.06; N%, 9.16.

6.4 Experimental for Chapter 4

6.4.1 Synthesis of [$(Me_2N)_3TaNSiPh_3$] (31)

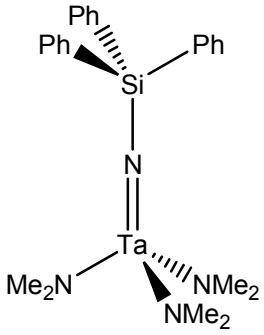

A stirred toluene (20 ml) solution of Ph_3SiNH_2, **1**, (0.57 g, 2 mmol) was treated with a toluene (10 ml) solution of $Ta(NMe_2)_5$ (0.83 g, 2 mmol). Solution was refluxed for 24 h, and the volume then reduced to a third under reduced pressure. Crystallisation from the reaction solution at –28 ^oC yielded [$(Me_2N)_3TaNSiPh_3$], **31**, as colourless crystals.
Yield 0.173 g, 14.8 %.

^1H NMR (300 MHz, C_6D_6):
δ_H 7.94-7.87 (m, 2H, meta-C_6H_5), 7.21-7.08 (br m, 3H, ortho- and para-C_6H_5), 3.01 (s, 6H, NMe_2).

$^{13}C\{^1H\}$ NMR (75.5 MHz, C_6D_6):
δ_C 140.2, 135.9, 129.2, 127.9, 42.2.

$^{13}C\{^1H\}$ NMR (75.5 MHz, C_6D_6):
δ_C 138.5, 134.3, 127.8, 44.4.

Analysis:
Calc.: C%, 49.15; H%, 5.63; N%, 9.56 and found: C%, 52.40; H%, 5.44; N%, 7.60.

6.4.2 Synthesis of [$(Me_2N)_3TaNSi(NMe_2)_3$] (32)

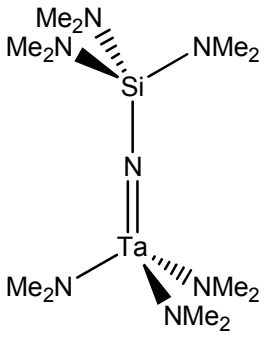

A stirred hexane (30 ml) solution of $(Me_2N)_3SiNH_2$, **5**, (3.52 g, 20 mmol) was treated with a hexane (20 ml) solution of $Ta(NMe_2)_5$ (8.02 g, 20 mmol). Solution was refluxed for 24 h, and the volume then reduced under reduced pressure. Crystallisation from the reaction solution at –28°C yielded [$(Me_2N)_3TaNSi(NMe_2)_3$], **32**, as colourless crystals.
Yield 5.8 g, 59 %.

^1H NMR (300 MHz, C_6D_6):
δ_H 3.20 (s, 1H, $TaNMe_2$), 2.76 (s, 1H, $SiNMe_2$).

$^{13}C\{^1H\}$ NMR (75.5 MHz, C_6D_6):
δ_C 46.0 (s, 1C, $TaNMe_2$), 38.1 (s, 1C, $SiNMe_2$).

^{29}Si NMR (99.35 MHz, C_6D_6):
δ_{Si} –51.21

Analysis:
Calc.: C%, 29.57; H%, 7.39; N%, 20.13 and found: C%, 27.10; H%, 6.98; N%, 18.70.

6.4.3 Synthesis of [{MeZnNHSiPh$_3$}$_2$] (33)

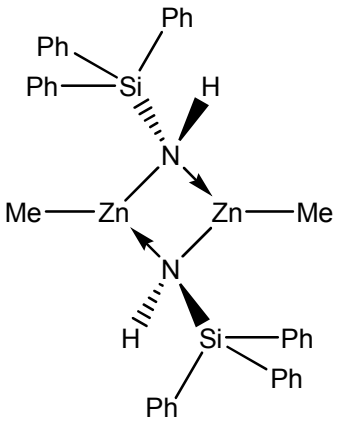

A stirred hexane (20 ml) solution of Ph_3SiNH_2, **1**, (1.38 g, 5 mmol) was treated with $ZnMe_2$ (2 M in toluene, 2.5 ml, 5 mmol). After stirring for 24 h a white precipitate formed. Volatiles were then removed *in vacuo*. Slow recrystallisation of the residue from hexane at room temperature yielded [{MeZnNHSi(NMe$_2$)$_3$}$_2$], **33**, as colourless crystals
Yield 1.05 g, 59 %.

^{1}H NMR (300 MHz, C_6D_6):
δ_H 7.74-7.63 (br m, 6H, meta-C_6H_5), 7.34-7.16 (br m, 9H, ortho- and para-C_6H_5), 0.01 (s, 1H, NH), -0.31 (s, 3H, ZnMe).

^{13}C{^{1}H} NMR (75.5 MHz, C_6D_6):
δ_C 138.5, 138.1, 130.5, 126.1 (C_6H_5), -9.2 (s, 1C, ZnMe).

^{29}Si NMR (99.35 MHz, C_6D_6):
δ_{Si} –11.86

Analysis:
Calc.: C%, 64.34; H%, 5.36; N%, 3.95 and found: C%, 64.74; H%, 5.38; N%, 3.95.

6.4.4 Synthesis of [{MeZnNHSi(NMe$_2$)$_3$}$_2$] (34)

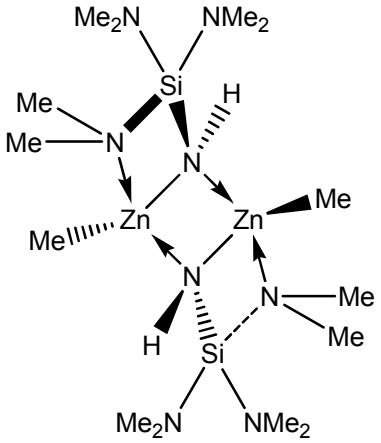

A stirred hexane (10 ml) solution of [(Me$_2$N)$_3$SiNH$_2$], **5**, (0.88 g, 5 mmol) was treated with ZnMe$_2$ (2 M in toluene, 2.5 ml, 5 mmol). After stirring for 24 h volatiles were then removed *in vacuo*. Recrystallisation of the residue from hexane at –28 ^{o}C yielded [{MeZnNHSi(NMe$_2$)$_3$}$_2$], **34**, as colourless crystals.

Yield 0.78 g, 61 %.

^{1}H NMR (300 MHz, C_6D_6):

δ_H 2.45 (s, 18H, NMe$_2$), 0.16 (s, 1H, NH), -0.25 (s, 3H, ZnMe).

^{13}C{^{1}H} NMR (75.5 MHz, C_6D_6):

δ_C 38.6 (s, 6C, NMe$_2$), -12.6 (s, 1C, ZnMe).

^{29}Si NMR (99.35 MHz, C_6D_6):

δ_{Si} –28.70

Analysis:

Calc.: C%, 32.89; H%, 8.61; N%, 21.93 and found: C%, 32.76; H%, 8.48; N%, 21.26.

6.4.5 Synthesis of [{(MeCp)MnNHSiPh$_3$}$_2$] (35)

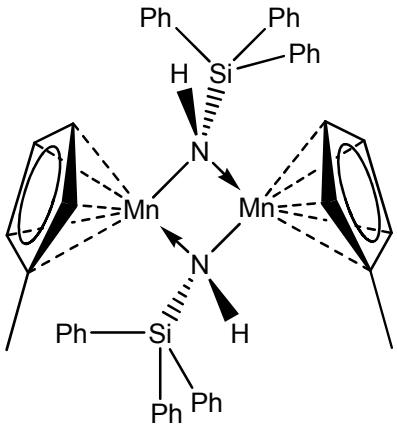

A stirred hexane (10 ml) solution of [Ph_3SiNH_2], **1**, (1.375 g, 5 mmol) was treated with a hexane (20 ml) solution of [$(MeCp)_2Mn$] (1.066 g, 5 mmol). Solution was refluxed for 24 h, and the volume then reduced to a third under reduced pressure. Crystallisation of the residue from the reaction solution at –28 ^oC yielded [{(MeCp)MnNHSiPh$_3$}$_2$], **35**, as brown crystals. Yield 0.52 g, 25 %.

Analysis:

Calc.: C%, 70.57; H%, 5.68; N%, 3.43 and found: C%, 61.44; H%, 4.84; N%, 2.62.

6.5 References for Chapter 6

1. H. E. Gottlieb, V. Kotlyar and A. Nudelman, *J. Org. Chem.*, 1997, **62**, 7512.
2. D. M. Choquette, M. J. Timm, J. L. Hobbs, M. M. Rahim, K. J. Ahmed and R. P. Planalp, *Organometallics*, 1992, **11**, 529.
3. J. R. Bowser, R. H. Neilson and R. L. Wells, *Inorg. Chem.*, 1978, **17**, 1882.
4. J. S. Bradley, F. Cheng, S. J. Archibald, R. Supplit, R. Rovai, C. W. Lehmann, C. Krüger and F. Lefebvre, *Dalton Trans.*, 2003, 1846.
5. W. A. Nugent and R. L. Harlow, *Inorg. Chem.*, 1979, **18**, 2030.
6. V. Passarelli, F. Benetollo, P. Zanella, G. Carta and G. Rossetto, *Dalton Trans.*, 2003, 1411.
7. V. Passarelli, F. Benetollo and P. Zanella, *Eur. J. Inorg. Chem.*, 2004, 1714.
8. R. Murugavel, N. Palanisami and R. J. Butcher, *J. Organomet. Chem.*, 2003, **675**, 65.
9. A. D. Horton and J. de With, *Organometallics*, 1997, **16**, 5424.
10. A. J. Blake, P. E. Collier, S. C. Dunn, W-S. Li, P. Mountford and O. V. Shishkin, *J. Chem. Soc., Dalton Trans.*, 1997, 1549.

Appendix A

Single Crystal X-ray Diffraction Data

7.1: Complex 6, [{$(Me_2N)_2Ti(\mu_2\text{-}NSiPh_3)\}_2$]

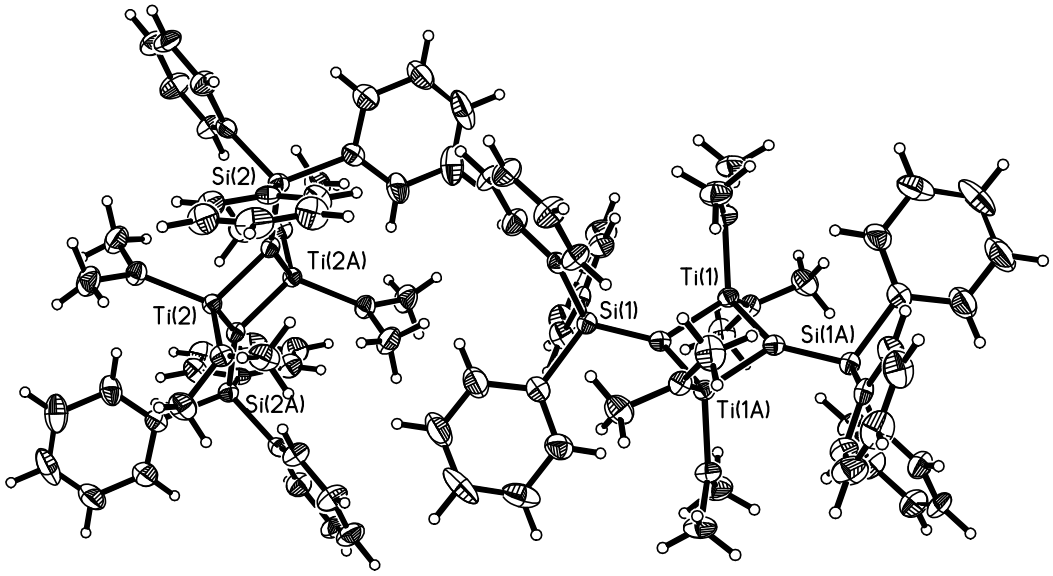

Figure 7.1.1: Asymmetric unit for the complex [{$(Me_2N)_2Ti(\mu_2\text{-}NSiPh_3)\}_2$], (**6**), containing two half dimers. The equivalent positions in each molecule are generated by symmetry operations.

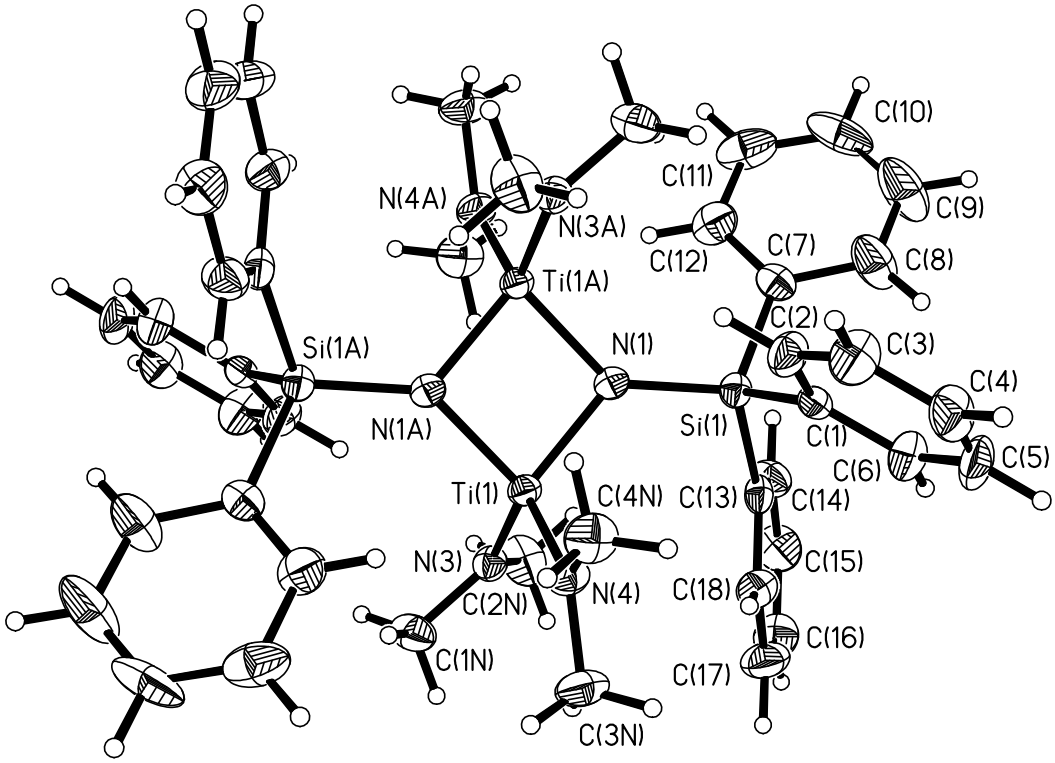

Figure 7.1.2: Molecular structure of the complex [{$(Me_2N)_2Ti(\mu_2\text{-}NSiPh_3)\}_2$], (**6**). Thermal ellipsoids are shown at 50 % probability and hydrogen atoms as hollow spheres.

Table 7.1:- Crystal data and structure refinement for [{$(Me_2N)_2Ti(\mu_2\text{-}NSiPh_3)\}_2$] (**6**).

Identification code	k03alj03
Empirical formula	C44 H54 N6 Si2 Ti2
Formula weight	818.91
Temperature	150(2) K
Wavelength	0.71073 Å
Crystal system	Triclinic
Space group	P-1
Unit cell dimensions	a = 12.8160(2) Å
	b = 13.0630(2) Å
	c = 13.0790(2) Å
	α= 87.2850(10)°.
	β= 89.9950(10)°.
	γ = 90.0000(10)°.
Volume	2187.17(6) $Å^3$
Z	2
Density (calculated)	1.243 Mg/m^3
Absorption coefficient	0.457 mm^{-1}
F(000)	864
Crystal size	0.25 x 0.25 x 0.20 mm^3
Theta range for data collection	8.20 to 20.81°.
Index ranges	-12<=h<=12, -13<=k<=13, -13<=l<=13
Reflections collected	23495
Independent reflections	4263 [R(int) = 0.0718]
Completeness to theta = 20.81°	93.3 %
Absorption correction	None
Max. and min. transmission	0.9142 and 0.8943
Refinement method	Full-matrix least-squares on F^2
Data / restraints / parameters	4263 / 0 / 496
Goodness-of-fit on F^2	0.997
Final R indices [I>2sigma(I)]	R1 = 0.0381, wR2 = 0.0847
R indices (all data)	R1 = 0.0551, wR2 = 0.0944
Extinction coefficient	0.000(2)
Largest diff. peak and hole	0.200 and -0.196 $e.Å^{-3}$

7.2: Complex 7, [{$(Me_2N)_2Zr(\mu_2\text{-}NSiPh_3)\}_2$]

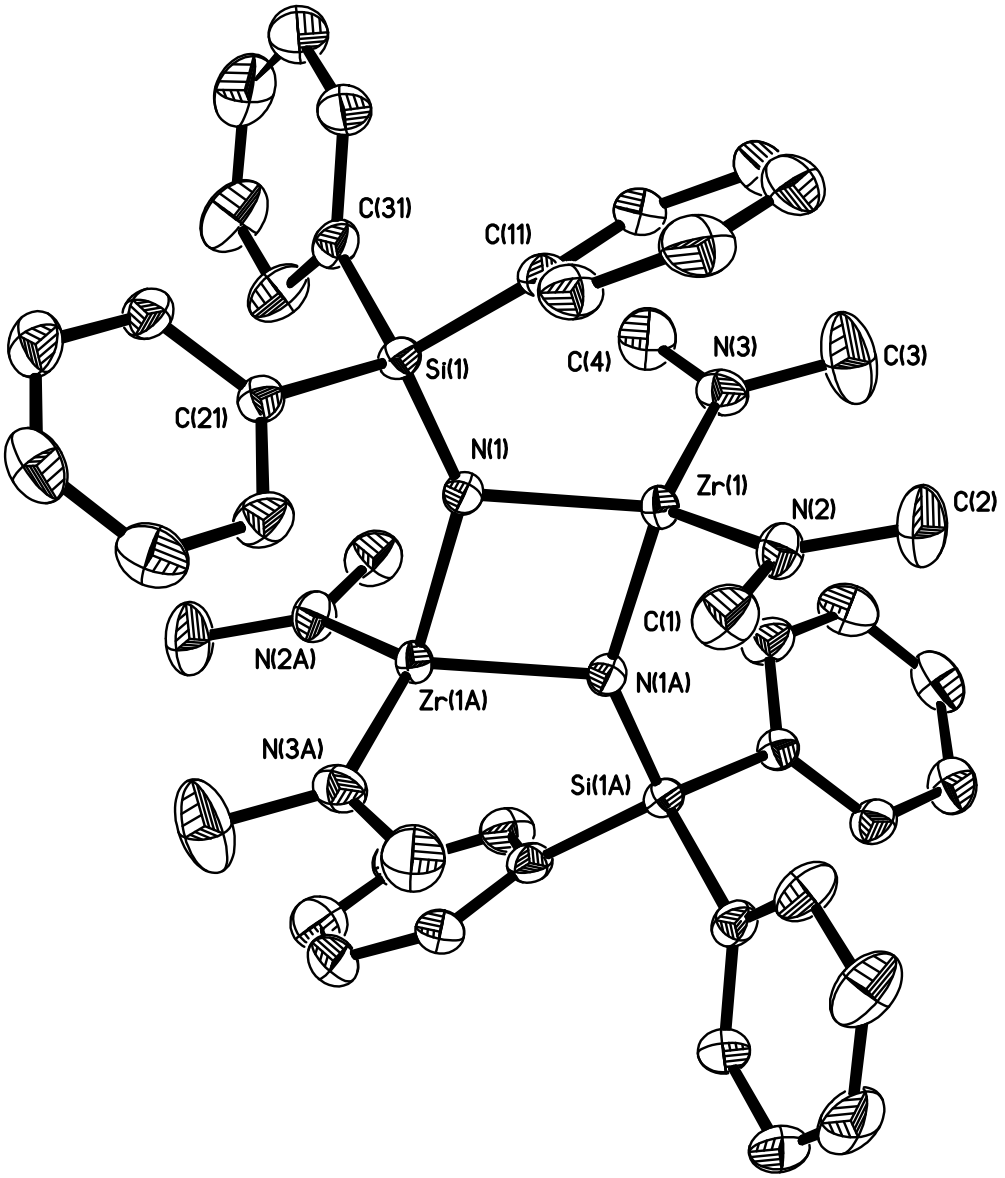

Figure 7.2: Molecular structure of the complex [{$(Me_2N)_2Zr(\mu_2\text{-}NSiPh_3)\}_2$], (**7**). Thermal ellipsoids are shown at 50 % probability, with hydrogen atoms omitted for clarity.

Table 7.2:- Crystal data and structure refinement for [{$(Me_2N)_2Zr(\mu_2\text{-}NSiPh_3)\}_2$] (**7**)

Identification code	k07alj02
Empirical formula	C44 H54 N6 Si2 Zr2
Formula weight	905.55
Temperature	150(2) K
Wavelength	0.71073 Å
Crystal system	Monoclinic
Space group	$P2_1/n$
Unit cell dimensions	a = 9.57000(10) Å
	b = 11.45400(10) Å
	c = 20.2050(2) Å
	α= 90°.
	β= 98.1630(10)°.
	γ = 90°.
Volume	2192.33(4) $Å^3$
Z	2
Density (calculated)	1.372 Mg/m^3
Absorption coefficient	0.567 mm^{-1}
F(000)	936
Crystal size	0.20 x 0.15 x 0.13 mm^3
Theta range for data collection	3.27 to 30.49°.
Index ranges	-13<=h<=13, -16<=k<=16, -28<=l<=28
Reflections collected	34645
Independent reflections	6664 [R(int) = 0.0526]
Completeness to theta = 30.49°	99.5 %
Absorption correction	None
Max. and min. transmission	0.9299 and 0.8950
Refinement method	Full-matrix least-squares on F^2
Data / restraints / parameters	6664 / 0 / 249
Goodness-of-fit on F^2	1.032
Final R indices [I>2sigma(I)]	R1 = 0.0274, wR2 = 0.0674
R indices (all data)	R1 = 0.0340, wR2 = 0.0711
Extinction coefficient	0.0000(5)
Largest diff. peak and hole	0.587 and -0.499 $e.Å^{-3}$

7.3: Complex 8, [{$(Me_2N)_2Hf(\mu_2\text{-}NSiPh_3)\}_2(HNMe_2)$]

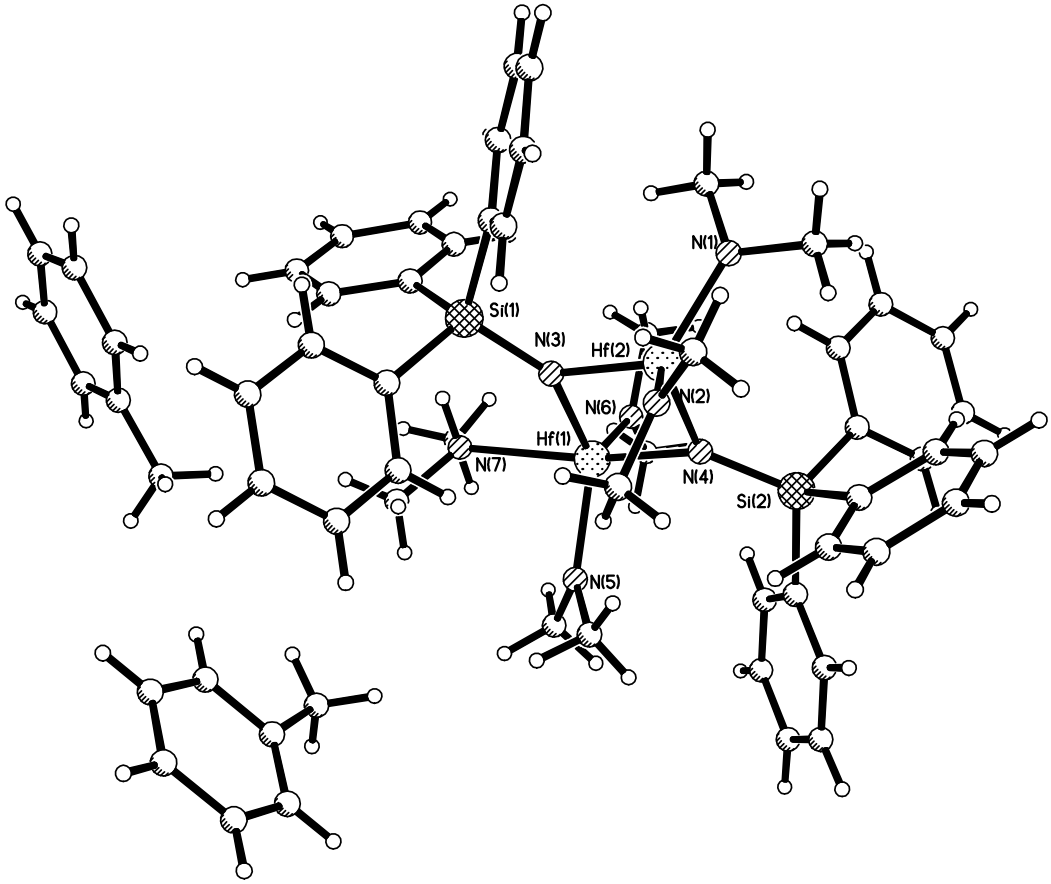

Figure 7.3.1: Asymmetric unit for the complex [{$(Me_2N)_2Hf(\mu_2\text{-}NSiPh_3)\}_2(HNMe_2)$], (**8**).

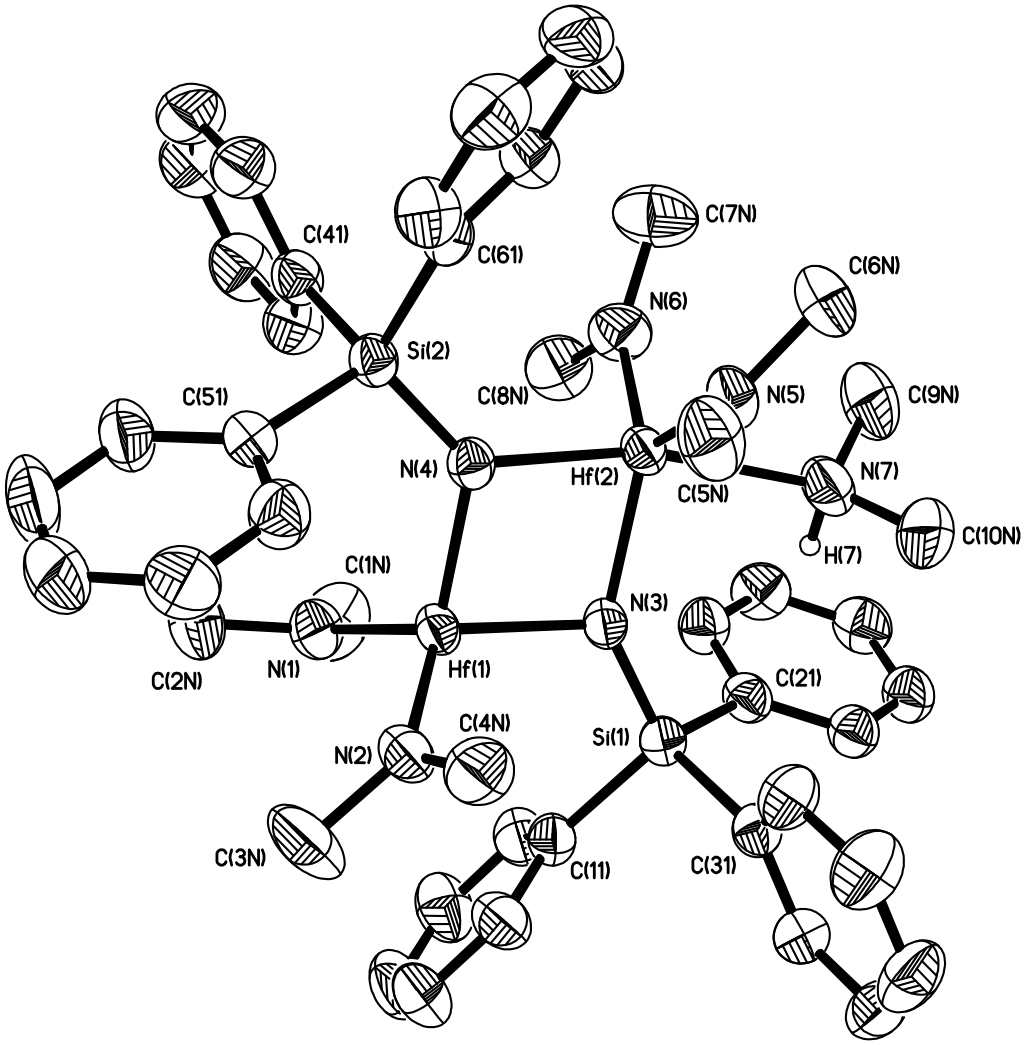

Figure 7.3.2: Molecular structure of the complex [{$(Me_2N)_2Hf(\mu_2\text{-}NSiPh_3)$}$_2$($HNMe_2$)], (**8**). Thermal ellipsoids are shown at 50 % probability, with hydrogen atoms and toluene solvent molecules omitted for clarity.

Table 7.3:- Crystal data and structure refinement for [{$(Me_2N)_2Hf(\mu_2\text{-}NSiPh_3)\}_2(HNMe_2)$] (**8**).

Identification code	H06alj10
Empirical formula	C60 H77 Hf2 N7 Si2
Formula weight	1309.45
Temperature	200(2) K
Wavelength	0.71073 Å
Crystal system	Triclinic
Space group	P-1
Unit cell dimensions	a = 11.4930(2) Å
	b = 14.3830(2) Å
	c = 18.4350(4) Å
	α= 85.9470(10)°.
	β= 80.4330(10)°.
	γ = 82.2700(10)°.
Volume	2974.04(9) $Å^3$
Z	2
Density (calculated)	1.462 Mg/m^3
Absorption coefficient	3.571 mm^{-1}
F(000)	1316
Crystal size	0.25 x 0.20 x 0.10 mm^3
Theta range for data collection	8.52 to 30.52°.
Index ranges	-16<=h<=16, -20<=k<=20, -26<=l<=26
Reflections collected	53103
Independent reflections	17220 [R(int) = 0.0463]
Completeness to theta = 30.52°	94.6 %
Max. and min. transmission	0.7166 and 0.4689
Refinement method	Full-matrix least-squares on F^2
Data / restraints / parameters	17220 / 0 / 556
Goodness-of-fit on F^2	1.008
Final R indices [I>2sigma(I)]	R1 = 0.0387, wR2 = 0.0832
R indices (all data)	R1 = 0.0775, wR2 = 0.0954
Extinction coefficient	0.0001(2)
Largest diff. peak and hole	1.383 and -0.940 $e.Å^{-3}$

7.4: Complex 9, [{$(Me_2N)_2Ti(\mu_2\text{-}N^tBu)\}_2$]

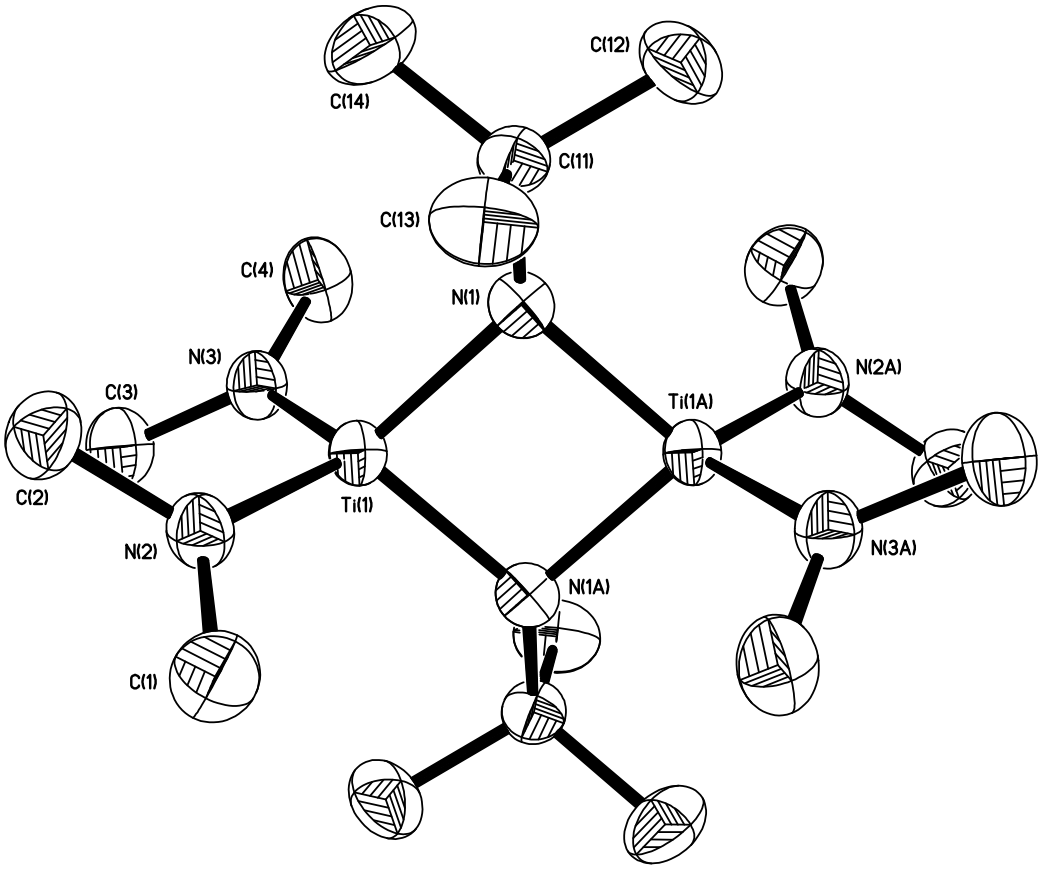

Figure 7.4: Molecular structure of the complex [{$(Me_2N)_2Ti(\mu_2\text{-}N^tBu)\}_2$], (**9**). Thermal ellipsoids are shown at 50 % probability, with hydrogen atoms omitted for clarity.

Table 7.4:- Crystal data and structure refinement for [{$(Me_2N)_2Ti(\mu_2\text{-}N^tBu)\}_2$] (**9**)

Identification code	h05alj14
Empirical formula	C16 H42 N6 Si0 Ti2
Formula weight	414.36
Temperature	150(2) K
Wavelength	0.71073 Å
Crystal system	Monoclinic
Space group	$P2_1/n$
Unit cell dimensions	a = 8.7000(3) Å
	b = 15.8910(7) Å
	c = 9.3500(4) Å
	α= 90°.
	β= 115.424(2)°.
	γ = 90°.
Volume	1167.47(8) $Å^3$
Z	2
Density (calculated)	1.179 Mg/m^3
Absorption coefficient	0.693 mm^{-1}
F(000)	448
Crystal size	0.13 x 0.10 x 0.10 mm^3
Theta range for data collection	4.23 to 30.48°.
Index ranges	-12<=h<=9, -17<=k<=22, -13<=l<=12
Reflections collected	10004
Independent reflections	3360 [R(int) = 0.0847]
Completeness to theta = 30.48°	94.4 %
Absorption correction	None
Max. and min. transmission	0.9339 and 0.9153
Refinement method	Full-matrix least-squares on F^2
Data / restraints / parameters	3360 / 0 / 117
Goodness-of-fit on F^2	1.007
Final R indices [I>2sigma(I)]	R1 = 0.0579, wR2 = 0.1381
R indices (all data)	R1 = 0.1059, wR2 = 0.1600
Extinction coefficient	0.005(5)
Largest diff. peak and hole	0.770 and -0.676 $e.Å^{-3}$

7.5: Complex 10, [{$(Me_2N)_2Ti(\mu_2\text{-}NSiEt_3)\}_2$]

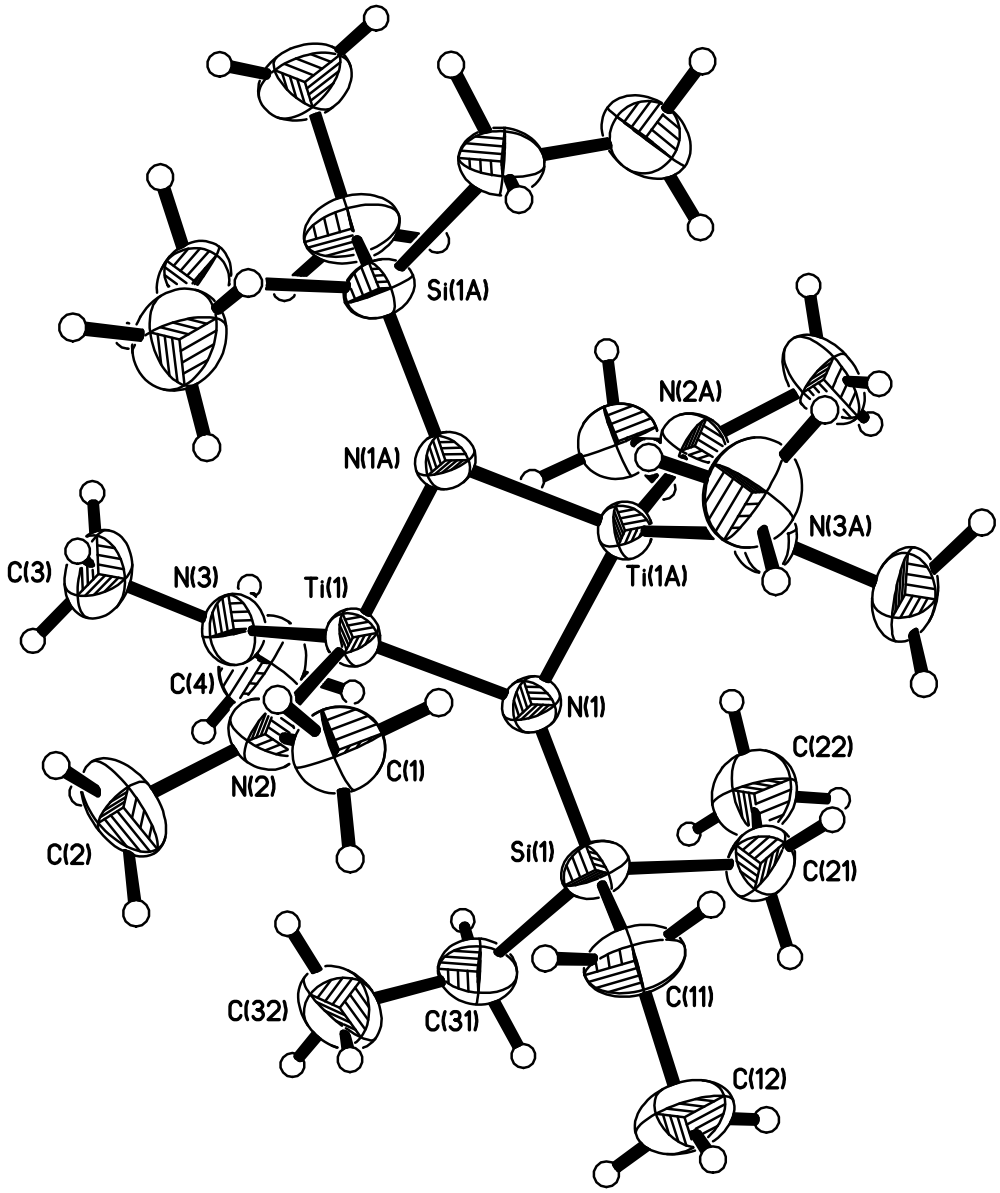

Figure 7.5: Molecular structure of the complex [{$(Me_2N)_2Ti(\mu_2\text{-}NSiEt_3)\}_2$], (**10**). Thermal ellipsoids are shown at 50 % probability.

Table 7.5:- Crystal data and structure refinement for [{$(Me_2N)_2Ti(\mu_2\text{-}NSiEt_3)\}_2$] (**10**).

Identification code	h07alj03
Empirical formula	C20 H54 N6 Si2 Ti2
Formula weight	530.67
Temperature	100(2) K
Wavelength	0.71073 Å
Crystal system	Monoclinic
Space group	$P2_1/n$
Unit cell dimensions	a = 10.6660(3) Å
	b = 12.7800(3) Å
	c = 11.5560(3) Å
	α= 90°.
	β= 97.4630(10)°.
	γ = 90°.
Volume	1561.87(7) $Å^3$
Z	2
Density (calculated)	1.128 Mg/m^3
Absorption coefficient	0.605 mm^{-1}
F(000)	576
Crystal size	0.25 x 0.20 x 0.20 mm^3
Theta range for data collection	7.86 to 30.52°.
Index ranges	-15<=h<=15, -15<=k<=18, -16<=l<=16
Reflections collected	28631
Independent reflections	4635 [R(int) = 0.0422]
Completeness to theta = 30.52°	97.2 %
Absorption correction	None
Max. and min. transmission	0.8886 and 0.8635
Refinement method	Full-matrix least-squares on F^2
Data / restraints / parameters	4635 / 0 / 144
Goodness-of-fit on F^2	1.142
Final R indices [I>2sigma(I)]	R1 = 0.0463, wR2 = 0.1157
R indices (all data)	R1 = 0.0630, wR2 = 0.1260
Extinction coefficient	0.033(6)
Largest diff. peak and hole	0.577 and -0.357 $e.Å^{-3}$

7.6: Complex 13, [{$(Me_2N)_2Ti(\mu_2\text{-}NSi^tBuMe_2)\}_2$]

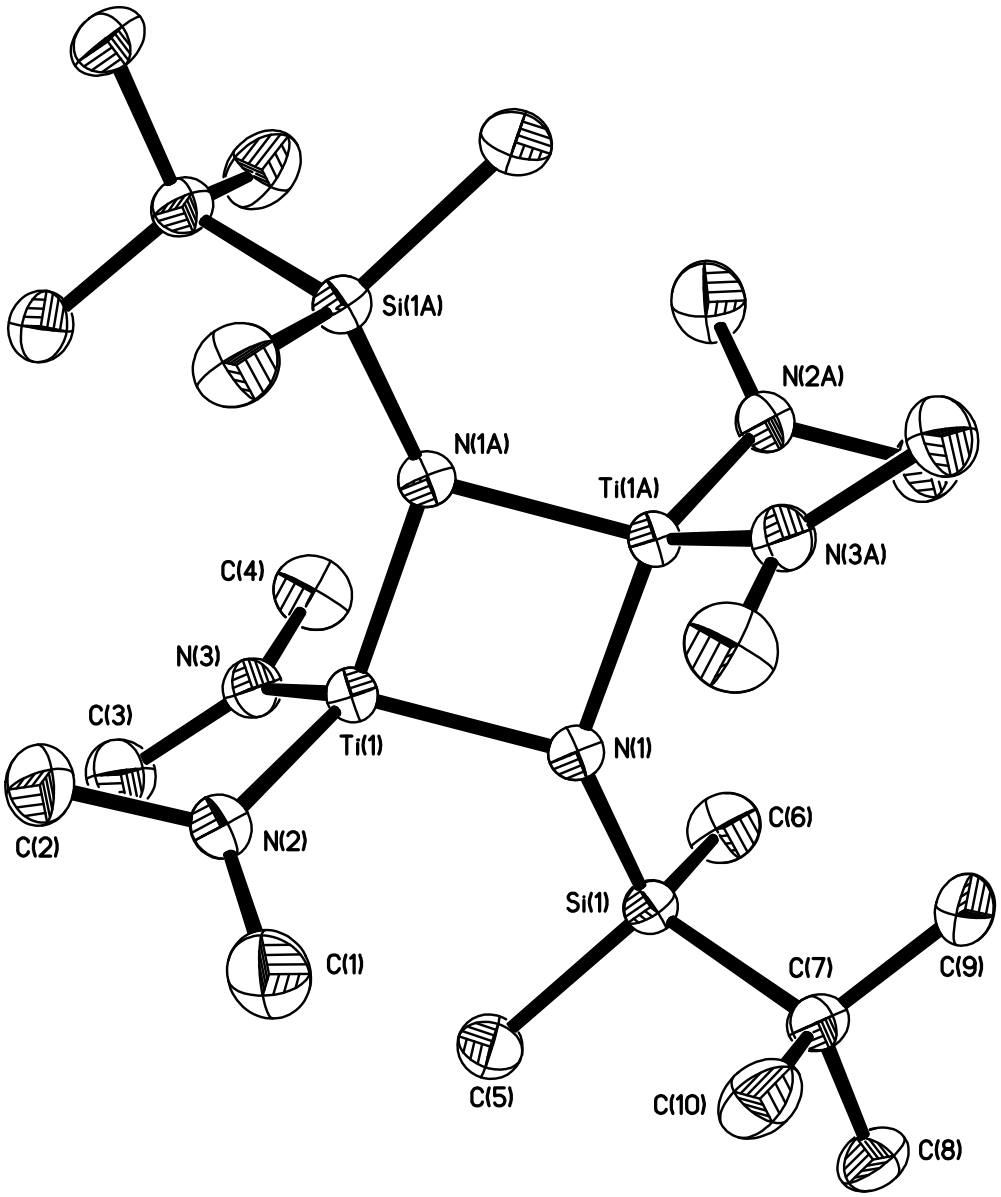

Figure 7.6: Molecular structure of the complex [{$(Me_2N)_2Ti(\mu_2\text{-}NSi^tBuMe_2)\}_2$], (**13**). Thermal ellipsoids are shown at 50 % probability, with hydrogen atoms omitted for clarity.

Table 7.6:- Crystal data and structure refinement for [{$(Me_2N)_2Ti(\mu_2\text{-}NSi^tBuMe_2)\}_2$] (**13**).

Identification code	h07alj05
Empirical formula	C20 H54 N6 Si2 Ti2
Formula weight	530.67
Temperature	150(2) K
Wavelength	0.71073 Å
Crystal system	Monoclinic
Space group	$P2_1/n$
Unit cell dimensions	a = 9.9270(2) Å
	b = 13.3320(3) Å
	c = 11.6030(3) Å
	α= 90°.
	β= 91.0290(10)°.
	γ = 90°.
Volume	1535.37(6) $Å^3$
Z	2
Density (calculated)	1.148 Mg/m^3
Absorption coefficient	0.615 mm^{-1}
F(000)	576
Crystal size	0.15 x 0.15 x 0.10 mm^3
Theta range for data collection	7.86 to 30.50°.
Index ranges	-14<=h<=14, -18<=k<=19, -15<=l<=16
Reflections collected	32777
Independent reflections	4571 [R(int) = 0.0926]
Completeness to theta = 30.50°	97.8 %
Absorption correction	None
Max. and min. transmission	0.9411 and 0.9134
Refinement method	Full-matrix least-squares on F^2
Data / restraints / parameters	4571 / 0 / 146
Goodness-of-fit on F^2	1.023
Final R indices [I>2sigma(I)]	R1 = 0.0392, wR2 = 0.0796
R indices (all data)	R1 = 0.0823, wR2 = 0.0872
Extinction coefficient	0.000(3)
Largest diff. peak and hole	0.302 and -0.427 $e.Å^{-3}$

7.7: Complex 14, [{$(Me_2N)_2Zr(\mu_2\text{-}NSi^tBuMe_2)\}_2$]

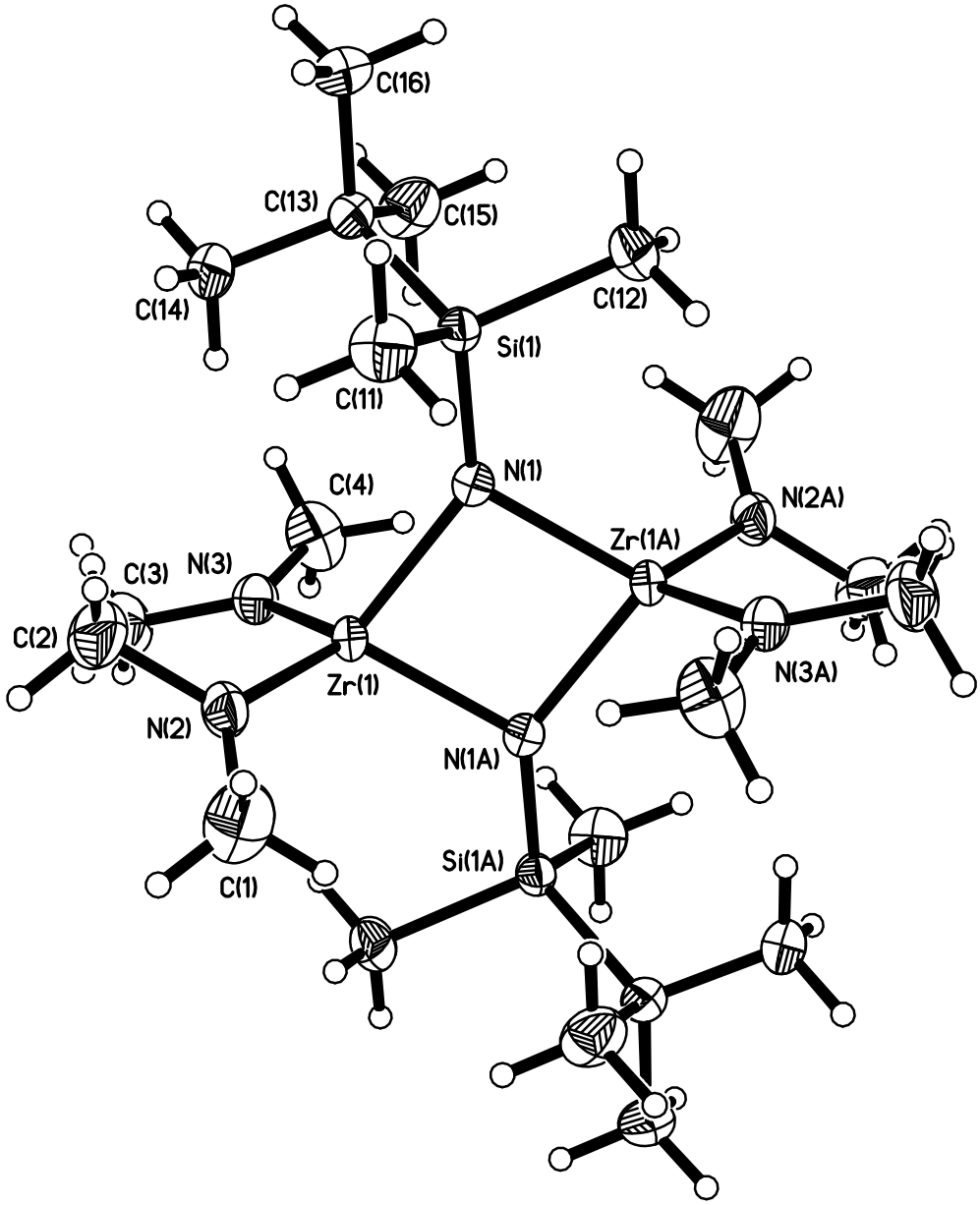

Figure 7.7: Molecular structure of the complex [{$(Me_2N)_2Zr(\mu_2\text{-}NSitBuMe_2)\}_2$], (**14**). Thermal ellipsoids are shown at 50 % probability.

Table 7.7:- Crystal data and structure refinement for [{$(Me_2N)_2Zr(\mu_2\text{-}NSi^tBuMe_2)\}_2$] (**14**).

Identification code	k08alj44
Empirical formula	C20 H54 N6 Si2 Zr2
Formula weight	617.31
Temperature	150(2) K
Wavelength	0.71073 Å
Crystal system	Monoclinic
Space group	$P2_1/n$
Unit cell dimensions	a = 9.9900(2) Å
	b = 13.6030(2) Å
	c = 11.6610(2) Å
	α= 90°.
	β= 90.8370(10)°.
	γ = 90°.
Volume	1584.49(5) $Å^3$
Z	2
Density (calculated)	1.294 Mg/m^3
Absorption coefficient	0.750 mm^{-1}
F(000)	648
Crystal size	0.17 x 0.13 x 0.10 mm^3
Theta range for data collection	7.87 to 28.31°.
Index ranges	-13<=h<=13, -18<=k<=18, -15<=l<=15
Reflections collected	26053
Independent reflections	3851 [R(int) = 0.0306]
Completeness to theta = 28.31°	97.5 %
Absorption correction	None
Max. and min. transmission	0.9288 and 0.8831
Refinement method	Full-matrix least-squares on F^2
Data / restraints / parameters	3851 / 0 / 146
Goodness-of-fit on F^2	1.078
Final R indices [I>2sigma(I)]	R1 = 0.0188, wR2 = 0.0493
R indices (all data)	R1 = 0.0214, wR2 = 0.0510
Extinction coefficient	0.0000(7)
Largest diff. peak and hole	0.392 and -0.416 $e.Å^{-3}$

7.8: Complex 15, [{$(Me_2N)_2Hf(\mu_2\text{-}NSi^tBuMe_2)\}_2$]

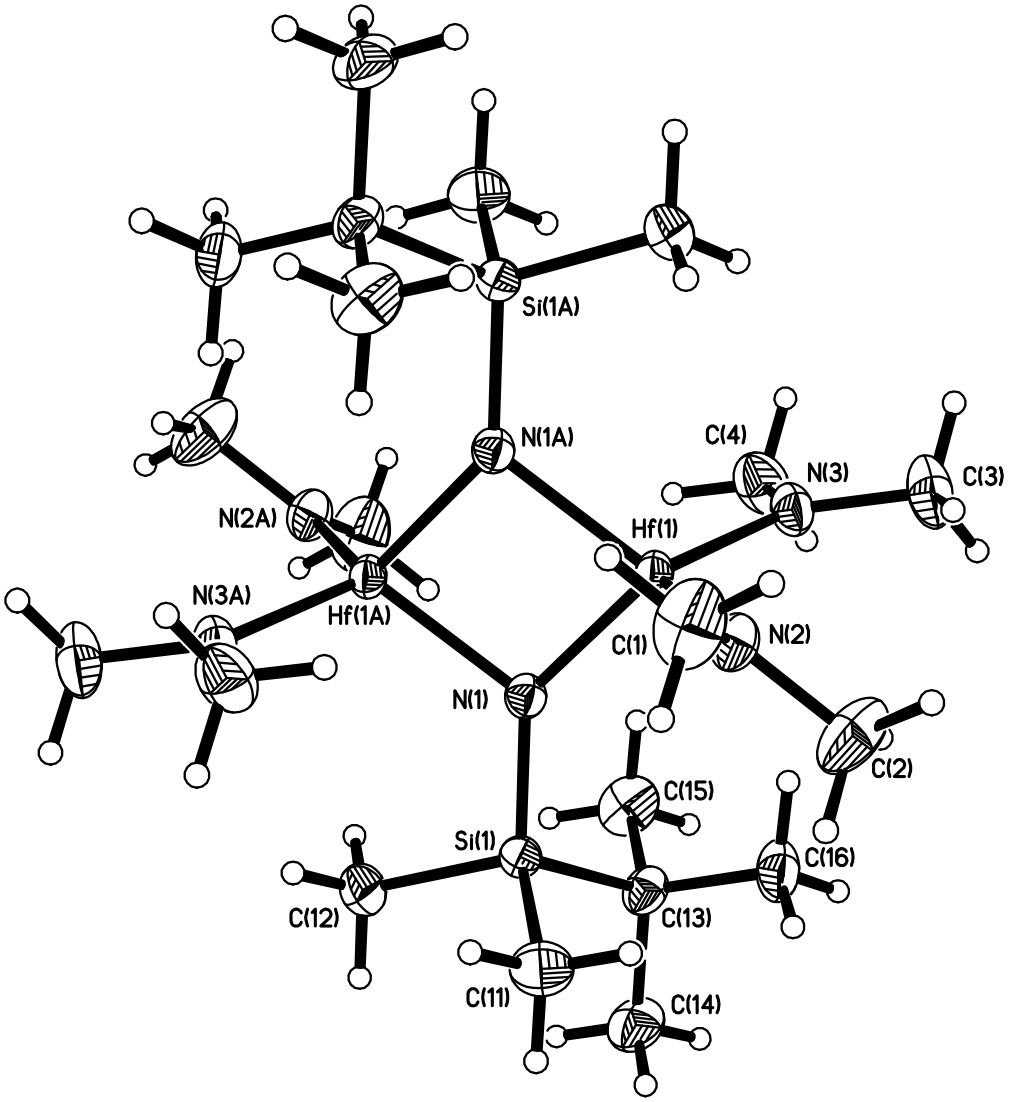

Figure 7.8: Molecular structure of the complex [{$(Me_2N)_2Hf(\mu_2\text{-}NSi^tBuMe_2)\}_2$], (**15**). Thermal ellipsoids are shown at 50 % probability.

Table 7.8:- Crystal data and structure refinement for [{$(Me_2N)_2Hf(\mu_2\text{-}NSi^tBuMe_2)\}_2$] (**15**).

Identification code	k08alj43
Empirical formula	C20 H54 Hf2 N6 Si2
Formula weight	791.85
Temperature	150(2) K
Wavelength	0.71073 Å
Crystal system	Monoclinic
Space group	$P2_1/n$
Unit cell dimensions	a = 9.9830(2) Å
	b = 13.5510(2) Å
	c = 11.6860(2) Å
	α= 90°.
	β= 90.8990(10)°.
	γ = 90°.
Volume	1580.68(5) $Å^3$
Z	2
Density (calculated)	1.664 Mg/m^3
Absorption coefficient	6.656 mm^{-1}
F(000)	776
Crystal size	0.20 x 0.17 x 0.10 mm^3
Theta range for data collection	7.86 to 28.31°.
Index ranges	-13<=h<=13, -18<=k<=18, -15<=l<=15
Reflections collected	25625
Independent reflections	3847 [R(int) = 0.0421]
Completeness to theta = 28.31°	97.6 %
Absorption correction	None
Max. and min. transmission	0.5558 and 0.3495
Refinement method	Full-matrix least-squares on F^2
Data / restraints / parameters	3847 / 0 / 146
Goodness-of-fit on F^2	1.127
Final R indices [I>2sigma(I)]	R1 = 0.0180, wR2 = 0.0442
R indices (all data)	R1 = 0.0208, wR2 = 0.0456
Extinction coefficient	0.00114(19)
Largest diff. peak and hole	1.033 and -1.246 $e.Å^{-3}$

7.9: Complex 16, [{$(Me_2N)_2Ti(\mu_2\text{-}NSi[NMe_2]_3)\}_2$]

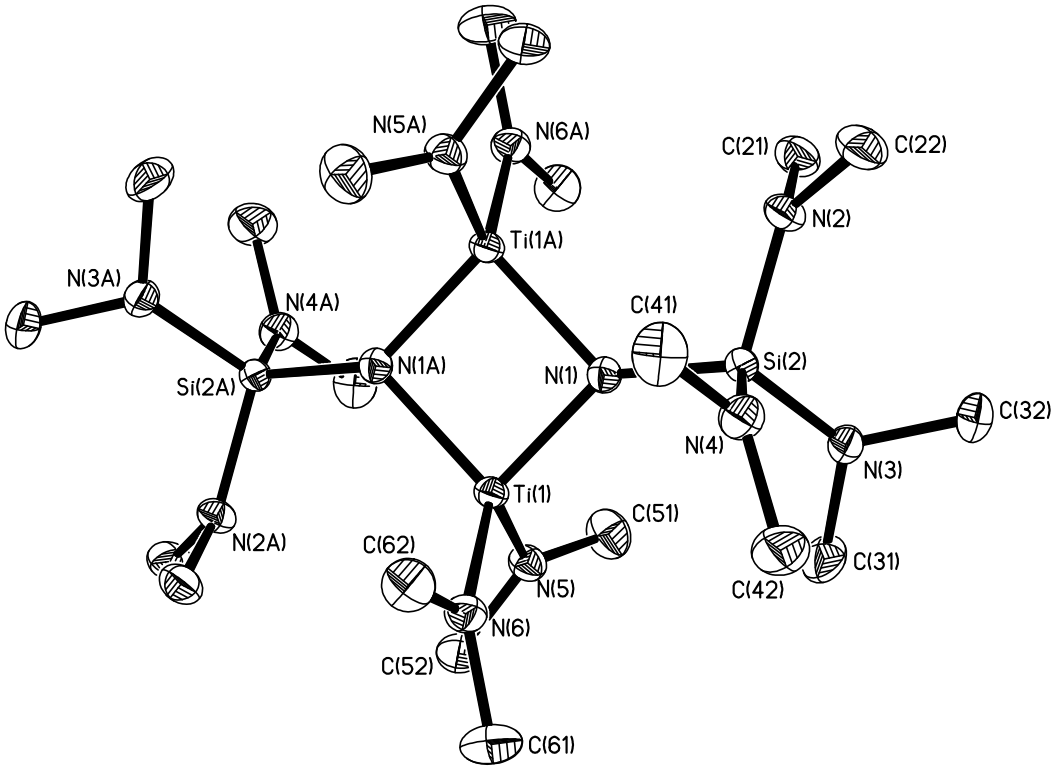

Figure 7.9: Molecular structure of the complex [{$(Me_2N)_2Ti(\mu_2\text{-}NSi(NMe_2)_3)\}_2$], (**16**). Thermal ellipsoids are shown at 50 % probability, with hydrogen atoms omitted for clarity.

Table 7.9:- Crystal data and structure refinement for [{$(Me_2N)_2Ti(\mu_2\text{-}NSi[NMe_2]_3)\}_2$] (**16**).

Identification code	k07alj12
Empirical formula	C20 H60 N12 Si2 Ti2
Formula weight	620.78
Temperature	150(2) K
Wavelength	0.71073 Å
Crystal system	Triclinic
Space group	P-1
Unit cell dimensions	a = 8.3630(2) Å
	b = 10.5940(2) Å
	c = 10.7400(2) Å
	α= 68.2060(10)°.
	β= 72.1390(10)°.
	γ = 78.3030(10)°.
Volume	836.68(3) $Å^3$
Z	1
Density (calculated)	1.232 Mg/m^3
Absorption coefficient	0.579 mm^{-1}
F(000)	336
Crystal size	0.20 x 0.10 x 0.08 mm^3
Theta range for data collection	3.42 to 30.55°.
Index ranges	-11<=h<=11, -15<=k<=15, -15<=l<=15
Reflections collected	16226
Independent reflections	5016 [R(int) = 0.0407]
Completeness to theta = 30.55°	97.9 %
Absorption correction	None
Max. and min. transmission	0.9579 and 0.8930
Refinement method	Full-matrix least-squares on F^2
Data / restraints / parameters	5016 / 0 / 174
Goodness-of-fit on F^2	1.032
Final R indices [I>2sigma(I)]	R1 = 0.0373, wR2 = 0.0881
R indices (all data)	R1 = 0.0606, wR2 = 0.0980
Extinction coefficient	0.004(3)
Largest diff. peak and hole	0.585 and -0.478 $e.Å^{-3}$

7.10: Complex 17, [{$(Me_2N)_2Zr(\mu_2\text{-}NSi[NMe_2]_3)\}_2$]

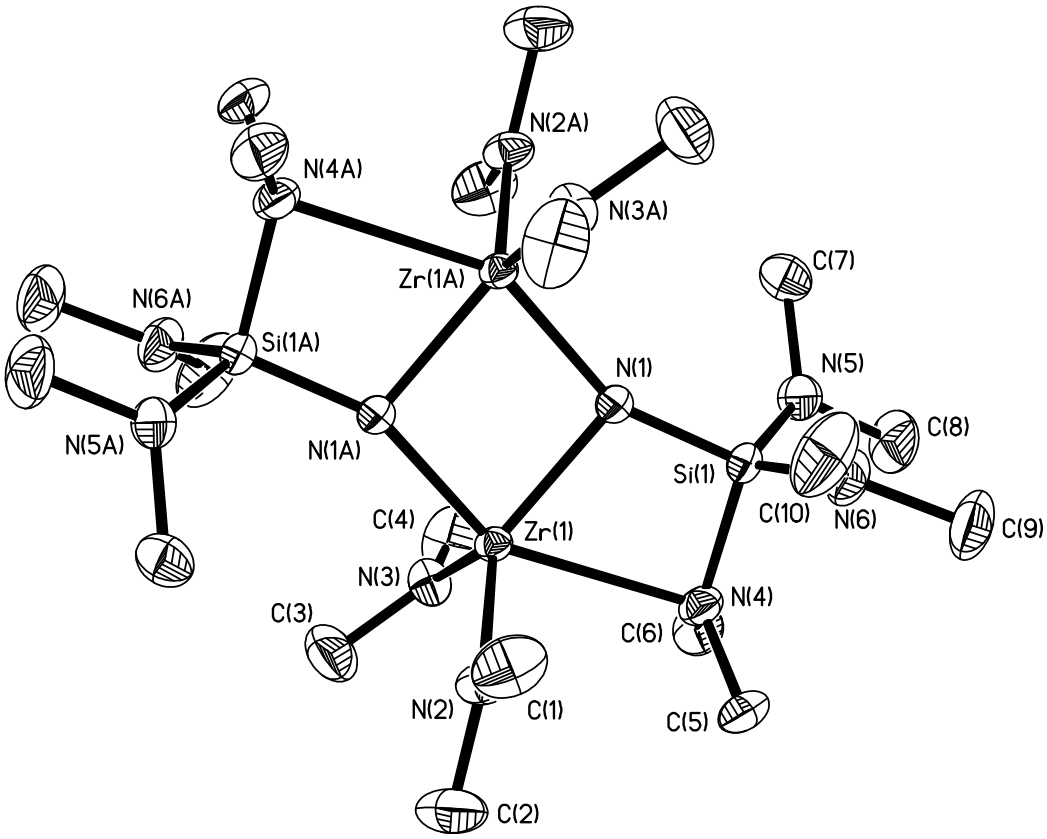

Figure 7.10: Molecular structure of the complex [{$(Me_2N)_2Zr(\mu_2\text{-}NSi(NMe_2)_3)\}_2$], (**17**). Thermal ellipsoids are shown at 50 % probability, with hydrogen atoms omitted for clarity.

Table 7.10:- Crystal data and structure refinement for [{$(Me_2N)_2Zr(\mu_2\text{-}NSi[NMe_2]_3)\}_2$] (**17**).

Identification code	h07alj12
Empirical formula	C10 H30 N6 Si Zr
Formula weight	353.71
Temperature	150(2) K
Wavelength	0.71073 Å
Crystal system	Monoclinic
Space group	C2/c
Unit cell dimensions	a = 17.1910(2) Å
	b = 12.7470(2) Å
	c = 15.7610(2) Å
	α= 90°.
	β= 90.1410(10)°.
	γ = 90°.
Volume	3453.76(8) $Å^3$
Z	8
Density (calculated)	1.360 Mg/m^3
Absorption coefficient	0.702 mm^{-1}
F(000)	1488
Crystal size	0.20 x 0.10 x 0.10 mm^3
Theta range for data collection	3.90 to 30.50°.
Index ranges	-24<=h<=23, -18<=k<=18, -22<=l<=22
Reflections collected	35910
Independent reflections	5230 [R(int) = 0.0439]
Completeness to theta = 30.50°	99.4 %
Absorption correction	None
Max. and min. transmission	0.9331 and 0.8723
Refinement method	Full-matrix least-squares on F^2
Data / restraints / parameters	5230 / 0 / 174
Goodness-of-fit on F^2	1.060
Final R indices [I>2sigma(I)]	R1 = 0.0239, wR2 = 0.0576
R indices (all data)	R1 = 0.0325, wR2 = 0.0610
Extinction coefficient	0.0015(2)
Largest diff. peak and hole	0.485 and -0.548 $e.Å^{-3}$

7.11: Complex 18, [{$(Me_2N)_2Hf(\mu_2\text{-}NSi[NMe_2]_3)\}_2$]

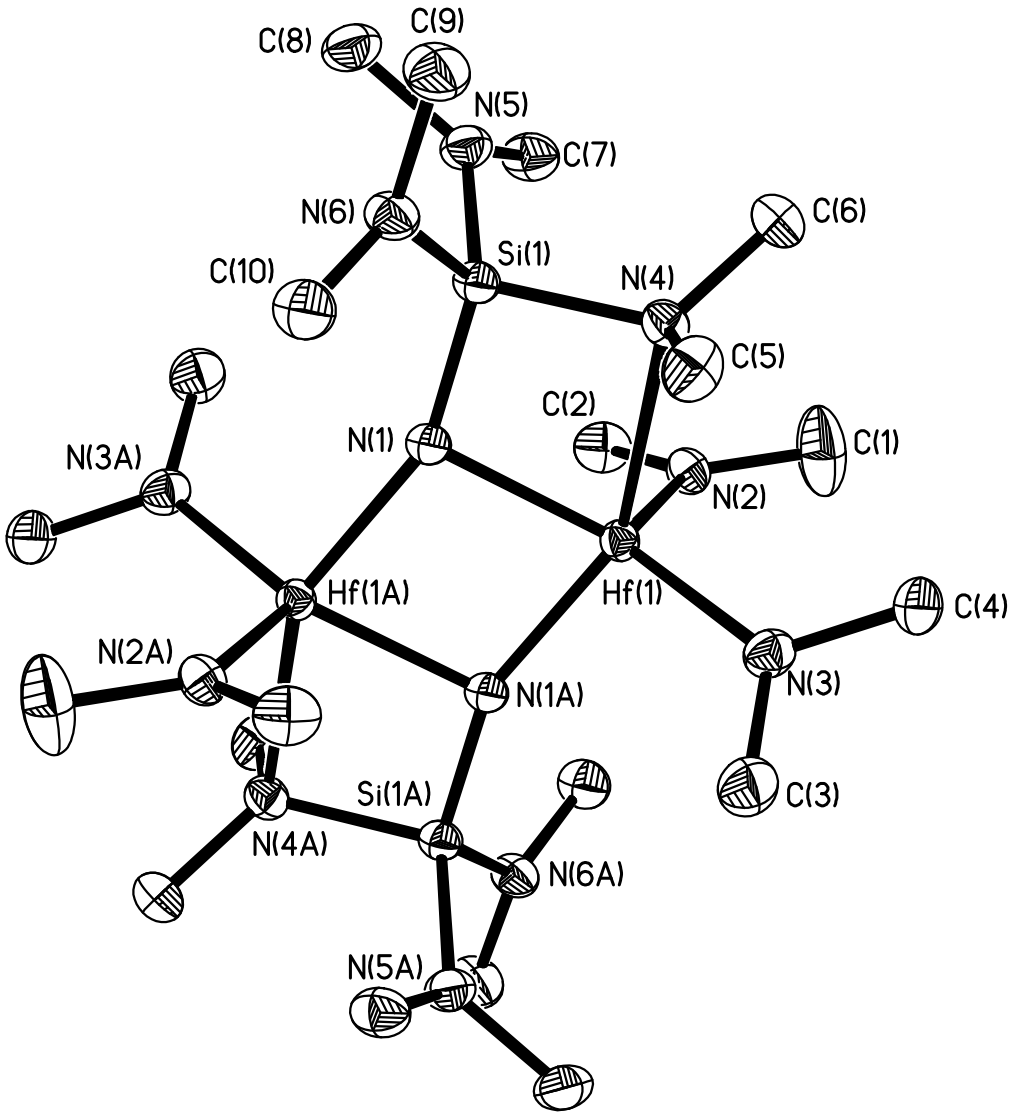

Figure 7.11: Molecular structure of the complex [{$(Me_2N)_2Hf(\mu_2\text{-}NSi(NMe_2)_3)\}_2$], (**18**). Thermal ellipsoids are shown at 50 % probability, with hydrogen atoms omitted for clarity.

Table 7.11:- Crystal data and structure refinement for [{$(Me_2N)_2Hf(\mu_2\text{-}NSi[NMe_2]_3)\}_2$] (**18**).

Identification code	h07alj07
Empirical formula	C20 H60 Hf2 N12 Si2
Formula weight	881.96
Temperature	150(2) K
Wavelength	0.71073 Å
Crystal system	Monoclinic
Space group	P21/n
Unit cell dimensions	a = 8.9930(2) Å
	b = 13.9280(3) Å
	c = 13.7290(3) Å
	α= 90°.
	β= 101.6260(10)°.
	γ = 90°.
Volume	1684.34(6) $Å^3$
Z	2
Density (calculated)	1.739 Mg/m^3
Absorption coefficient	6.260 mm^{-1}
F(000)	872
Crystal size	0.12 x 0.10 x 0.10 mm^3
Theta range for data collection	3.73 to 30.51°.
Index ranges	-12<=h<=12, -19<=k<=19, -19<=l<=19
Reflections collected	35022
Independent reflections	5114 [R(int) = 0.0723]
Completeness to theta = 30.51°	99.6 %
Absorption correction	None
Max. and min. transmission	0.5733 and 0.5204
Refinement method	Full-matrix least-squares on F^2
Data / restraints / parameters	5114 / 0 / 175
Goodness-of-fit on F^2	0.984
Final R indices [I>2sigma(I)]	R1 = 0.0270, wR2 = 0.0446
R indices (all data)	R1 = 0.0500, wR2 = 0.0490
Extinction coefficient	0.00226(14)
Largest diff. peak and hole	1.174 and -1.356 $e.Å^{-3}$

7.12: Complex 24, [{$Ph_2Si(N[Li]^tBu)_2\}_2$]

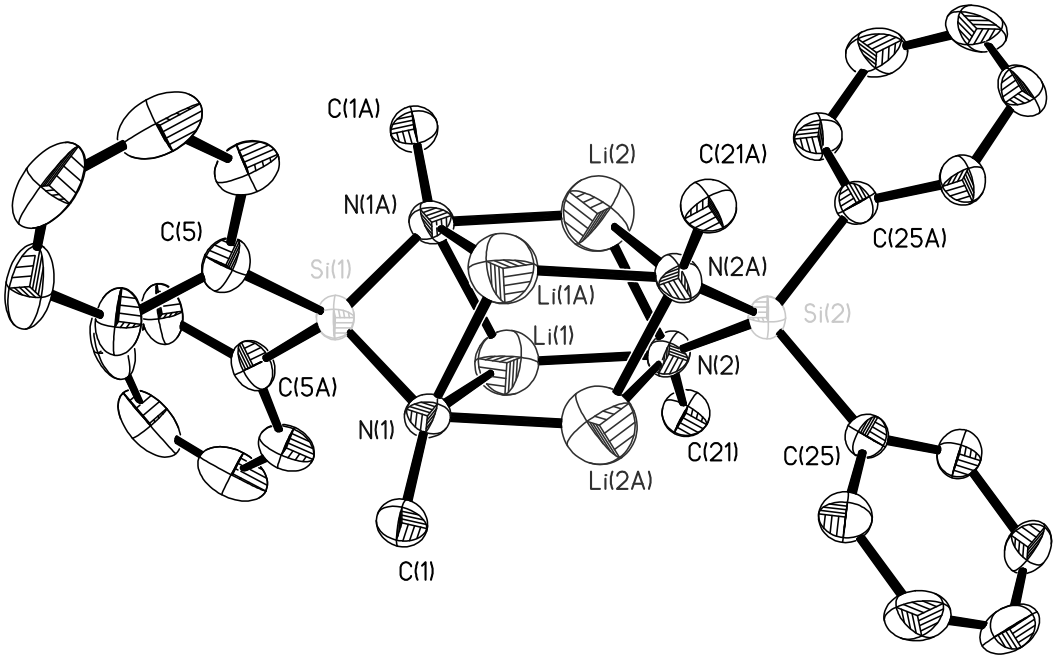

Figure 7.12: The molecular structure of the dimeric complex $[Ph_2Si\{N(Li)^tBu\}_2]_2$, (**24**). Thermal ellipsoids are shown at 50% probability. Hydrogen atoms are omitted for clarity.

Table 7.12:- Crystal data and structure refinement for [{$Ph_2Si(N[Li]^tBu)_2\}_2$] (**24**).

Identification code	k06alj07
Empirical formula	C40 H56 Li4 N4 Si2
Formula weight	676.83
Temperature	150(2) K
Wavelength	0.71073 Å
Crystal system	Monoclinic
Space group	C2/c
Unit cell dimensions	a = 17.8850(4) Å
	b = 12.9600(3) Å
	c = 17.4340(5) Å
	α= 90°.
	β= 100.4410(10)°.
	γ = 90°.
Volume	3974.11(17) $Å^3$
Z	4
Density (calculated)	1.131 Mg/m^3
Absorption coefficient	0.121 mm^{-1}
F(000)	1456
Crystal size	0.17 x 0.12 x 0.10 mm^3
Theta range for data collection	2.91 to 30.49°.
Index ranges	-25<=h<=24, -18<=k<=18, -24<=l<=24
Reflections collected	38263
Independent reflections	5718 [R(int) = 0.0967]
Completeness to theta = 30.49°	94.3 %
Absorption correction	None
Max. and min. transmission	0.9880 and 0.9797
Refinement method	Full-matrix least-squares on F^2
Data / restraints / parameters	5718 / 0 / 234
Goodness-of-fit on F^2	1.200
Final R indices [I>2sigma(I)]	R1 = 0.1224, wR2 = 0.2745
R indices (all data)	R1 = 0.1689, wR2 = 0.2957
Extinction coefficient	0.0033(12)
Largest diff. peak and hole	2.246 and -0.723 $e.Å^{-3}$

7.13: Complex 25, [{$Me_2Si(N^tBu)_2$}$_2$Ti]

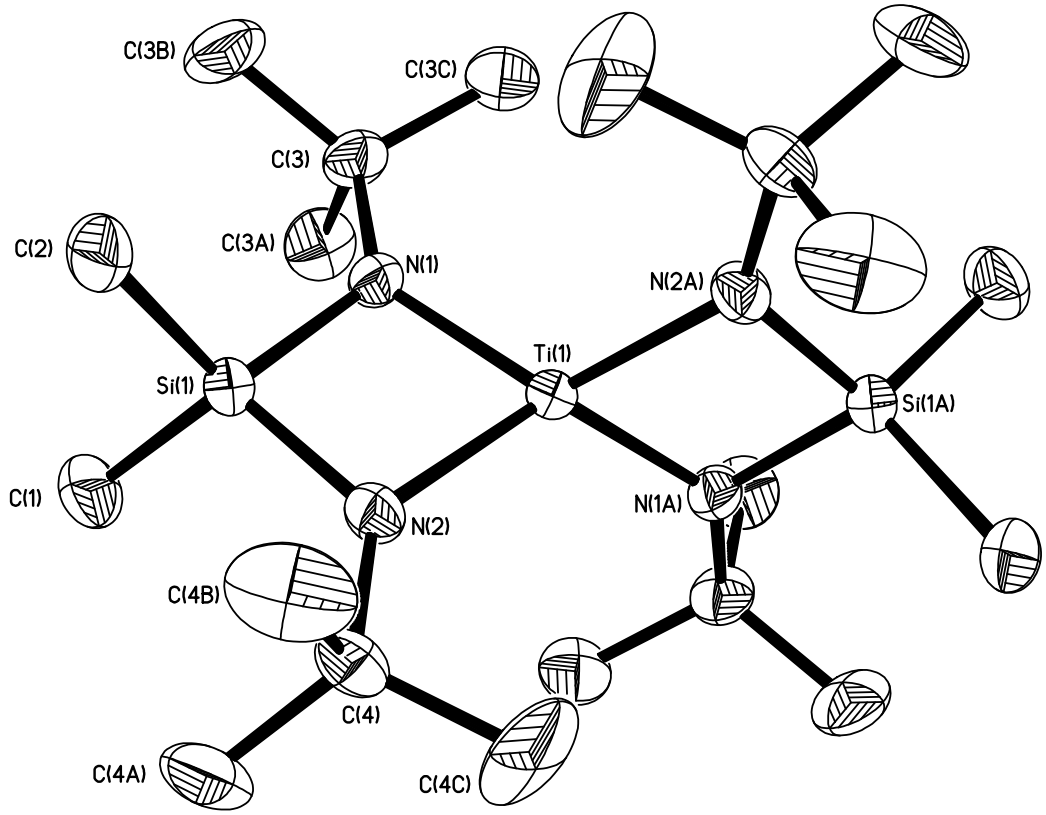

Figure 7.13: Molecular structure of the complex [{$Me_2Si(N^tBu)_2$}$_2$Ti], (**25**). Thermal ellipsoids are shown at 50% probability, with hydrogen atoms omitted for clarity.

Table 7.13:- Crystal data and structure refinement for [{$Me_2Si(N^tBu)_2\}_2Ti$] (**25**).

Identification code	k05alj26
Empirical formula	C20 H48 N4 Si2 Ti
Formula weight	448.70
Temperature	150(2) K
Wavelength	0.71073 Å
Crystal system	Monoclinic
Space group	C_2/c
Unit cell dimensions	a = 18.5970(4) Å
	b = 8.8140(2) Å
	c = 18.4880(4) Å
	α= 90°.
	β= 112.7110(10)°.
	γ = 90°.
Volume	2795.47(11) $Å^3$
Z	4
Density (calculated)	1.066 Mg/m^3
Absorption coefficient	0.403 mm^{-1}
F(000)	984
Crystal size	0.20 x 0.17 x 0.05 mm^3
Theta range for data collection	3.83 to 30.54°.
Index ranges	-24<=h<=26, -12<=k<=12, -26<=l<=25
Reflections collected	26601
Independent reflections	4033 [R(int) = 0.0759]
Completeness to theta = 30.54°	94.1 %
Absorption correction	None
Max. and min. transmission	0.9801 and 0.9237
Refinement method	Full-matrix least-squares on F^2
Data / restraints / parameters	4033 / 0 / 194
Goodness-of-fit on F^2	1.057
Final R indices [I>2sigma(I)]	R1 = 0.0489, wR2 = 0.1066
R indices (all data)	R1 = 0.0915, wR2 = 0.1247
Extinction coefficient	0.0000(8)
Largest diff. peak and hole	0.284 and -0.280 $e.Å^{-3}$

7.14: Complex 28, [{[$Me_2Si(N^tBu)_2$]Ti(μ_2-N^tBu)}$_2$]

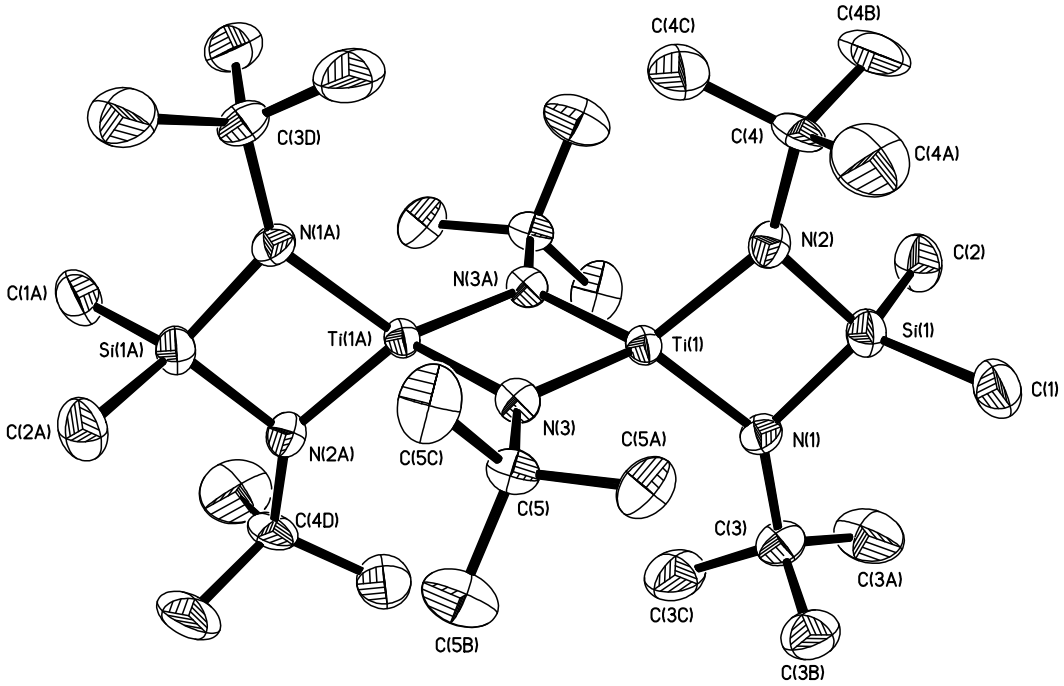

Figure 7.14: Molecular structure of the complex [{$Me_2Si(N^tBu)_2Ti(\mu_2\text{-}N^tBu)$}$_2$], (**28**). Thermal ellipsoids are shown at 50 % probability, with hydrogen atoms omitted for clarity.

Table 7.14:- Crystal data and structure refinement for [{[$Me_2Si(N^tBu)_2$]Ti(μ_2-N^tBu)}$_2$] (**28**).

Identification code	k06alj06
Empirical formula	C28 H66 N6 Si2 Ti2
Formula weight	638.85
Temperature	150(2) K
Wavelength	0.71073 Å
Crystal system	Triclinic
Space group	P-1
Unit cell dimensions	a = 9.3260(3) Å
	b = 10.1100(4) Å
	c = 11.0860(5) Å
	α= 99.470(2)°.
	β= 94.118(2)°.
	γ = 114.546(2)°.
Volume	926.32(6) $Å^3$
Z	1
Density (calculated)	1.145 Mg/m^3
Absorption coefficient	0.520 mm^{-1}
F(000)	348
Crystal size	0.25 x 0.20 x 0.08 mm^3
Theta range for data collection	8.18 to 20.81°.
Index ranges	-9<=h<=9, -10<=k<=10, -11<=l<=11
Reflections collected	7687
Independent reflections	1807 [R(int) = 0.0542]
Completeness to theta = 20.81°	93.3 %
Absorption correction	None
Max. and min. transmission	0.9596 and 0.8809
Refinement method	Full-matrix least-squares on F^2
Data / restraints / parameters	1807 / 0 / 184
Goodness-of-fit on F^2	1.290
Final R indices [I>2sigma(I)]	R1 = 0.0762, wR2 = 0.1991
R indices (all data)	R1 = 0.0789, wR2 = 0.2004
Extinction coefficient	0.064(17)
Largest diff. peak and hole	0.814 and -0.346 $e.Å^{-3}$

7.15: Complex 30, [{(Me$_3$SiNSiMe$_2$CH$_2$)Ti(N^{t}Bu)}$_2$]

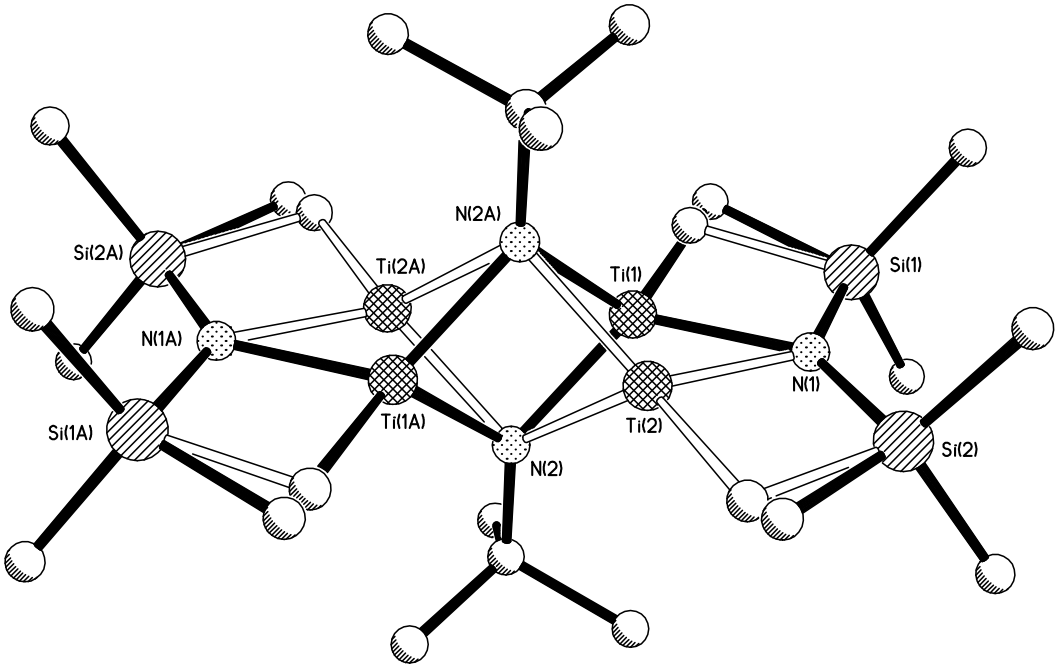

Figure 7.15.1: Structure of the complex [{(Me$_3$SiNSiMe$_2$CH$_2$)Ti(μ$_2$-N^{t}Bu)}$_2$], **30**, in which the atoms are disordered over two positions. Bonds attributed to the crystallographic isomer containing the atom [Ti(1)] are shown in bold, whilst equivalent bonds within the second molecule containing [Ti(2)] are unshaded.

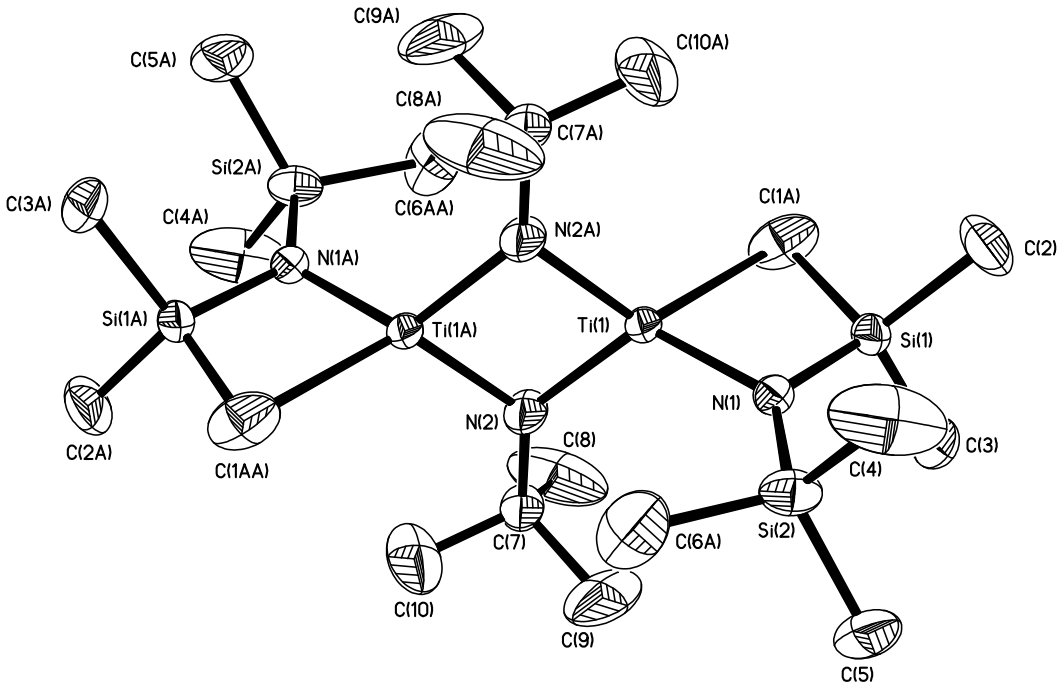

Figure 7.15.2: Molecular structure of molecule 1 of the complex [{(Me$_3$SiNSiMe$_2$CH$_2$)Ti(μ$_2$-N^{t}Bu)}$_2$], (**30**). Thermal ellipsoids are shown at 30 % probability, with hydrogen atoms omitted for clarity.

Table 7.15:- Crystal data and structure refinement for [{($Me_3SiNSiMe_2CH_2$)Ti(N^tBu)}$_2$] (**30**).

Identification code	h08alj05
Empirical formula	C20 H52 N4 Si4 Ti2
Formula weight	556.82
Temperature	150(2) K
Wavelength	0.71073 Å
Crystal system	Triclinic
Space group	P-1
Unit cell dimensions	a = 8.6030(2) Å
	b = 9.3860(3) Å
	c = 11.4260(4) Å
	α= 88.0910(10)°.
	β= 73.7020(10)°.
	γ = 68.976(2)°.
Volume	824.26(4) $Å^3$
Z	1
Density (calculated)	1.122 Mg/m^3
Absorption coefficient	0.643 mm^{-1}
F(000)	300
Crystal size	0.25 x 0.20 x 0.17 mm^3
Theta range for data collection	7.94 to 30.56°.
Index ranges	-11<=h<=12, -13<=k<=13, -16<=l<=16
Reflections collected	15428
Independent reflections	4862 [R(int) = 0.0533]
Completeness to theta = 30.56°	96.0 %
Absorption correction	None
Max. and min. transmission	0.8985 and 0.8558
Refinement method	Full-matrix least-squares on F^2
Data / restraints / parameters	4862 / 0 / 174
Goodness-of-fit on F^2	1.026
Final R indices [I>2sigma(I)]	R1 = 0.0652, wR2 = 0.1707
R indices (all data)	R1 = 0.0916, wR2 = 0.1909
Extinction coefficient	0.07(2)
Largest diff. peak and hole	0.803 and -0.437 $e.Å^{-3}$

7.16: Complex 31, [$(Me_2N)_3TaNSiPh_3$]

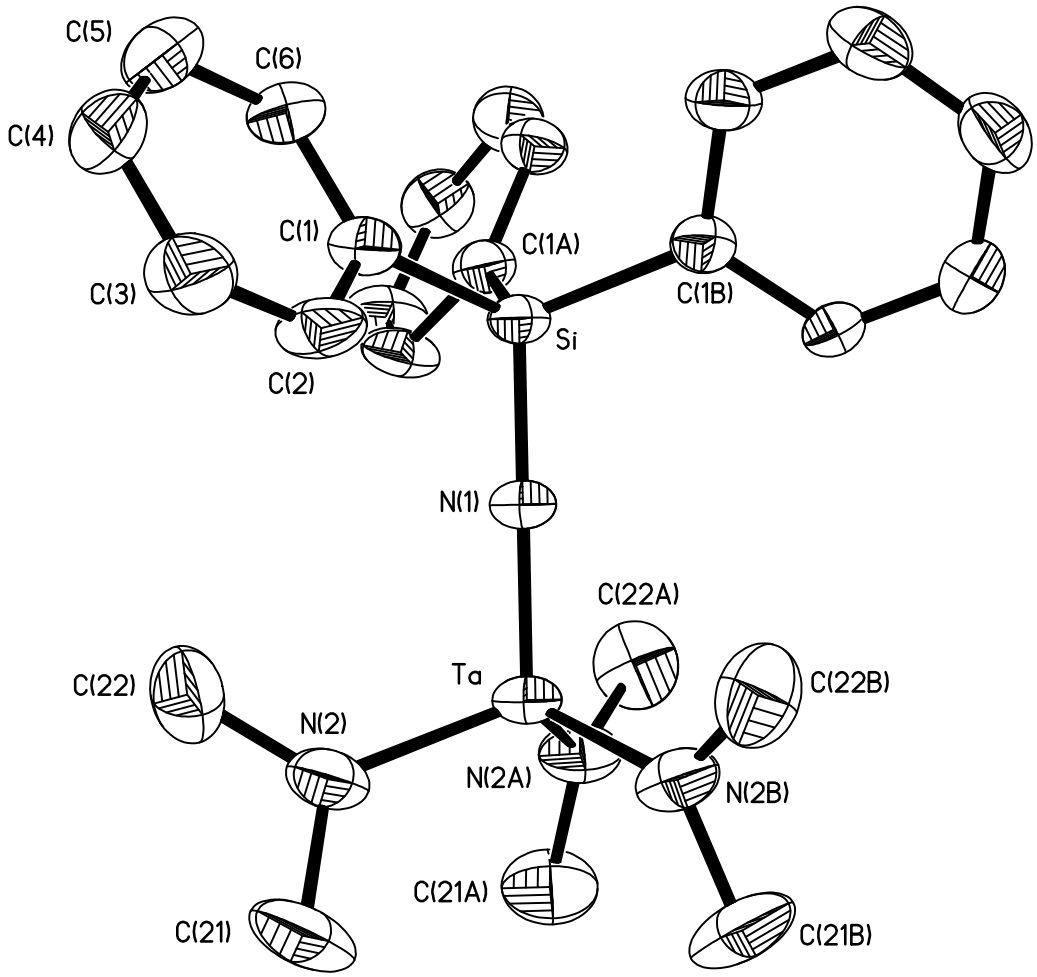

Figure 7.16: The molecular structure of the complex [$(Me_2N)_3TaNSiPh_3$], (**31**). Thermal ellipsoids are shown at 50% probability. Hydrogen atoms are omitted for clarity.

Table 7.16:- Crystal data and structure refinement for $[(Me_2N)_3TaNSiPh_3]$ (**31**).

Identification code	k06alj02
Empirical formula	C31 H39 N4 Si Ta
Formula weight	676.70
Temperature	150(2) K
Wavelength	0.71073 Å
Crystal system	Trigonal
Space group	*R*-3
Unit cell dimensions	a = 11.25300(10)
	b = 11.25300(10) Å
	c = 43.4650(4) Å
	α= 90°.
	β= 90°.
	γ = 120°.
Volume	4766.58(7) $Å^3$
Z	6
Density (calculated)	1.414 Mg/m^3
Absorption coefficient	3.521 mm^{-1}
F(000)	2040
Crystal size	0.25 x 0.20 x 0.20 mm^3
Theta range for data collection	3.89 to 27.47°.
Index ranges	-14<=h<=14, -14<=k<=14, -55<=l<=56
Reflections collected	27662
Independent reflections	2440 [R(int) = 0.1663]
Completeness to theta = 27.47°	99.5 %
Absorption correction	None
Max. and min. transmission	0.5394 and 0.4731
Refinement method	Full-matrix least-squares on F^2
Data / restraints / parameters	2440 / 2 / 140
Goodness-of-fit on F^2	1.226
Final R indices [I>2sigma(I)]	R1 = 0.0397, wR2 = 0.0866
R indices (all data)	R1 = 0.0429, wR2 = 0.0879
Largest diff. peak and hole	0.974 and -0.985 $e.Å^{-3}$

7.17: Complex 32, $[(Me_2N)_3TaNSi(NMe_2)_3]$

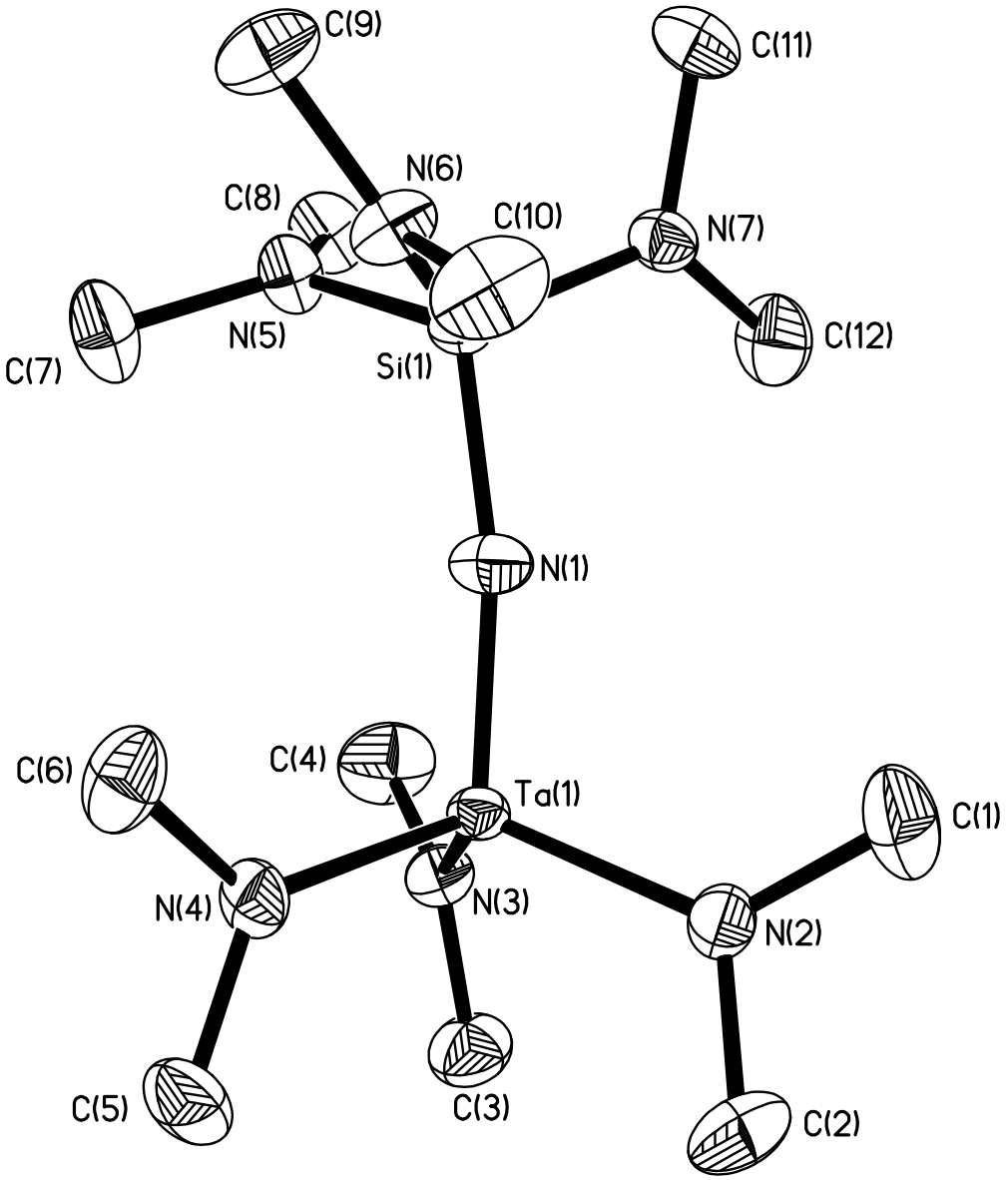

Figure 7.17: The molecular structure of the complex $[(Me_2N)_3TaNSi(NMe_2)_3]$, (**32**). Thermal ellipsoids are shown at 50% probability. Hydrogen atoms are omitted for clarity.

Table 7.17:- Crystal data and structure refinement for $[(Me_2N)_3TaNSi(NMe_2)_3]$ (**32**).

Identification code	h07alj04
Empirical formula	C12 H36 N7 Si Ta
Formula weight	487.52
Temperature	150(2) K
Wavelength	0.71073 Å
Crystal system	Monoclinic
Space group	$P2_1/n$
Unit cell dimensions	a = 8.30000(10) Å
	b = 16.4590(2) Å
	c = 15.5100(2) Å
	α= 90°.
	β= 101.8300(10)°.
	γ = 90°.
Volume	2073.81(4) $Å^3$
Z	4
Density (calculated)	1.561 Mg/m^3
Absorption coefficient	5.364 mm^{-1}
F(000)	976
Crystal size	0.20 x 0.20 x 0.17 mm^3
Theta range for data collection	7.86 to 30.50°.
Index ranges	-11<=h<=11, -23<=k<=23, -22<=l<=21
Reflections collected	31613
Independent reflections	6205 [R(int) = 0.0843]
Completeness to theta = 30.50°	98.1 %
Absorption correction	None
Max. and min. transmission	0.4537 and 0.4134
Refinement method	Full-matrix least-squares on F^2
Data / restraints / parameters	6205 / 0 / 203
Goodness-of-fit on F^2	1.047
Final R indices [I>2sigma(I)]	R1 = 0.0280, wR2 = 0.0682
R indices (all data)	R1 = 0.0384, wR2 = 0.0722
Extinction coefficient	0.0017(3)
Largest diff. peak and hole	2.337 and -2.526 $e.Å^{-3}$

7.18: Complex 33, [{MeZnNHSiPh$_3$}$_2$]

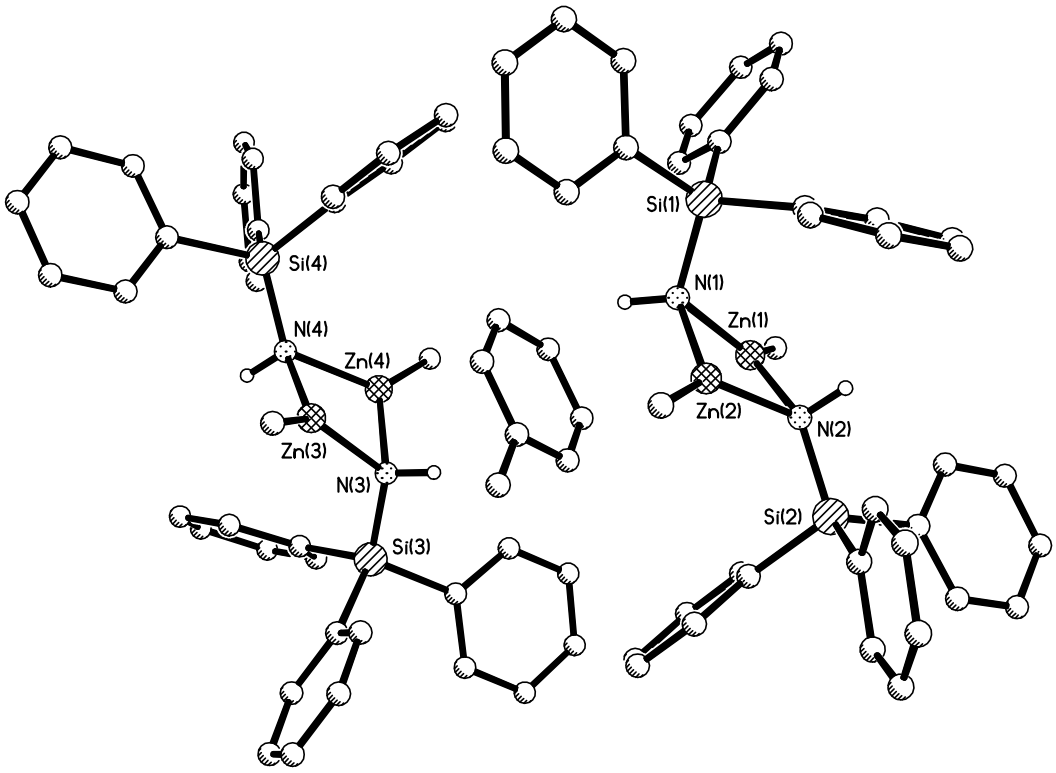

Figure 7.18.1: Asymmetric unit for the complex [{MeZn(μ_2-NHSiPh$_3$)}$_2$], **33**, containing two dimers and one molecule of toluene. Hydrogen atoms except for amido protons are omitted for clarity.

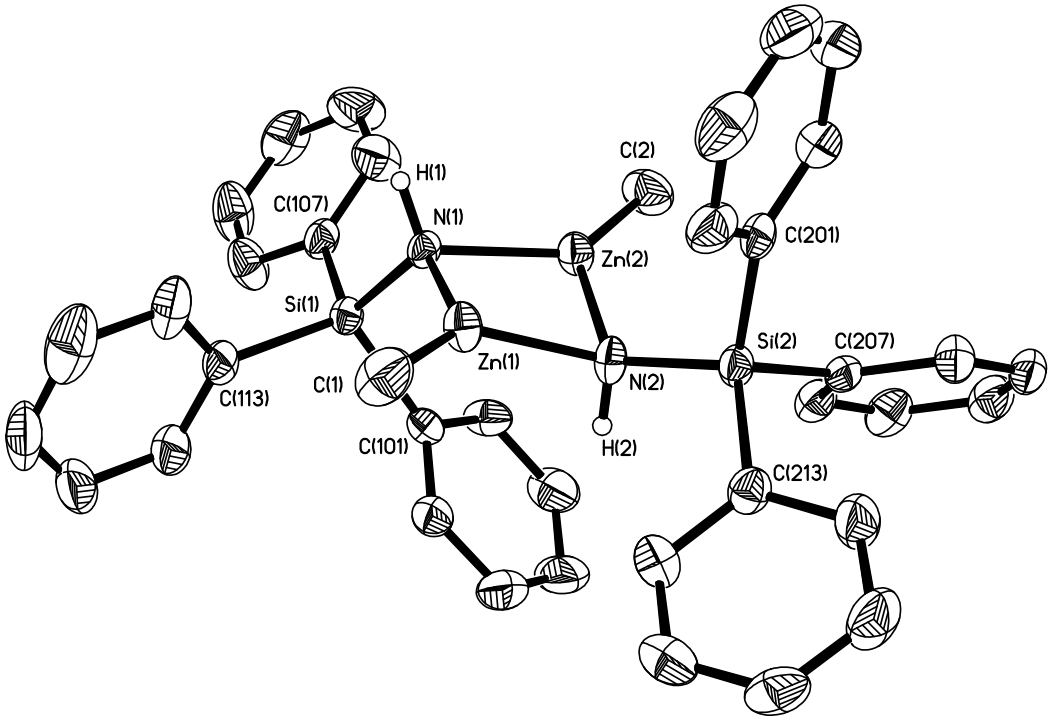

Figure 7.18.2: Molecular structure of molecule 1 of the complex [{MeZn(μ_2-NHSiPh$_3$)}$_2$], (**33**). Thermal ellipsoids are shown at 50% probability. Hydrogen atoms except for {ZnNH} amide protons are omitted for clarity.

Table 7.18:- Crystal data and structure refinement for [{$MeZnNHSiPh_3$}$_2$] (**33**).

Identification code	k07alj10
Empirical formula	C83 H84 N4 Si4 Zn4
Formula weight	1511.38
Temperature	150(2) K
Wavelength	0.71073 Å
Crystal system	Monoclinic
Space group	Cc
Unit cell dimensions	a = 26.2840(3) Å
	b = 9.4770(2) Å
	c = 32.3190(4) Å
	α= 90°.
	β= 110.2770(10)°.
	γ = 90°.
Volume	7551.5(2) $Å^3$
Z	4
Density (calculated)	1.329 Mg/m^3
Absorption coefficient	1.365 mm^{-1}
F(000)	3144
Crystal size	0.15 x 0.10 x 0.08 mm^3
Theta range for data collection	2.81 to 27.53°.
Index ranges	-34<=h<=34, -12<=k<=12, -41<=l<=41
Reflections collected	37187
Independent reflections	15351 [R(int) = 0.0594]
Completeness to theta = 27.53°	97.9 %
Absorption correction	None
Max. and min. transmission	0.8987 and 0.8215
Refinement method	Full-matrix least-squares on F^2
Data / restraints / parameters	15351 / 2 / 862
Goodness-of-fit on F^2	1.018
Final R indices [I>2sigma(I)]	R1 = 0.0485, wR2 = 0.0995
R indices (all data)	R1 = 0.0725, wR2 = 0.1144
Absolute structure parameter	0.00
Extinction coefficient	0.00000(5)
Largest diff. peak and hole	0.760 and -0.583 $e.Å^{-3}$

7.19: Complex 34, [{MeZnNHSi(NMe$_2$)$_3$}$_2$]

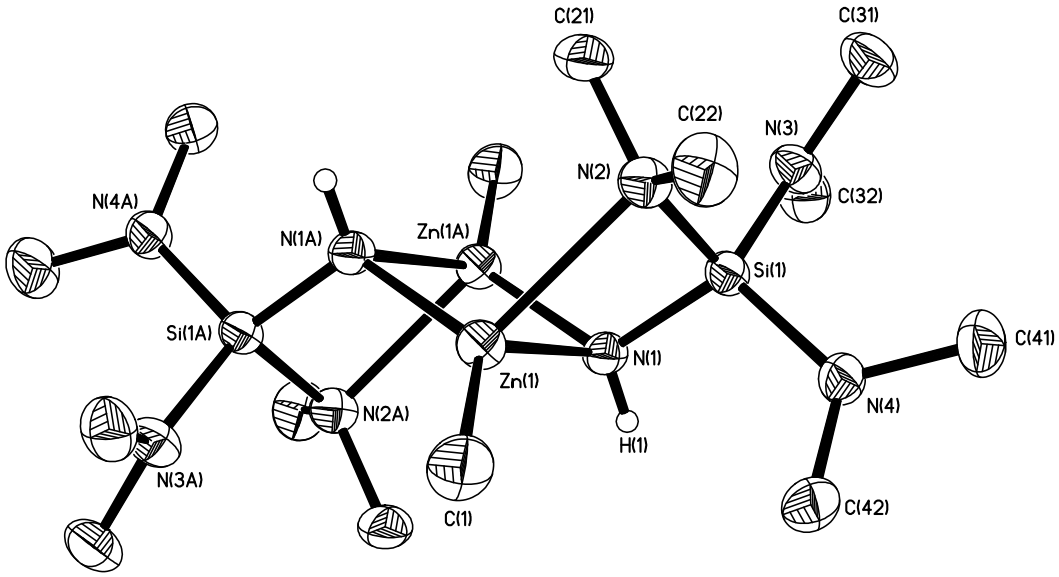

Figure 7.19: The molecular structure of the complex [MeZn{NHSi(NMe$_2$)$_3$}], (**34**). Thermal ellipsoids are shown at 50% probability. Hydrogen atoms except for {NH} amide protons are omitted for clarity.

Table 7.19:- Crystal data and structure refinement for [{MeZnNHSi(NMe$_2$)$_3$}$_2$] (**34**).

Identification code	h07alj11
Empirical formula	C7 H22 N4 Si Zn
Formula weight	255.75
Temperature	150(2) K
Wavelength	0.71073 Å
Crystal system	Monoclinic
Space group	$P2_1/c$
Unit cell dimensions	a = 7.83400(10) Å
	b = 10.0490(2) Å
	c = 15.9980(3) Å
	α= 90°.
	β= 91.4860(10)°.
	γ = 90°.
Volume	1259.00(4) Å^3
Z	4
Density (calculated)	1.349 Mg/m^3
Absorption coefficient	2.015 mm^{-1}
F(000)	544
Crystal size	0.17 x 0.10 x 0.08 mm^3
Theta range for data collection	7.93 to 30.53°.
Index ranges	-11<=h<=11, -14<=k<=14, -22<=l<=22
Reflections collected	30366
Independent reflections	3786 [R(int) = 0.0629]
Completeness to theta = 30.53°	98.1 %
Absorption correction	None
Max. and min. transmission	0.8554 and 0.7257
Refinement method	Full-matrix least-squares on F^2
Data / restraints / parameters	3786 / 0 / 130
Goodness-of-fit on F^2	1.042
Final R indices [I>2sigma(I)]	R1 = 0.0294, wR2 = 0.0717
R indices (all data)	R1 = 0.0511, wR2 = 0.0786
Extinction coefficient	0.0057(18)
Largest diff. peak and hole	0.426 and -0.492 e.Å^{-3}

7.20: Complex 35, [{(MeCp)Mn(NHSiPh$_3$)}$_2$]

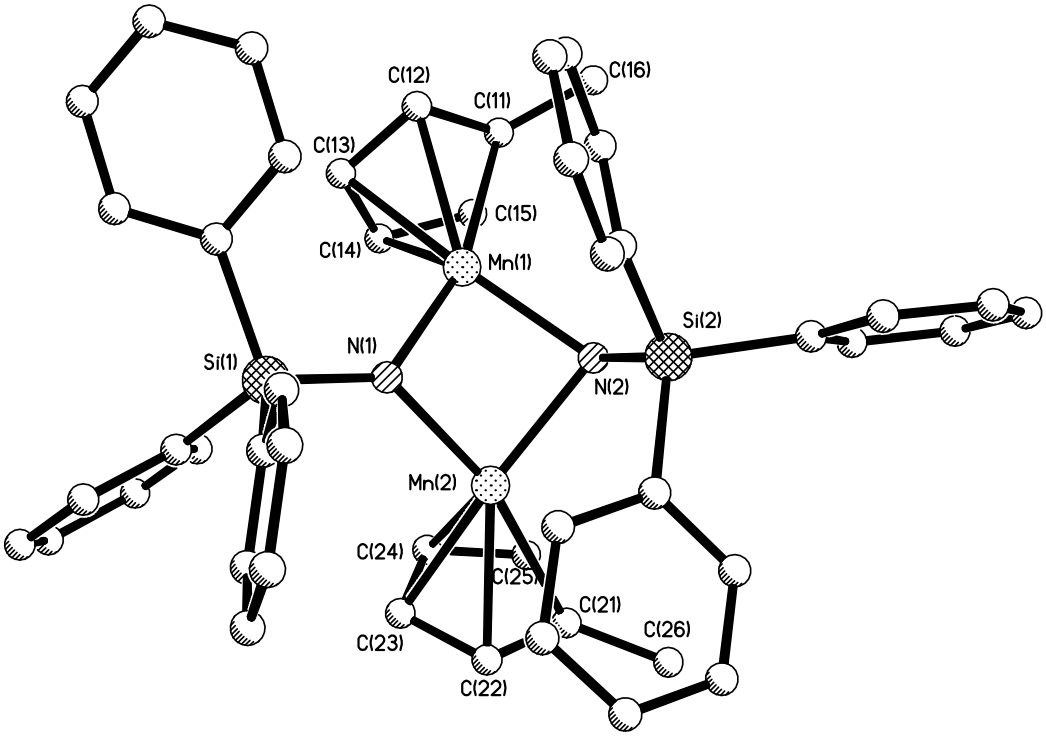

Figure 7.20.1: Asymmetric unit of the complex [(MeCp)Mn(NHSiPh$_3$)], (**35**). Hydrogen atoms are omitted for clarity.

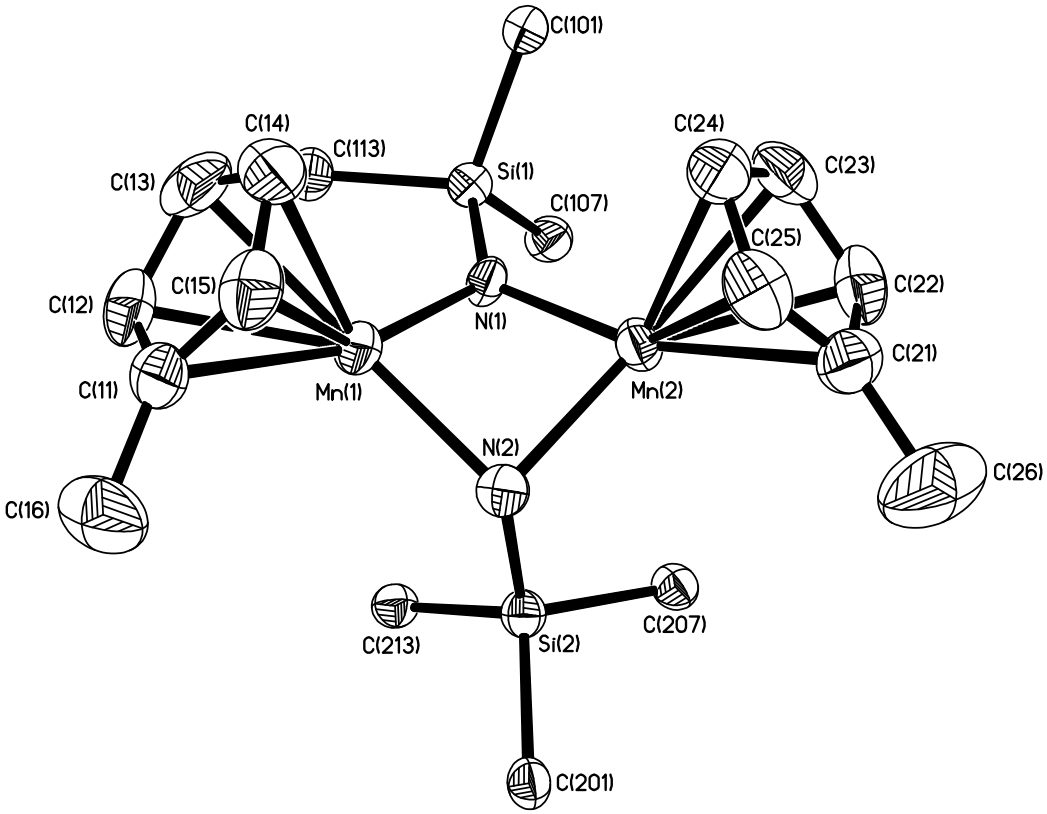

Figure 7.20.2: The molecular structure of the complex [(MeCp)Mn(NHSiPh$_3$)], (**35**). Thermal ellipsoids are shown at 50% probability. Hydrogen atoms are omitted and only *ipso*- carbon atoms displayed for the phenyl groups for clarity.

Table 7.20:- Crystal data and structure refinement for [{(MeCp)Mn(NHSiPh$_3$)}$_2$] (**35**).

Identification code	k08alj15
Empirical formula	C48 H46 Mn2 N2 Si2
Formula weight	816.93
Temperature	150(2) K
Wavelength	0.71073 Å
Crystal system	Triclinic
Space group	P-1
Unit cell dimensions	a = 9.7700(2) Å
	b = 10.8770(2) Å
	c = 19.5050(5) Å
	α= 85.3660(10)°.
	β= 86.4470(10)°.
	γ = 87.6440(10)°.
Volume	2060.66(8) Å^3
Z	2
Density (calculated)	1.317 Mg/m^3
Absorption coefficient	0.707 mm^{-1}
F(000)	852
Crystal size	0.30 x 0.20 x 0.13 mm^3
Theta range for data collection	8.52 to 30.36°.
Index ranges	-13<=h<=13, -14<=k<=15, -26<=l<=26
Reflections collected	29039
Independent reflections	10841 [R(int) = 0.0487]
Completeness to theta = 30.36°	87.3 %
Max. and min. transmission	0.9138 and 0.8160
Refinement method	Full-matrix least-squares on F^2
Data / restraints / parameters	10841 / 0 / 494
Goodness-of-fit on F^2	1.020
Final R indices [I>2sigma(I)]	R1 = 0.0470, wR2 = 0.0998
R indices (all data)	R1 = 0.0811, wR2 = 0.1168
Extinction coefficient	0.0077(19)
Largest diff. peak and hole	0.731 and -0.487 e.Å^{-3}